A MORPHABLE ENTRY SYSTEM FOR SMALL SATELLITE AEROCAPTURE AT MARS

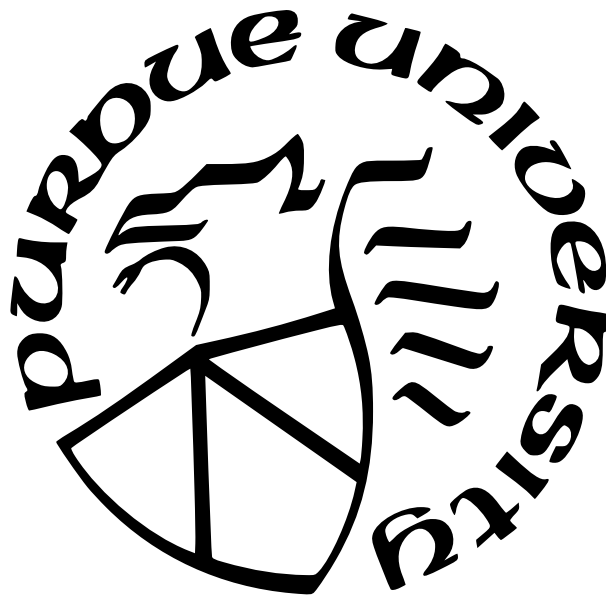by

Jannuel Vincenzo Valdez Cabrera

A Dissertation

Submitted to the Faculty of Purdue University

In Partial Fulfillment of the Requirements for the degree of

Doctor of Philosophy

School of Aeronautics and Astronautics

West Lafayette, Indiana

May 2022

THE PURDUE UNIVERSITY GRADUATE SCHOOL
STATEMENT OF COMMITTEE APPROVAL

Dr. David A. Spencer, Chair

School of Aeronautics and Astronautics

and

Jet Propulsion Laboratory, California Institute of Technology

Dr. Alina Alexeenko

School of Aeronautics and Astronautics

Dr. James Longuski

School of Aeronautics and Astronautics

Dr. Sarah D'Souza

NASA Ames Research Center

Approved by:

Dr. Gregory Blaisdell

To God,

to my parents, Vincent and Cherrylyn, and my siblings Camille, Jose Ramon, and Jillian,

to my uncles, Felipe Jose ("Binky") and Roberto ("Robert"),

and to my aunt Michaela ("Mitch").

ACKNOWLEDGMENTS

First and foremost, I would like thank my research advisor, Dr. David Spencer, for challenging me to do my best work and for dedicating time to ensure that my dissertation reached its conclusion. I also thank my committee members Dr. Alina Alexeenko and Dr. James Longuski for providing thoughtful suggestions that greatly improved this research. These individuals are all excellent educators and I feel privileged to have been their student.

I also thank my committee member Dr. Sarah D'Souza of NASA Ames Research Center, for providing additional insight into the world of deployable entry vehicles. Her mentoring during my time as an intern for the Pterodactyl project is greatly appreciated too. The knowledge I gained through that experience prepared me to perform the specialized computational analyses that were instrumental in this research.

I am also grateful to Drs. Tom West, Laura White, Pete Lillehei, and David Bennett of NASA Langley Research Center for supporting me, both as a Pathways student and as a PhD candidate. Their mentoring has allowed me to find my footing at Langley, despite the challenges brought on by the pandemic, and their flexibility in accommodating my dissertation schedule is extremely appreciated.

I would be remiss if I did not recognize and thank my colleagues from the Academic Success Center, which include Katie Dufault, Dr. Karen Jacobsen, and Mary Kirk. Their support and understanding were crucial in this effort. To my fellow graduate assistants Marquetta Strait, Laurie Sites, Sierra Longmire, and Temi Adeoye, I extend my warmest thanks and best wishes for a bright future ahead. And to the rest of my ASC teammates, past and present, know that I will fondly remember our time together.

To the friends I made in grad school including Julio Hernandez, Akshay Thomas, and the rest of the Grill and Chill crew, I offer my sincerest thanks and best wishes for continued success. I am also appreciative of my friends from the Spaceflight Projects Laboratory especially Dr. Rohan Deshmukh, Dr. Sylvain Renevey, Dr. Justin Mansell, Tom Cunningham, Mitch Wang, Arly Black, Juan Maldonado, and Sebastian Tamrazian. Our movie nights, dinner get-togethers, and "renaissance discussions" will be missed. A very special thanks to

Morgan Delaney too, whose reminder emails and AAE wizardry enabled me to stay on track with my plan of study.

To the "Patatas" (Rooney, Carolina, and Nyansafo), you hold a special place in my heart. I will never forget our dream team semester as ASC GAs. May we stay in touch through all the years ahead of us.

To the Messersmiths (Ashlee, Betsy, Noelle, and Sarena), know that you are deeply appreciated for making West Lafayette my home away from home.

To the mentors and friends I met at Syracuse University, which include Dr. John F. Dannenhoffer III, Jonathan Berk, and Ting Dong, you have my sincerest thanks for helping me rise above my greatest challenges.

To my best friends growing up in Lakehurst, NJ, including Tj Patenaude, Ryan Thomas, Stevie Ray Butler, and Christian Robinson, I am thankful to have you in my life. To the countless more that have not been named, a big thank you for being a part of my journey.

Lastly, I am deeply grateful to my whole family for their love and support through the years. To my parents Vincent and Cherrylyn, thank you for all that you did and continue to do for your children. To my siblings Camille (Ate Cel), Jose Ramon (Kuya Pipoy), and Jillian (Ading Jian), thank you for everything and know that I'm forever yours.

TABLE OF CONTENTS

LIST OF TABLES

LIST OF FIGURES

ABBREVIATIONS

ACM   apoapsis correction maneuver

ADEPT   adaptive deployable entry and placement technology

BAM   bank angle modulation

CFD   computational fluid dynamics

DEV   deployable entry vehicle

DFC   direct force control

DM   drag modulation

DSMC   direct simulation Monte Carlo

EOM   equation of motion

ESPA   Evolved expendable launch vehicle (EELV) secondary payload adapter

HIAD   hypersonic inflatable aerodynamic decelerator

ICM   inclination correction maneuver

LAURA   Langley Aerothermodynamic Upwind Relaxation Algorithm

MES   morphable entry system

MSL   Mars Science Laboratory

NASA   National Aeronautics and Space Administration

NPC   numerical predictor-corrector

P1, P4   petal 1, petal 4

PID   proportional integral derivative

PRM   periapsis raise maneuver

R2, R5   rib 2, rib 5

Smallsat   small satellite

SPARTA   Stochastic PArallel Rarefied-gas Time-accurate Analyzer

TPS   thermal protection system

VSS   variable soft sphere

3-DOF   three degrees of freedom

6-DOF   six degrees of freedom

ABSTRACT

As space agencies look to conduct more scientific missions beyond Earth orbit, low-cost access to space becomes indispensable. Small satellites (smallsats) fulfill this need as they can be developed at a fraction of the cost of traditional large satellites. Consequently, smallsats are being envisioned for planetary science missions at several destinations including Mars. However, a significant challenge for interplanetary smallsats is performing fully-propulsive orbit insertion because modern smallsat propulsion technologies have limited total velocity change (ΔV) capabilities. At destinations with significant atmospheres, this challenge can be circumvented via *aerocapture*, a technique that uses a single atmospheric pass to convert a hyperbolic approach trajectory into a captured elliptical orbit. Aerocapture has been shown to enable significant propellant mass savings as compared to fully-propulsive orbit insertion, making it an attractive choice for smallsats. Performing aerocapture with smallsats requires a suitable vehicle design that satisfies the associated control requirements and volumetric constraints. To address this requirement, this dissertation proposes the *morphable entry system* (MES), a conceptual deployable entry vehicle that utilizes shape morphing to follow a desired atmospheric flight profile during aerocapture. The aerocapture performance of the MES at Mars is investigated using a six degree-of-freedom aerocapture simulation environment. The shape morphing strategy employed by the MES is shown to be feasible for targeting desired angle of attack and sideslip angle profiles that lead to successful orbit captures. Furthermore, the robustness of the MES to simulated day-of-flight uncertainties while employing angle of attack control is demonstrated through a Monte Carlo dispersion analysis. The major contributions of this research as well as areas of future work are described.

1. INTRODUCTION

In 2018, twin CubeSats called Mars Cube One (MarCO) [1] accompanied the InSight lander mission to Mars. Before leaving the Martian system, the MarCO CubeSats relayed data provided by the lander during its entry operations back to Earth. In doing so, the MarCO CubeSats demonstrated deep space communications relay capability as well as interplanetary travel for small satellites for the first time.

Small satellites (smallsats) like CubeSats originated as low-cost platforms used by government, private, and university sectors to conduct scientific missions. Spurred by the low-cost, high-value posture they embody, the space industry has contributed significant developments to mature smallsat technologies over the first two decades of this millennium. Due to these advancements, approximately 7% of all mass launched into orbit by 2019 was made up of smallsats weighing less than 180 kg [2]. As space agencies look to conduct missions beyond Earth orbit [3], the low-cost, high-value posture embodied by smallsats becomes increasingly indispensable. By demonstrating deep space smallsat capabilities, the MarCO mission ushered in an exciting new era in which high-value planetary science can be conducted at a fraction of what it once cost with traditional large satellites.

The ongoing exploration efforts on Mars make it a likely destination for future deep space smallsat missions. Such missions would continue to support the exploration of the planet in preparation for the ultimate goal of landing humans on its surface. Human landings will benefit from the establishment of telecommunications infrastructure [4] and atmospheric observations [5] that could utilize smallsats. However, deep space smallsats need to overcome significant challenges to make planetary missions routine. The challenge that this research seeks to address is orbit insertion.

Getting into orbit around Mars is challenging for smallsats because of the large change in velocity (ΔV) required to convert the hyperbolic approach trajectory to an elliptical orbit around the planet. Recorded magnitudes of required ΔV to achieve Mars orbit insertion have ranged between 1 and 3 km/s. Prior Mars missions like Mars Reconnaissance Orbiter [6] as well as the Viking 1 and 2 orbiters [7] have achieved this level of ΔV with chemical propulsion systems. However, a mass penalty is incurred because the required propellant

mass fraction scales exponentially with ΔV, per the ideal rocket equation. An additional complication is that current smallsat propulsion systems are limited in their capability to deliver large ΔV budgets. There are exceptions, as determined by Miller et. al. [8] who found that some small chemical thrusters can deliver up to 1 km/s. Although this ΔV budget is remarkable for small propulsion systems, it is limited for insertion into certain orbit profiles (e.g., low eccentricity orbits). Combining multiple thrusters to increase the available impulse has been suggested [9], but this adds propulsion system volume that takes away from the available payload volume. This option could also force a costly upgrade to a larger launch vehicle to accommodate the volume increase. Reference [8] found that electric propulsion systems can deliver up to 2 km/s. However, this is a low-thrust solution and can lead to long transfer times that may exceed the lifetimes of on-board systems [10].

The use of atmospheric drag to slow down the smallsat is an alternative to propulsive orbit insertion. Aerobraking, for example, uses repeated passes, or "dips", through the upper atmosphere of the planet to induce drag that reduces the orbital energy of the spacecraft to lower the apoapsis altitude [11]. Successful Mars aerobraking examples include the Mars Global Surveyor (MGS) [12] and Odyssey [13] campaigns. These missions benefited from the large solar panels that acted as drag devices during aerobraking. Braking must occur high enough in the atmosphere to ensure that aerodynamic heating constraints on the drag devices are obeyed while still generating sufficient drag to lower the apoapsis after each atmospheric pass. Therefore, the drag induced per pass is incremental at best, which prolongs the aerobraking period. It took MGS [12] approximately 1300 orbits over 500 days to complete its aerobraking campaign, while Odyssey took 332 orbits over 76 days [13]. Again, the prolonged mission carries consequences concerning the lifetime of on-board systems.

The complications of propulsive orbit insertion as well as aerobraking may be circumvented through the application of aerocapture. An aerocapture vehicle utilizes a single atmospheric pass to convert a hyperbolic approach trajectory into a captured elliptic orbit. Figure 1.1 illustrates the aerocapture concept of operations. After the vehicle enters the atmosphere (1), the guidance and control system safely navigates the vehicle towards atmospheric exit (2). Then, a burn is conducted at the apoapsis of the transfer orbit (3) to raise the periapsis out of the atmosphere. A final burn is conducted at the new periapsis

(4) to correct the residual apoapsis error and allow the aerocapture vehicle to settle into the desired parking orbit (dashed line). The atmospheric drag induced between (1) and (2) provides significant ΔV that reduces the overall orbit insertion cost from thousands to only hundreds of meters per second. The single atmospheric pass is also orders of magnitude faster to perform than an aerobraking campaign.
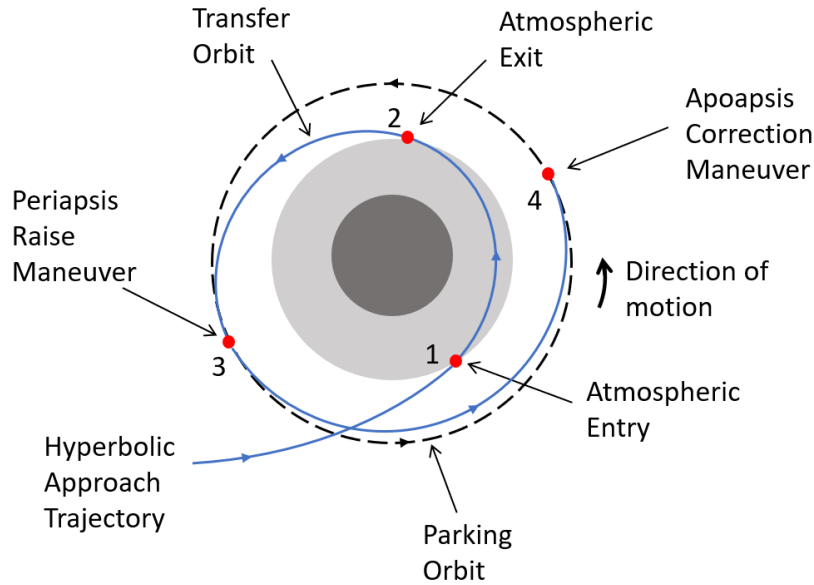
Figure 1.1. Aerocapture concept of operations.

The concept of aerocapture was proposed as early as 1961 [14], but interest waned over the years. Interest was renewed in the late 1970s when Cruz showed the propellant savings that could be achieved by robotic missions to Mars by using aerocapture [15]. In a later cost-benefit analysis, Hall et. al. [16] showed that aerocapture could achieve 15% more mass delivered to Mars circular orbit for the same delivery cost ($M/kg) as the best nonaero-capture alternative. Despite the promising benefits of aerocapture though, it has not yet been demonstrated via a flight test. Changing attitudes regarding the need for a technology demonstration has been cited as a reason [17]. Whether a flight demonstration is necessary or not is beyond the scope of the present work. However, this research fully anticipates aerocapture being implemented by smallsat systems in future planetary missions at Mars and beyond because it is a necessary technique to circumvent the challenges posed by either retropropulsion or aerobraking.

This dissertation proposes the *morphable entry system* (MES) for smallsat aerocapture at Mars. The MES is a conceptual aerocapture vehicle that uses shape morphing to follow a desired flight profile in the atmosphere. Its design and concept of operations are developed with the understanding that vehicle design should be complementary to the chosen flight control method. This research aims to investigate the performance of the MES as an aerocapture system. Achieving this objective requires the following steps: (1) develop a candidate geometry with dimensions appropriate for a smallsat payload, (2) construct an aerodynamics database of sufficient fidelity for trajectory simulations, (3) develop a control system that translates guidance system commands into shape deflections, and (4) carry out aerocapture trajectory simulations of the MES. These steps constitute the contributions of this research and are discussed in more detail in Section 1.4.

In the following sections of this chapter, a review of the state-of-the-art in aerocapture vehicle configurations and flight control methods is provided. Then, the adoption of the direct force control method in this research is discussed. The flight actuator options for implementing direct force control are then presented, after which, shape morphing is established as the actuator method employed by the MES. This chapter concludes by outlining the contributions of this research.

1.1 Aerocapture Vehicles

The atmospheric flight portion of the aerocapture maneuver is where most of the energy management occurs to ensure that the vehicle exits the atmosphere on a transfer orbit that leads to the desired parking orbit. The survival of the aerocapture vehicle during this critical stage as well as the guidance and control of the vehicle are influenced by the vehicle configuration. This section outlines different vehicle configurations that have appeared in the aerocapture literature. Two major types are considered: rigid and semi-rigid vehicles. Rigid vehicles do not undergo configuration changes during flight, while semi-rigid vehicles do.

Rigid vehicles in previous studies of aerocapture have been either blunt or slender. During the Apollo era, Repic et. al. envisioned a manned aerocapture mission at Mars using slender

bi-conic shapes, as shown in Figure 1.2 [18]. A decade later, Cruz revisited aerocapture and proposed its use to deliver unmanned robotic missions on the surface of Mars [15]. Cruz also considered rigid, slender bi-conic vehicles. These studies adopted slender vehicles because they allow for moderate to high lift-to-drag ratios ($0.5 < L/D < 1.5$) as compared to blunt capsules ($L/D < 0.3$). A higher L/D value translates to better flight control authority from the perspective of bank angle guidance, which was the flight control method of choice in these studies.

	MARS ORBITER	MARS LANDER
BASE DIAMETER	10M	10M
TOTAL LENGTH	23M	28M
ENTRY WEIGHT 1000 KG	174	204
INJECTED WEIGHT 1000 KG	190	248

Figure 1.2. Rigid bi-conic aerocapture vehicle configurations [18].

Despite this advantage, other studies have also considered blunt bodies for potential aerocapture application on Mars and other planetary destinations. For example, a NASA systems study of Martian aerocapture adopted a 70 deg blunt aeroshell configuration and paired it with bank angle guidance, despite having only a trimmed $L/D = 0.24$ [19]. The lower L/D capability was found to provide acceptable aerocapture performance. Another reason for adopting a blunt shape is that it excels at rejecting heat. As noted by Allen and Eggers in their seminal paper, the maximum convective heat rate at the nose of the vehicle is lower for blunt shapes than slender shapes [20]. Their well-known result is that the convective heat rate at the stagnation point is inversely proportional to the square root of the nose radius - the greater the nose radius, the lesser the convective heat transfer.[1]

For their heritage, rigid vehicles are relevant to aerocapture flight. However, their rigidity constrains the available payload volume. Because a deep-space smallsat is likely to fly as

---

[1]↑Note that convective heat transfer is the dominant aerodynamic heating mode on Mars entry trajectories. Radiative heating is shown to be smaller in most practical cases (see Ref. [21]).

a secondary payload on a launch vehicle, its volume allocation is limited, which precludes the use of a rigid, blunt aeroshell. This issue can be circumvented by using a deployable entry vehicle (DEV) that can be re-configured to conform to stricter volume requirements. Over the last decade, NASA has invested in the development of DEV concepts that can be stowed during launch and re-deployed before atmospheric entry to act as the decelerator. A notional view of a stowed DEV fitting within the volume allocation of an ESPA[2] ring is provided in Figure 1.3.
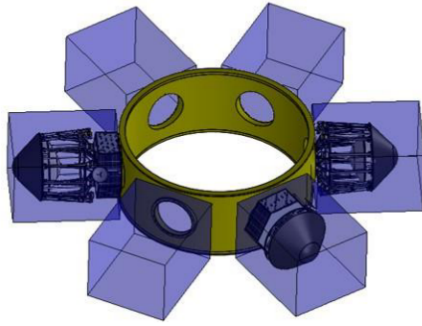
Figure 1.3. A stowed DEV can be flown to orbit as a secondary payload in an ESPA ring [23].

One of two DEV concepts under investigation at NASA is the hypersonic inflatable aerodynamic decelerator (HIAD). It consists of a rigid nose cap attached to a center body to which the inflatable structures are attached. The HIAD vehicle is capable of increasing its stowed diameter to tens of meters to increase deceleration during entry. The fully-deployed HIAD is shown in Figure 1.4(a). The HIAD's lack of a backshell leads to a significant reduction in launch and entry mass [24], which is advantageous from a launch and retropropulsion cost perspective. Because of the large diameters it can accommodate, the HIAD concept has been envisioned for precision human landings on Mars. Presently, a 6 meter diameter HIAD is scheduled to fly in 2022 on a technology demonstration mission known as the Low-Earth Orbit Flight Test of an Inflatable Decelerator (LOFTID) [25].

---

[2]↑Evolved expendable launch vehicle (EELV) secondary payload adapter (ESPA) [22].
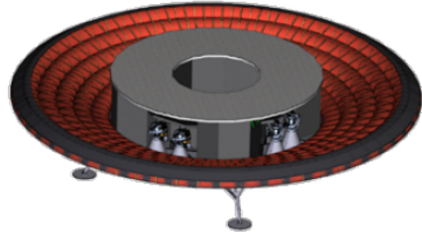
Reprinted with permission from A. Dwyer Cianciolo.   Reprinted with permission from A. Cassell.
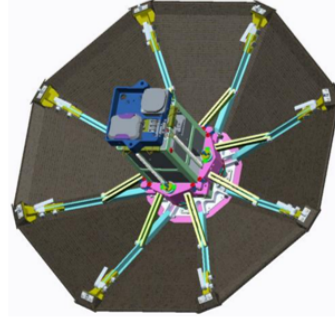
(a) HIAD [26]   (b) ADEPT [27]

Figure 1.4. The HIAD and ADEPT deployable entry vehicles.

The second DEV that NASA is investigating is the mechanically deployed adaptive deployable entry and placement technology (ADEPT) [27]. The ADEPT is an umbrella-like structure that uses a rib actuation system to deploy and retract a fabric thermal protection system as shown in Figure 1.4(b). The ADEPT vehicle has the potential benefit of delivering the same payload volume as a rigid vehicle, but with a diameter that is 3 to 4 times smaller [23]. Like the HIAD concept, ADEPT lacks a backshell, which translates to a reduction in the system's launch and entry mass.

Clearly, DEVs offer a space-saving benefit that is promising for smallsat application. Therefore, this research adopts the DEV concept for aerocapture. In the following section, potential methods of controlling an aerocapture DEV are introduced.

1.2 Flight Control Methods for Aerocapture

In the literature, the three flight control options described for aerocapture implementation are bank angle modulation (BAM), drag modulation (DM), and direct force control (DFC). Among these methods, BAM is the only one with flight heritage, having been used for guided Earth entry (Apollo [28] and Space Shuttle [29]), as well as guided Mars entry (Mars Science Laboratory [30] and Mars 2020 [31]). DM has drawn increased attention recently due to further development of the ADEPT concept as well as its perceived operational simplicity. When compared to BAM and DM, DFC is currently the least discussed control method in

the aerocapture literature. The following sections discuss each flight control method in more detail.

1.2.1 Bank Angle Modulation

In bank angle modulation (BAM), the bank angle of the vehicle is rotated about the planet-relative velocity vector to vary the direction of the lift vector as shown in Figure 1.5. Changing the lift vector's direction steers the vehicle along a desired flight path. Lift is generated primarily by flying a constant non-zero trim angle of attack.
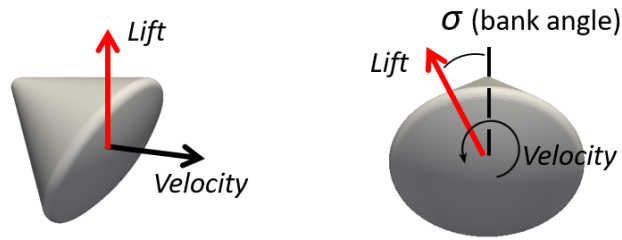
Figure 1.5. Modulating the bank angle σ changes the lift vector's orientation to steer the vehicle.

Studies of Mars aerocapture dating back to the 1960's have primarily considered BAM for trajectory control. For example, Repic et. al. [18] developed a high-L/D (L/D=1.3) biconic vehicle concept that could carry an 8-man crew to Mars and perform aerocapture. In their analysis, the vehicle modulates the bank angle to correct dispersions from an on-board reference trajectory and target desired velocity and flight path angle profiles. Cruz [15] later studied the feasibility of performing aerocapture at Mars using unmanned entry vehicles with moderate (≈ 0.8) to high (> 1.0) L/D capability. In that study, the vehicle continuously adjusts the bank angle to achieve the commanded L/D value and follow a constant reference drag value.

BAM has also been applied to blunt bodies. For example, the use of a roll control thruster system on a low L/D 70 deg rigid sphere-cone vehicle was assumed in a systems-level study of Martian aerocapture [19]. The implementation of BAM on a lifting variant of the ADEPT geometry was also investigated by Alunni et. al. [32]. The latter investigation found that BAM is a viable flight control option for a DEV.

The extensive flight heritage of BAM makes it a competitive flight control method. However, it requires reaction control system (RCS) thrusters that take up space in the aft region of a DEV. This lowers the stowage efficiency [32] and reduces the available payload volume. For mass constrained smallsats, this is an undesirable consequence.

1.2.2 Drag modulation

Another trajectory control option for aerocapture is drag modulation (DM), in which the ballistic coefficient of the vehicle is varied to modulate the energy of the vehicle and change its downrange motion during atmospheric flight. The ballistic coefficient of a vehicle, BC, is defined as

$$BC = \frac{m}{C_D A}$$

where m is the vehicle's mass, C_D is its drag coefficient, and A is the wetted area (or drag area). Decreasing the ballistic coefficient has the effect of increasing energy depletion due to drag and producing the ΔV needed for capture. Because it would be impractical to vary the mass of a vehicle, commanding changes to the effective drag area is the commonly suggested method of changing the ballistic coefficient.

A study of DM control options by Putnam and Braun [33] suggests varying the ballistic coefficient with a single-stage jettison system, a two-stage jettison system, or a continuously variable system. In a single-stage jettison system, the vehicle enters the atmosphere in a low ballistic coefficient state by deploying a drag skirt. After the proper amount of energy has been depleted, the drag skirt is jettisoned and the vehicle coasts to atmospheric exit as shown in Figure 1.6. Meanwhile, a two-stage jettison system employs two concentric drag skirts that are jettisoned in series at the appropriate times. The outer drag skirt is jettisoned first to minimize the final apoapsis error. The inner drag skirt is jettisoned later to null out any residual transfer orbit apoapsis error. This provides the two-stage jettison system additional control authority later in the trajectory unlike the single-stage jettison system. A continuously variable system utilizes a deployable-retractable drag skirt for an unlimited number of actuator events. Due to its bi-directional drag area changes, a continuously variable system promises the most control authority out of the three DM options mentioned.

Note that the proposed morphable entry system is one approach to achieving continuously variable DM.
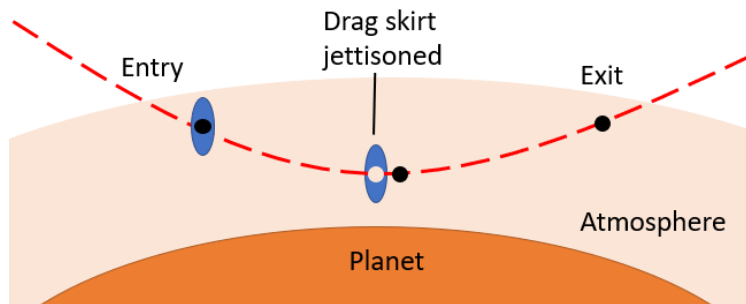
Figure 1.6. An illustration of a jettison event for drag modulation.

Earlier studies of drag modulated aerocapture (pre-2010) were primarily concerned with delivering high mass systems. Inflatable aerodynamic decelerators, referred to as "ballutes" in these studies, were heavily favored to achieve the large drag areas needed for energy dissipation and lowering the aerodynamic heating. Rohrschneider and Braun [34] surveyed ballute technology for aerocapture and identified trailing and clamped ballute concepts as the most extensively studied. Eventually, the clamped ballute concepts led to NASA's Inflatable Reentry Vehicle Experiment (IRVE) [35], which furthered the development of the modern HIAD.

More recent studies of drag modulated aerocapture have shifted focus from delivering large payloads via ballutes to delivering smallsats via rigid or deployable drag skirts. For example, Austin et. al. [36] studied the feasibility of smallsat aerocapture at Venus with a single-stage jettison concept using a rigid drag skirt with a 45 deg half-cone angle. The rigid drag skirt was chosen to reduce system complexity. The deployable ADEPT has also been proposed as an alternative to a fully rigid drag skirt for Venus and Mars aerocapture [23]. A rigid skirt with a 60 deg half-cone was also considered by Werner and Braun [37] in developing a mission architecture for an Earth demonstration of smallsat aerocapture. For Mars aerocapture, a 70 deg half-cone deployable drag skirt was assumed by Falcone et. al. [38].

When compared to BAM, DM eliminates the need for a reaction control system and center of gravity offsets while allowing for the use of only modest avionics algorithms, sensors,

and actuators [37]. However, there are disadvantages associated with DM worth noting. For example, DM does not allow for out-of-plane control during atmospheric flight. Therefore, orbit plane correction burns are necessary after atmospheric exit. This implies added propellant mass that could negatively impact the available payload volume.

DM also suffers from a lack of control authority after all the available drag skirts have been jettisoned. This is a significant drawback of single-stage systems. To alleviate this issue, Putnam and Braun [33], Roelke and Braun [39], and Roelke et. al. [40] have developed guidance architectures employing multiple jettison events (two or more stages) to extend control authority into the later portions of the trajectory. Putnam and Braun [33] and Deshmukh et al. [41] have also showed orbit targeting performance improvements offered by a continuously variable drag system. The latter also showed that a continuously variable DM system could even outperform a vehicle using BAM at several destinations including Mars.

Another notable risk of DM is post-jettison re-contact between the spacecraft and drag skirt. For reducing the risk of recontact, discretizing the drag skirt is a potential solution [37]. Other alternatives also include a rail and roller system to allow for a cleaner separation of the drag skirt from the spacecraft [36].

Despite these potential disadvantages, DM has been shown in these prior studies to provide sufficient, if not excellent, orbit insertion performance. The perceived simplicity of deploying and jettisoning a drag skirt is another reason to consider DM as a potential flight control option for smallsat aerocapture.

1.2.3   Direct Force Control

The third flight control option is direct force control (DFC), which involves modulating the aerodynamic lift and side forces of the vehicle shown in Figure 1.7. Lift modulation provides downrange control and is accomplished through changes in the angle of attack α. Side force modulation provides crossrange control and is done through changes in the sideslip angle β. DFC independently modulates these angles, which eliminates the cross-control error that arises for BAM as well as the crossrange error that arises for DM. This hints at

an increased ability to target a desired flight path and therefore less ΔV expenditures for correcting trajectory errors. Notable studies of DFC in the aeroassist literature are presented below.
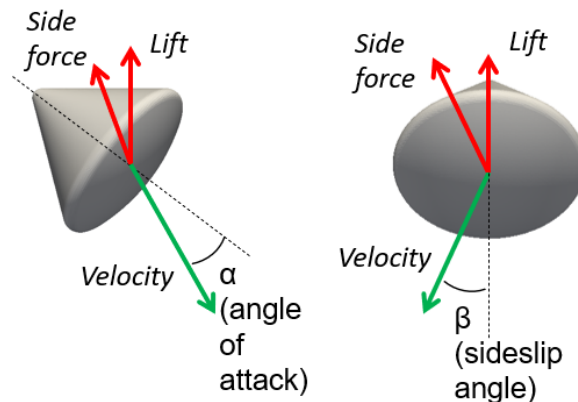
Figure 1.7. The lift and side forces are illustrated on an entry body.

Dwyer and Powell [42] investigated precision landing of a human mission with an inflatable aeroshell at Mars using DFC and BAM. They found that the independent downrange and crossrange control capability of DFC led to increased landing accuracy and propellant savings compared to BAM. Deshmukh et. al. [43] investigated the use of DFC for aerocapture of a blunt body at Neptune. They found that DFC enabled a low-L/D blunt body to perform aerocapture at Neptune with comparable performance to mid-L/D vehicles using BAM considered in previous Neptune studies like that of Lockwood et. al. [44]. Matz and Cerimele developed a numeric-predictor guidance scheme to study the aerocapture performance on Mars of human-scale entry vehicles [45], [46]. They compared the implementation of BAM and DFC on a low-L/D configuration and found that the latter control scheme resulted in less required ΔV for orbit clean-up. Deshmukh et. al. [41] performed the same comparison, but for smallsats. Their analysis also showed that DFC generally incurred less ΔV costs than either BAM or DM at Mars.

The studies above have described the increased flight path targeting performance of DFC compared to BAM and DM. This translates to ΔV savings because less fuel is needed for trajectory corrections. Less fuel would then allow for either increased science payload volume allocation or a smaller launch mass. From the perspective of a smallsat, these potential

benefits are compelling and therefore, this research will focus on the DFC flight control approach.

1.3 Flight Actuators for Direct Force Control

The following schemes have been proposed for controlling angle of attack and sideslip angle: mass shifting, aerodynamic control flaps, and shape morphing. This section outlines each method and provides corresponding examples of flight tests or studies.

1.3.1 Mass Shifting

In mass shifting, the location of the center of gravity (c.g.) of the vehicle is shifted during flight to change its trim characteristics. In 2012, NASA's Inflatable Reentry Vehicle Experiment 3 (IRVE-3) flight test successfully demonstrated the use of a c.g. offset system to alter the L/D of a HIAD. IRVE-3 demonstrated that mass shifting could potentially be used for downrange and crossrange control during direct entry of a HIAD [47]. The c.g offset (CGO) system in Figure 1.8(a) provided radial translation of the c.g during the experiment.

NASA's Pterodactyl project also studied a mass shifting control architecture for the precision entry of an ADEPT vehicle variant. Mass shifting was accomplished by moving masses along the ribs of the vehicle as shown in Figure 1.8(b). The study found that mass shifting control could not adequately follow pitch and yaw commands without exceeding packaging and mass restrictions. However, the study found that the aerodynamic flaps offered better control capability for the DEV platform [32], [48], [49].

1.3.2 Aerodynamic Control Flaps

Aerodynamic control flaps are akin to conventional trim tabs found on aircraft and can be used to induce aerodynamic moments to pitch and yaw the vehicle. Previous investigations of flap usage on entry vehicles considered their use for changing the trim characteristics with the goal of improving landing accuracy. For Earth entry, flaps have been studied as early as the 1960's for the Mercury and Apollo vehicles [50], [51]. At Mars, a configuration using a single trim tab for L/D modulation was also investigated and found to increase the landed

(a) IRVE-3 [47]. (b) Pterodactyl [49].
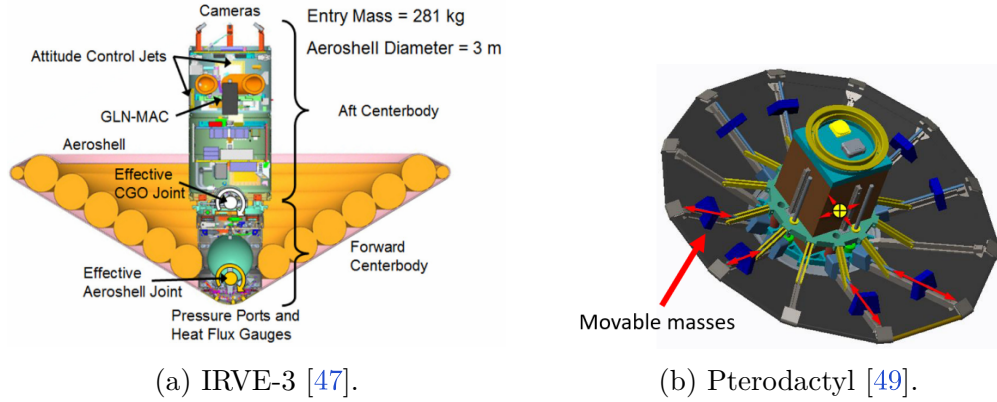
Figure 1.8. The IRVE-3 test article and the Pterodactyl conceptual design using movable masses both utilize mass shifting.

payload mass capability when compared to the landed mass of the actual MSL system, which used entry ballast masses to achieve the same L/D [52]. However, these studies have focused on using flaps to enhance BAM control.

The Pterodactyl project also investigated flaps but did so with the goal of achieving simultaneous downrange and crossrange control to increase landing accuracy [48]. Eight flaps were adjoined to an asymmetric lifting variant of the ADEPT vehicle as shown in Figure 1.9(a). The Pterodactyl group found that a flap control system for implementing DFC is feasible and offered better pitching and yawing performance than mass shifting. Because the flaps are exposed to hot gasses during operation however, their mechanical integration to the vehicle as well as the design of their thermal protection system (TPS) are significant challenges [49], [53].

Ciancolo et. al. [24] also investigated the use of flaps during Mars entry. Four flaps were envisioned on the outer edge of a 16-meter HIAD as shown in Figure 1.9(b). The flaps located at the 12 o'clock and 6 o'clock positions pitch the vehicle, while the flaps at the 3 o'clock and 9 o'clock positions yaw the vehicle. Their analysis indicated that using flaps improved the landing accuracy of a low L/D HIAD and resulted in small miss distances that were on the order of tens of meters.

(a) Pterodactyl [54].   (b) HIAD [24].
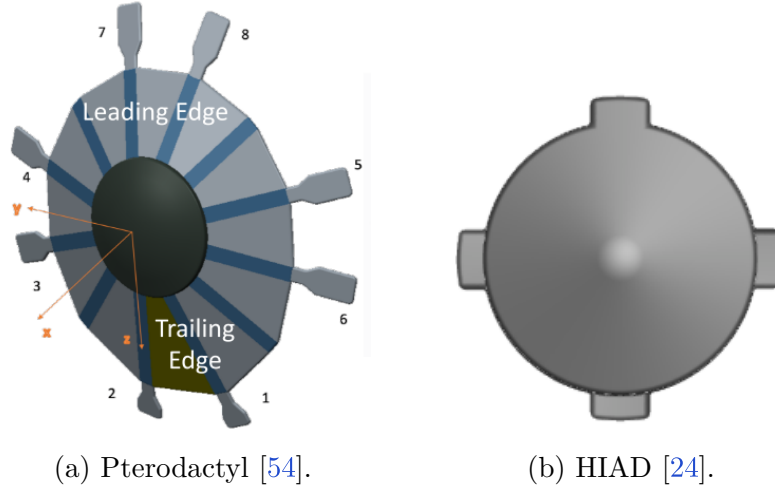
Figure 1.9. The Pterodactyl vehicle and a HIAD both utilizing flaps.

1.3.3 Shape Morphing

Shape morphing is the third flight actuation method suggested for DFC. This unique method varies the shape of the aeroshell to change the vehicle's trim state. DEVs that lack a backshell, such as HIAD and ADEPT, are suited for this actuation method. This is because the lack of a backshell enables the variation of the vehicle's outer mold line, which is impossible for rigid aeroshells with a backshell.

A morphing inflatable aeroshell has been suggested as early as 2007 by Reza et. al. [55], who conceptualized using inflatable radial beams to generate asymmetry. Their study incorporated shape morphing to generate lift for aerocapture trajectory control at Mars and Titan. Further work to advance morphing HIADs for precision landing trajectory control later followed. Green evaluated lift and drag modulation trajectory control through morphing inflatable aeroshells using a three degree-of-freedom simulation environment at Earth [56], [57]. Later, Milne-Slagle extended Green's analysis and developed a shape morphing methodology to implement DFC for precision landing on Mars [58]. Cianciolo et. al. [24] subsequently studied the landing performance of a morphing HIAD on Mars using the morphing methodology developed by Milne-Slagle. Morphing the HIAD is accomplished by pulling on straps attached to the outer edge of the structure as shown in Figure 1.10(a). A notional view of the morphed shape is shown in Figure 1.10(b).

(a) Straps for morphing.   (b) Morphed shape.
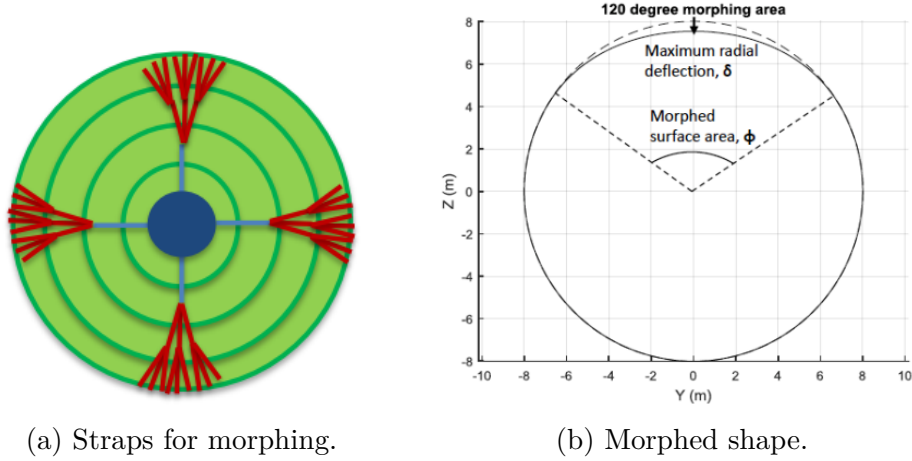
Figure 1.10. Morphing a HIAD is accomplished by pulling on straps [24].

As previously mentioned, researchers have envisioned using ADEPT for drag modulated aerocapture because of its ability to act as a drag skirt. However, the adaptable nature of this semi-rigid vehicle can also be leveraged for shape morphing to implement DFC. An earlier study of ADEPT did suggest employing differential deflection in one of its gores to achieve an asymmetric shape that produces lift for trajectory control [59]. However, there has not been a follow-up study regarding this and thus shape morphing of an ADEPT-like vehicle remains not fully understood. Perhaps the re-imagining of ADEPT as a drag modulation device has precluded further investigation. If shape morphing for aerocapture trajectory control can be shown to be feasible however, it can become a compelling alternative to aerodynamic control flaps because it negates the aerodynamic heating and structural integration issues that accompany the latter.

1.4 Research Contributions

This research focuses on DFC for smallsat aerocapture flight control because of its ΔV-saving potential. Due to smallsat volume restrictions, the available volume for control actuators is limited. Therefore, an actuator solution that does not introduce much in mass and volume is attractive. Shape morphing is one such solution because it leverages the deployable aeroshell structure for control without requiring additional parts like flaps or moving masses. However, its feasibility must be demonstrated first to warrant further technological

developments. *Therefore, the main objective of this doctoral research is to demonstrate that morphing the shape of a deployable entry vehicle is a feasible method for controlling the angle of attack and sideslip angle to enable direct force controlled aerocapture at Mars for smallsats.* The specific contributions of this research are stated below.

1.4.1 Morphable Entry System Design

A mechanically deployed DEV referred to as the morphable entry system (MES) is introduced. The MES design is inspired by the ADEPT geometry. Like ADEPT, the MES is an umbrella-like structure with panels that are connected by ribs. This concept is chosen over an inflatable system because the latter requires space for the shape morphing actuation system and the inflation system - space that a smallsat mission may not be able to afford. In contrast, the MES is envisioned to only require the shape morphing actuation system.

The morphology of the MES is also inspired by the crocus flower, a species that deploys and retracts its petals in response to temperature changes. Because of the floral inspiration, the panels of the MES geometry are referred to as "petals" in this research. These petals are envisioned to be made of flexible thermal protection system (TPS) materials. This allows the petals of the MES to be deflected from their initial fully-deployed configurations.

Deflecting the panels is accomplished by actuating the ribs connecting them. Petals are deflected away from the oncoming flow, which creates the asymmetry that produces aerodynamic moments. Pitching moments generated by deflecting panels in the pitching plane modulate the angle of attack. Similarly, yaw moments generated by panels in the yaw plane modulate the sideslip angle. Because the MES is envisioned for small satellite payloads, it is sized to adhere to the volume requirements for an ESPA-class secondary payload.

1.4.2 Static Aerodynamics Database

A static aerodynamics database for the MES geometry is developed. The database will contain aerodynamic force and moment coefficients for the different shapes that the MES can assume. Additionally, the database is a function of flow regime because the MES is expected to experience free molecular, rarefied transitional, and continuum flow conditions

as an aerocapture vehicle. Different analysis methods are employed for each flow regime including panel methods and computational fluid dynamics (CFD). Developing the database is a computationally intensive effort. To address computational limitations, a bridging relation method is employed to reduce the total number of expensive CFD calculations. Vehicle symmetry is also leveraged to further reduce computational burden.

1.4.3 Shape Morphing Control System Development

A proportional-integral-derivative (PID) controller is also developed. The PID controller ensures that the MES achieves the attitude commands that come from a guidance system. For angle of attack control, the PID controller takes as input the current state of the system and compares that to the desired state. The PID controller then outputs the proper petal deflections that the MES must employ to achieve the desired angle of attack. The same approach is taken for sideslip angle control.

Angle of attack and sideslip angle modulation will be demonstrated through numerical simulation of the fully non-linear rotational equations of motion of a rigid body. Given a target attitude state, the PID controller will be employed to generate the proper petal deflections. The system response to the commanded deflections will be numerically propagated in time using the rotational equations of motion. The PID controller performance will be assessed during these simulations and adjustments, where necessary, will be made to ensure that the controller can accurately follow the targeted attitudes.

1.4.4 Simulations of Aerocapture via Shape Morphing

The aerodynamics database and PID controllers are integrated into an aerocapture simulation framework developed by Deshmukh [60]. The framework employs a numerical predictor-corrector (NPC) guidance algorithm that determines the proper angle of attack and sideslip angle profiles that yield minimized post-atmospheric ΔV impulses required to achieve the target orbit. The framework was originally developed to simulate three degree-of-freedom (3-DOF) trajectories. This research extends the framework by adding the three rotational degrees of freedom to enable six degree-of-freedom (6-DOF) simulations. To the

author's knowledge, no prior 6-DOF study of a smallsat aerocapture vehicle employing shape morphing control exists.

6-DOF aerocapture simulations are carried out to assess the capability of the MES to modulate angle of attack and sideslip angle through shape morphing. The simulations are expected to yield information on the ΔV performance of this control approach. A Monte Carlo dispersion analysis is also carried out to assess the robustness of the MES to day-of-flight uncertainties. Lastly, challenges associated with the application of the MES for aerocapture trajectory control are also discussed.

1.5   Dissertation Outline

In Chapter 2, the development of the MES design and concept of operations are described. Then, the mathematical modeling employed to construct a 6-DOF simulation environment are presented in Chapter 3. This is followed by the presentation of aerocapture simulation results in Chapter 4. A discussion of the performance and limitations of the MES are also given. Chapter 5 provides concluding remarks as well as research areas that warrant future investigation.

2. MORPHABLE ENTRY SYSTEM

The design of the morphable entry system (MES) is presented in this chapter. A history of the design process is provided to explain the changes that led to the finalized conceptual design. The configuration changes employed by the MES to implement shape morphing for DFC are also explained. Because the objective of this dissertation is to study the feasibility of shape morphing for DFC, a detailed mechanical design of the system that would accomplish the envisioned shape deflections is not within the scope of the current investigation.

2.1 Initial Designs

A bio-inspired design approach during the early stages of this research led to the discovery of the crocus flower shown in Figure 2.1. The crocus flower opens its petals in response to a rise in temperature [61]. A drop in temperature, like that experienced when night draws near, leads the flower to close its petals. This process, called thermonasty, allows diurnal pollinators to access the pollen inside the crocus while also protecting it from cold and dewy evenings.[1] The deployment and retraction of the crocus petals inspired the question, "What if an entry vehicle morphed its shape like the crocus flower to control its flight path?" Since the discovery of the crocus flower, an effort was made to retain a bio-inspired aspect to the development of the MES. This is how each panel of the final MES design came to be referred to as a "petal".

Figure 2.1. A crocus flower[3]

Using the crocus flower as a launch point, the introductory design of the MES featured a spherical nose cap and five ribs connected by webbing, as shown in Figure 2.2. The five ribs that extend beyond the edges of the webbing were intended to imitate the petals of the crocus flower. In this design, the ribs are to be deflected away from the flow to induce an aerodynamic moment to change the vehicle attitude. The webbing connected to the deflected ribs would also deflect away from the flow.
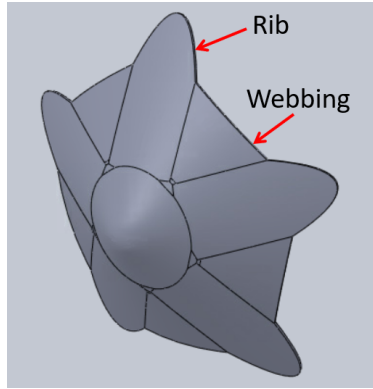
Figure 2.2. The first design of the MES.

Ultimately, this design was deemed problematic because its asymmetry did not allow for pitch and yaw to be completely decoupled. To illustrate this, consider the front view of the initial design shown in Figure 2.3. In this case, a rib 1 deflection deflects equal surface areas on either side of the $x - z$ plane. This results in rotational motion purely in the pitch plane. Consider now deflecting rib 2 to yaw the vehicle. The surface area differential created on either sides of the Rib 2 plane are also equal and therefore, rotational motion would also be contained in this plane. However, the Rib 2 plane is not parallel to either pitch or yaw planes. Therefore, a rib 2 deflection introduces coupled pitching and yawing motion. The same pitch-yaw coupling would also result from deflecting ribs 3 to 5. Because of this coupling, designing a control system to target a desired sideslip angle without changing the angle of attack, or vice-versa, would be challenging. Consequently, implementing DFC would also be challenging with this vehicle design.

---

[3]https://www.flickr.com/photos/158350039@N03/26340253247
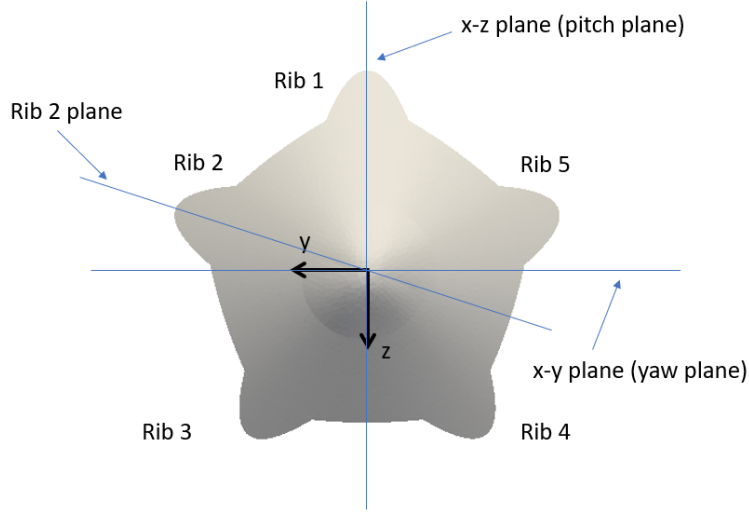
Figure 2.3. Front view of the initial 5-petal MES design.

To circumvent the issue above, a sixth rib was added to the foreshell configuration to introduce symmetry, as shown in Figure 2.4. In this design update, a simultaneous rib 1 and 6 deflection away from the flow pulls petal 1 away from the flow to pitch the nose down (a rotation about the $-y$ axis). For this petal 1 deflection, the surface area deflection is equal on both sides of the pitching plane, which means that motion is contained within that plane. Similarly, a rib 2 deflection that pulls petals 2 and 3 away from the flow causes the vehicle to yaw about the $-z$ axis. Because the surface area deflections are again equal on both sides of the yaw plane, the motion is contained within that plane. Therefore, this design update allowed for pitch and yaw to be decoupled.
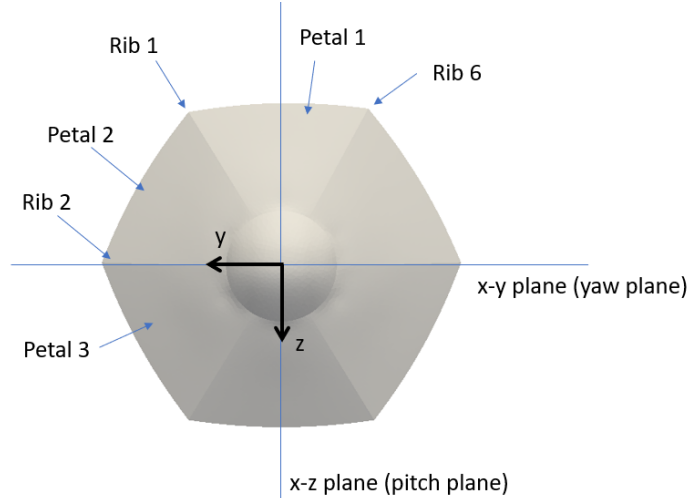
Figure 2.4. Front view of the second design.

The gaps between the ribs created by the shorter intermediate webbing were also eliminated from the preliminary design. This was done to prevent potentially severe aerodynamic heating from occurring at the corners where the ribs and webbing connect. Eliminating the gaps also prevents the potential of flow impinging upon the payload behind the foreshell at higher incidence angles. During the development of the second design, dimensions of the small-scale ADEPT test article called Nano-ADEPT [62] were used as a baseline. This research adopted the following dimensions inspired by Nano-ADEPT: a 0.30 m nose cap radius and a deployed diameter of approximately 1 m.

The second design iteration featured a raised nose cap, which produced a compression corner at the nose-to-petal transition point, as shown in Figure 2.5. This compression corner was deemed undesirable because it introduced the risk of severe aerodynamic heating during flight. To address this concern, the transition point connecting the spherical nose cap to the rib-petal assembly was moved closer to the tip of the nose as illustrated in Figure 2.6. This eliminated the compression corner by creating a smooth transition between the nose cap and petal surfaces. This was the final major design update made to the MES.
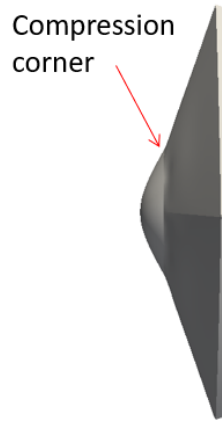
Figure 2.5. The compression corner on the second design is shown.
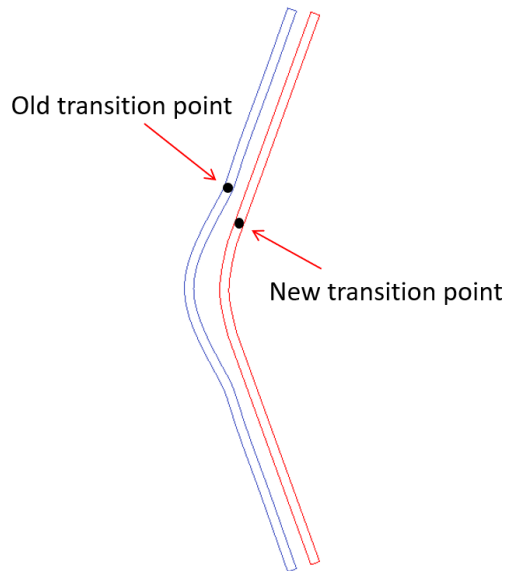
Figure 2.6. A side view slice of the MES illustrating the translation of the nose-to-petal transition point towards the nose.

2.2 Final Conceptual Design

The third and final design of the MES is shown in Figure 2.7. The foreshell is comprised of six petals adjoined by six ribs and a spherical nose cap. The dimensions of the stowed configuration shown in Figure 2.8 can fit within the payload volume allocated to a single port of the standard Evolved Expendable Launch Vehicle (EELV) Secondary Payload Adapter

(ESPA) ring. Note that each standard ESPA ring port can accommodate a 0.61 m × 0.71 m × 0.97 m volume [22]. In the fully deployed configuration shown in Figure 2.8, the rib and petal surfaces are oriented at 70 deg with respect to the local horizontal direction. Note that the local horizontal direction is parallel with the x-axis that points out of the nose, as shown in Figure 2.9.[4] This design decision was derived from the 70 deg sphere-cone aeroshells of previous Mars missions such as Pathfinder [63] and Mars Science Laboratory (MSL) [64]. The ribs connecting the petals are each 0.609 m in length from the nose transition point to the outer tip. The maximum diameter measured rib tip to rib tip is 1.35 m as shown in Figure 2.8.
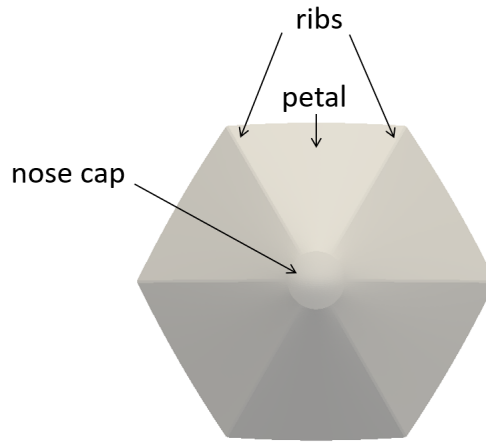
Figure 2.7. The anatomy of the final MES design.

---

[4]↑An alternative definition is that the angle between the outward normal vector of each rib/petal surface and the body x-axis is 20 deg when the ribs and petals are fully deployed.
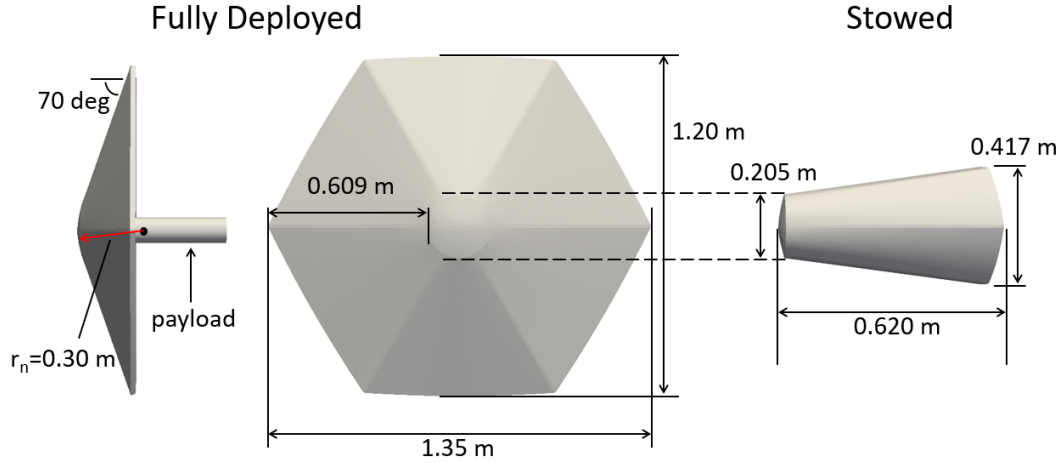
Figure 2.8. The dimensions of the final MES design.

The petal and rib numbering system is illustrated in Figure 2.9(a). To create aerodynamic moments for trajectory control, a set of ribs are actuated to form an asymmetric shape. For example, ribs 1 and 6 are actuated to deflect petals 1, 2, and 6 away from the flow as seen in Figure 2.9(b). This deflection results in a negative pitching moment that modulates angle of attack (α) negatively (i.e., nose down). The opposite strategy of actuating ribs 3 and 4 to deflect petals 3, 4, and 5 would generate a positive pitching moment that modulates α positively (i.e., nose up). For simplicity, the deflection of petals 1, 2, and 6 to decrease α is referred to as a "P1 deflection", as shown in Figure 2.9(b). Similarly, the deflection of petals 3, 4, and 5 is referred to as a "P4 deflection".

(a) Petal and rib numbering system

(b) Petal and rib deflection
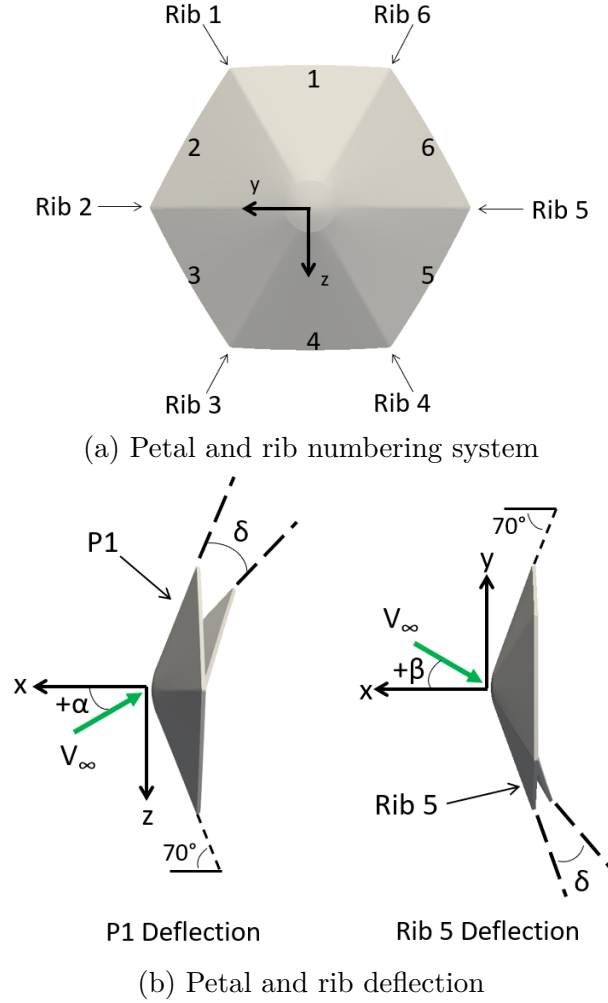
Figure 2.9. The petal and rib numbering system and deflection strategies are shown.

Yawing motion is achieved by deflecting petals 2 and 3 or 5 and 6 away from the flow. Actuating rib 2 to deflect petals 2 and 3 simultaneously causes a negative yaw moment that increases the sideslip angle (β) (i.e., nose left). Conversely, actuating rib 5 to deflect petals 5 and 6, as shown in Figure 2.9(b), produces a positive yaw moment that decreases β (i.e., nose right). Once again for simplicity, these deflections are referred to as "R2 deflection" and "R5 deflection", respectively.

Petals are kept at their original 70 deg orientations when not used to control the vehicle. When a petal is deflected by the angle δ, the length from its tip to the nose cap transition point is assumed to remain fixed. However, the petal's wetted area, as seen by the flow, will change due to the deflection as illustrated in Figure 2.10. The surface area differential

between the upper and lower halves of the MES creates the aerodynamic moments used for trajectory control.

Neither a formal TPS sizing study nor a rib actuator design study were conducted as they were deemed to be beyond the scope of this research. Instead, this research assumes that a flexible thermal protection system (TPS) suited for DEVs [59], [65], [66] can accommodate the petal deflections and remain taut. It is also assumed that a rib deployment system could be designed and sized to achieve the envisioned deflections of the MES geometry. The recent ADEPT sounding rocket flight test successfully demonstrated aeroshell deployment via a rib-strut mechanical system [27]. A similar mechanical subsystem could be employed by the MES.
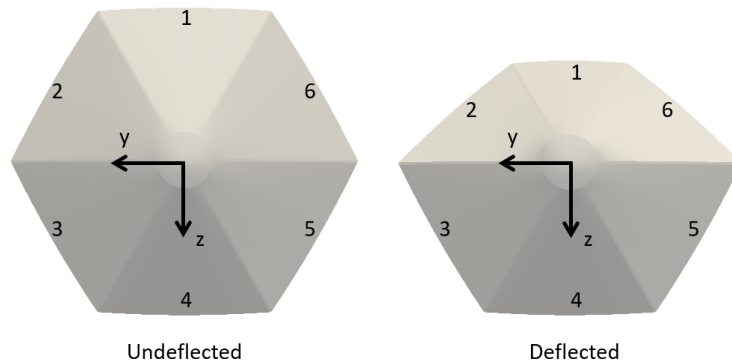
Figure 2.10. A P1 deflection changes the surface area seen by the incoming flow.

There are potential advantages of the MES over other DEV concepts employing DFC. For example, the rib actuation system for the MES is anticipated to be lighter than the control actuator system of a morphing HIAD concept. This is because the latter requires an inflation system in addition to the shape morphing actuation system (e.g., strap system studied in Ref. [58]). The reduced control system mass fraction for the MES would then allow for additional mass allocations to be dedicated to other subsystems and the payload. When compared to the ADEPT concept employing a flap control system, the MES avoids exposing actuators with small leading edges to the hypersonic flow thereby eliminating aerodynamic heating and structural integration concerns [49].

3. MATHEMATICAL MODEL

This chapter presents the mathematical modeling used to enable aerocapture simulations of the MES. First, the six degree-of-freedom (6 DOF) equations of motion (EOMs) for atmospheric flight of a planetary entry vehicle are presented in Section 3.1. It is shown that aerodynamic forces are inputs to the EOMs. Therefore, an aerodynamics model for the MES was also developed and is presented in Section 3.2. Simulating the actuation of the MES' petals to control the atmospheric flight path also requires a dedicated control system, which is developed in Section 3.3.

3.1 Atmospheric Flight Mechanics

This section derives the equations governing the translation and rotation of the MES during its flight in the Martian atmosphere.

3.1.1 Translational Motion

The translational EOMs are composed of the kinematics equations, which describe the time evolution of the vehicle's position vector, and the force equations, which describe the time evolution of the vehicle's velocity vector. The independent variables of the EOMs are the magnitude of the radius vector (r), longitude (θ), latitude (ϕ), the magnitude of the velocity vector (V), flight-path angle (γ), and heading angle (ψ). Together, these six quantities make up the planet-relative state variables illustrated in Figure 3.1.
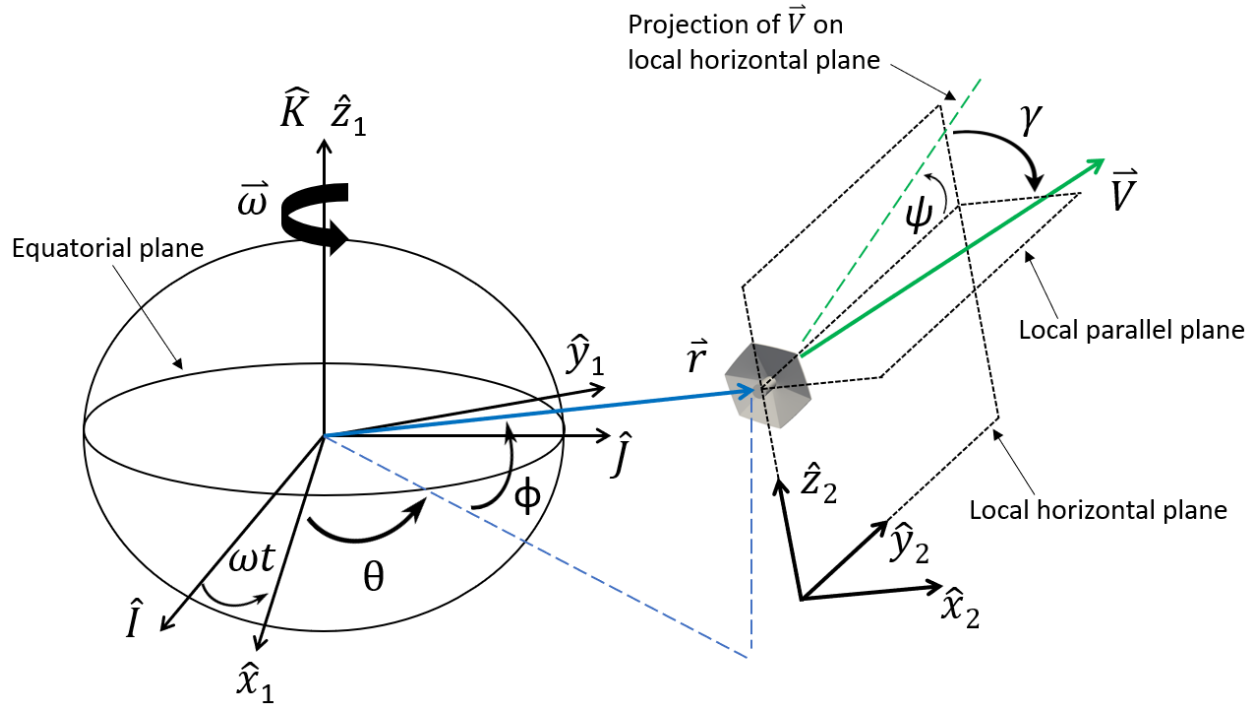
Figure 3.1. The planet-relative state variables.

Because the motion of the aerocapture vehicle is completely restricted within the sphere of influence of the target planet, it is instructive to express the EOMs relative to a planet-fixed coordinate frame defined as follows. Let the vector basis $\{\hat{I}, \hat{J}, \hat{K}\}$ in Figure 3.1 correspond to a non-moving inertial frame of reference with its origin fixed at the center of the planet. $\hat{I}$ points along the vernal equinox, $\hat{K}$ is directed out of the north pole, and $\hat{J}$ completes the orthogonal triad such that $\hat{K}$ is normal to the equatorial plane. Now let the vector basis $\{\hat{x}_1, \hat{y}_1, \hat{z}_1\}$ correspond with the planet-fixed coordinate frame, which rotates with the planet at a constant angular velocity given by $\vec{\omega} = \omega\,\hat{z}_1$. It is assumed that $\{\hat{I}, \hat{J}, \hat{K}\}$ and $\{\hat{x}_1, \hat{y}_1, \hat{z}_1\}$ are initially aligned. As the planet-fixed frame rotates, the angle between $\hat{I}$ and $\hat{x}_1$ is given by ωt, where t is the elapsed time. The planet-relative state variables are thus referenced with respect to $\{\hat{x}_1, \hat{y}_1, \hat{z}_1\}$.

The position of the vehicle is described by $\vec{r}$, θ, and ϕ, which are shown in Figure 3.1. The magnitude of $\vec{r}$ gives the distance of the vehicle measured from the origin of the planet-fixed frame. The angle that the projection of $\vec{r}$ on the equatorial plane makes with $\hat{x}_1$ corresponds

with the longitude, θ. Furthermore, the angle between $\vec{r}$ and the equatorial plane is given by the latitude, ϕ. Note that θ is measured positively in the right-handed direction about the $\hat{z}_1$ axis, while ϕ is measured positively above the equator.

The planet-relative velocity can be described by $\vec{V}$, γ, and ψ. The magnitude of $\vec{V}$ is the speed of the vehicle seen by an observer standing at the origin of the $\{\hat{x}_1, \hat{y}_1, \hat{z}_1\}$ frame. The flight path angle γ is the angle between $\vec{V}$ and the local horizontal plane. The heading angle ψ is the angle made by the projection of $\vec{V}$ on the local horizontal plane with the local parallel plane.[1] As shown in Figure 3.1, γ is positive above the local horizontal plane (away from the planet), while ψ is measured positively in the right-handed direction about $\vec{r}$. Based on these geometric definitions, γ indicates how much $\vec{V}$ contributes to the vehicle's ascent or descent along $\vec{r}$, while ψ indicates whether $\vec{V}$ moves the vehicle toward or away from the equator [67].

The kinematics equations that describe the time evolution of r, θ, and ϕ are now derived. Consider the orthogonal basis $\{\hat{x}_2, \hat{y}_2, \hat{z}_2\}$ shown in Figure 3.1, where $\hat{x}_2$ is aligned with the position vector and the $\hat{y}_2$-$\hat{z}_2$ plane corresponds with the local horizontal plane. For ease of reference, let this secondary basis be called the "local horizon frame". To get to the local horizon frame from the planet-fixed frame, a rotation about $\hat{z}_1$ by the angle θ is made followed by a rotation about $-\hat{y}_2$ by the angle ϕ. The resulting transformation equation is:

$$\begin{Bmatrix} \hat{x}_2 \\ \hat{y}_2 \\ \hat{z}_2 \end{Bmatrix} = \begin{bmatrix} \cos\theta\cos\phi & \sin\theta\cos\phi & \sin\phi \\ -\sin\theta & \cos\theta & 0 \\ -\cos\theta\sin\phi & -\sin\theta\sin\phi & \cos\phi \end{bmatrix} \begin{Bmatrix} \hat{x}_1 \\ \hat{y}_1 \\ \hat{z}_1 \end{Bmatrix} \tag{3.1}$$

The rotation sequence also results in the following angular velocity vector describing the rotation of the local horizon frame relative to the planet-fixed frame:

$$\vec{\Omega} = \dot{\theta}\hat{z}_1 - \dot{\phi}\hat{y}_2 \tag{3.2}$$

_____

[1] ↑ The local horizontal frame is perpendicular to $\vec{r}$ whereas the local parallel plane is parallel with $\vec{r}$.

Using Eq. 3.1, this expression can be rewritten and expressed wholly in the local horizon frame:

$$\vec{\Omega} = \dot{\theta} \sin \phi \, \hat{x}_2 - \dot{\phi} \, \hat{y}_2 + \dot{\theta} \cos \phi \, \hat{z}_2 \tag{3.3}$$

Expressing the radius vector of the vehicle in the local horizon frame provides:

$$\vec{r} = r \, \hat{x}_2 \tag{3.4}$$

The time-derivative of $\vec{r}$ seen by an observer at the origin of the planet-fixed frame, but expressed in the local horizon frame, is obtained via the transport theorem (or basic kinematic equation):

$$^1\frac{d\vec{r}}{dt} = {}^2\frac{d\vec{r}}{dt} + \vec{\Omega}^{2/1} \times \vec{r} \tag{3.5}$$

In Eq. 3.5, the superscripts 1 and 2 signify that the derivative is with respect to the planet-fixed and local horizon frames, respectively. Also, $\vec{\Omega}^{2/1}$ is the angular velocity of the local horizon frame with respect to the planet-fixed frame. Inserting Eqs. 3.3-3.4 into Eq. 3.5 and carrying out the vector algebra provides:

$$^1\frac{d\vec{r}}{dt} = \dot{r} \, \hat{x}_2 + r\dot{\theta} \cos \phi \, \hat{y}_2 + r\dot{\phi} \, \hat{z}_2 \tag{3.6}$$

Eq. 3.6 expresses the planet-relative rate of change of $\vec{r}$ in the local horizon frame.

From Figure 3.1, the velocity vector $\vec{V}$ expressed in the local horizon frame is:

$$\vec{V} = V \sin \gamma \, \hat{x}_2 + V \cos \gamma \cos \psi \, \hat{y}_2 + V \cos \gamma \sin \psi \, \hat{z}_2 \tag{3.7}$$

Equating the individual components of Eqs. 3.6-3.7 gives the following:

$$\dot{r} = V \sin \gamma$$
$$r\dot{\theta} \cos \phi = V \cos \gamma \cos \psi$$
$$r\dot{\phi} = V \cos \gamma \sin \psi$$

Solving for the time derivatives finally yields the kinematics equations governing the position of the entry vehicle with respect to the planet:

$$\dot{r} = V \sin \gamma \tag{3.8}$$

$$\dot{\theta} = \frac{V \cos \gamma \cos \psi}{r \cos \phi} \tag{3.9}$$

$$\dot{\phi} = \frac{V \cos \gamma \sin \psi}{r} \tag{3.10}$$

The force equations will now be derived from Newton's second law, $\sum \vec{F} = m\vec{a}$. The acceleration vector $\vec{a}$ must be taken with respect to an inertial frame of reference to correctly apply Newton's law. Recall that acceleration is the second time-derivative of the position. Because intermediate frames like the planet-fixed frame were set up to easily express vector quantities, the transport theorem must again be employed to ensure that the correct inertial derivatives are obtained. The velocity vector is obtained from the planet-relative $\vec{r}$ as follows:

$$^{I}\vec{V} = \frac{^{I}d\vec{r}}{dt} = \frac{^{1}d\vec{r}}{dt} + \vec{\omega}^{1/I} \times \vec{r} \tag{3.11}$$

where the superscripts I and 1 signify that the derivative is taken with respect to the inertial and planet-fixed frames, respectively. Additionally, $\vec{\omega}^{1/I}$ is the constant angular velocity of the planet-fixed frame with respect to the inertial frame shown previously in Figure 3.1. The acceleration is obtained by taking the derivative of $^{I}\vec{V}$ and applying the transport theorem again:

$$
\begin{aligned}
^{I}\vec{a} = \frac{^{I}d\vec{V}}{dt} &= \frac{^{1}d\vec{V}}{dt} + \vec{\omega}^{1/I} \times \vec{V} \\
&= \frac{^{1}d}{dt}\left[\frac{^{1}d\vec{r}}{dt} + \vec{\omega}^{1/I} \times \vec{r}\right] + \vec{\omega}^{1/I} \times \left[\frac{^{1}d\vec{r}}{dt} + \vec{\omega}^{1/I} \times \vec{r}\right] \\
&= \frac{^{1}d^{2}\vec{r}}{dt^{2}} + 2\vec{\omega}^{1/I} \times \frac{^{1}d\vec{r}}{dt} + \vec{\omega}^{1/I} \times (\vec{\omega}^{1/I} \times \vec{r})
\end{aligned} \tag{3.12}
$$

where $\omega^{1/I} \times (\vec{\omega}^{1/I} \times \vec{r})$ is the centripetal acceleration and

$$2\vec{\omega}^{1/I} \times \frac{^{1}d\vec{r}}{dt}$$

is the Coriolis acceleration. With the acceleration vector formulated in Eq. 3.12, Newton's law can be rewritten as follows:

$$\sum \vec{F} = m \frac{{}^I d\vec{V}}{dt} = m \left[\frac{{}^1 d^2 \vec{r}}{dt^2} + 2\vec{\omega}^{1/I} \times \frac{{}^1 d\vec{r}}{dt} + \vec{\omega}^{1/I} \times (\vec{\omega}^{1/I} \times \vec{r}) \right] \qquad (3.13)$$

Isolating the planet-relative acceleration vector on one side gives the following:

$$m \frac{{}^1 d^2 \vec{r}}{dt^2} = \sum \vec{F} - 2m\vec{\omega}^{1/I} \times \frac{{}^1 d\vec{r}}{dt} - m\vec{\omega}^{1/I} \times (\vec{\omega}^{1/I} \times \vec{r}) \qquad (3.14)$$

Note that the above derivatives are with respect to the rotating planet-fixed frame as indicated by the superscript 1. Eq. 3.14 is important because it is the source of the desired force equations. However, these equations are not yet ready to "fall out" of Newton's law as the external forces acting on the vehicle also need to be formulated. These external forces are the aerodynamic forces (drag, side force, and lift) and the gravitational force.

The aerodynamic forces are more easily described by introducing another reference frame. A two-rotation sequence about $\hat{x}_2$ and $-\hat{z}_2$ by the angles ψ and γ, respectively, results in the coordinate frame $\{\hat{x}_F, \hat{y}_F, \hat{z}_F\}$ shown in Figure 3.2 (referred to here as the "force frame"). In this new frame, $\hat{y}_F$ is aligned with the planet-relative velocity vector, $\hat{z}_F$ lies in the local horizontal plane, and $\hat{x}_F$ completes the right-handed triad. The local horizon and force frames are related as follows:

$$\begin{Bmatrix} \hat{x}_F \\ \hat{y}_F \\ \hat{z}_F \end{Bmatrix} = \begin{bmatrix} \cos\gamma & -\sin\gamma\cos\psi & -\sin\gamma\sin\psi \\ \sin\gamma & \cos\gamma\cos\psi & \cos\gamma\sin\psi \\ 0 & -\sin\psi & \cos\psi \end{bmatrix} \begin{Bmatrix} \hat{x}_2 \\ \hat{y}_2 \\ \hat{z}_2 \end{Bmatrix} \qquad (3.15)$$
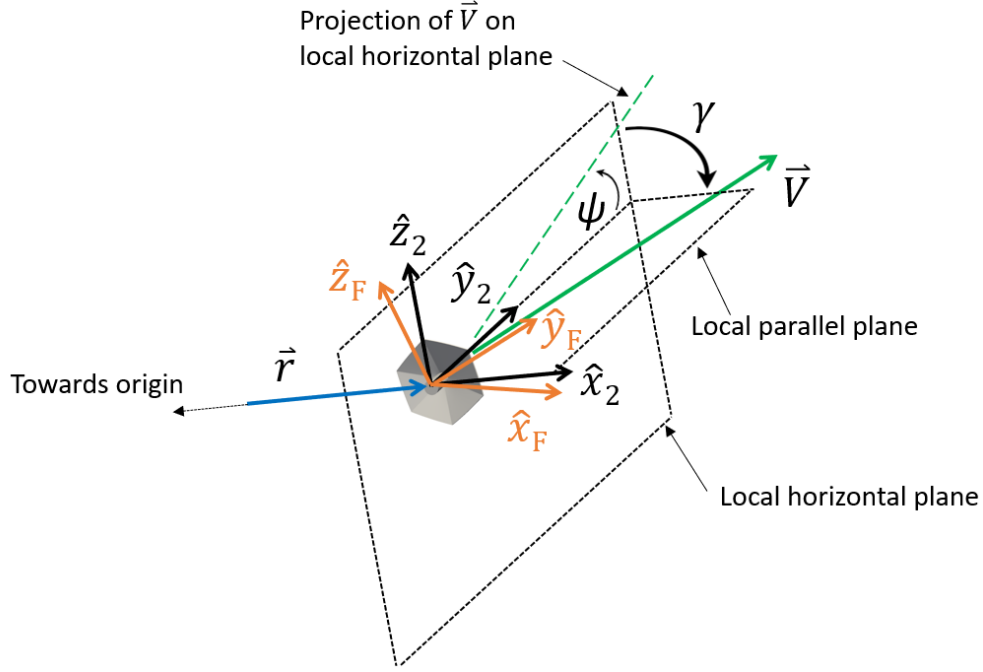
Figure 3.2. The local horizon and force frames.

The relationship between the aerodynamic forces and the force frame is illustrated in Figure 3.3. The drag vector $(\vec{D})$ by definition is anti-parallel to the planet-relative velocity vector $\vec{V}$ and the lift vector $(\vec{L})$ is perpendicular to $\vec{D}$. The angle σ shown is called the bank angle, which describes the "clock angle" of $\vec{L}$ with respect to the $\vec{r}$-$\vec{V}$ plane. Note that a positive σ results from a right-handed rotation about $\vec{V}$. The side force vector $(\vec{Q})$ acts along the direction that completes a right-handed triad according to the following:

$$\frac{\vec{L}}{|\vec{L}|} \times \frac{\vec{D}}{|\vec{D}|} = \frac{\vec{Q}}{|\vec{Q}|}$$
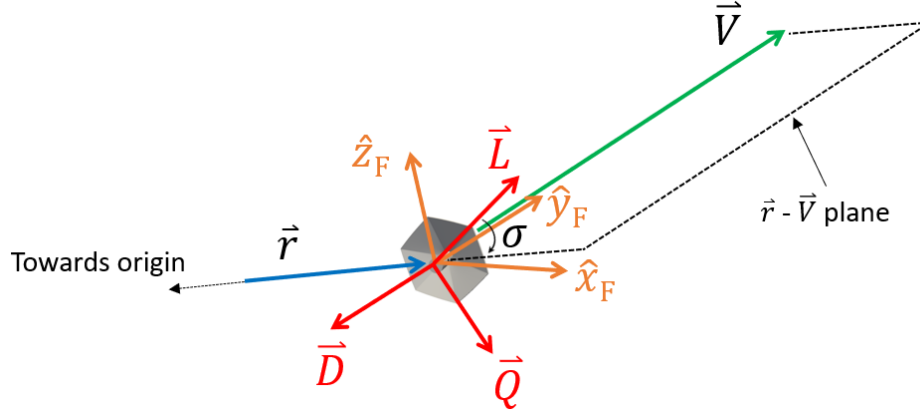
Figure 3.3. The aerodynamic forces relative to the force frame.

In the force frame above, the aerodynamic forces are expressed as follows:

$$\vec{D} = -D\,\hat{y}_F \tag{3.16}$$

$$\vec{Q} = Q\sin\sigma\,\hat{x}_F - Q\cos\sigma\,\hat{z}_F \tag{3.17}$$

$$\vec{L} = L\cos\sigma\,\hat{x}_F + L\sin\sigma\,\hat{z}_F \tag{3.18}$$

where D, Q, and L are the magnitudes of the respective force vectors. Using the transformation in Eq. 3.15, the forces are rewritten with respect to the local horizon frame:

$$\vec{D} = -D\sin\gamma\,\hat{x}_2 - D\cos\gamma\cos\psi\,\hat{y}_2 - D\cos\gamma\sin\psi\,\hat{z}_2 \tag{3.19}$$

$$\vec{Q} = Q\sin\sigma\cos\gamma\,\hat{x}_2 + (-Q\sin\sigma\sin\gamma\cos\psi + Q\cos\sigma\sin\psi)\,\hat{y}_2 +$$
$$(-Q\sin\sigma\sin\gamma\sin\psi - Q\cos\sigma\cos\psi)\,\hat{z}_2 \tag{3.20}$$

$$\vec{L} = L\cos\sigma\cos\gamma\,\hat{x}_2 + (-L\cos\sigma\sin\gamma\cos\psi - L\sin\sigma\sin\psi)\,\hat{y}_2 +$$
$$(-L\cos\sigma\sin\gamma\sin\psi + L\sin\sigma\cos\psi)\,\hat{z}_2 \tag{3.21}$$

Gravity is the remaining force to be formulated. For now, it is assumed that gravity acts purely anti-parallel to the radial direction. Therefore, the associated force can easily be written as follows:

$$m\vec{g} = -mg(r)\hat{x}_2 \tag{3.22}$$

where $g(r)$ denotes that the gravitational acceleration g is dependent on the radius.

Eqs. 3.19-3.22 provide the external forces needed to obtain the force equations from Eq. 3.14. Because the force equations are scalar differential equations, Eq. 3.14 is to be broken up into its components. For convenience, the vector basis chosen for this procedure is the local horizon frame (i.e., $\{\hat{x}_2, \hat{y}_2, \hat{z}_2\}$). Recall from Eq. 3.6 that the relative velocity can be expressed as follows:

$$^1\frac{d\vec{r}}{dt} = \dot{r}\,\hat{x}_2 + r\dot{\theta}\cos\phi\,\hat{y}_2 + r\dot{\phi}\,\hat{z}_2$$

Using Eq. 3.1, the angular velocity vector can also be rewritten relative to the local horizon frame as follows:

$$\vec{\omega}^{1/I} = \omega\hat{z}_1 = \omega\sin\phi\hat{x}_2 + \omega\cos\phi\hat{z}_2$$

With these equations, the Coriolis term can be expanded into the following form:

$$2\vec{\omega}^{1/I} \times \frac{^1d\vec{r}}{dt} = 2\omega\left(-r\dot{\theta}\cos^2\phi\,\hat{x}_2 + (\dot{r}\cos\phi - r\dot{\phi}\sin\phi)\,\hat{y}_2 + r\dot{\theta}\sin\phi\cos\phi\,\hat{z}_2\right) \tag{3.23}$$

Substituting Eqs. 3.8-3.10 for $\dot{r}$, $\dot{\theta}$, and $\dot{\phi}$ into the previous equation yields the following expression for the Coriolis term:

$$\begin{aligned}
2\vec{\omega}^{1/I} \times \frac{^1d\vec{r}}{dt} = &-2V\omega\cos\phi\cos\gamma\cos\psi\,\hat{x}_2 \\
&+ 2V\omega(\cos\phi\sin\gamma - \sin\phi\cos\gamma\sin\psi)\,\hat{y}_2 \\
&+ 2V\omega\sin\phi\cos\gamma\cos\psi\,\hat{z}_2
\end{aligned} \tag{3.24}$$

The centripetal acceleration term in Eq. 3.14 is expanded next. Recalling that the vector expression for the radius is $\vec{r} = r\,\hat{x}_2$, the following expansion can be obtained:

$$\omega^{1/I} \times (\vec{\omega}^{1/I} \times \vec{r}) = -r\omega^2\cos^2\phi\,\hat{x}_2 + r\omega^2\sin\phi\cos\phi\,\hat{z}_2 \tag{3.25}$$

Note that Eqs. 3.19-3.22, 3.24, and 3.25 provide the quantities on the right-hand side of Eq. 3.14. The final step before the force equations can be obtained is to write out the time derivative of velocity that appears on the left hand side of Eq. 3.14. The derivative of the planet-relative velocity vector $\vec{V}$ expressed in the local horizon frame (superscript 2) as seen from the planet-fixed frame (superscript 1) is obtained through another application of the transport theorem:

$$\frac{^1 d^2 \vec{r}}{dt^2} = \frac{^1 d\vec{V}}{dt} = \frac{^2 d\vec{V}}{dt} + \vec{\Omega}^{2/1} \times \vec{V} \tag{3.26}$$

where $\vec{\Omega}^{2/1}$ is the angular velocity of the local horizon frame with respect to the planet-fixed frame given by Eq. 3.3. Carrying out the derivative and cross product gives the following expression for acceleration:

$$\frac{^1 d\vec{V}}{dt} = \left(\dot{V} \sin\gamma + V\dot{\gamma}\cos\gamma - \frac{V^2 \cos^2\gamma}{r} \right) \hat{x}_2 +$$

$$\left(\dot{V}\cos\gamma\cos\psi - V\dot{\gamma}\sin\gamma\cos\psi - V\dot{\psi}\cos\gamma\sin\psi + \right.$$

$$\left. \frac{V^2}{r}\cos\gamma\cos\psi(\sin\gamma - \tan\phi\cos\gamma\sin\psi) \right) \hat{y}_2 +$$

$$\left(\dot{V}\cos\gamma\sin\psi - V\dot{\gamma}\sin\gamma\sin\psi + V\dot{\psi}\cos\gamma\cos\psi + \right.$$

$$\left. \frac{V^2}{r}\cos\gamma(\cos\gamma\cos^2\psi\tan\phi + \sin\gamma\sin\psi) \right) \hat{z}_2 \tag{3.27}$$

Now that the left and right-hand sides of Newton's second law have been determined, the components along the three directions can be equated to obtain three simultaneous and coupled scalar differential equations. They are as follows:

$$\dot{V}\sin\gamma + V\dot{\gamma}\cos\gamma - \frac{V^2\cos^2\gamma}{r} = -\frac{D}{m}\sin\gamma + \frac{Q}{m}\sin\sigma\cos\gamma + \frac{L}{m}\cos\sigma\cos\gamma$$

$$+ 2V\omega\cos\phi\cos\gamma\cos\psi + r\omega^2\cos^2\phi - g(r) \tag{3.28}$$

56

$$\dot{V} \cos\gamma \cos\psi - V\dot{\gamma} \sin\gamma \cos\psi - V\dot{\psi} \cos\gamma \sin\psi +$$

$$\frac{V^2}{r} \cos\gamma \cos\psi (\sin\gamma - \tan\phi \cos\gamma \sin\psi) =$$

$$-\frac{D}{m} \cos\gamma \cos\psi + \frac{Q}{m} (-\sin\sigma \sin\gamma \cos\psi + \cos\sigma \sin\psi) +$$

$$\frac{L}{m} (-\cos\sigma \sin\gamma \cos\psi - \sin\sigma \sin\psi) - 2V\omega (\cos\phi \sin\gamma - \sin\phi \cos\gamma \sin\psi) \qquad (3.29)$$

$$\dot{V} \cos\gamma \sin\psi - V\dot{\gamma} \sin\gamma \sin\psi + V\dot{\psi} \cos\gamma \cos\psi +$$

$$\frac{V^2}{r} \cos\gamma (\cos\gamma \cos^2\psi \tan\phi + \sin\gamma \sin\psi) =$$

$$-\frac{D}{m} \cos\gamma \sin\psi + \frac{Q}{m} (-\sin\sigma \sin\gamma \sin\psi - \cos\sigma \cos\psi) +$$

$$\frac{L}{m} (-\cos\sigma \sin\gamma \sin\psi + \sin\sigma \cos\psi) - 2V\omega \sin\phi \cos\gamma \cos\psi - r\omega^2 \sin\phi \cos\phi \qquad (3.30)$$

Eqs. 3.28-3.30 can then be solved for $\dot{V}$, $\dot{\gamma}$, and $\dot{\psi}$ to finally obtain the force equations:

$$\dot{V} = -\frac{D}{m} - g\sin\gamma + r\omega^2 \cos\phi (\sin\gamma \cos\phi - \cos\gamma \sin\psi \sin\phi) \qquad (3.31)$$

$$V\dot{\gamma} = \frac{L\cos\sigma}{m} + \frac{Q\sin\sigma}{m} + \left(\frac{V^2}{r} - g\right)\cos\gamma$$

$$+ r\omega^2 \cos\phi (\sin\gamma \sin\psi \sin\phi + \cos\gamma \cos\phi) + 2V\omega \cos\psi \cos\phi \qquad (3.32)$$

$$V\dot{\psi} = \frac{L\sin\sigma}{m\cos\gamma} - \frac{Q\cos\sigma}{m\cos\gamma} - \frac{r\omega^2 \cos\psi \sin\phi \cos\phi}{\cos\gamma}$$

$$- \frac{V^2 \cos\gamma \cos\psi \tan\phi}{r} + 2V\omega (\tan\gamma \sin\psi \cos\phi - \sin\phi) \qquad (3.33)$$

These force equations govern the time evolution of the entry vehicle's planet-relative velocity vector. Note that these equations were derived using methods similar to those presented in [67]. With the exception of the terms involving the side force Q, these force equations are identical to the equations derived in Refs. [67], [68]. To compare the equations stated here to those presented in Ref. [67], [68], one only needs to set $Q = 0$.

Because Mars is not perfectly spherical, the gravitational acceleration experienced by the entry vehicle does not purely act along the radial direction. Rather, there is also a component that varies with the latitude of the vehicle. The force equations can thus be modified

further by incorporating the effect of planetary oblateness on the gravitational acceleration. Deshmukh [60], for example, modified the force equations as follows to incorporate the perturbations due to a non-spherical gravity model:

$$\dot{V} = -\frac{D}{m} - g_r \sin\gamma - g_\phi \cos\gamma \sin\psi + r\omega^2 \cos\phi \left(\sin\gamma \cos\phi - \cos\gamma \sin\psi \sin\phi\right) \tag{3.34}$$

$$V\dot{\gamma} = \frac{L\cos\sigma}{m} + \frac{Q\sin\sigma}{m} + \left(\frac{V^2}{r} - g_r\right)\cos\gamma + g_\phi \sin\gamma \sin\psi$$

$$r\omega^2 \cos\phi \left(\sin\gamma \sin\psi \sin\phi + \cos\gamma \cos\phi\right) + 2V\omega \cos\psi \cos\phi \tag{3.35}$$

$$V\dot{\psi} = \frac{L\sin\sigma}{m\cos\gamma} - \frac{Q\cos\sigma}{m\cos\gamma} - g_\phi \frac{\cos\psi}{\cos\gamma} - \frac{r\omega^2 \cos\psi \sin\phi \cos\phi}{\cos\gamma}$$

$$- \frac{V^2 \cos\gamma \cos\psi \tan\phi}{r} + 2V\omega \left(\tan\gamma \sin\psi \cos\phi - \sin\phi\right) \tag{3.36}$$

where the terms g_r and g_ϕ are the radial and latitudinal components of the gravitational acceleration. These are given by the following expressions [60]:

$$g_r = \frac{\mu}{r^2}\left(1 + J_2\left(\frac{R_e}{r}\right)^2\right)\left(\frac{3}{2} - \frac{9}{2}\sin^2\phi\right) \tag{3.37}$$

$$g_\phi = \frac{\mu}{r^2}J_2\left(\frac{R_e}{r}\right)^2 \left(3\sin\phi \cos\phi\right) \tag{3.38}$$

where R_e, μ, and J_2 are the equatorial radius, gravitational parameter, and second zonal term of the gravitational potential, respectively, of the planet.

To summarize, Eqs. 3.8-3.10 represent the three kinematics equations governing the time evolution of the entry vehicle's position relative to the planet-fixed frame. Eqs. 3.31-3.33 represent the three force equations governing the time evolution of the planet-relative velocity. Together, these six equations form the EOMs governing the translational motion of the vehicle flying in the atmosphere of a planet. These equations were employed to simulate the aerocapture flight of the MES on Mars. Note that Eqs. 3.34-3.36 were adopted to incorporate planetary oblateness effects on the simulated trajectories.

3.1.2 Rotational Motion

The addition of the rotational motion to the translational motion enables a full 6-DOF study of the MES' motion in the Martian atmosphere. The rotational EOMs are also essential for the development of the flight controller, which in turn, enables the targeting of the desired angle of attack (α) and sideslip angle (β) for DFC. In this section, the kinematics and dynamic expressions governing the rotational motion of the MES are derived.

Consider the diagram of the MES shown in Figure 3.4. The right-handed triad, denoted by $\{\hat{x}^B, \hat{y}^B, \hat{z}^B\}$, is fixed to the body and rotates with it (referred to here as the body-fixed frame). The external moments acting upon each axis of the body-fixed frame are denoted by M_x, M_y, and M_z. The angular velocity vector of the MES is denoted by $\vec{\omega}$, which can be further broken down into its axial components p, q, and r, as shown in Figure 3.4.
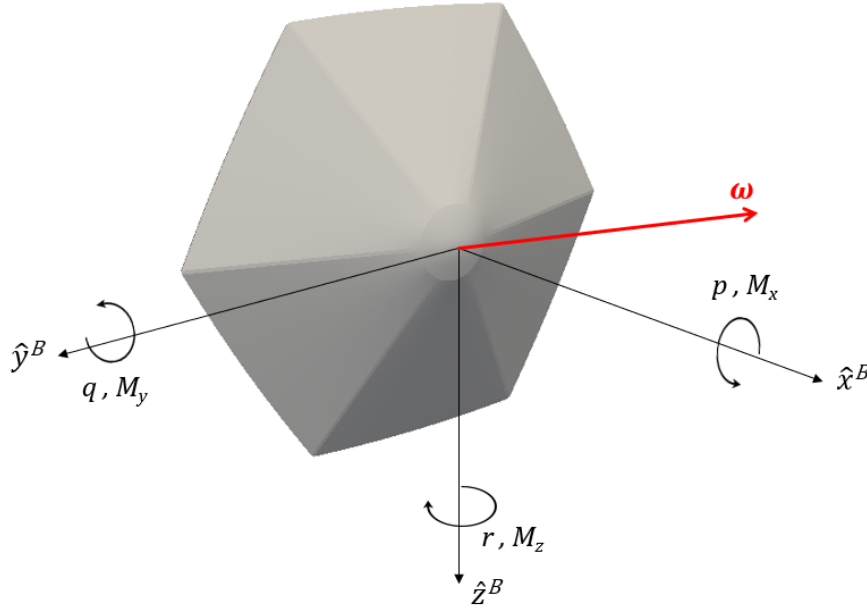
Figure 3.4. Definition of the angular velocities and external moments associated with the MES expressed in the body-fixed frame.

The rotational dynamics equations can be obtained by setting the sum of the external moments acting on the vehicle equal to the time derivative of the angular momentum vector as shown in the following vector equation:

$$\sum \vec{M} = \dot{\vec{H}} \tag{3.39}$$

The inertial time-derivative of the angular momentum vector is given by,

$$\frac{^I d\vec{H}}{dt} = \frac{^B d\vec{H}}{dt} + \vec{\omega}^{B/I} \times \vec{H} \tag{3.40}$$

where the superscript B indicates that the derivative is taken with respect to the body-fixed frame. Inserting Eq. 3.40 into Eq. 3.39 results in

$$\sum \vec{M} = \frac{^B d\vec{H}}{dt} + \vec{\omega}^{B/I} \times \vec{H} \tag{3.41}$$

The angular momentum vector is obtained from

$$\vec{H} = \bar{\bar{I}} \vec{\omega} \tag{3.42}$$

where the inertia tensor of the vehicle, $\bar{\bar{I}}$, is written as follows:

$$\bar{\bar{I}} = \begin{bmatrix} I_{xx} & I_{xy} & I_{xz} \\ I_{yx} & I_{yy} & I_{yz} \\ I_{zx} & I_{zy} & I_{zz} \end{bmatrix}$$

The angular velocity of the vehicle in the body-fixed frame is also given by

$$\vec{\omega} = p\hat{x}^B + q\hat{y}^B + r\hat{z}^B \tag{3.43}$$

where p, q, and r are the angular rate components about $\hat{x}^B$, $\hat{y}^B$, and $\hat{z}^B$, respectively.

With Eq. 3.43, Eq. 3.42 can be expanded as follows:

$$\vec{H} = \begin{bmatrix} I_{xx}p & I_{xy}q & I_{xz}r \\ I_{yx}p & I_{yy}q & I_{yz}r \\ I_{zx}p & I_{zy}q & I_{zz}r \end{bmatrix} \begin{Bmatrix} \hat{x} \\ \hat{y} \\ \hat{z} \end{Bmatrix} \tag{3.44}$$

In component form, Eq. 3.44 leads to three scalar equations:

$$H_x = I_{xx}p + I_{xy}q + I_{xz}r \tag{3.45}$$

$$H_y = I_{yx}p + I_{yy}q + I_{yz}r \tag{3.46}$$

$$H_z = I_{zx}p + I_{zy}q + I_{zz}r \tag{3.47}$$

In adopting the body-fixed frame, the moments and inertia properties become invariant with time. Inserting Eqs. 3.44-3.47 into Eq. 3.41 provides the general rotational dynamics equations:

$$M_x = I_{xx}\dot{p} + I_{xy}\dot{q} + I_{xz}\dot{r} + H_z q - H_y r \tag{3.48}$$

$$M_y = I_{yx}\dot{p} + I_{yy}\dot{q} + I_{yz}\dot{r} + H_x r - H_z p \tag{3.49}$$

$$M_z = I_{zx}\dot{p} + I_{zy}\dot{q} + I_{zz}\dot{r} + H_y p - H_x q \tag{3.50}$$

Substituting the individual expressions for H_x, H_y, and H_z into Eqs. 3.48-3.50 and collecting like terms yields:

$$M_x = I_{xx}\dot{p} + I_{xy}(\dot{q} - pr) + I_{xz}(\dot{r} + pq) + (I_{zz} - I_{yy})qr + I_{yz}(q^2 - r^2) \tag{3.51}$$

$$M_y = I_{xy}(\dot{p} + qr) + I_{yy}\dot{q} + I_{yz}(\dot{r} - pq) + (I_{xx} - I_{zz})pr + I_{xz}(r^2 - p^2) \tag{3.52}$$

$$M_z = I_{xz}(\dot{p} - qr) + I_{yz}(\dot{q} + pr) + I_{zz}\dot{r} + (I_{yy} - I_{xx})pq + I_{xy}(p^2 - q^2) \tag{3.53}$$

Solving for the rates of change of p, q, and r yields the following expressions:

$$
\begin{aligned}
\dot{p} = -P\Big\{ &(I_{xz}I_{yy} - I_{xy}I_{yz})\Big[-I_{xz}\left(I_{xx}pq - I_{xy}p^2 + I_{xy}q^2 + I_{xz}qr - I_{yy}pq - I_{yz}pr + M_z\right) + \\
&I_{zz}\left(I_{xy}pr - I_{xz}pq + I_{yy}qr - I_{yz}q^2 + I_{yz}r^2 + M_x\right) - I_{zz}^2 qr \Big] - \\
&(I_{xz}I_{yz} - I_{xy}I_{zz})\Big[I_{xz}\left(I_{xx}pr + I_{xy}qr - I_{xz}p^2 + I_{xz}r^2 - I_{zz}pr - M_y\right) + \\
&I_{yz}(I_{xy}pr - 2I_{xz}pq + I_{yy}qr - I_{zz}qr + M_x) + I_{yz}^2\left(r^2 - q^2\right) \Big] \Big\} \tag{3.54}
\end{aligned}
$$

61

where

$$P = \frac{1}{I_{xz}\left[I_{xx}\left(I_{yz}^2 - I_{yy}I_{zz}\right) + I_{xy}^2 I_{zz} - 2I_{xy}I_{xz}I_{yz} + I_{xz}^2 I_{yy}\right]}$$

$$
\begin{aligned}
\dot{q} = Q\Bigg\{ & I_{xz}\Big[I_{xy}(pq(I_{xx} - I_{yy} + I_{zz}) + M_z) + I_{yz}(M_x - qr(I_{xx} - I_{yy} + I_{zz})) + I_{xx}I_{zz}\left(p^2 - r^2\right) + \\
& I_{xy}^2\left(q^2 - p^2\right) + I_{yz}^2\left(r^2 - q^2\right)\Big] - I_{xz}^2(r(-I_{xx}p - 2I_{xy}q + I_{zz}p) + 2I_{yz}pq + M_y) + \\
& I_{xy}\left(-I_{zz}\left(qr(I_{xx} + I_{yy}) + I_{yz}\left(r^2 - q^2\right) + M_x\right) + I_{xx}I_{yz}\left(p^2 - q^2\right) + I_{zz}^2 qr\right) + \\
& I_{xx}\left(I_{yz}p(-I_{xx}q + I_{yy}q + I_{yz}r) + I_{zz}(-I_{xx}pr + I_{yz}pq + M_y) - I_{yz}M_z + I_{zz}^2 pr\right) - \\
& \qquad\qquad\qquad\qquad\qquad\qquad\qquad\qquad I_{xy}^2 I_{zz}pr + I_{xz}^3\left(r^2 - p^2\right)\Bigg\} \quad (3.55)
\end{aligned}
$$

where

$$Q = \frac{1}{I_{xx}I_{yy}I_{zz} - I_{xx}I_{yz}^2 + I_{xy}^2(-I_{zz}) + 2I_{xy}I_{xz}I_{yz} - I_{xz}^2 I_{yy}}$$

$$
\begin{aligned}
\dot{r} = R\Bigg\{ & I_{xz}\Big[I_{yy}\left(-I_{xx}qr + I_{xy}pr - I_{yz}q^2 + I_{yz}r^2 - I_{zz}qr + M_x\right) - I_{xy}(pr(I_{zz} - I_{xx}) + M_y) + \\
& I_{xx}I_{yz}\left(p^2 - r^2\right) + 2I_{xy}^2 qr + I_{yy}^2 qr\Big] + I_{xy}^2(p(I_{xx}q - I_{yy}q - 2I_{yz}r) + M_z) + \\
& I_{xy}\Big[- I_{yz}(qr(I_{xx} + I_{yy} - I_{zz}) + M_x) + I_{xx}I_{yy}\left(p^2 - q^2\right) + I_{yz}^2\left(q^2 - r^2\right)\Big] + \\
& I_{xx}\Big[I_{yz}pr(-I_{xx} + I_{yy} + I_{zz}) + I_{yy}pq(I_{yy} - I_{xx}) - I_{yy}M_z + I_{yz}^2 pq + I_{yz}M_y\Big] + \\
& \qquad\qquad\qquad\qquad I_{xy}^3\left(q^2 - p^2\right) - I_{xz}^2\left(I_{xy}\left(p^2 - r^2\right) + I_{yy}pq\right)\Bigg\} \quad (3.56)
\end{aligned}
$$

where

$$R = \frac{1}{I_{xx}\left(I_{yz}^2 - I_{yy}I_{zz}\right) + I_{xy}^2 I_{zz} - 2I_{xy}I_{xz}I_{yz} + I_{xz}^2 I_{yy}}$$

Although Eqs. 3.54-3.56 do not yield new information, the explicit expressions for $\dot{p}$, $\dot{q}$, and $\dot{r}$ are useful for writing computer programs to solve for the time histories of p, q, and r. These histories can be obtained once the applied moments M_x, M_y, and M_z are known. However, the time-integrals of these rates do not correspond to any physically-meaningful

angles. Therefore, the angular kinematics are used to map p, q, and r to actual angles that describe the body's attitude (these physical angles are the so-called Euler angles).

3.1.3   Angular Kinematics

To obtain the angular kinematics, the relationship between the body-fixed frame and the aerodynamic wind-frame is established. As discussed later, the aerodynamic coefficients of the MES are referenced to the body-fixed frame, whereas the aerodynamic forces present in the translational dynamics equations are reference to the so-called *wind frame*. In this research, an intrinsic 1-3-2 rotation sequence is employed to write out the direction cosine matrix that expresses the body-fixed frame's orientation with respect to the wind frame. The numbers in the sequence refer to the axis around which the rotation occurs: 1 corresponds to x, 2 corresponds to y, and 3 corresponds to z. Let the wind frame and the body-fixed frame be described by the right-handed triads $\{\hat{x}^W, \hat{y}^W, \hat{z}^W\}$ and $\{\hat{x}^B, \hat{y}^B, \hat{z}^B\}$, respectively. The wind frame is defined such that $\hat{x}^W$ is aligned with the planet-relative velocity vector of the vehicle. Prior to the first rotation of the sequence, both frames are aligned with each other.

The first rotation is clockwise about $\hat{x}^W$ by the angle σ that leads to the primed frame $\{x', y', z'\}$ as shown in Figure 3.5(a). This is followed by a counter-clockwise rotation about the z' axis by the angle β that leads to the double-primed frame $\{x'', y'', z''\}$ as shown in Figure 3.5(b). The final rotation is clockwise about y'' by the angle α that leads to the body fixed frame as shown in Figure 3.5(c). The angles used in the rotation sequence are, in this case, Euler angles that define the orientation of the body fixed frame (and thus the body) with respect to the relative wind (i.e. the wind frame). A graphical representation of these Euler angles as well as the relationship between the aforementioned frames is given in Figure 3.6.

(a) 1st rotation

(b) 2nd rotation

(c) 3rd rotation
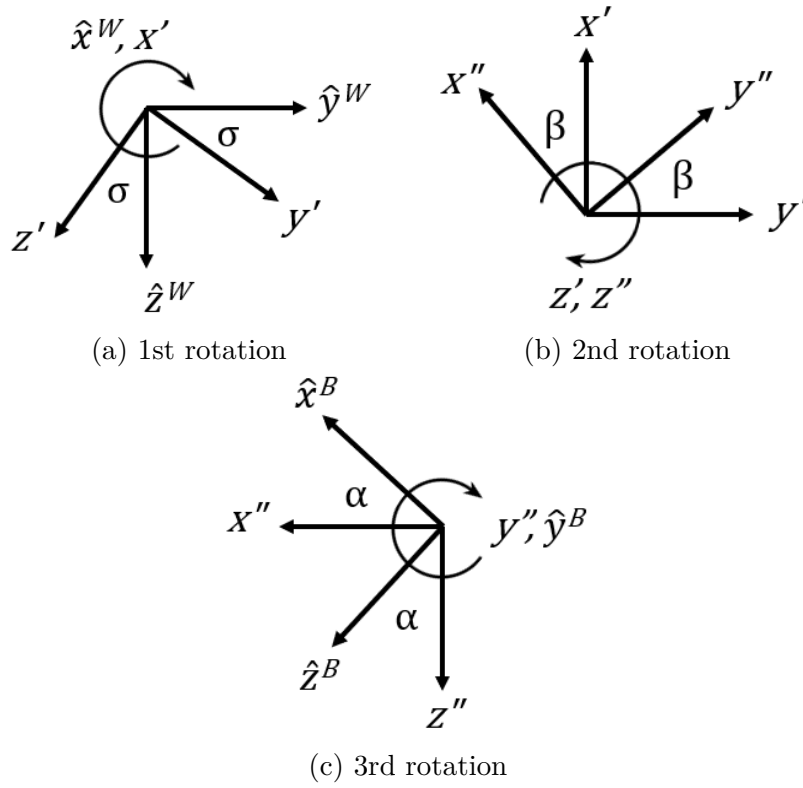
Figure 3.5. The intrinsic 1-3-2 rotation sequence.
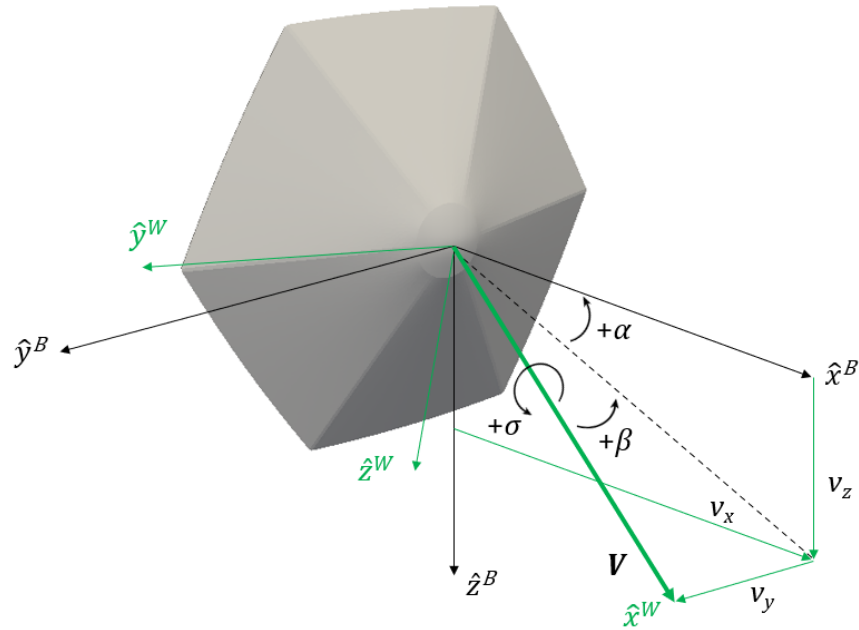
Figure 3.6. An illustration of the Euler angles (σ, α, β) and the orientation of the body-fixed frame with respect to the wind frame.

The individual rotations can be expressed through the following rotation matrices:

$$C_1(\sigma) = \begin{bmatrix} 1 & 0 & 0 \\ 0 & \cos\sigma & -\sin\sigma \\ 0 & \sin\sigma & \cos\sigma \end{bmatrix} \tag{3.57}$$

$$C_3(-\beta) = \begin{bmatrix} \cos(-\beta) & \sin(-\beta) & 0 \\ -\sin(-\beta) & \cos(-\beta) & 0 \\ 0 & 0 & 1 \end{bmatrix} \tag{3.58}$$

$$C_2(\alpha) = \begin{bmatrix} \cos\alpha & 0 & \sin\alpha \\ 0 & 1 & 0 \\ -\sin\alpha & 0 & \cos\alpha \end{bmatrix} \tag{3.59}$$

When Eqs. 3.57-3.59 are multiplied as follows, the general direction cosine matrix (DCM) relating the orientation of the body-fixed frame with respect to the wind frame is obtained:

$$
\begin{aligned}
{}^{W}C^{B} &= C_1(\sigma)C_3(-\beta)C_2(\alpha) \\[6pt]
&= \begin{bmatrix} \cos\beta\cos\alpha & -\sin\beta & \cos\beta\sin\alpha \\ \left(\cos\sigma\sin\beta\cos\alpha + \sin\sigma\sin\alpha\right) & \cos\sigma\cos\beta & \left(\cos\sigma\sin\beta\sin\alpha - \sin\sigma\cos\alpha\right) \\ \left(\sin\sigma\sin\beta\cos\alpha - \cos\sigma\sin\alpha\right) & \sin\sigma\cos\beta & \left(\sin\sigma\sin\beta\sin\alpha + \cos\sigma\cos\alpha\right) \end{bmatrix}
\end{aligned}
$$

$$\tag{3.60}$$

It is from this rotation sequence that the angular kinematic expressions are obtained. Recall from Eq. 3.43 that the angular velocity vector $\vec{\omega}$ of the body can be written out in component form as follows:

$$\vec{\omega} = p\hat{x}^B + q\hat{y}^B + r\hat{z}^B$$

It is also known that $\vec{\omega}$ can be expressed in terms of the rates of the Euler angles σ, β, and α as follows:[2]

$$\vec{\omega} = \dot{\vec{\sigma}} + \dot{\vec{\beta}} + \dot{\vec{\alpha}}$$
$$= \dot{\sigma}\,\hat{x}' + \dot{\beta}\,(-\hat{z}'') + \dot{\alpha}\,\hat{y}^B \tag{3.61}$$

Using Eqs. 3.58-3.59, $\hat{x}'$ and $\hat{z}''$ can be rewritten in terms of the body-fixed axes as follows:

$$\hat{x}' = \cos\beta\,\hat{x}'' - \sin\beta\,\hat{y}'' = \cos\beta\cos\alpha\,\hat{x}^B - \sin\beta\,\hat{y}^B + \cos\beta\sin\alpha\,\hat{z}^B$$
$$\hat{z}'' = -\sin\alpha\,\hat{x}^B + \cos\alpha\,\hat{z}^B$$

Substituting these expressions into Eq. 3.61 results in

$$\vec{\omega} = \left(\dot{\sigma}\cos\beta\cos\alpha + \dot{\beta}\sin\alpha\right)\hat{x}^B + (\dot{\alpha} - \dot{\sigma}\sin\beta)\,\hat{y}^B + \left(\dot{\sigma}\cos\beta\sin\alpha - \dot{\beta}\cos\alpha\right)\hat{z}^B \tag{3.62}$$

Finally, equating the components of Eq. 3.43 and Eq. 3.62 provides the desired angular kinematics relationships:

$$p = \dot{\sigma}\cos\beta\cos\alpha + \dot{\beta}\sin\alpha \tag{3.63}$$

$$q = \dot{\alpha} - \dot{\sigma}\sin\beta \tag{3.64}$$

$$r = \dot{\sigma}\cos\beta\sin\alpha - \dot{\beta}\cos\alpha \tag{3.65}$$

Inverting these equations provides expressions for the Euler angle rates in terms of the body angular rates:

$$\dot{\sigma} = p\cos\alpha\sec\beta + r\sin\alpha\sec\beta \tag{3.66}$$

$$\dot{\alpha} = p\cos\alpha\tan\beta + q + r\sin\alpha\tan\beta \tag{3.67}$$

$$\dot{\beta} = p\sin\alpha - r\cos\alpha \tag{3.68}$$

---

[2]↑As discussed in classical dynamics texts like Ref. [69].

Through Eqs. 3.66-3.68, the histories of p, q, and r obtained via integration of Eqs. 3.54-3.56 can be mapped to physically meaningful angles to describe the attitude history of the MES.

To summarize, the essential equations governing the rotational motion of the MES are Eqs. 3.54-3.56 (dynamics) and Eqs. 3.66-3.68 (kinematics). These equations combined with the governing equations of translational motion make possible the 6-DOF analysis of the MES performed in this dissertation.

3.2 Aerodynamics Model

An aerodynamics model is necessary to properly compute the external aerodynamic forces and moments acting on the MES. Trajectory analyses performed for Mars vehicles flying direct entries have employed aerodynamics databases (aerodatabases), examples of which are described in Refs. [70]–[73]. Although it did not fly, the Aeroassist Flight Experiment (AFE) vehicle was proposed for Mars aerocapture and aerodynamics data was developed to compliment trajectory simulations as described in Refs. [74], [75]. Aerodatabases for DEVs such as ADEPT [76] and Pterodactyl [77], [78] were also developed recently, albeit for an Earth atmosphere. These aerodatabases typically contain the aerodynamic force and moment coefficients of the vehicle for different combinations of flight conditions and attitudes. In the case of the Pterodactyl and MES vehicles, their respective databases are also functions of control surface deflections.

The construction of these databases involved the following steps. First, a reference trajectory for the vehicle was generated from which several trajectory points were extracted for further analysis. At the selected points, detailed calculations of the vehicle's aerodynamics were performed via computational fluid dynamics (CFD). At select conditions, wind tunnel measurements were also gathered to supplement the CFD results. For these calculations and measurements, a full 3D model of the vehicle was used. Note that analysis methods varied according to flow rarefaction, as discussed later in Secs. 3.2.2-3.2.3. The results were then compiled into a database to be used in conjunction with a trajectory simulation tool.

The above approach of database development was adopted for this research with the following modifications. The database does not contain data for supersonic, transonic, and

subsonic flow conditions simply because they are not encountered by an aerocapture vehicle. Additionally, the aerodynamic coefficients reported were obtained by only considering the forebody geometry. At hypersonic speeds, the aft region does not greatly impact the aerodynamics, although its contribution does become significant when supersonic and subsonic conditions are encountered [76]. Lastly, this research only directly computed the MES aerodynamics at three flow conditions and instead employed a bridging method to fill in the database as described in Sec. 3.2.4. In the sections that follow, the aerodynamics analyses employed for aerodatabase construction are described in further detail.

3.2.1 Aerodynamic Coefficients and Reference Frame

Aerodynamic coefficients are non-dimensional quantities commonly used in applied aerodynamics.[3] Particularly for the present aerodatabase, the coefficients represented are the axial, side, and normal force coefficients (C_A, C_Y, and C_N, respectively) and the roll, pitch, and yaw moment coefficients (C_l, C_m, and C_n, respectively). These body force and moment coefficients are defined as follows:

$$C_A = \frac{A}{q_\infty S} \tag{3.69}$$

$$C_Y = \frac{Y}{q_\infty S} \tag{3.70}$$

$$C_N = \frac{N}{q_\infty S} \tag{3.71}$$

$$C_l = \frac{M_x}{q_\infty S L} \tag{3.72}$$

$$C_m = \frac{M_y}{q_\infty S L} \tag{3.73}$$

$$C_n = \frac{M_z}{q_\infty S L} \tag{3.74}$$

where $q_\infty = 0.5 \rho_\infty V_\infty^2$ is the freestream dynamic pressure, S is the reference area, and L is the reference length. In Eqs. 3.69-3.71, A, Y, and N are the axial, side, and normal forces acting in the $\hat{x}$, $\hat{y}$, and $\hat{z}$ body axes, respectively. In Eqs. 3.72-3.74, M_x, M_y, and M_z are

---

[3]↑The reader is referred to pp. 262-68 of Ref. [79] for an insightful discussion of the importance of using aerodynamic coefficients in applied aerodynamics.

the roll, pitch, and yaw moments acting about the $\hat{x}$, $\hat{y}$, and $\hat{z}$ body axes, respectively. The conventions adopted for these body force and moment coefficients are presented in Figure 3.7. The wind frame angles α, β, and σ are also shown.
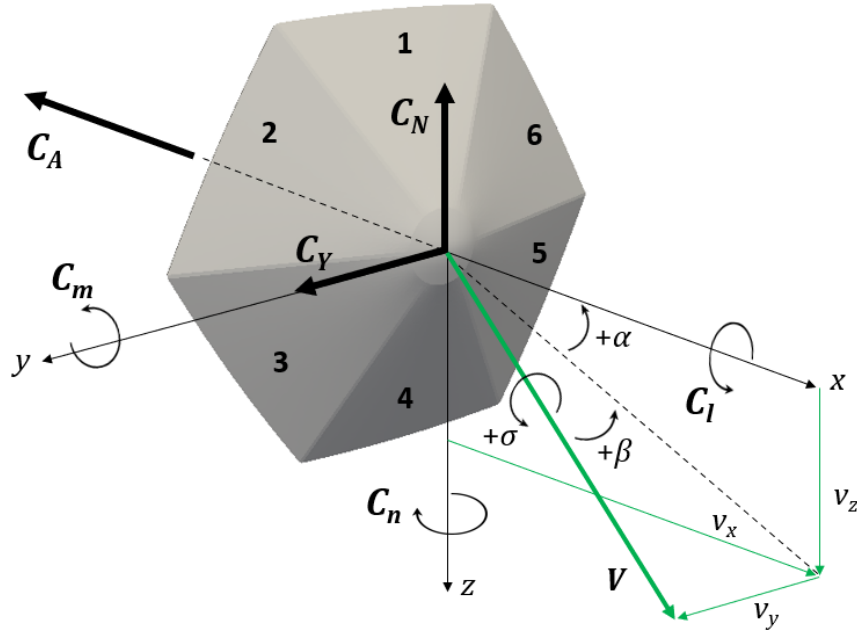
Figure 3.7. The body force and moment conventions as well as the wind frame angles.

Because the translational equations of motion require the wind-relative drag (D), side (Q), and lift (L) forces, the body-relative forces must be converted. The following conversion equation is used to map the body force coefficients into the wind frame and obtain the desired wind-relative force coefficients C_D, C_Q, and C_L:

$$\begin{Bmatrix} C_D \\ C_Q \\ C_L \end{Bmatrix} = \begin{bmatrix} \cos\beta\cos\alpha & -\sin\beta & \cos\beta\sin\alpha \\ \sin\beta\cos\alpha & \cos\beta & \sin\beta\sin\alpha \\ -\sin\alpha & 0 & \cos\alpha \end{bmatrix} \begin{Bmatrix} C_A \\ C_Y \\ C_N \end{Bmatrix} \tag{3.75}$$

69

The drag, side, and lift force coefficients are defined as follows:

$$C_D = \frac{D}{q_\infty S} \tag{3.76}$$

$$C_Q = \frac{Q}{q_\infty S} \tag{3.77}$$

$$C_L = \frac{L}{q_\infty S} \tag{3.78}$$

Note that the direction cosine matrix in Eq. 3.75 is obtained from Eq. 3.60 after setting $\sigma = 0$.

The orientations of the wind-relative forces are illustrated in Figure 3.8. The direction of drag represented by C_D is acting anti-parallel to the velocity vector $\vec{V}$. On the other hand, the lift direction corresponding with C_L is acting perpendicular to the direction of drag and directed along $-\hat{z}^W$. Lastly, the side force represented by C_Q acts in the direction that completes the right-handed triad.
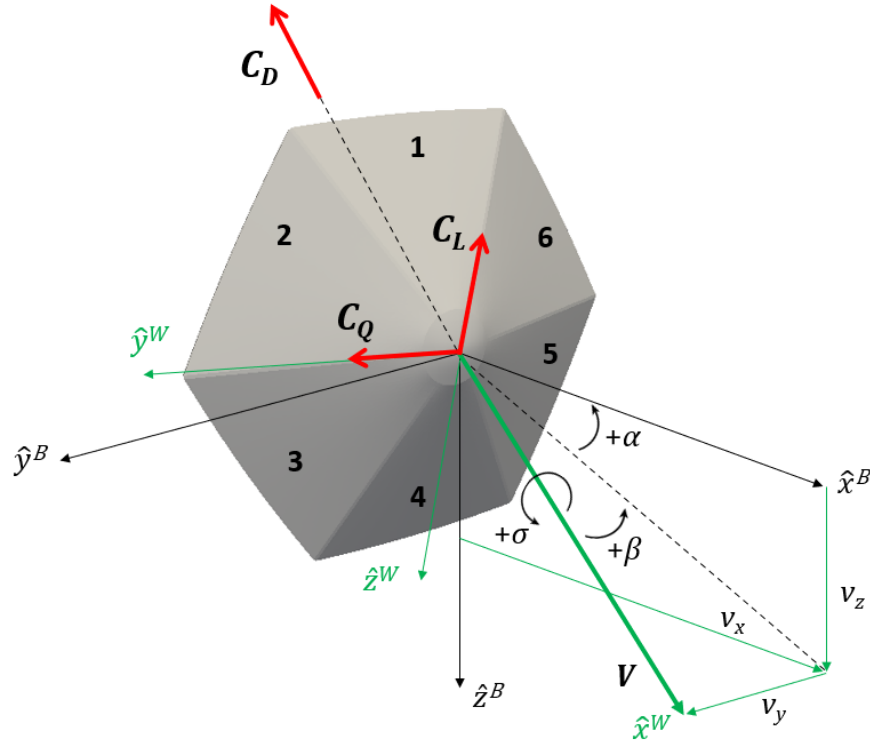
Figure 3.8. The wind-relative force conventions.

3.2.2 Flow Regimes

Planetary entry vehicles experience different flow regimes during their descent into the target body's atmosphere. These flow regimes have typically been demarcated using the Knudsen number (Kn), a dimensionless parameter that aerodynamicists use to indicate the level of rarefaction of a given gas flow. Kn is defined as the ratio of the mean free path (λ) travelled by a gas particle in the flow to the characteristic length of the flow (L):

$$Kn = \frac{\lambda}{L} \tag{3.79}$$

In entry aerodynamics, L is often arbitrarily set equal to the reference length of the vehicle (e.g., maximum diameter of the vehicle). Mean free path, λ, is a function of the thermodynamic state of the gas flow. For very dense flows, there are enough fluid particles such that a single particle need not travel long distances before colliding with another particle. The average distance traveled between collisions is the mean free path of a gas particle. In the opposite limit of very low density, a gas particle may travel long distances before interacting with another particle. In the case of free molecular flow, λ is on the same order of magnitude as L, although λ can even exceed L by a great factor. This flow regime is typically defined as follows:

$$Kn_{fm} \geq 1 \tag{3.80}$$

where the subscript fm denotes "free molecular". In the limit $Kn \to \infty$, the particle-to-particle collisions are so infrequent that the flow can be thought of as collisionless.

When an entry vehicle first enters the atmosphere, it typically encounters free molecular flow conditions because of the very low densities in the upper atmosphere. As the vehicle continues its descent and the ambient density increases, the vehicle departs from free molecular conditions and soon encounters rarefied transitional flow. In practice, the rarefied transitional regime corresponds to the following range of Knudsen numbers:

$$0.1 < Kn_{tr} < 1 \tag{3.81}$$

where the subscript tr denotes "transitional".

As the vehicle continues its descent, the gas flow density becomes sufficiently high such that $\lambda << L$. At these conditions, the flow is said to be in continuum, which corresponds to:

$$Kn_{co} << 1 \tag{3.82}$$

In the limit $Kn \to 0$, the flow becomes what is known as inviscid flow.

Demarcating the flow regimes expected for a flight vehicle is important because the flight conditions impact the flow physics and therefore the aerodynamic characteristics of the vehicle. Static stability and petal/rib control authority are aerodynamic characteristics that impact the flight performance of the MES. To ensure accurate simulations, the aerodatabase must be of sufficient fidelity and capture the dependence of the aerodynamics on flight conditions. To do so, the appropriate mathematical model corresponding with each flow regime must be utilized.

In order, the MES is expected to encounter the free molecular, rarefied transitional, and continuum flow regimes. Because the aerocapture vehicle also exits the atmosphere, it is expected to encounter rarefied transitional and free molecular flow conditions twice. Distinct mathematical models were employed to compute the MES aerodynamics at each of these three flight regimes.

3.2.3   Computing Knudsen Number

The essence of fluid flow is dictated by the intermolecular interactions, namely collisions, at the microscopic level. The familiar macroscopic fluid quantities like viscosity are averaged values derived from molecular quantities in the flow. Therefore, fluid flow can also be described using a molecular model, sometimes referred to as the particulate model. The governing equation of the molecular model is the Boltzmann equation. It is generally not amenable to neither analytic nor numerical solution for practical problems because the number of independent variables increases proportionally to the number of molecules in the flow.[4] However, the particulate structure of a given flow allows for direct simulation of its motion

---

[4]↑See Bird's description in Ref. [80] for further details.

through numerical means, which circumvents the issue of solving the Boltzmann equation. The method of direct simulation was originated by Bird in the 1960s [81] and it is now known as direct simulation Monte Carlo (DSMC).

The density of the flow can be used to determine whether the direct simulation of particle motion is appropriate. Naturally, denser gas flows like those encountered in hypersonic continuum contain a very large number of particles per unit volume. While direct simulation as a method does not discriminate based on the number of particles in a given flow, it would be computationally impractical to simulate continuum flow. Therefore, direct simulation is usually reserved for low density entry flows. A significant motivator of the utilization of DSMC is that the Navier-Stokes equations become indeterminate when the flow density is sufficiently small. At very low densities, gradients of the macroscopic quantities of the flow cannot be maintained because the collision rate of molecules is greatly reduced. Therefore, the transport terms of the Navier-Stokes equations that depend on these gradients fail, rendering the equations unsolvable.

The density of the flow is inversely proportional to λ. The range of validity of the Navier-Stokes equations can therefore be defined using Kn. Bird stated that the continuum model must be replaced with the molecular model if the local Kn is 0.2 or greater [80]. The validity of the continuum and microscopic models as a function of Kn are illustrated in Figure 3.9.
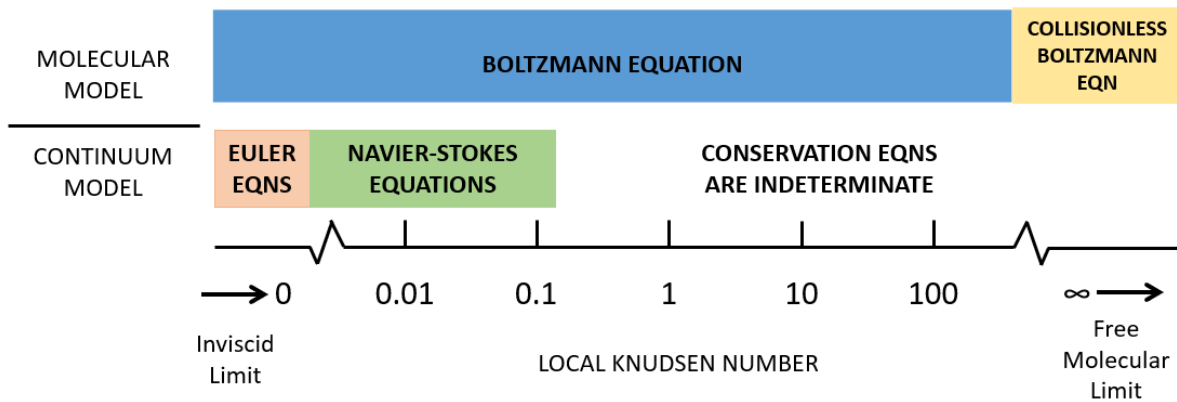
Figure 3.9. The range of validity of the continuum (macroscopic) and molecular (microscopic) models (Image adapted from Ref. [80]).

To compute Kn, an appropriate model for the λ is necessary. It is known that the mean free path of the molecules in the freestream flow is a function of intermolecular collisions. It is defined as the ratio of the mean thermal speed of the molecule $(\bar{c}')$ to the collision frequency (ν):

$$\lambda = \frac{\bar{c}'}{\nu} \tag{3.83}$$

This research adopted the variable soft-sphere (VSS) model of Koura and Matsumoto [82], [83] to compute λ. The VSS model was chosen because it incorporates the dependence of molecular diameter on the temperature of the gas. The mean free path under the VSS assumption can be expressed as follows:

$$\lambda = \frac{1}{\sqrt{2}\,\pi\,d_{ref}^2\,n\,\left(\frac{T_{ref}}{T}\right)^{\omega - 1/2}} \tag{3.84}$$

where n is the number density of the gas, T is the ambient temperature of the gas, d_{ref} is the reference diameter of the VSS molecule, T_{ref} is the reference temperature, and ω is the viscosity index of the VSS molecule. The number density may be computed from the mass density (ρ) and species molar mass (M_i) of the gas as follows:

$$n = \frac{N_A\,\rho}{M_i} \tag{3.85}$$

where $N_A = 6.022 \times 10^{23}$ parts per mole is Avogadro's constant. Because the Martian atmosphere is dominated by CO_2, the reference values and molar mass used were those of the CO_2 molecule. The reference values are shown in Table 3.1.[5]

Table 3.1. Reference values for CO_2 used to compute mean free path

Variable	Reference Value	Notes
d_{ref}	5.54×10^{-10} m	(1 atm, 273 K)
T_{ref}	273.0 K	
ω	0.93	(1 atm, 273 K)
M_{CO_2}	0.04401 kg/mol	

[5]↑The reference values were retrieved from Appendix A of Ref. [80].

A reference aerocapture trajectory with the MES was computed via three-DOF simulation [41] and used to estimate a Kn range. The freestream density and temperature of the reference trajectory were inserted into Eq. 3.84 to compute the local λ. Then, by setting the reference length equal to the maximum diameter of the MES ($L = 1.35$ m), the corresponding Kn range encompassed by the reference trajectory was computed from Eq. 3.79. Figure 3.10 shows the Kn values between the entry and minimum altitudes. The maximum and minimum Kn were 232 and 2.6E-04, respectively. The reference Kn range and Figure 3.9 were leveraged to identify the domain of applicability corresponding with free molecular, rarefied, and continuum flow calculation techniques.
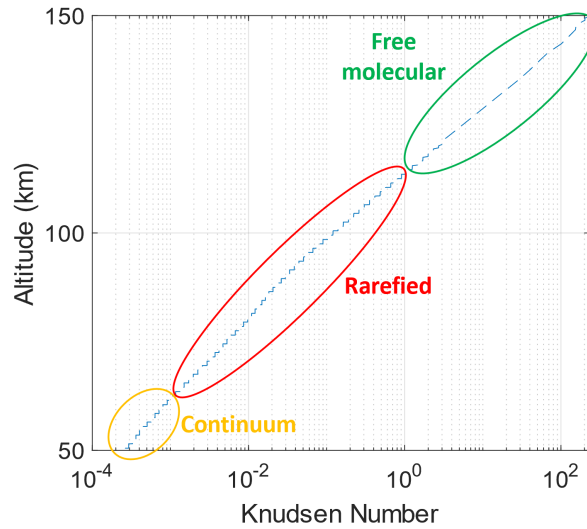
Figure 3.10. Estimated Knudsen number range for the reference MES trajectory.

3.2.4 Bridging Method

The aerodatabase should be of sufficient fidelity such that it captures the effects of flow rarefaction on the vehicle aerodynamics, which would allow for a more meaningful evaluation of vehicle performance. Increased fidelity could be achieved by computing the aerodynamic coefficients at several trajectory points within each flow regime for the range of expected α and β. For the MES, additional computations must also be carried out to incorporate the range of possible δ deflections. By varying Kn, α, β, and δ, it becomes apparent that the

computational burden of building an aerodatabase can become large. Additionally, CFD calculations are notably time and resource intensive. Because of limited computational resources, reducing the total computational cost of building the database was considered immensely beneficial.

In the 1990s, an innovative approach to reducing the computational cost of aerodatabase building was developed using *bridging relations*. Bridging relations are mathematical functions that can be coupled with a limited set of high-fidelity CFD data to compute aerodynamic coefficients for flight conditions that have not been analyzed via CFD. In effect, this approach "fills in" the aerodatabase using only a handful of CFD solutions. From a computational expense perspective, this approach is clearly an attractive alternative to running CFD calculations that sweep through a wide range of flight conditions, attitudes, and vehicle shapes.

This research adopted the single-point bridging method developed by Wilmoth et. al. [84]. The "single point" refers to the lone DSMC solution required at one combination of flight condition (Kn), attitude (α, β), and petal deflection (δ). This DSMC data point supplies the corresponding aerodynamic coefficients at that particular Kn condition. Aside from the DSMC solution, the bridging method also requires continuum and free molecular flow data points. The advantage of the method is that for each combination of α, β, and δ, only three coefficients (one from each flow regime) are needed to compute corresponding values of that coefficient at intermediate flow conditions without having to carry out additional calculations. This method is illustrated in Figure 3.11, which shows three known values of the coefficient C: C_{cont}, C_{DSMC}, and C_{fm}. With these three C values known, other values of C that lie along the solid curve can be computed for intermediate values of Kn using the bridging function P_b rather than DSMC or Navier-Stokes CFD.

Each aerodynamic coefficient C has a bridging relation of the form:[6]

$$C = P_b C_{fm} + (1 - P_b)C_{co} \tag{3.86}$$

---

[6]↑This explanation of the bridging process, which concludes before Sec. 3.2.5 was adapted from the discussion that previously appeared in Refs. [85], [86].
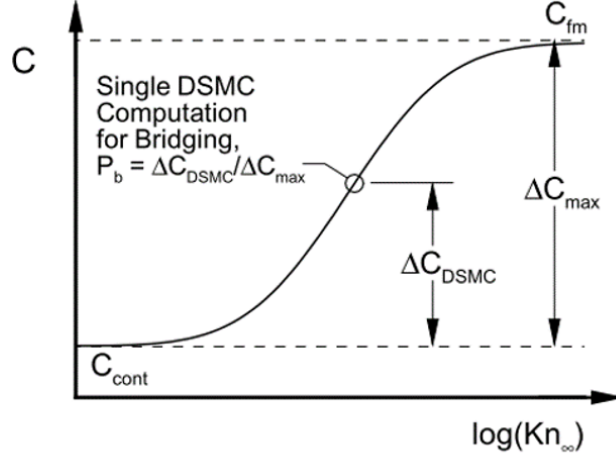
Reprinted with permission from R. Wilmoth.

Figure 3.11. The single point bridging method illustrated [84].

where the error function-logarithmic (erf-log) bridging function of Ivanov et. al. [87] is given by:

$$P_b = \frac{1}{2}\left(1 + erf\left\{\frac{\sqrt{\pi}}{\Delta Kn}log\left[\frac{Kn_\infty}{Kn_m}\right]\right\}\right) \qquad (3.87)$$

and C_{fm} and C_{co} are the known free molecular and continuum values of the coefficient, respectively. Note that C_{fm} and C_{co} correspond to the extremes of the Kn range illustrated in Figure 3.9. In Eq. 3.87, ΔKn is the logarithmic width of the transitional regime and Kn_m is the midpoint of the transitional regime where $P_b = 1/2$. To illustrate the bridging process, suppose that the free molecular, rarefied transitional, and continuum values for the axial force coefficient ($C_{A,fm}$, $C_{A,tr}$, and $C_{A,co}$, respectively) at $\alpha = 0$ deg and $\beta = 0$ deg are known. It is further noted that $C_{A,tr}$ can be for an arbitrary Kn condition, so long as that Kn lies somewhere in the transitional region between the free molecular and continuum limits. First, $C_{A,tr}$ is inserted into the left-hand side of Eq. 3.86 while $C_{A,fm}$ and $C_{A,co}$ are inserted into the right-hand side. Solving for P_b at the transitional condition that $C_{A,tr}$ corresponds to gives:

$$P_{b,tr} = \frac{C_{A,tr} - C_{A,co}}{C_{A,fm} - C_{A,co}} \qquad (3.88)$$

$P_{b,tr}$ is then substituted back into Eq. 3.87 to solve for Kn_m as follows:

$$Kn_m = \frac{Kn_{tr}}{exp\left(\frac{\Delta Kn}{\sqrt{\pi}}erf^{-1}(2P_{b,tr} - 1)\right)} \tag{3.89}$$

With Kn_m known, the erf-log function value P_b at any intermediate Kn_∞ can be obtained from Eq. 3.87. Lastly, this intermediate P_b is substituted back into Eq. 3.86 to obtain the C_A value at any Kn_∞ within the ΔKn range. The same procedure applies when calculating the other aerodynamic force coefficients (C_Y, C_N) and moment coefficients (C_l, C_m, C_n). The resulting coefficients are functions of Kn that vary for different α, β, and δ combinations. In this work, the logarithmic width was defined as $\Delta Kn = log(Kn_{fm} - Kn_{co})$. From the reference trajectory presented, the logarithmic width is therefore $\Delta Kn = log(232.24 - 0.000263) = 5.448$.[7]

In summary, the application of Eqs. 3.86-3.89 provides the bridging relation for any aerodynamic coefficient needed at a given combination of Kn, α, β, and δ. On the aforementioned reference trajectory, three trajectory points were chosen for the bridging process. These sample points are marked with red circles in Figure 3.12 and the corresponding flight conditions are listed in Table 3.2. The following sections describe the methods employed to compute the aerodynamic coefficients at these distinct flow regimes.

---

[7]↑Note that Ref. [84] defined the universal transitional width as $\Delta Kn = log(500) = 6.2146$, which was based on existing DSMC data for different entry vehicles such as Viking, Pathfinder, and Stardust.
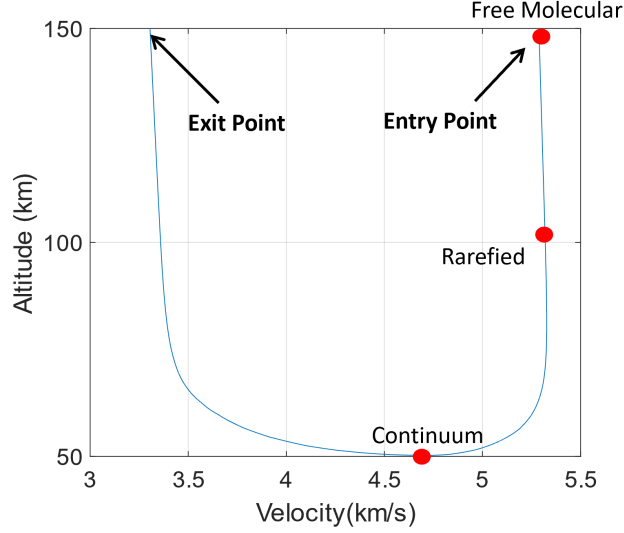
Figure 3.12. The sample points along the reference trajectory for the bridging method are marked.

Table 3.2. Flow conditions used in the single-point bridging method

Alt (km)	V_∞ (km/s)	ρ_∞ (kg/m^3)	T_∞ (K)	Kn_∞	Ma_∞	Flow Regime
150.0	5.2869	1.756e-10	290.72	232.24	19.56	Free Molecular
106.7	5.3138	8.882e-08	140.98	0.3364	28.23	Rarefied Transitional
50.5	4.8350	1.186e-04	155.36	2.63e-04	24.47	Continuum

3.2.5 Free Molecular Aerodynamics

In the free molecular regime, λ can be on the same order of magnitude as the reference length of the vehicle, or greater. DSMC can be used to compute free molecular aerodynamics. However, a sample DSMC calculation carried out for a single Kn, α, β, and δ combination took a few hours to complete, which was undesirable. Fortunately, analytical expressions for pressure and shear stress in this flow regime are available. These mathematical expressions were adapted into a panel code to facilitate faster computation times (on the order of minutes per Kn, α, β, δ combination). This section discusses the development of the free molecular aerodynamics tool employed in this dissertation.

Consider a surface element of the MES subject to the freestream flow V_∞ as shown in Figure 3.13. The pressure (p) and shear stress (τ) acting on the element result from particles

colliding with the surface. For free molecular flows, these quantities are expressed as follows [80]:

$$\frac{p}{p_\infty} = \left[\frac{1+\epsilon}{\sqrt{\pi}} s \sin\phi + \frac{1}{2}(1-\epsilon)\sqrt{\frac{T_r}{T_\infty}} \right] \exp(-s^2 \sin^2\phi) +$$

$$\left[(1+\epsilon)\left(\frac{1}{2} + s^2\sin^2\phi\right) + \frac{1}{2}(1-\epsilon)\sqrt{\pi}\sqrt{\frac{T_r}{T_\infty}} s\sin\phi \right][1 + \text{erf}(s\sin\phi)] \quad (3.90)$$

$$\frac{\tau}{p_\infty} = \frac{1-\epsilon}{\sqrt{\pi}} s\cos\phi \left[\exp(-s^2\sin^2\phi) + \sqrt{\pi} s\sin\phi\{1 + \text{erf}(s\sin\phi)\} \right] \quad (3.91)$$

where the speed ratio (s) is obtained from:

$$s = \frac{V_\infty}{\sqrt{2RT_\infty}}$$
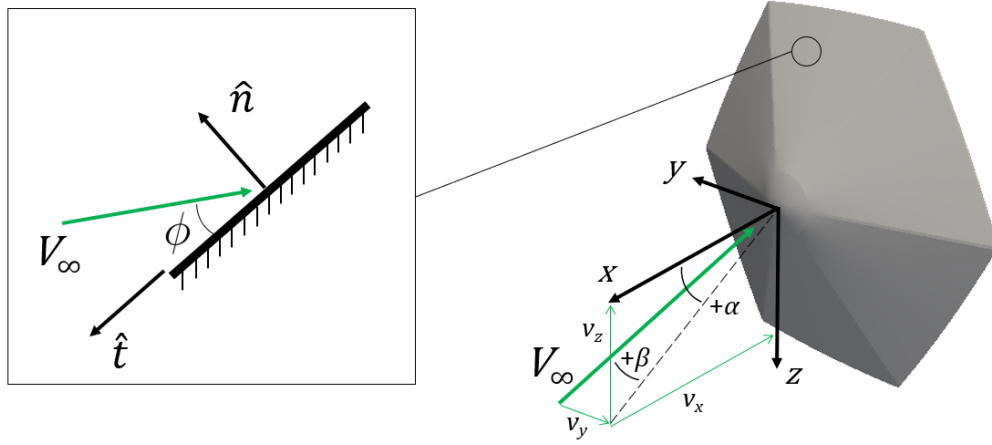
Figure 3.13. A surface element of the MES subject to oncoming flow.

In the preceding equations, V_∞ is the freestream velocity, ϕ is the inclination angle of the surface element with respect to the freestream direction, T_∞ is the freestream temperature of the gas flow, and ϵ is the fraction of specularly-reflected particles from the surface.[8] The

---

[8]↑$\epsilon = 1$ means that all particles are reflected *specularly* after colliding with the surface of the vehicle. A specular reflection is perfectly elastic in which a particle that collides with a surface rebounds with a velocity that is equal in magnitude but opposite in direction to the pre-collision velocity. $\epsilon = 0$ means that all particles are *diffusely* reflected away from the surface. A diffuse reflection is one in which the particle's post-collision velocity independent of its incoming velocity.

symbol T_r in Eq. 3.90 is the temperature of particles that are reflected from the surface. By assuming full thermal accommodation, T_r may be replaced by the wall temperature T_w (i.e., the surface temperature).

The unit direction of the incoming freestream flow is given by:

$$\hat{\mathbf{V}}_\infty = [-\cos\alpha\cos\beta \quad -\sin\beta \quad -\sin\alpha\cos\beta]^T \tag{3.92}$$

The incidence angle ϕ of each surface element is then obtained from the geometry shown in Figure 3.13 through:

$$\sin\phi = -\hat{\mathbf{V}}_\infty \cdot \hat{\mathbf{n}} \tag{3.93}$$

With ϕ known, the p and τ acting on each surface element can be computed via Eqs. 3.90-3.91. Then, the differential aerodynamic force $\mathbf{df}$ acting on a surface element dA becomes available from the following:

$$\mathbf{df} = \left(C_p\,\hat{\mathbf{n}} + C_f\,\hat{\mathbf{t}}\right) dA \tag{3.94}$$

where the following expressions for modified pressure and skin-friction coefficients are used:

$$C_p = \frac{p/p_\infty}{s^2} \tag{3.95}$$

$$C_f = \frac{\tau/p_\infty}{s^2} \tag{3.96}$$

In Eq. 3.94, $\hat{\mathbf{n}}$ is the outward normal unit vector of the surface element and $\hat{\mathbf{t}}$ is the tangential unit vector of the element as shown in Figure 3.13. Note that $\hat{\mathbf{t}}$ is obtained from the following expression [88]:

$$\hat{\mathbf{t}} = \frac{\hat{\mathbf{n}} \times (-\hat{\mathbf{V}}_\infty \times \hat{\mathbf{n}})}{\sqrt{1 - (\hat{\mathbf{V}}_\infty \cdot \hat{\mathbf{n}})^2}}$$

Integrating **df** over the total surface area of the vehicle yields the total aerodynamic forces acting on the vehicle and scaling appropriately yields the aerodynamic force coefficients. Therefore, the aerodynamic force and moment coefficients are obtained through the following:

$$\begin{Bmatrix} C_A \\ C_Y \\ C_N \end{Bmatrix} = \frac{1}{A_{ref}} \iint_S \begin{Bmatrix} \mathbf{df} \cdot \hat{\mathbf{x}} \\ \mathbf{df} \cdot \hat{\mathbf{y}} \\ \mathbf{df} \cdot \hat{\mathbf{z}} \end{Bmatrix} \tag{3.97}$$

$$\begin{Bmatrix} C_l \\ C_m \\ C_n \end{Bmatrix} = \frac{1}{A_{ref}\, l_{ref}} \iint_S \begin{Bmatrix} (\mathbf{r} \times \mathbf{df}) \cdot \hat{\mathbf{x}} \\ (\mathbf{r} \times \mathbf{df}) \cdot \hat{\mathbf{y}} \\ (\mathbf{r} \times \mathbf{df}) \cdot \hat{\mathbf{z}} \end{Bmatrix} \tag{3.98}$$

where the unit directions $\hat{x}$, $\hat{y}$, and $\hat{z}$ correspond with the body-fixed axes shown in Figure 3.13. Also, A_{ref} is the reference area, l_{ref} is the reference length, and **r** is the position vector of the surface element with respect to the moment reference point.

For a simple shape like a sphere, the analytic formulation of the aerodynamic coefficients can readily provide the desired values. However, a numerical solution was necessary for the more complex MES geometry. A numerical panel code was developed to compute the aerodynamic coefficients of the MES using the above free molecular aerodynamics theory. The code receives as input the flow conditions, vehicle attitude, and the vehicle geometry. The MES geometry was triangulated as shown in Figure 3.14 and supplied as a stereolithography (STL) mesh file. The pressure and shear stress acting on each triangular surface element was computed using the above equations. Note that if a surface element is shadowed (i.e., $\hat{\mathbf{V}}_\infty \cdot \hat{\mathbf{n}} > 0$), then the code enforces $C_p = 0$ and $C_f = 0$ for that surface element. With C_p and C_f computed for every element, the code then computes the individual force and moment contributions and sums them over the entire vehicle surface according to Eqs. 3.97-3.98. Thus, the free molecular aerodynamic coefficients become available for any given combination of flow condition, α, β, and δ. Note that the source code of the panel method is listed in Appendix D.

For verification, the results of the free molecular panel code were compared to published data. Hart et. al. developed validated analytic formulations for free molecular aerodynamic
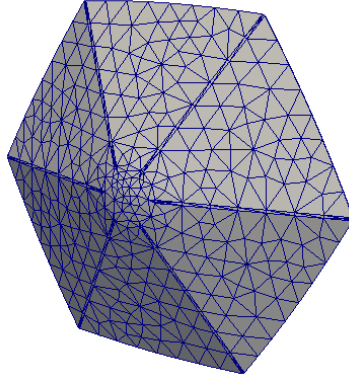
Figure 3.14. A triangulated surface mesh of the MES.

coefficients of general shapes like a sphere and a cylinder [88], [89]. Using the same numerical parameters employed by Hart et. al., the aerodynamics of a sphere and a cylinder were computed using the panel code. The results are compared with the published figures in Figures 3.15 and 3.16. Because raw data was not available from Hart et. al., a direct numerical comparison could not be performed. However, a qualitative comparison indicates good agreement between both methods.

(a) Panel code results

(b) Ref. [88]
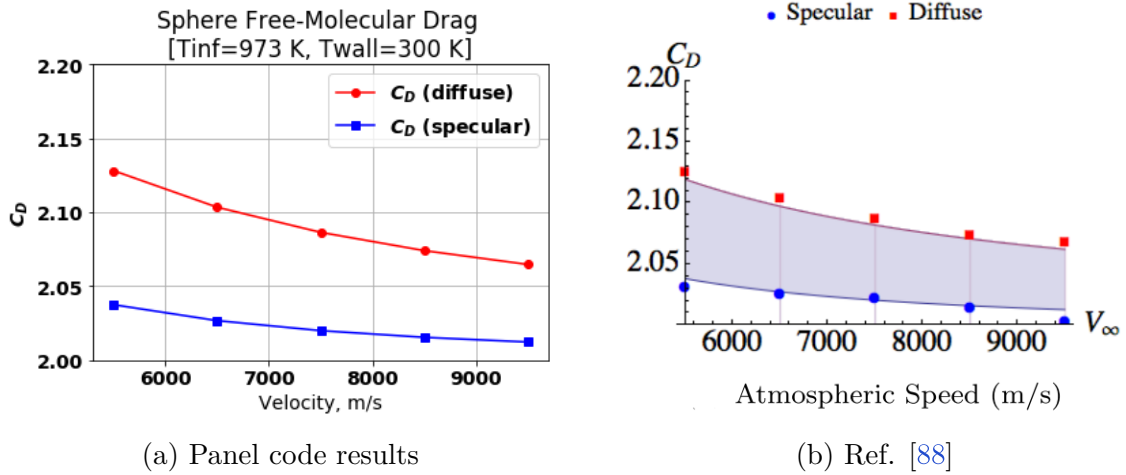
Figure 3.15. The free molecular drag of a sphere as a function of the freestream velocity.
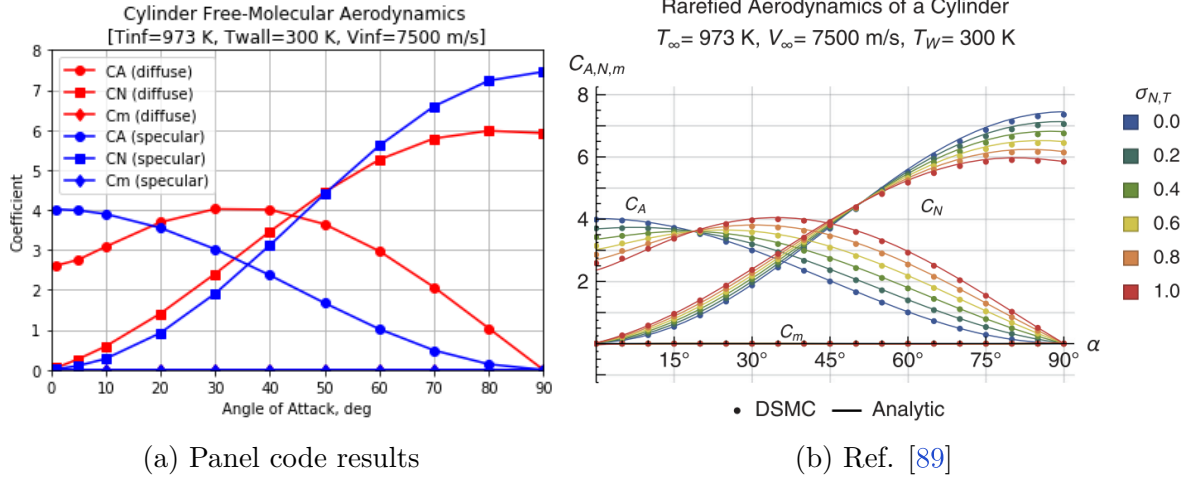
Figure 3.16. The free molecular aerodynamics of a cylinder with a length-to-diameter ratio of 2.18.

The panel code was also used to compute the coefficients for the Apollo capsule and compared with data obtained by Moss et. al. [90] through DSMC analysis. Again, the same flight conditions assumed by Moss et. al. were adopted for the analysis to facilitate a meaningful comparison. The aerodynamics for α =-25 deg at 200 km and 170 km altitudes were computed and the results are provided in Table 3.3. The good agreement between the panel code results and the published data is evident.

Table 3.3. Comparison of free molecular aerodynamics for the Apollo entry capsule (α =-25 deg)

Source	Alt (km)	C_A	C_N	$C_{m,0}$	C_D	C_L	L/D
Moss et. al., [90]	200.0	1.731	-0.777	0.113	1.898	0.027	0.014
Panel code	200.0	1.720	-0.776	0.112	1.887	0.023	0.012
Moss et. al., [90]	170.0	1.734	-0.775	0.112	1.899	0.030	0.016
Panel code	170.0	1.727	-0.777	0.112	1.893	0.026	0.014

Changing the atmospheric composition is straightforward in the panel code and is done by specifying the appropriate gas constant R, which enters the analysis through the speed ratio s. At Mars, the dominant chemical species in the atmosphere is CO_2, for which $R = 188.92$ J/kg/K. Additional verification calculations were carried out for the Mars Pathfinder entry vehicle. Using the flight conditions assumed in the DSMC analysis performed by Moss et.

al. [91], the panel code was again employed to compute aerodynamic coefficients for the Mars Pathfinder aeroshell. Two flight Kn conditions are compared in Table 3.4. Aside from minor differences in the values, a favorable comparison is again evident.

Table 3.4.   Comparison of free molecular aerodynamics for the Mars Pathfinder entry aeroshell ($\alpha =5$ deg)

Source	Kn	C_A	C_N	$C_{m,cg}$	C_D	C_L
Moss et. al., [91]	100.0	2.049	0.173	0.015	2.056	-0.007
Panel code	100.0	2.059	0.174	0.015	2.066	-0.006
Moss et. al., [91]	24.09	2.040	0.169	0.014	2.047	-0.010
Panel code	24.09	2.069	0.174	0.015	2.076	-0.007

The good agreement between published data and the results of the panel code indicates that the code is properly computing the aerodynamics in the free molecular regime.

3.2.6   Rarefied Transitional Aerodynamics

There are no closed form equations for pressure and shear stress like Eqs. 3.90-3.91 that correspond with the rarefied transitional regime. Therefore, the DSMC method was adopted by this dissertation to compute the MES aerodynamics at the rarefied transitional trajectory point indicated in Figure 3.12 and Table 3.2. A formal description of the DSMC algorithm is considered beyond the scope of the present discussion and the reader is referred to Bird's 1994 book [80]. Instead, this section describes the setup of the DSMC calculations carried out with the open-source solver SPARTA (**S**tochastic **PA**rallel **R**arefied-gas **T**ime-accurate **A**nalyzer) developed at Sandia National Laboratories [92].[9] The main input groups needed by SPARTA are the vehicle attitude, flow domain, flow conditions, and any problem-dependent physical models. Vehicle attitude is simply the α and β combinations chosen for database building to be described in Sec. 3.2.9. The following describes how the latter three input groups were generated.

The flow domain employed in SPARTA was a 1.6 m $\times$ 2.0 m $\times$ 2.0 m rectangular box. These dimensions were chosen to fully enclose the triangulated MES surface mesh as shown in Figure 3.17. A two-level Cartesian cell hierarchy was used to discretize the domain into

---

[9]↑https://sparta.github.io/

58,212 cell volumes. This refinement level was chosen based on the rule-of-thumb that cell dimensions must be approximately one-third of the local λ [80]. All DSMC computations used $\lambda = 0.45$ m, which corresponds with the conditions at the rarefied transitional trajectory point in Figure 3.12.
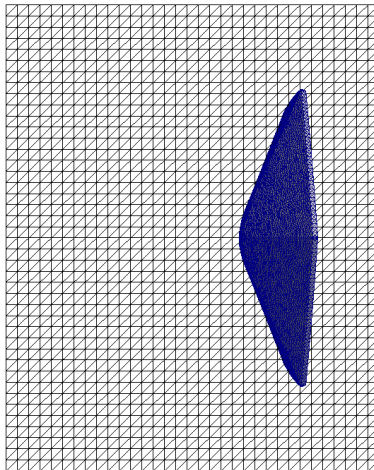
Figure 3.17. The DSMC computational domain that fully encloses the MES geometry [86].

The flight velocity, chemical composition of the gas, flow number density, and flow temperature make up the flow conditions needed for a single SPARTA calculation. The flight velocity is readily available from the reference trajectory previously shown in Figure 3.12. For the chemical composition of the gas flow, the Mars atmosphere was assumed to be 97% CO_2 and 3% N_2 by mass for consistency with previous DSMC analyses of Mars entry flows [93], [94].[10] The number density is determined from Eq. 3.85 using the density profile of the reference trajectory as well as the molar mass of CO_2 indicated in Table 3.1. Lastly, the temperature was obtained from a fourth-order polynomial function derived by fitting COSPAR[11] temperature vs. altitude data for Mars [97].

A major numerical approximation made in DSMC is the number of simulated gas particles that represent the real number of particles in a given unit volume of a flow. In SPARTA, a driving simulation parameter is F_{num}, defined as the ratio of the real particle count to

---

[10]↑An alternative breakdown of 95% CO_2 and 5% N_2 has also been assumed in other Mars entry flow analyses (e.g., Refs. [95], [96]).

[11]↑Committee on Space Research, https://cosparhq.cnes.fr/.

that of the simulated particles. Each cell volume in the computational domain was assigned 20 simulated particles so that enough collisions could be modeled and sampled. A sample calculation was carried to compare the effect of increasing the particles-per-cell count to the aerodynamics of the baseline MES configuration. As shown in Table 3.5, simulating 40 particles per cell did not significantly change the aerodynamic coefficients. Because less simulated particles also translates to a faster computational time, 20 particles per cell was adopted for all DSMC calculations.

Table 3.5. Results of particle count convergence study for the baseline vehicle $(Kn = 0.05, \alpha = -15 \text{ deg}, \beta = 0 \text{ deg})$

Particle Count (per cell)	C_A	C_N	C_m
20	1.55005	-0.22116	-0.00609
40	1.55029	-0.22124	-0.00612

The aforementioned molecular collisions give rise to microscopic properties that, when averaged, provide the macroscopic properties of the gas flow (e.g., density). To adequately capture these molecular interactions, the time step (Δt) over which DSMC simulates molecular motion must be sufficiently small. Bird recommends setting the time step to be much smaller than the mean collision time (Δt_m), defined as the mean time between successive collisions suffered by a molecule. Δt_m is related to the mean free path as follows:

$$\lambda = V_{th}\Delta t_m \tag{3.99}$$

After rearranging, this provides:

$$\Delta t_m = \frac{\lambda}{V_{th}} \tag{3.100}$$

where V_{th} is the mean thermal speed of the gas molecules in the flow:

$$V_{th} = \sqrt{\frac{8k_B T_\infty}{\pi m_x}} \tag{3.101}$$

In Eq. 3.101, k_B is the Boltzmann constant[12], T_∞ is the static temperature of the gas, and m_x is the mass of 1 molecule of the gas species x. Because CO_2 is the dominant molecular species in the Martian atmosphere, m_x was set to $m_{CO_2} = 7.306 \times 10^{-26}$ kg. Carrying out the calculations via Eqs. 3.100-3.101, the mean collision time was found to be 0.00174 sec. This number was then divided by 1000 such that Δt was smaller, per Bird's recommendation. Therefore, $\Delta t = 1.74 \times 10^{-6}$ sec in all DSMC simulations carried out.

The VSS model was adopted for carrying out collisions in SPARTA because this model incorporates the dependence on temperature of the molecular diameter and hence the collision cross-sections. Internal energy exchange between collision partners was also modeled by accounting for the rotational and vibrational energy modes of CO_2. Parameter values associated with these modeling assumptions are included in Appendix A.

Particle-to-surface collisions were assumed to be fully-diffuse meaning that the reflected velocity of the molecule after striking the vehicle surface is independent of its initial velocity. SPARTA determines the reflected velocity by sampling from a Gaussian distribution that is dependent on the wall temperature (T_w). T_w was assumed to be a constant, which was estimated via the Stefan-Boltzmann Law:

$$q_{rerad} = \varepsilon \sigma T_w^4 \tag{3.102}$$

where ε is the emissivity of the surface and σ is the Stefan-Boltzmann constant.[13] The re-radiated heat flux q_{rerad} was approximated as the sum of the convective and radiative heat rates to the vehicle surface. The Sutton-Graves correlation was employed to generate a first-order estimate of the instantaneous convective heat rate at the trajectory point of interest. The radiative heat rate was ignored because it is nominally insignificant compared to the convective heat rate for practical Mars flows [21]. By assuming the emissivity of the PICA TPS material ($\varepsilon = 0.8$), the constant wall temperature used in all DSMC calculations was estimated to be $T_w = 764.98$ K.

---

[12]$\uparrow k_B = 1.3806 \times 10^{-23}\, m^2\, kg\, s^{-2} K^{-1}$

[13]$\uparrow \sigma = 5.67 \times 10^{-8}\, W\, m^{-2}\, K^{-4}$

Surface mesh grid density was varied to understand the effects of the mesh refinement on the resulting aerodynamics. Calculations were then carried out for a mesh with 83,000 elements and another with 328,000 elements. Table 3.6 demonstrates that increasing the element count did not significantly change the aerodynamic coefficients. Because the coarser mesh corresponds with a faster computation time, it was adopted for all DSMC calculations.

Table 3.6. Results of surface mesh refinement study with P1 deflected at $\delta = 30$ deg ($Kn = 0.34$, $\alpha = 0$ deg, $\beta = 0$ deg)

Element count	C_A	C_m
83,000	1.464576	-0.099200
328,000	1.464543	-0.099205

The convergence of each DSMC case was monitored by checking the history of collisions and the particle count. When both numbers were no longer changing by much, this was treated as a qualitative indication that the case had reached a steady state. A more exact convergence criterion involving the aerodynamic body forces was also adopted. A case was considered converged if the change in the forces was less than 1 % over 50,000 consecutive time steps. All DSMC cases converged after 100,000 total time steps with this criterion.

A summary of the DSMC run parameters for the rarefied transitional condition of interest is provided in Table 3.7.

Table 3.7. DSMC simulation parameters

Parameter	Value
Knudsen number	0.3364
Number density (m^{-3})	1.21e18
Simulated particles	1.16e06
$F_{num} = \frac{\text{Real particles}}{\text{Simulated particles}}$	6.68e12
CO_2 mass fraction	0.97
N_2 mass fraction	0.03
Time-step size (s)	1.74e-06
Total time-steps	100,000

3.2.7 Hypersonic Continuum Aerodynamics

Methods for computing continuum flow aerodynamics range from high-fidelity Navier-Stokes solvers like NASA's Langley Aerothermodynamic Upwind Relaxation Algorithm (LAURA) code [98] to simple prediction methods like the Newtonian flow theory [99]. The LAURA code in particular is a storied solver that has been used to compute aerodynamics data for Mars vehicles like Pathfinder [70], Mars Smart Lander [73], Phoenix [100], and Mars Science Laboratory (MSL) [71]. A great challenge associated with Navier-Stokes solvers is computational cost. Because the MES design is conceptual, it was deemed more favorable to use cheaper computational methods to compute its hypersonic continuum aerodynamics.

Fortunately, the aerodynamics of a blunt shape like the MES in this flow regime is pressure-dominated. Therefore, the Newtonian theory for pressure was deemed an acceptable alternative to expensive Navier-Stokes analyses. Due to its increased accuracy for determining blunt body aerodynamics, the modified Newtonian theory introduced by Lees [101] was adopted instead of the classical sine-squared Newtonian theory. As was done for the free molecular regime, a panel code that implements the modified Newtonian theory was also developed.

The modified Newtonian theory reduces the problem of determining hypersonic aerodynamics to a simple equation involving the incidence angle of the body surface relative to the flow direction. This so-called local surface inclination method expresses the pressure coefficient acting on the local surface as follows:

$$C_p = C_{p,max} \sin^2 \theta \qquad (3.103)$$

where θ is the angle of incidence of the surface with respect to the incoming flow direction as shown in Figure 3.18 and $C_{p,max}$ is obtained via:

$$C_{p,max} = \frac{2}{\gamma M_\infty^2} \left\{ \left[\frac{(\gamma+1)^2 M_\infty^2}{4\gamma M_\infty^2 - 2(\gamma-1)} \right]^{\gamma/(\gamma-1)} \left[\frac{1 - \gamma + 2\gamma M_\infty^2}{\gamma+1} \right] - 1 \right\} \qquad (3.104)$$

In Eq. 3.104, M_∞ is the freestream Mach number and γ is the specific heat ratio of the gas flow.

The above sine-squared law can also be expressed as a cosine-squared law by replacing the angle θ with $\phi = \pi/2 - \theta$. Here, ϕ is the angle that the inward unit normal vector of the surface ($\hat{\mathbf{n}}$) makes with the incoming flow as shown in Figure 3.18 and it is computed as follows:

$$\cos\phi = \hat{\mathbf{V}}_\infty \cdot \hat{\mathbf{n}} \tag{3.105}$$

where the unit direction of the freestream velocity vector is given by:

$$\hat{\mathbf{V}}_\infty = [-\cos\alpha\cos\beta \quad -\sin\beta \quad -\sin\alpha\cos\beta]^T \tag{3.106}$$
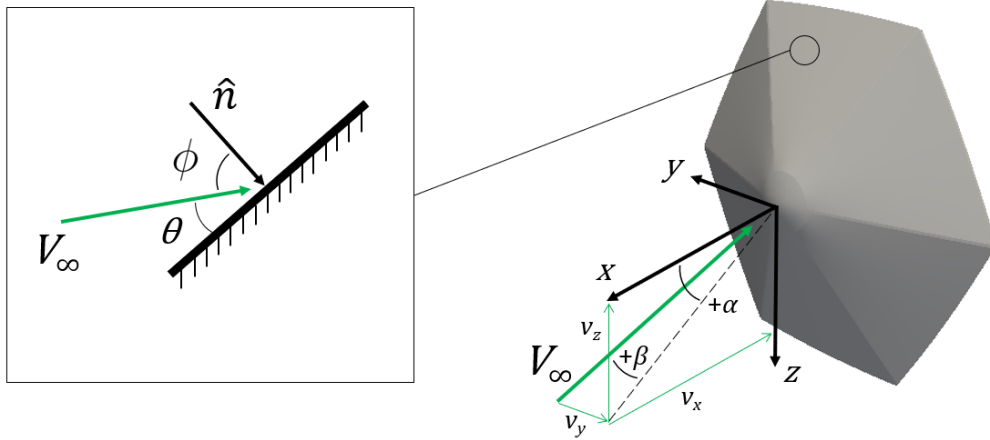
Figure 3.18. A surface element inclined with respect to the incoming flow direction.

With Eq. 3.105, the modified Newtonian expression is rewritten as follows:

$$C_p = C_{p,max}\cos^2\phi = C_{p,max}\left(\hat{\mathbf{V}}_\infty \cdot \hat{\mathbf{n}}\right)^2 \tag{3.107}$$

The panel code takes as input a triangulated surface mesh of the MES and computes C_p at each mesh element. If the inward normal of a given element is opposite in direction to

91

the flow (i.e., $\hat{\mathbf{V}}_\infty \cdot \hat{\mathbf{n}} < 0$), then it is shadowed from the flow and the code enforces $C_p = 0$ at that surface.

The pressure-induced force on an element of the body can be obtained from:

$$\mathbf{df} = C_p \, \hat{\mathbf{n}} \, dA \tag{3.108}$$

where dA is the surface area of the element. Integrating $\mathbf{df}$ over the entire surface area of the vehicle yields the force and moment coefficients:

$$\begin{Bmatrix} -C_A \\ C_Y \\ -C_N \end{Bmatrix} = \frac{1}{A_{ref}} \iint_S \begin{Bmatrix} \mathbf{df} \cdot \hat{\mathbf{x}} \\ \mathbf{df} \cdot \hat{\mathbf{y}} \\ \mathbf{df} \cdot \hat{\mathbf{z}} \end{Bmatrix} = \frac{1}{A_{ref}} \iint_S C_p \begin{Bmatrix} \hat{\mathbf{n}} \cdot \hat{\mathbf{x}} \\ \hat{\mathbf{n}} \cdot \hat{\mathbf{y}} \\ \hat{\mathbf{n}} \cdot \hat{\mathbf{z}} \end{Bmatrix} dA \tag{3.109}$$

$$\begin{Bmatrix} C_l \\ C_m \\ C_n \end{Bmatrix} = \frac{1}{A_{ref} \, l_{ref}} \iint_S \begin{Bmatrix} (\mathbf{r} \times \mathbf{df}) \cdot \hat{\mathbf{x}} \\ (\mathbf{r} \times \mathbf{df}) \cdot \hat{\mathbf{y}} \\ (\mathbf{r} \times \mathbf{df}) \cdot \hat{\mathbf{z}} \end{Bmatrix} = \frac{1}{A_{ref} \, l_{ref}} \iint_S C_p \begin{Bmatrix} (\mathbf{r} \times \hat{\mathbf{n}}) \cdot \hat{\mathbf{x}} \\ (\mathbf{r} \times \hat{\mathbf{n}}) \cdot \hat{\mathbf{y}} \\ (\mathbf{r} \times \hat{\mathbf{n}}) \cdot \hat{\mathbf{z}} \end{Bmatrix} dA \tag{3.110}$$

where A_{ref} is the reference area, l_{ref} is the reference length, and $\mathbf{r}$ is the position vector of the surface element with respect to the moment reference point. Note that the unit directions $\hat{x}$, $\hat{y}$, and $\hat{z}$ are as shown in Figure 3.18.

Equations 3.109-3.110 are exact formulations for obtaining the force and moment coefficients from C_p. For simpler shapes where the surface position vector $\mathbf{r}$ can be parameterized, these equations can lead to analytical expressions for the aerodynamic coefficients [102]. However, more complex geometries like the MES can be difficult to describe through parametric equations, which justified the implementation of a numerical panel code.

As with the free molecular panel code, the present panel code reads the STL file of the MES. The aerodynamic coefficients are then computed through numerical integrations of Eqs. 3.109-3.110. For example:

$$-C_A \approx \frac{1}{A_{ref}} \sum_{i=1}^{N} C_{p,i} \, \hat{\mathbf{n}}_i \cdot \hat{\mathbf{x}} \, \Delta A_i \tag{3.111}$$

The pressure coefficient acting on each panel of the geometry $C_{p,i}$ is then computed using Eq. 3.107. $C_{p,i}$, $\hat{\mathbf{n}}$, and the area of each panel ΔA_i are then substituted into Eq. 3.111. Lastly, a summation of the individual $C_{p,i}$ contributions over all N surface elements is performed to calculate the corresponding aerodynamic coefficient.

To verify the Newtonian panel code, hypersonic aerodynamics of the Apollo command module and MSL foreshell were computed. Three-dimensional surface mesh models using the actual dimensions of both vehicles were developed. Figure 3.19 shows the force, moment, and angle of attack conventions adopted for the analysis to be consistent with published data.

(a) Apollo Command Module [103]   (b) Mars Science Laboratory
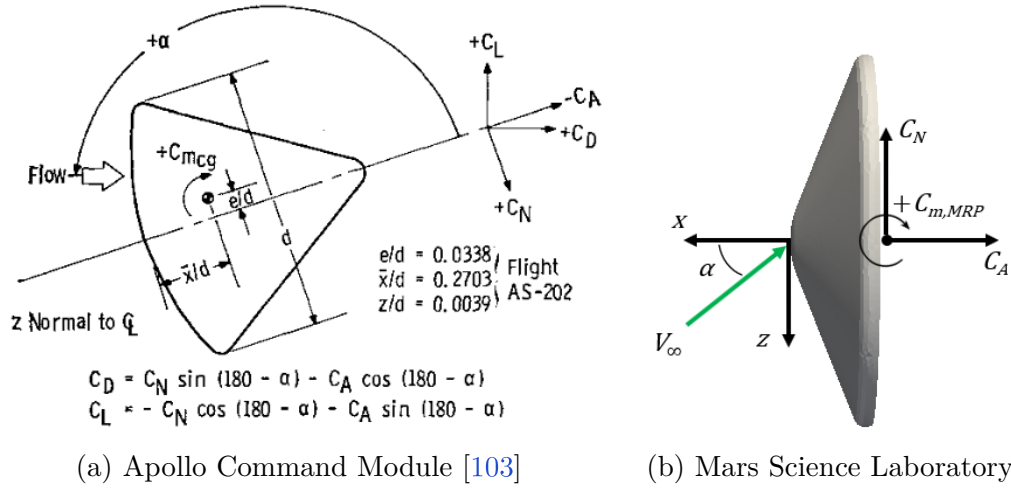
Figure 3.19. Force, moment, and angle of attack conventions used for the Apollo command module and the MSL forebody.

Wind tunnel measurements of C_A, C_N, and $C_{m,cg}$ at $M_\infty = 20$ that were obtained by Griffith and Boylan [103] are presented in Figure 3.20. Using the same Mach number value and assuming a specific heat ratio of $\gamma = 1.4$ for air, the panel code produced the aerodynamic coefficient estimates shown in Figure 3.21. Figures 3.20 and 3.21 reveal comparable qualitative trends for the behavior of C_A, C_N, and $C_{m,cg}$ with respect to α. Despite this qualitative agreement, there are noticeable discrepancies present. For example, the panel code over-predicts the magnitude of C_A at α closer to 180 deg and under-predicts C_N as α approaches 150 deg. A significant deficiency of the modified Newtonian theory is that it neglects viscosity effects and assumes perfect gas flow. It is to these deficiencies that

the numerical discrepancies are attributed. However, the qualitative agreement between the panel code results and the measurements verify that the code is computing the coefficients properly.

(a) Axial force coefficient

(b) Normal force and pitch moment coefficient
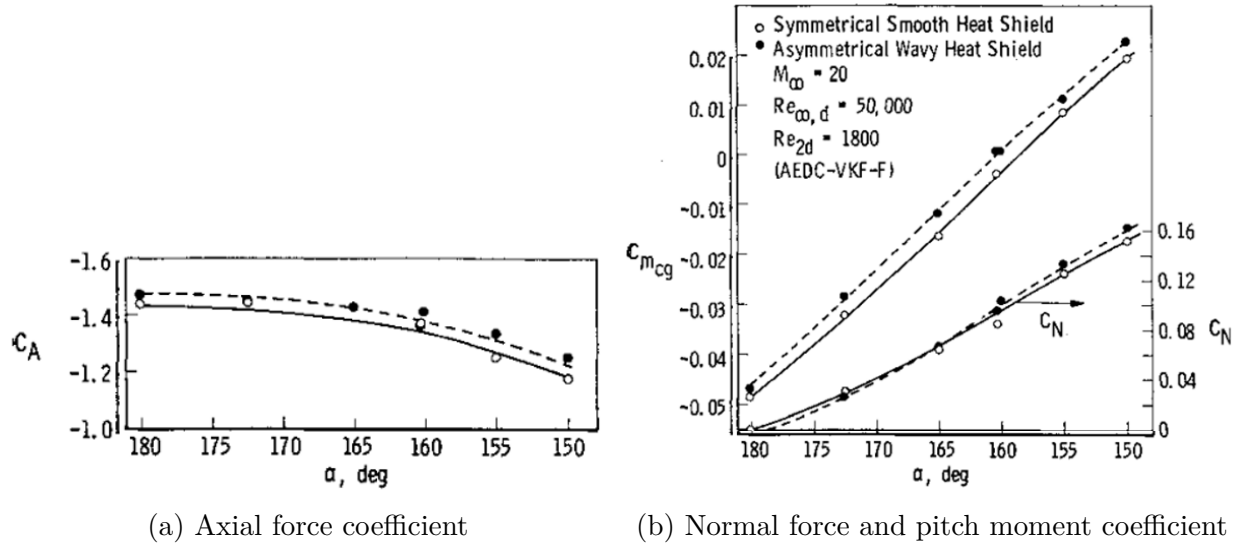
Figure 3.20. Apollo command module aerodynamics wind tunnel measurements at $M_\infty = 20$ (Image source: [103]).

(a) Axial force coefficient

(b) Normal force and pitch moment coefficient
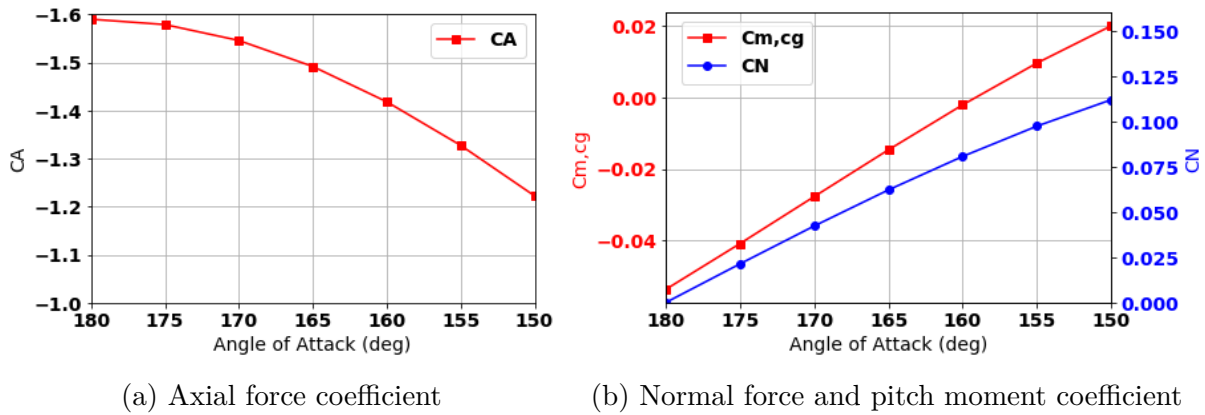
Figure 3.21. Apollo command module aerodynamics at $M_\infty = 20$ computed by the modified Newtonian panel code.

Similarly, aerodynamic coefficient estimates for the MSL forebody were generated using the panel code and compared against published LAURA CFD data [71]. Using a Mach number of 20.01 and assuming a specific heat ratio of $\gamma = 1.33$ for the CO_2-dominated flow, the panel code generated the coefficient estimates shown in Figure 3.22. It is evident

94

from Figure 3.22 that the qualitative behavior of the aerodynamic coefficients are similar between the panel code results and the CFD data. Again, the differences in the values are attributed to the higher physical fidelity of the LAURA solutions. Despite this, the favorable comparison verifies again that the Newtonian method is properly computing the coefficients.

(a) Axial and normal force coefficients   (b) Pitch moment coefficient
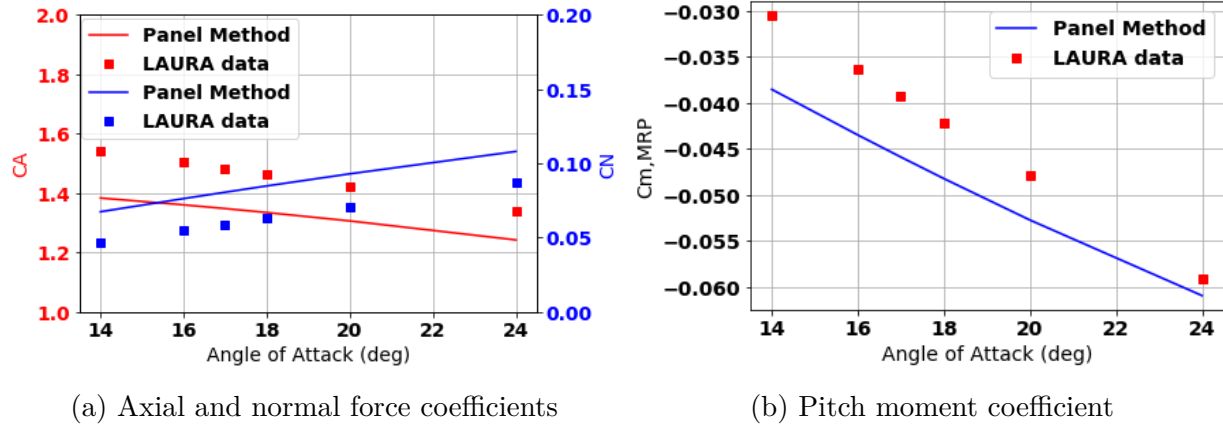
Figure 3.22. MSL forebody aerodynamic coefficients at $M_\infty = 20.01$ (LAURA data extracted from Ref. [71]).

According to Eq. 3.104, both the freestream Mach number (M_∞) and the specific heat ratio (γ) of the gas impact the calculated pressure. For all MES calculations carried out, γ was set to 1.33 to represent the CO_2 environment at Mars. Furthermore, Ma_∞ was set to 24.47, which corresponds with the continuum trajectory point in Table 3.2. A code listing for the panel method is included in Appendix D for reference.

3.2.8 Chemistry Modeling

It is known that collisions between particles can result in chemical reactions.[14] A brief study was conducted using SPARTA to determine the influence of a chemically-reacting flow on the MES aerodynamic coefficients at modest Knudsen numbers ($0.01 < Kn < 1$) . The chemical reactions modeled were adapted from Ref. [95] and included 40 dissociation reactions and 14 exchange reactions involving CO_2, CO, C, N_2, N, NO, O_2, and O. The study

---

[14]↑Note that the discussion of chemistry modeling presented in Sec. 3.2.8 was taken from an existing journal publication (Ref. [86]) and modified where necessary for narrative flow.

indicated that accounting for chemical reactions did not significantly alter the aerodynamic coefficients of the vehicle in the rarefied transitional regime. For instance, the surface pressure contours are very similar regardless of chemical reactions in the flow as shown in Figure 3.23. The low sensitivity of the rarefied transitional aerodynamics to chemical reactions is further supported by Table 3.8, which indicates a small difference in C_A of the baseline vehicle as a result of simulating chemical reactions. As the flow increases in rarefaction and collision frequency decreases, the effects of chemistry are expected to be negligible. Therefore, all DSMC simulations in this work did not simulate chemical reactions due to particle collisions.
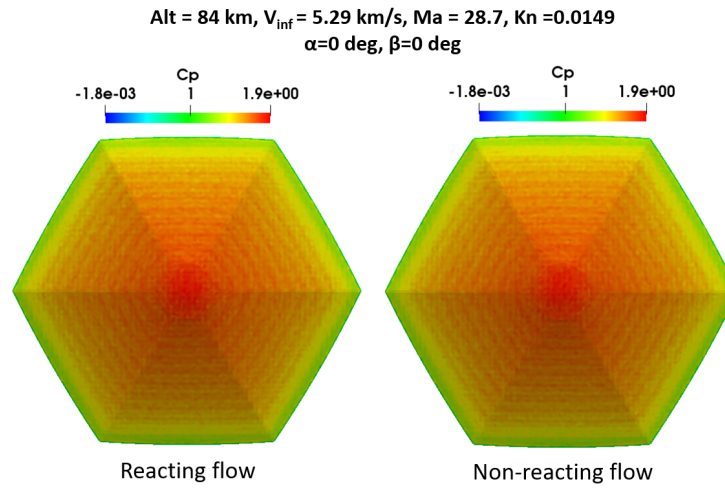
Figure 3.23. DSMC comparison of chemistry effects on surface pressure distribution.

Table 3.8. Effect of chemical reactions on the aerodynamics at two rarefied flow conditions

Altitude (km)	Kn	α (deg)	β (deg)	C_A (reactions)	C_A (no reactions)
94	0.0519	0	0	1.6412	1.6411
84	0.0149	0	0	1.5478	1.5477

By using the modified Newtonian approach in the continuum regime, chemistry effects were also neglected. To gauge the impact of doing so, a set of higher fidelity calculations for the baseline configuration was carried out using the LAURA solver [98] at the continuum flow condition shown in Table 3.2. Non-equilibrium chemistry was modeled using a two-temperature gas model with eight species (CO_2, CO, C, N_2, N, NO, O_2, and O). The

freestream composition was modeled as 97% CO_2 and 3% N_2 by mass. The LAURA results for lift-to-drag ratio (L/D) and C_m are presented in Figure 3.24 (open symbols). The non-reacting, modified Newtonian results are included for comparison (solid lines).

(a)   (b)
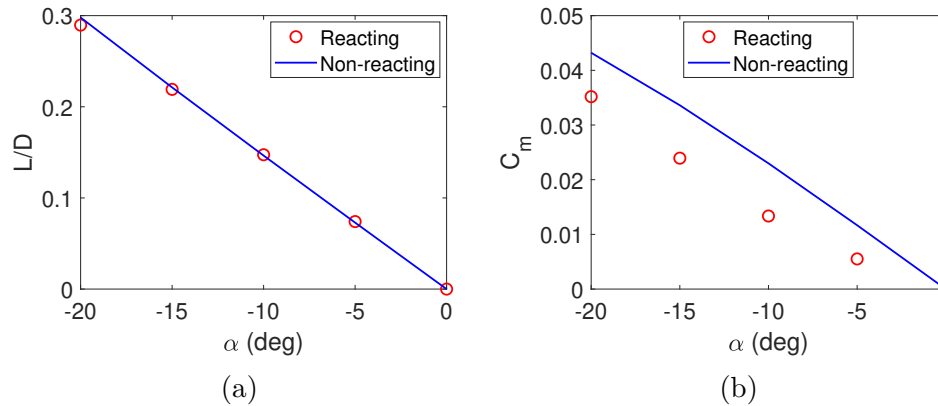
Figure 3.24. A comparison of continuum aerodynamics with and without chemistry effects.

Because the lift and drag are greatly influenced by the pressure distribution on the body, the modified Newtonian and LAURA results for L/D agree well as shown in Figure 3.24(a). Although the C_m trends are similar in Figure 3.24(b), the modified Newtonian results for C_m are greater in magnitude than those predicted by LAURA at non-zero α. The maximum absolute difference is 0.00967, which occurs at $\alpha = -15$ deg. The maximum viscous shearing was found near the shoulder of the vehicle and was only about 5% of the local surface pressure ($\alpha = -15$ deg case). Based on this, it can be inferred that gas chemistry has the greater influence on the difference in C_m, rather than viscous effects. An example of this influence is that of reactions in the shock layer shifting the sonic line location on the aeroshell surface, which can influence the resulting pitching moment as described by Gnoffo et. al. [104].

These results indicate that modeling gas chemistry in the continuum regime is important for computing the moment coefficients. However, this comes at the cost of additional computational effort. Limited computational resources necessitated a balance between accuracy and computational effort. As previously noted, the modified Newtonian approach can reasonably capture hypersonic continuum aerodynamics for blunt bodies because it is pressure-dominated. Therefore, the modified Newtonian approach was deemed acceptable

for the present study, although the reduction in the accuracy of the moment coefficients by neglecting chemistry is acknowledged. The use of correction factors to account for the effects of reacting gas on the moment coefficients is suggested, although not implemented in the present study.

3.2.9 Definition of the Run Matrix

The run matrix lists the range of flow conditions, attitudes, and vehicle deflections analyzed using the aforementioned tools to construct the aerodatabase of the MES.[15] As previously noted, the three flow conditions required by the single-point bridging method are shown in Table 3.2. The first row of Table 3.2 is at the atmospheric interface where the flow conditions are free-molecular. The corresponding panel code was used to compute the aerodynamic coefficients of the MES at this altitude. The middle row of the table corresponds with the rarefied transitional analysis point where DSMC is appropriate. The last row gives the continuum conditions where the modified Newtonian panel code was used.

At each analysis point, the deflected configurations of the MES were evaluated according to the run matrix in Table 3.9. For the pitching configuration shown in Figure 2.9(b), the petal deflection angles analyzed for petal 1 (P1) were $\delta = \{0, 10, 20\}$ deg. As for the yawing configurations in Figure 2.9(b), the deflection angles analyzed for rib 5 (R5) were $\delta = \{0, 5, 10\}$ deg. Note that $\delta = 0$ deg is simply the undeflected baseline vehicle shape seen in Figure 2.10.

Table 3.9. The run matrix used to construct the aerodatabase of the MES

Flow condition	Alt (km)	α (deg)	β (deg)	P1 δ (deg)	R5 δ (deg)
Free molecular	150.0	{-30:5:30}	{-10:5:10}	{0, 10, 20}	{0, 5, 10}
Rarefied	106.7	{-30:5:30}	{-10:5:10}	{0, 10, 20}	{0, 5, 10}
Continuum	50.5	{-30:5:30}	{-10:5:10}	{0, 10, 20}	{0, 5, 10}

According to the run matrix in Table 3.9, only P1 deflections were analyzed. This was enabled by the inherent symmetry of the deflected shapes of the MES. For example, Figure

---

[15]↑The discussion presented in Sec. 3.2.9 was taken from a previous publication (Ref. [86]) and modified where necessary for narrative flow.

3.25 shows that a P4 deflection is symmetric to a P1 deflection in the xz plane. Therefore, the aerodynamics associated with a P4 deflection are available from the P1 values. The same reasoning was applied to justify analyzing only R5 deflections.
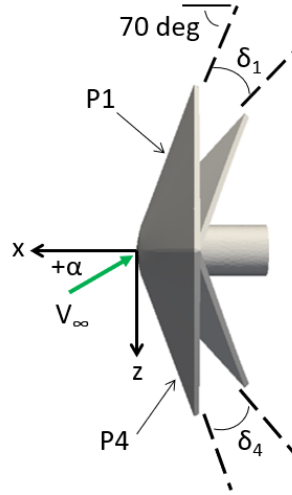
Figure 3.25. An illustration of P1 and P4 deflections.

3.2.10 Static Aerodynamics of the MES

The static aerodynamic coefficients of the MES at the various configurations were computed with the single-point erf-log bridging method. The results were compiled into a database, which could be queried based on Kn or q_∞, as well as α, β, and δ. This section presents data extracted from the database to discuss notable aerodynamic characteristics of the MES.[16]

The static aerodynamics of the MES are presented in Figures 3.26-3.28. Representative results from each of the three flow regimes are included to show the effect of flow rarefaction. The L/D characteristics of the baseline vehicle (i.e., all $\delta = 0$ deg) are shown in Figure 3.26. In all three flow regimes, the MES produces positive lift at negative angles of attack. This is consistent with other blunt body aeroshells that have flown on Mars. The L/D is

---

[16]↑The discussion presented in Sec. 3.2.10 was taken from a previous publication (Ref. [86]) and modified where necessary for narrative flow.

also largest in the continuum regime due to the greater atmospheric density. Because drag increases with rarefaction, L/D decreases as the flow approaches free molecular conditions.
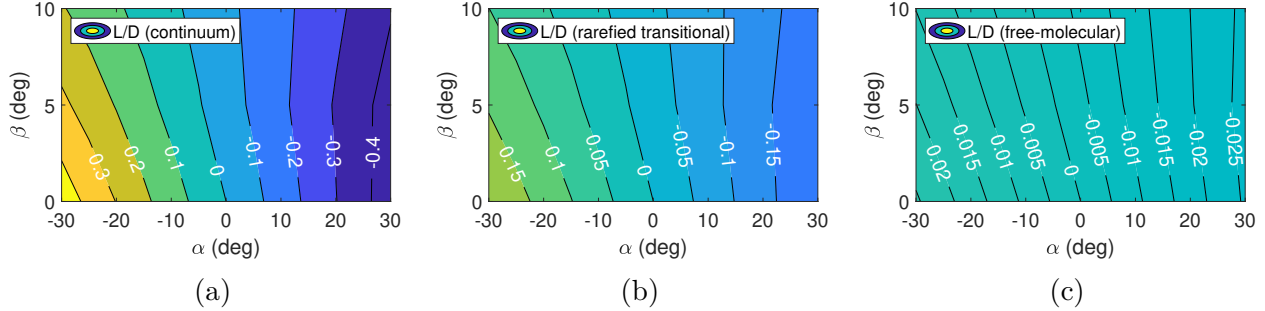
Figure 3.26. Lift-to-drag characteristics of the MES baseline vehicle.

The pitching characteristics of the MES are shown in Figure 3.27. All moment coefficients were computed relative to the moment reference point located $0.3D$ (0.405 m) aft of the nose on the x axis. Knowing where in its trajectory the MES is stable and unstable in pitch is important for future trajectory simulations. Static stability in pitch is demonstrated when $\partial C_m/\partial \alpha < 0$, meaning that a restoring pitch moment exists for non-zero α. On the other hand, $\partial C_m/\partial \alpha > 0$ means that a destabilizing pitching moment exists for non-zero α. The MES must employ its petal deflection control to manage pitching instabilities. Figure 3.27(a) demonstrates that the baseline shape is statically stable in pitch in hypersonic continuum conditions. In the rarefied transitional and free-molecular conditions shown in Figures 3.27(d) and 3.27(g), the vehicle is statically unstable in pitch. Frictional forces at higher flow rarefaction cause this destabilizing motion, which has been observed in other blunt-body entry vehicles such as Mars Pathfinder [91]. The observed instability persists until $0.04 < Kn < 0.05$, which corresponds to an altitude of approximately 93 km and $q_\infty = 9.4$ Pa on the nominal trajectory. Below this altitude, $\partial C_m/\partial \alpha < 0$ and the baseline vehicle is always stable. The same pitch static stability trends can be observed for the deflected cases in Figure 3.27. Note that β does not greatly affect C_m, except when δ is significant in rarefied transitional conditions (see Figure 3.27(f)).
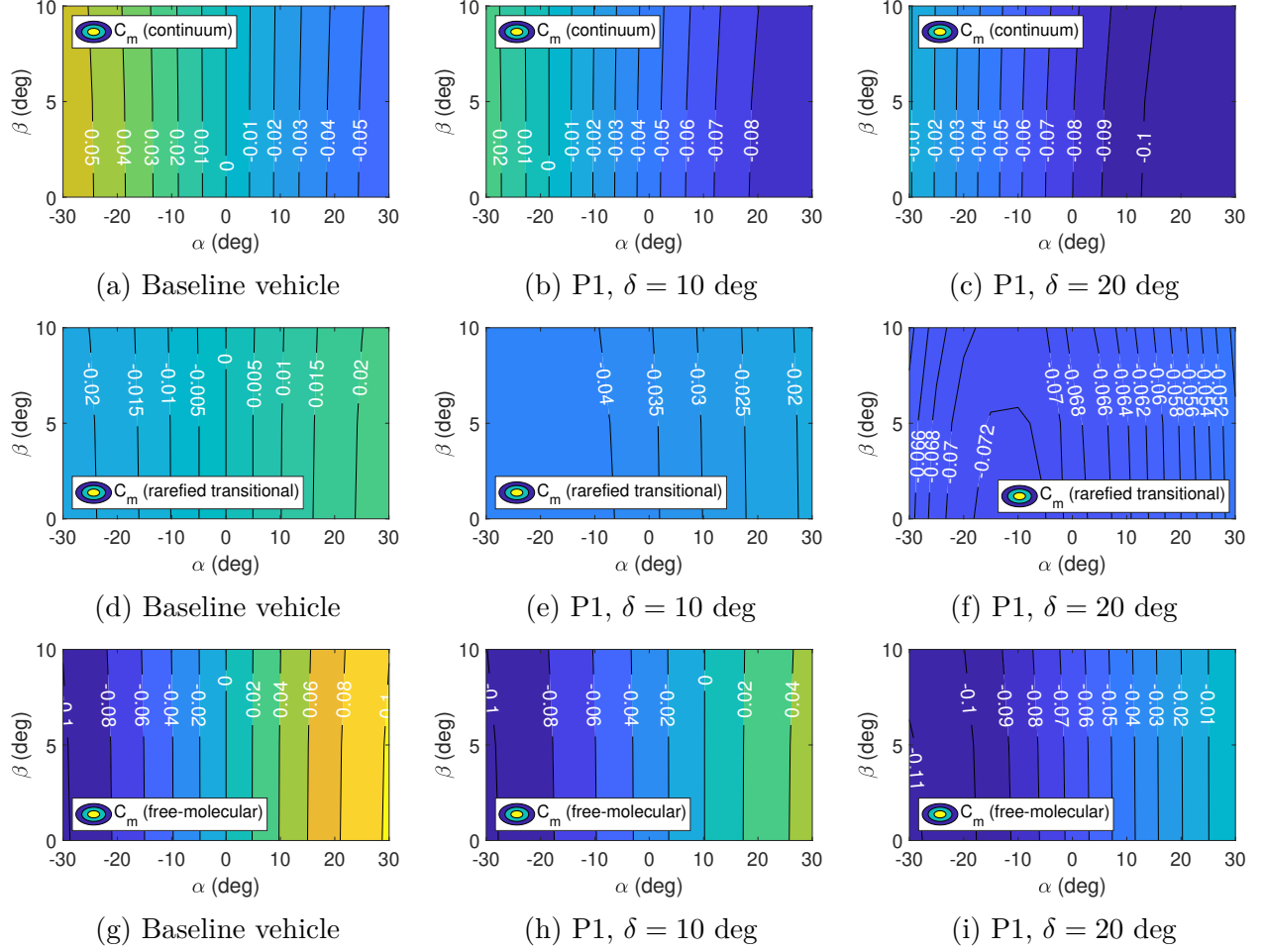
Figure 3.27. Pitching characteristics of the MES [86].

By deflecting P1 as shown in Figure 2.9(b), the MES can achieve a negative moment that decreases α for pitch-down control. Alternatively, pitch-up control is achieved by deflecting P4, which is the direct opposite of P1. Figure 3.27 shows C_m for the pitch-down configuration at $\delta = 10$ and $\delta = 20$ deg. Clearly, the pitch-down configuration is statically unstable at higher flow rarefaction in the present α and δ ranges. Again, β does not significantly affect C_m, but the flow rarefaction does.

A new trim α can be achieved through non-zero δ. For example, $\alpha_{trim} = -18.5$ deg for $\delta = 10$ deg in the continuum condition shown in Figure 3.27(b). This indicates that the envisioned petal deflections of the MES can be utilized to achieve a desired trim orientation. Intermediate δ values may be necessary to achieve some desired attitudes. Therefore, cubic

interpolation was employed to enable the querying of coefficients based on intermediate Kn and δ combinations. Cubic interpolation was also employed whenever intermediate values of α and β were needed. To handle instances in simulations when either α or β exceed their corresponding ranges in the database, a cubic extrapolation method was also used.

Non-zero β values were simulated to obtain the yawing characteristics of the vehicle. Figure 3.28 shows the yawing coefficient C_n as a function of α and β at varying levels of rarefaction. In the continuum regime, the baseline vehicle is stable in yaw because $\partial C_n/\partial \beta > 0$, meaning a restoring yaw moment exists for a non-zero β. The baseline vehicle is also statically unstable in yaw (as it is in pitch) for increasing levels of flow rarefaction because $\partial C_n/\partial \beta < 0$ at these conditions. The instability persists until $Kn \approx 0.04$. The baseline vehicle appears to trim in yaw at $\beta = 0$ deg and $\beta = -6.8$ deg at the rarefied transitional flow condition shown in Figure 3.28(d). This odd trim behavior warrants further investigation, but this was considered beyond the scope of the present work because no β control is anticipated in the rarefied portions of the MES trajectory. Therefore, any potential complications due to the dual β_{trim} values may be avoided.
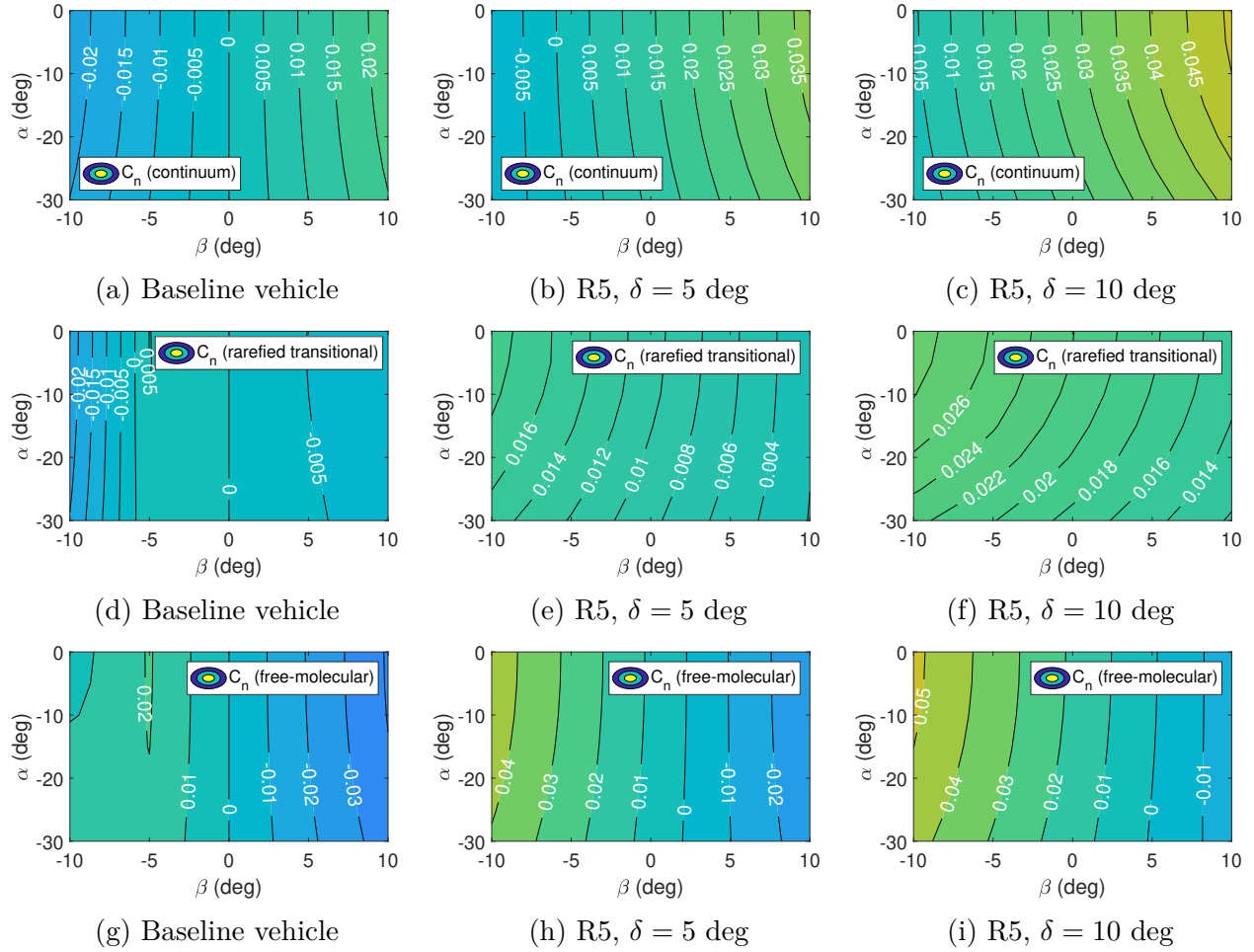
Figure 3.28. Yawing characteristics of the MES [86].

The yawing strategy for the MES is to deflect R2 or R5. The yawing shapes produced by R5 deflections were used in all computations and representative results for C_n are also shown in Figure 3.28. Deflecting R5 induces a positive moment about the body-z axis $(+C_n)$, which corresponds to a "yaw-to-the-right" strategy to modulate β negatively. The results show that the R5 shape is capable of this in the continuum regime. At moderate α, the trim β shifts from 0 deg to approximately 6 deg via a R5 deflection of $\delta = 5$ deg as shown in Figure 3.28(b). Figure 3.28 also indicates that the yawing configurations are statically stable in yaw in the continuum regime only. In the envisioned application of the MES, out-of-plane motion control will be limited to small changes in β. Therefore, the database includes data

for a R5 deflection of up to 10 deg only. Note that α moderately impacts C_n for the R5 shapes especially in rarefied transitional conditions as shown in Figures 3.28(e) and 3.28(f).

As previously noted in Sec. 3.2.9, only the P1 and R5 configurations were analyzed to further reduce the overall computational cost. Deflecting P4 produces the same shape as when P1 is deflected, only it is rotated about the body-x axis by 180 deg. This symmetry is leveraged and the aerodynamic coefficients corresponding to the P4 shape are taken directly from the P1 shape's computed values and assigned the appropriate algebraic sign. For example, $C_m = -0.056$ when deflecting P1 by $\delta = 10$ deg at $\alpha = 5$ deg, $\beta = 0$ deg in the continuum regime as shown in Figure 3.27(b). Because P4 produces an equal but opposite pitch effect as P1, $C_m = 0.056$ for the P4 shape at the same δ and Kn combination for $\alpha = -5$ deg, $\beta = 0$ deg. The same symmetry argument applies to the yawing configurations of the MES.

The pitching and yawing effectiveness of the different configurations shown can also be extracted from the database. Computing the gradients of C_m and C_n with respect to δ yields the control authority measures $\partial C_m / \partial \delta$ and $\partial C_n / \partial \delta$, which are later used for the MES' flight controller (see Secs. 3.3.2 and 3.3.4). Figure 3.29 shows the pitching effectiveness of the P1 deflections ($\partial C_m / \partial \delta$) and the yawing effectiveness of R5 deflections ($\partial C_n / \partial \delta$) as functions of δ and Kn. From Figure 3.29(a), the magnitude of $\partial C_m / \partial \delta$ increases with smaller δ in the continuum limit. Conversely, $\partial C_m / \partial \delta$ increases in magnitude with δ in the free molecular limit. This trend is preserved for all α and β combinations studied.

Representative values of $\partial C_n / \partial \delta$ are also shown in Figure 3.29(b). As expected, the control authority of R5 deflections appears to increase with decreasing Kn. This trend is consistent regardless of the α and β combination. The nearly vertical contour lines for $\beta = 0$ deg in Figure 3.29(b) indicates that $\partial C_n / \partial \delta$ is quasi-constant with δ in the continuum regime. This is not true however in the free-molecular limit as $\partial C_n / \partial \delta$ always varies with δ. This quasi-constant behavior also disappears in the continuum regime at non-zero β.

104

$\partial \, C_m / \partial \delta$

$\partial \, C_n / \partial \delta$
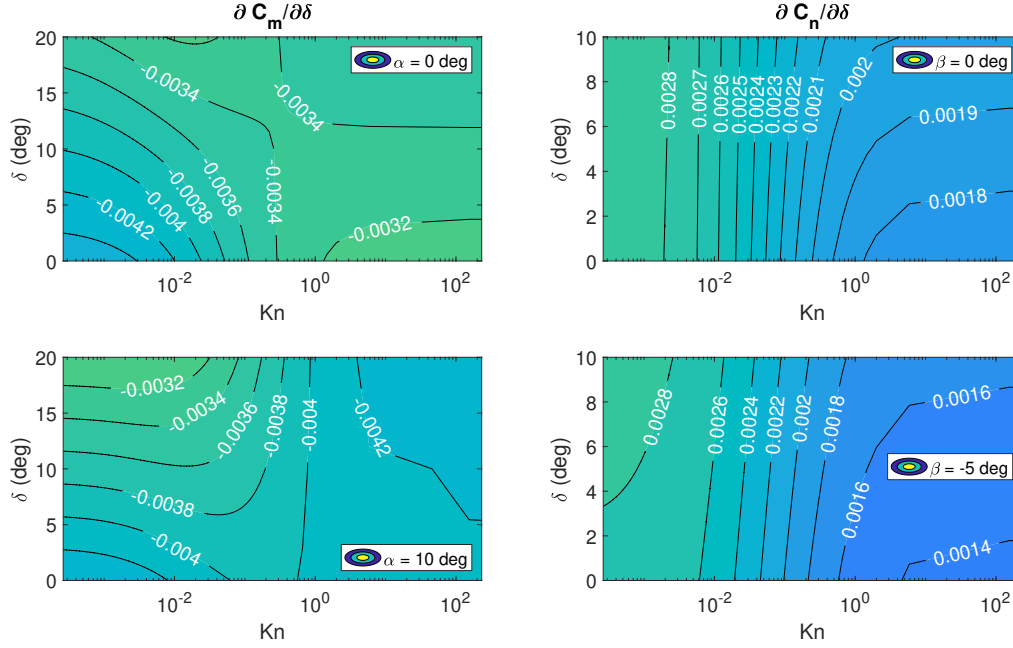
(a) P1 deflections for $\beta = 0$ deg.

(b) R5 deflections for $\alpha = 0$ deg.

Figure 3.29. The pitching effectiveness of P1 deflections and yawing effectiveness of R5 deflections.

Note that during numerical simulations of the EOMs, the flight dynamic pressure (q_∞) is more readily available than Kn. This is because q_∞ is easily computed using only atmospheric density and flight velocity, whereas more quantities are needed to compute Kn as discussed in Sec. 3.2.3. Therefore, q_∞ replaced Kn as the flow rarefaction query variable when extracting aerodynamic coefficients for EOM propagation as well as flight controller implementation (to be discussed in Sec. 3.3).

3.2.11 Database Verification

Additional DSMC calculations were carried out to generate aerodynamics data for comparison with the database.[17] Figure 3.30 shows C_m at $\alpha = -15$ deg, $\beta = 0$ deg for the baseline and P1-deflected MES configurations. The solid and dashed lines correspond to the C_m values of the P1-deflected and baseline configurations, respectively, for the entire

---

[17]↑The discussion presented in Sec. 3.2.11 was taken from a previous publication (Ref. [86]) and modified where necessary for narrative flow.

Kn range of the database. The circle and square markers correspond to the C_m values for the P1-deflected and baseline configurations, respectively, that were obtained via DSMC. The maximum difference observed between the DSMC and database values in Figure 3.30 is 0.00475. This maximum difference corresponds to the data point closest to the continuum limit ($Kn = 0.0507$), as indicated in Figure 3.30. This suggests that the agreement between DSMC data and the database may degrade as Kn continues to decrease. Qualitatively, a good fit exists between the DSMC data and the database in the rarefied transitional regime. This highlights the usefulness of the bridging method in generating rarefied transitional aerodynamics data, while reducing the number of expensive DSMC simulations.
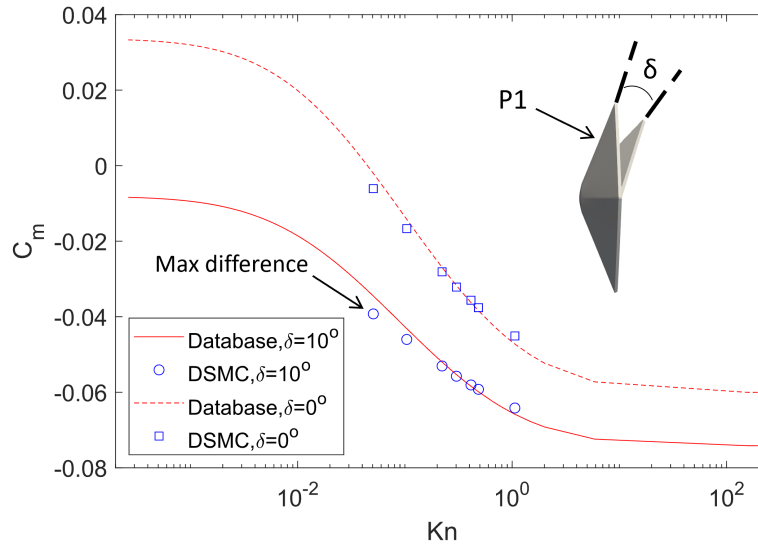
Figure 3.30. A comparison of C_m from the database and DSMC calculations at $\alpha = -15$ deg, $\beta = 0$ deg [86].

As noted in Ref. [84], the accuracy of bridging methods is dependent upon the accuracy of the continuum and free-molecular construction points used to generate the bridging parameters. The engineering-level panel methods used to compute the aerodynamics at these Kn extremes led to a reduction in fidelity, as noted in previous sections. Using higher fidelity tools could improve the fit between the DSMC data and the bridged database. For example, additional Navier-Stokes solutions could be carried out to replace the modified Newtonian estimates used to build the database. Running additional DSMC with no collisions is also an alternative method of computing free-molecular aerodynamics for future

refinements of the database. However, the increase in fidelity translates to increased computational cost. Presently, the study of applying the MES to direct force controlled aerocapture is at the proof-of-concept level. Therefore, the modified Newtonian and free-molecular methods described were determined to be sufficient. The current database is an acceptable initial estimate of the vehicle's aerodynamic characteristics that enables the study of its flight performance in subsequent trajectory simulations.

3.3 Control System Design

DFC involves targeting desired angle of attack (α) and sideslip angle (β) profiles to control the downrange and crossrange motion of the flight vehicle, respectively. In aerocapture, the downrange motion influences the apoapsis and periapsis of the transfer orbit after atmospheric exit. Therefore, accurate α tracking performance reduces the periapsis raise and apoapsis correction maneuvers (PRM and ACM, respectively) required to achieve the target operational orbit. On the other hand, crossrange control influences the plane of the transfer orbit. Accurate β tracking performance reduces the inclination correction maneuver (ICM) required to settle into the target orbit.

This dissertation investigated two approaches to DFC: α-only control and β-to-α control. In the former approach, only α is modulated throughout the aerocapture maneuver. This approach demonstrates that the MES can be controlled in the downrange direction. The latter approach employs β-only control during the early segments of the atmospheric flight and then α-only control in later portions of the trajectory. This approach demonstrates that the MES can be controlled in both downrange and crossrange directions.

In turn, tracking α and β requires a flight controller, which receives commanded α and β values and outputs the proper MES petal deflection δ. The proportional-integral-derivative (PID) controller is a simple yet reliable feedback compensator approach that was deemed sufficient for this dissertation despite potentially more robust methods such as the linear quadratic regulator (LQR) [105]. The proportional-derivative (PD) variant of the PID controller was even implemented for the entry of MSL [106], demonstrating the effectiveness of

107

this control approach. In this section, the development of the PID controllers for α and β modulation is presented.

3.3.1 PID Controller Overview

To illustrate how the PID controller works, consider the unity-feedback system sketched in Figure 3.31.
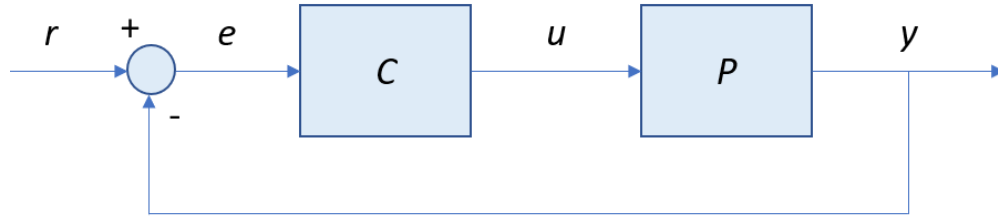
Figure 3.31. A unity-feedback system.

The block labeled C is the controller and the P block is the plant (i.e., the system being controlled). The error signal (e) is fed into C, which subsequently outputs the system input (u). The system's response to u is y, which is fed back and compared to the reference value (r) to obtain the new error signal e. The PID controller computes u according to the formula

$$u(t) = K_p\,\mathrm{e}(t) + K_i \int \mathrm{e}(t)\,dt + K_d \frac{d}{dt}\mathrm{e}(t) \tag{3.112}$$

where K_p is the proportional gain, K_i is the integral gain, and K_d is the derivative gain. In Eq. 3.112, the error is multiplied by K_p, the time integral of the error is multiplied by K_i, and the time derivative of the error is multiplied by K_d. While the controller is active, u is regularly updated using Eq. 3.112.

K_p increases u in proportion to the current error e. That is, as K_p increases, so too does u for a given error. This leads to a reduction in the steady state error. An example of the effect of K_p on the unit step response for a given dynamic system is illustrated in Figure 3.32. Clearly, a larger K_p helps to reduce error by bringing the system closer to the desired unit amplitude. However, the proportional gain alone does not fully eliminate the steady state error. The system also overshoots the set point as K_p increases.
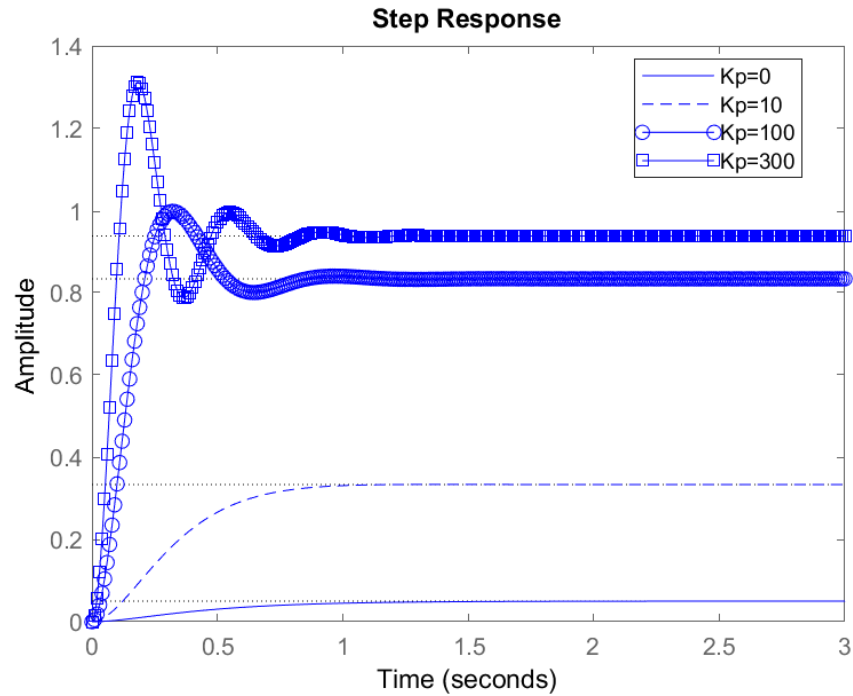
Figure 3.32. An example of the effect of K_p on the step response of a dynamic system.

As seen in Figure 3.32, larger overshooting leads to oscillations that tend to increase the time it takes for the system to settle into its steady state response. Damping the overshoots is accomplished by including the derivative term. As shown in Figure 3.33, increasing the value of K_d damps out the oscillations more and reduces the settling time. Despite this improvement, increasing K_d does not help reduce the steady state error.
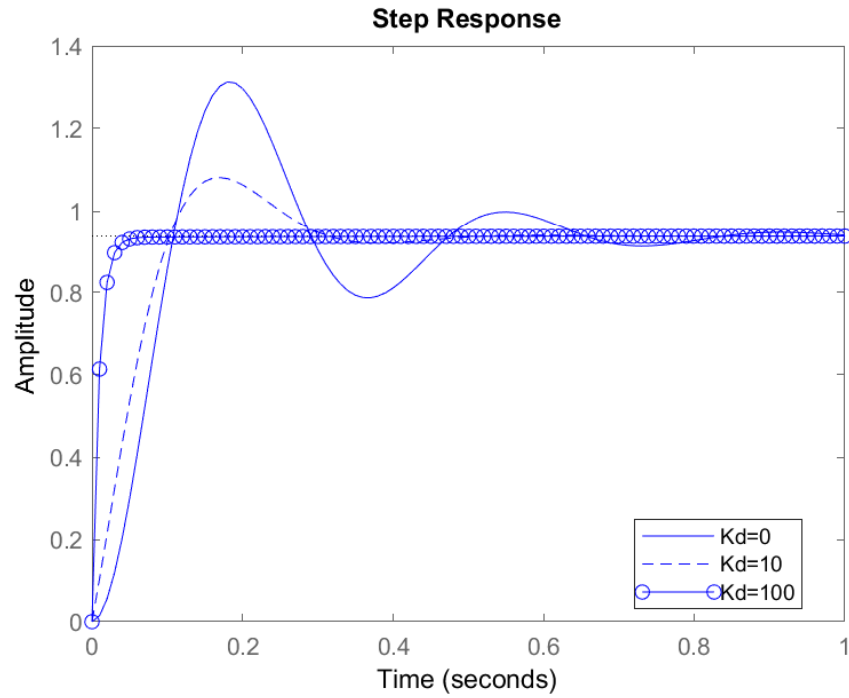
Figure 3.33. An example of the effect of K_d on the step response of a dynamic system (assuming fixed K_p value).

A persistent steady state error compounds as it is integrated in time. This allows the integral term to increase the commanded u to help reduce the steady state error. The effect of adding the integral gain K_i is shown in Figure 3.34. Clearly, increasing the value of K_i improves the reduction of the steady state error.
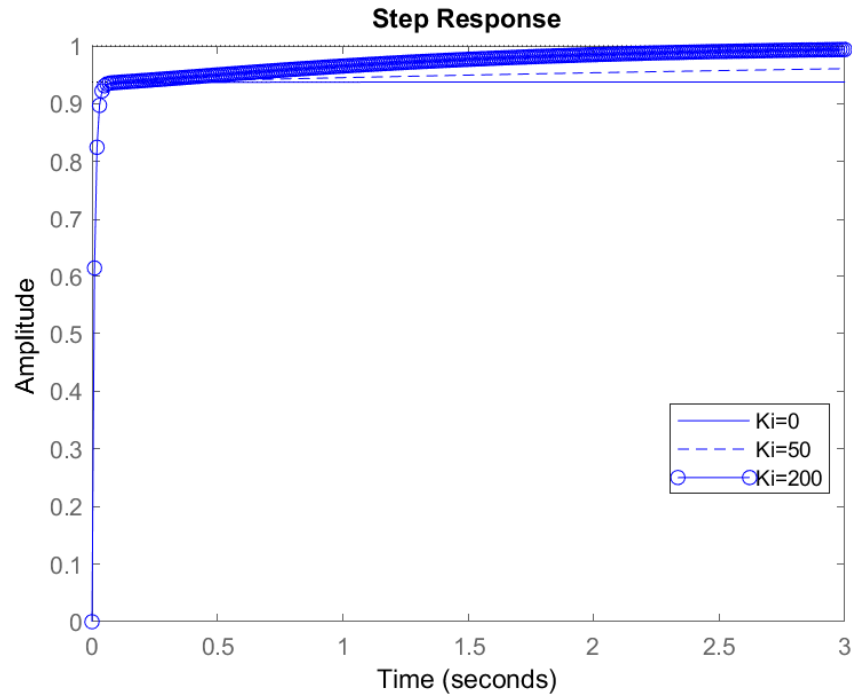
Figure 3.34. An example of the effect of K_i on the step response of a dynamic system (assuming fixed K_p and K_d values).

The general effects of the PID gains on the system response are summarized in Table 3.10.[18] It is important to note that these trends may not apply for some systems. In such instances, system testing or further analysis would provide more insight into the effects of the gains.

Table 3.10. A summary of the effects of the three PID gains on system response

	Rise Time	Overshoot	Settling Time	Steady State Error
K_p	Decrease	Increase	Small Change	Decrease
K_i	Decrease	Increase	Increase	Decrease
K_d	Small Change	Decrease	Decrease	No Change

---

[18]↑This table appears on a PID controller design tutorial available on https://ctms.engin.umich.edu/CTMS/index.php?example=Introduction&section=ControlPID.

111

3.3.2 Formulation of α Controller Gains

In this section, the PID gains for α control are formulated. As described earlier in Section 3.2, the aerodynamic characteristics of the MES change with the flow rarefaction. Therefore, the control authority of the petal deflections changes with the flight environment. The PID controller must then adapt to these changes mid-flight to ensure accurate targeting of α. This is accomplished by formulating gain expressions that take into account flow rarefaction, specifically. This work adapts the approach of Johnson et. al. [107] to derive expressions for K_p and K_d.

The first step of deriving the gain expressions is to linearize the pitch moment equation about a known trim condition. For the α controller, this trim condition was chosen to be when sideslip angle is zero because there is no yawing motion that results from deflecting the pitching petals of the MES. At the trim sideslip condition, the bank angle and its rate are also zero. Therefore, the body angular rates are:

$$p = 0$$
$$q = \dot{\alpha}$$
$$r = 0 \tag{3.113}$$

Inserting Eq. 3.113 into Eq. 3.49 provides the linearized pitching EOM:

$$M_y = I_{yy}\dot{q} = I_{yy}\ddot{\alpha} \tag{3.114}$$

The aerodynamic moment M_y produced when either P1 or P4 is deflected away from the flow is given by:

$$M_y = q_\infty SLC_m(\alpha, \beta, \delta, q_\infty) \tag{3.115}$$

where C_m is the pitching moment coefficient, q_∞ is the freestream dynamic pressure, S is the reference area, and L is the reference length. C_m is queried from the aerodynamics database

described previously. Therefore, inserting Eq. 3.115 into Eq. 3.114 and solving for $\ddot{\alpha}$ results in:

$$\ddot{\alpha} = \frac{q_\infty SLC_m}{I_{yy}} \tag{3.116}$$

The total pitch moment coefficient can be approximated as

$$C_m = C_{m_\alpha}\alpha + C_{m_\delta}\delta \tag{3.117}$$

where C_{m_α} is the partial derivative of C_m with respect to α for the undeflected baseline vehicle and C_{m_δ} is the partial derivative of C_m with respect to δ. These stability derivatives are readily available from the aerodynamics database. Inserting Eq. 3.117 into Eq. 3.116 provides:

$$\ddot{\alpha} = \Delta\left(C_{m_\alpha}\alpha + C_{m_\delta}\delta\right) \tag{3.118}$$

where $\Delta = q_\infty SL/I_{yy}$.

Temporarily setting aside the integral term in Eq. 3.112, the control variable equation becomes:

$$u = \delta = K_p\mathrm{e} + K_d\dot{\mathrm{e}} \tag{3.119}$$

Defining the error term e as the difference between the commanded and the instantaneous values of α, or $\mathrm{e} = \alpha_c - \alpha$, the control variable equation is then rewritten as:

$$\delta = K_p(\alpha_c - \alpha) - K_d\dot{\alpha} \tag{3.120}$$

Inserting Eq. 3.120 into Eq. 3.118 yields

$$\ddot{\alpha} = \Delta C_{m_\alpha}\alpha + \Delta C_{m_\delta}\left(K_p\alpha_c - K_p\alpha - K_d\dot{\alpha}\right) \tag{3.121}$$

Rearranging the previous equation to isolate the α terms on one side provides the linearized second-order differential equation for α:

$$\ddot{\alpha} + \Delta C_{m_\delta}K_d\dot{\alpha} + \Delta(C_{m_\delta}K_p - C_{m_\alpha})\alpha = \Delta C_{m_\delta}K_p\alpha_c = const \tag{3.122}$$

The functional form of Eq. 3.122 is comparable to the second-order differential equation:

$$\ddot{\alpha} + 2\xi\omega_n\dot{\alpha} + \omega_n^2\alpha = c \tag{3.123}$$

Equating the coefficients of the α terms in Eqs. 3.122-3.123 and solving for K_p and K_d provides the following equations for these gains:

$$K_p = \frac{\omega_n^2/\Delta + C_{m_\alpha}}{C_{m_\delta}} \tag{3.124}$$

$$K_d = \frac{2\xi\omega_n}{\Delta C_{m_\delta}} \tag{3.125}$$

Note that the flow rarefaction is accounted for in these gain expressions through the quantities Δ, C_{m_α}, and C_{m_δ}, which are all functions of the dynamic pressure q_∞. Substituting Eqs. 3.124-3.125 into Eq. 3.112 yields the following expression for petal deflection:

$$\delta = \frac{\omega_n^2/\Delta + C_{m_\alpha}}{C_{m_\delta}}\left(\alpha_c - \alpha\right) + K_i \int \mathrm{e}(t)\,dt - \frac{2\xi\omega_n}{\Delta C_{m_\delta}}\dot{\alpha} \tag{3.126}$$

where the integral gain K_i is treated here as a constant that can be tuned and scheduled based on dynamic pressure.

3.3.3 α Controller Testing and Implementation

An α controller simulation environment was developed in MATLAB[19] to emulate the unity-feedback system displayed in Figure 3.31. As sketched in Figure 3.35, the simulation test bed featured a controller function (`pid.m`) and a dynamics function (`eoms.m`). The former function computed the MES petal deflection (δ) needed to reduce the error (e) and achieve the commanded angle of attack (α_c). The latter function contained the coupled nonlinear rotational equations of motion. The system's response (y) to δ was obtained by numerically integrating Eqs. 3.48-3.50. Refinement of the control system design was aided by this simulation test bed.

---

[19]↑https://www.mathworks.com/products/matlab.html
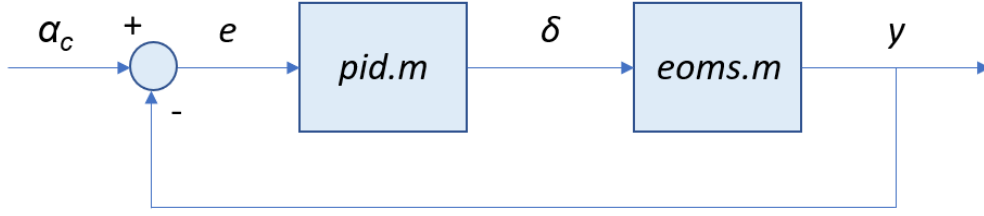
Figure 3.35. A sketch of the simulation test bed workflow.

Besides computing the magnitude of δ, the controller must also identify the proper petal to deflect. As mentioned in Chapter 2, a P1 deflection (δ_1) modulates α negatively (nose-down) while a P4 deflection (δ_4) modulates α positively (nose-up). Therefore, the controller issues a P1 deflection whenever $\alpha_c < 0$ and a P4 deflection whenever $\alpha_c > 0$. However, these rules are modified when preventing attitude excursions due to destabilizing behavior, as discussed later.

Gain Tuning

The main advantage of Eqs. 3.124-3.125 is that they allow for automatic gain calculations in response to the drastic changes in the vehicle's attitude and flight environment. Therefore, the controller should always be able to command the proper δ magnitudes in response to the error state of the MES. As previously mentioned, the quantities Δ, C_{m_α}, and C_{m_δ} are dependent on flow conditions, namely the dynamic pressure q_∞. Additionally, both C_{m_α} and C_{m_δ} are also functions of the vehicle attitude because these are aerodynamic quantities. Therefore, they are dependent on where in the atmosphere the MES is flying and cannot be tuned. Instead, the gain parameters that can be tuned to improve controller performance are the natural frequency (ω_n) and the damping ratio (ξ).

Simulations of different ω_n and ξ values were carried out to determine the effect of each parameter on the controller's ability to track a step command. Figure 3.36(a) illustrates the effect of ω_n for a fixed ξ ($\xi = 0.7$). As seen in this figure, increasing ω_n reduces the observable oscillations. However, increasing ω_n also extended the settling time. For the case shown, using $\omega_n = 2.0$ rad/s reduced the amplitude of the oscillations compared to the curve

corresponding with $\omega_n = 1.0$ rad/s. Additionally, the MES was able to reach α_c quicker than when $\omega_n = 3.0$ rad/s. This implies that the accuracy of the controller can be optimized by determining the bounding ω_n values and choosing an intermediate value for implementation.

(a) $\xi = 0.70$ (fixed)　　　　(b) $\omega_n = 1.0$ rad/s (fixed)
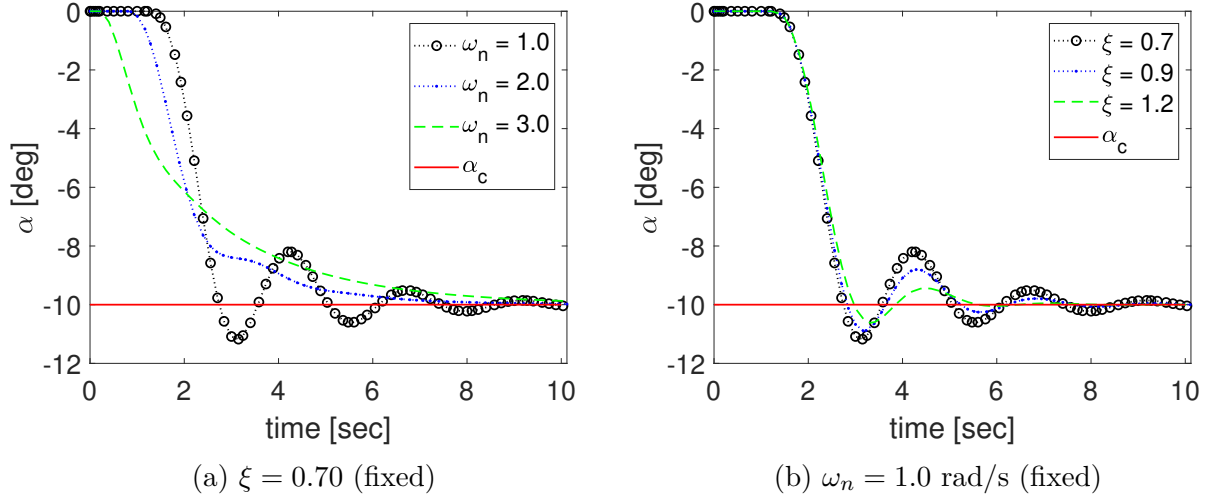
Figure 3.36. The impact of ω_n and ξ on the response of the MES.

Figure 3.36(b) shows the impact of ξ for a fixed ω_n ($\omega_n = 1.0$ rad/s). According to the figure, increasing ξ, and therefore K_d, attenuates the amplitude of the oscillations about α_c, as expected. Damping is crucial to prevent massive overshoots that could lead to severe attitude excursions.

As mentioned earlier in this chapter, the deflected MES is statically unstable at low dynamic pressures but stable at high dynamic pressures. To account for the changing stability characteristics of the MES, different combinations of ω_n and ξ were assigned to different ranges of q_∞. That is, these gain parameters were varied depending on the flow rarefaction. To determine appropriate combinations of ω_n and ξ, the effect of q_∞ on the system response to a step command was investigated. Figure 3.37 shows a sample result of this investigation in which ω_n and ξ were held constant at 1 rad/s and 1.2, respectively. This figure demonstrates that the MES is prone to large attitude excursions in very rarefied conditions (low q_∞). In continuum flow where q_∞ is high, the MES can be controlled easily due to its stability. For intermediate q_∞, the MES can be brought to a trim α condition but the resulting steady state error is large.

116
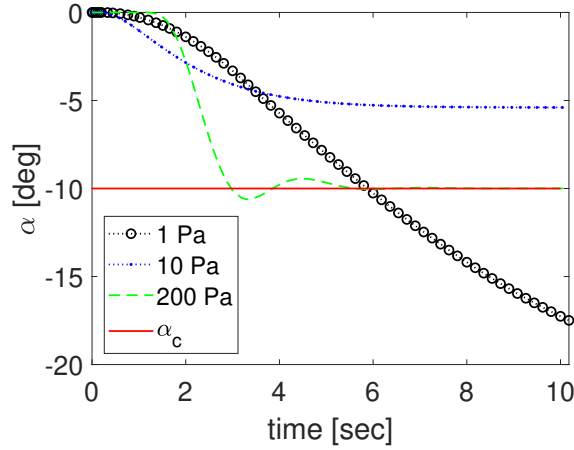
Figure 3.37. The effect of dynamic pressure on the response of the MES for constant ω_n and ξ ($\omega_n = 1.0$ rad/s and $\xi = 1.2$).

To reduce the large steady state error observed for $q_\infty = 10$ Pa above, ω_n was increased from 1.0 rad/s to 1.7 rad/s. The improved response is shown in Figure 3.38(a). In a similar manner, the overshoot observed for $q_\infty = 1$ Pa was addressed by increasing ξ from 1.2 to 4.0. The improved response is illustrated in Figure 3.38(b). These results demonstrate that scheduling ω_n and ξ according to q_∞ is necessary to ensure that the controller can accurately track the commanded α across different levels of flow rarefaction.

(a) $q_\infty = 10$ Pa, $\xi = 1.2$

(b) $q_\infty = 1$ Pa, $\omega_n = 1.0$ rad/s
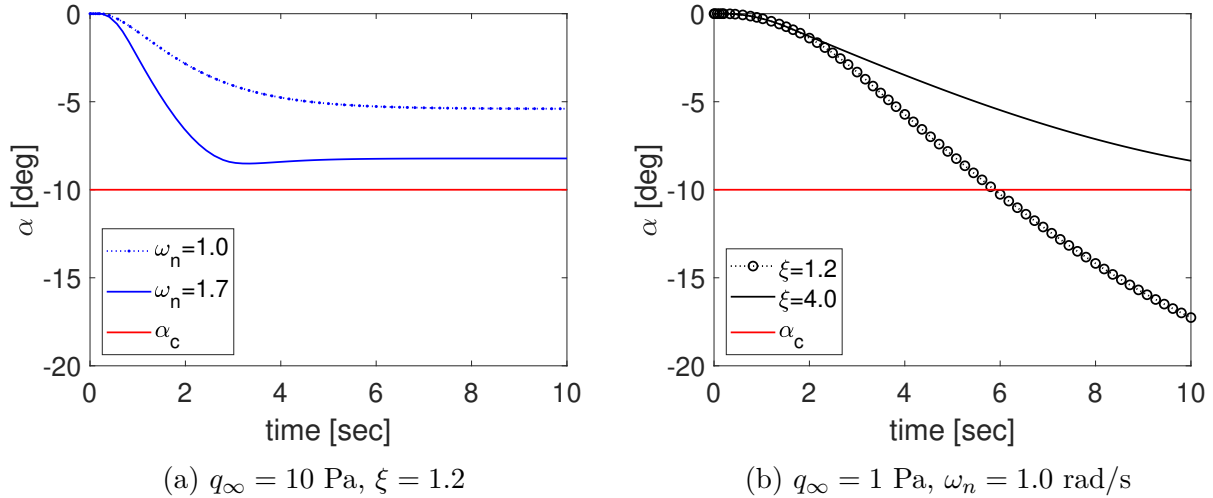
Figure 3.38. The effect of varying ω_n and ξ based on dynamic pressure.

The integral gain (K_i) was left as a constant and was tuned based on dynamic pressure. Through similar testing as above, K_i values for different q_∞ ranges were determined. The ω_n, ξ, and K_i combinations for different q_∞ ranges were identified and are provided in Table 3.11. These were the final values used to generate all controlled simulations presented in Chapter 4.

Table 3.11. The α controller gain parameters are scheduled based on q_∞

Range of q_∞ (Pa)	ω_n (rad/s)	ξ	K_i
$q_\infty \leq 10$	1.25	4.0	± 0.005
$10 < q_\infty \leq 20$	1.4	1.2	± 0.04
$20 < q_\infty \leq 100$	2.8	1.2	± 0.04
$q_\infty > 100$	2.8	1.2	± 0.10

Controller Command Frequency

The aerocapture guidance system commands a new α_c at the beginning of each guidance cycle, which recurs at some prescribed frequency (e.g., every 10 seconds of flight time). A good α controller must then accurately track α_c within each guidance cycle or else the desired flight path cannot be flown accurately. To ensure that the MES arrives at α_c within every guidance cycle, the controller was set to update δ at a higher frequency than that of the guidance calls. This was accomplished by dividing each guidance cycle window into smaller time steps of size dt. At the beginning of each dt, the controller computes a new δ and the system response is fed back to the controller to generate an updated δ for the following time step.

Smaller dt values imply that the controller is fed the α error more frequently thus increasing the updates in δ. In contrast, larger dt values imply fewer error updates and therefore less δ updates. Holding one δ command long enough can potentially lead to undesirable overshoots. To identify an appropriate step size, the controller's ability to track a step change of 10 deg was evaluated for a few dt values. The system's response to three representative dt values are illustrated in Figure 3.39. The figure demonstrates that the smaller dt values led to better controller performance as predicted.

118
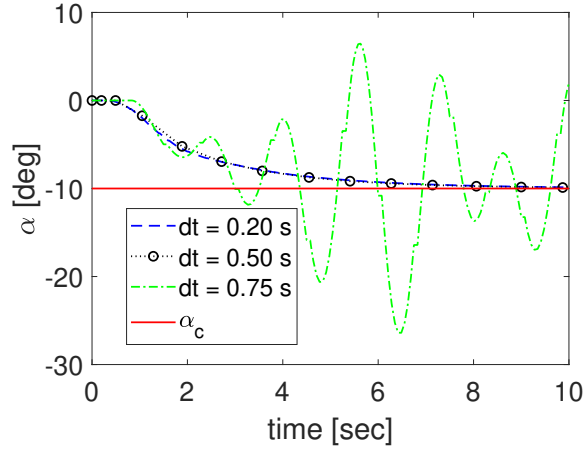
Figure 3.39. The effect of larger time steps in the controller accuracy.

For $dt = 0.20$ sec, the controller was fed more information about the error state of the vehicle. In response, the controller was able to issue more appropriate δ_1 magnitudes to contain the error. This is demonstrated by the smooth error and δ_1 profiles in Figure 3.40. On the other hand, taking larger steps in time before the next error update led to overshooting, which caused the controller to over-compensate and issue larger δ_1 magnitudes to correct the growing error. This over-correcting only exacerbated the overshoots, thereby causing more over-compensation and eventually oscillations in the attitude profile. This is demonstrated by the jagged curves corresponding with $dt = 0.75$ sec in Figure 3.40.

(a) Error   (b) Deflection
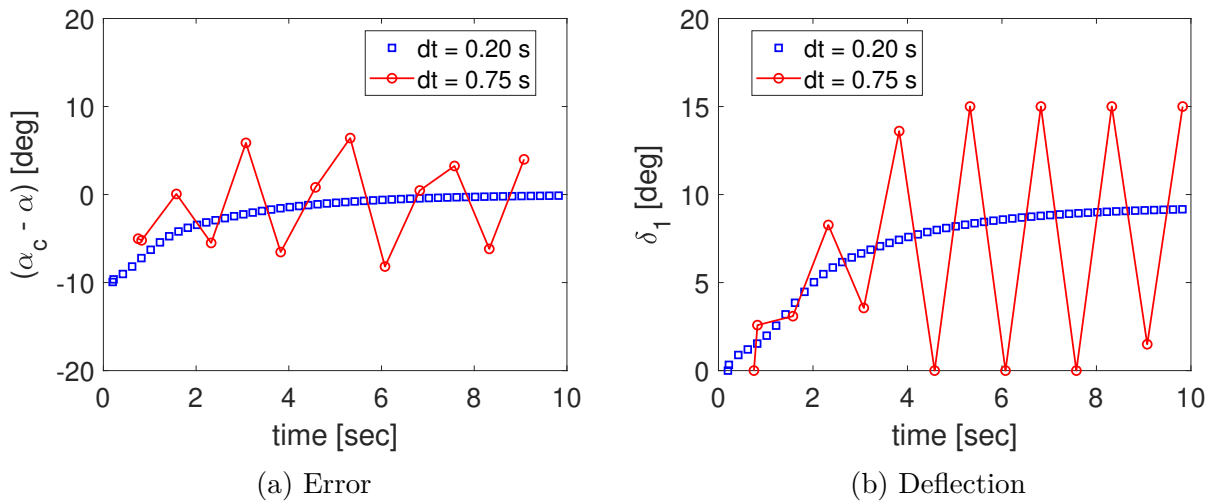
Figure 3.40. The error and deflection histories for $dt = 0.20$ sec and $dt = 0.75$ sec.

While the α histories for $dt = 0.20$ sec and $dt = 0.50$ sec were nearly identical in Figure 3.39, the computational run time associated with the latter time step was twice faster than that of the former. Despite being slower at run time, the smaller dt offered better controller accuracy, which was deemed more important. Therefore $dt = 0.20$ sec was adopted for the α controller implementation in this dissertation. Note that this decision was also carried over to the β controller implementation for consistency.

Constant C_{m_δ} Assumption

Recall that C_{m_δ} factors into the calculation of K_p and K_d. For the controller implementation, C_{m_δ} could either be queried from the database constantly or kept constant. The advantage of using a constant value is that it would reduce the computational complexity thereby speeding up the simulation. To check the validity of using a constant C_{m_δ}, contours that were functions of α and δ_1 for representative values of q_∞ were created, which are shown in Figure 3.41. The ranges of α and δ are -30 deg $\leq \alpha \leq$ 30 deg and 0 deg $\leq \delta_1 \leq$ 20 deg, respectively. Note that the data shown corresponds with no sideslip angle. The contours demonstrate that C_{m_δ} only changes slightly across the α and δ ranges shown. This trend encourages the assumption of holding C_{m_δ} constant for the calculations.

Sample values were extracted from the data shown in Figure 3.41 and tabulated in Table 3.12. The values corresponding to $q_\infty = 1$ Pa and $q_\infty = 1386$ Pa were then used to simulate the impact on controller accuracy for a 10 deg step change command at $q_\infty = 1$ Pa. As shown in Figure 3.42(a), both C_{m_δ} values resulted in the same system response. The same comparison was conducted at $q_\infty = 1386$ Pa and the results in Figure 3.42(b) also show that the system response did not greatly vary between the two C_{m_δ} values. These results combined with the small changes in C_{m_δ} displayed by Figure 3.41 validated the assumption of a constant C_{m_δ} for the K_p and K_d gain calculations. The C_{m_δ} value at the maximal q_∞ condition in Table 3.12 was chosen for controller implementation.
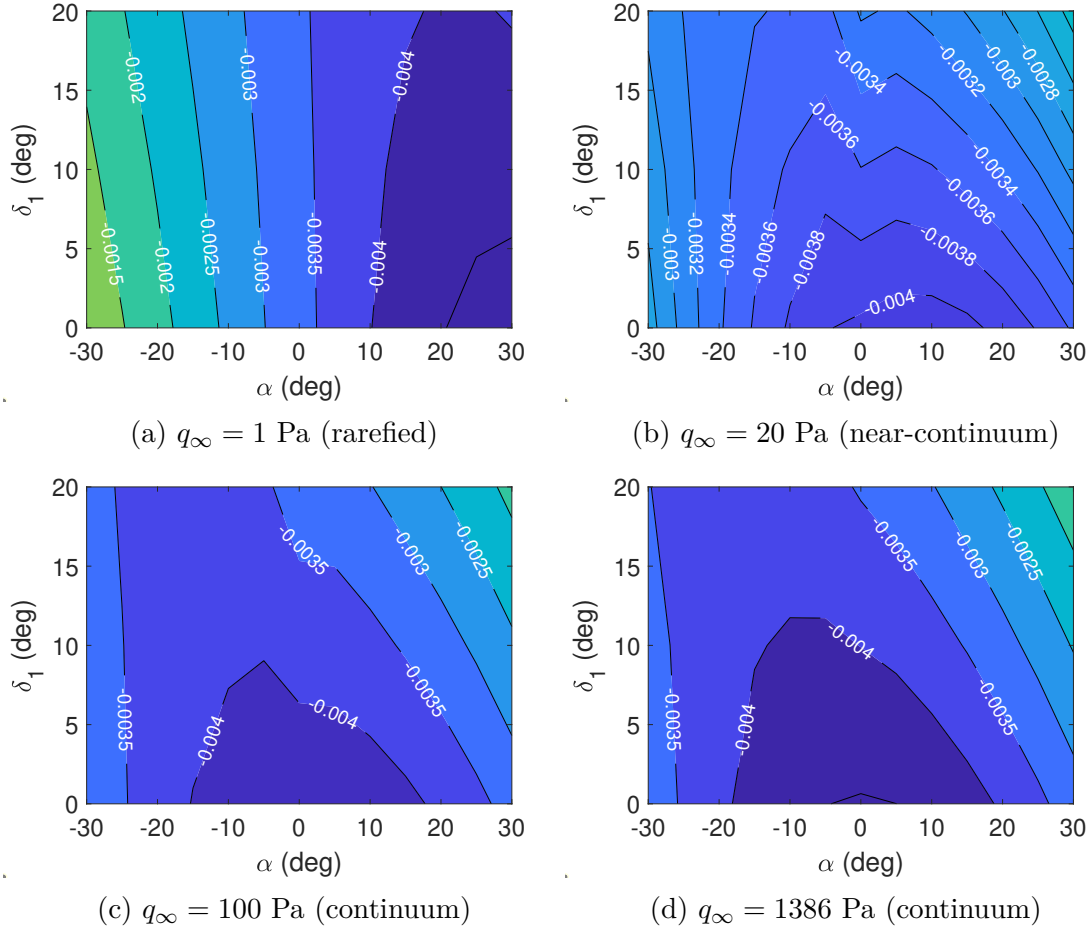
Figure 3.41. C_{m_δ} as a function of α and δ_1 for different q_∞.

Table 3.12. C_{m_δ} value at $\alpha = 0$ deg and $\delta_1 = 10$ deg from each flow condition in Figure 3.41.

q_∞ [Pa]	Kn	C_{m_δ} [deg^{-1}]	Flow Regime
1	0.4	-0.0034	Rarefied
20	0.02	-0.0036	Rarefied/Near-Continuum
100	0.004	-0.0038	Continuum
1386	0.0003	-0.0040	Continuum
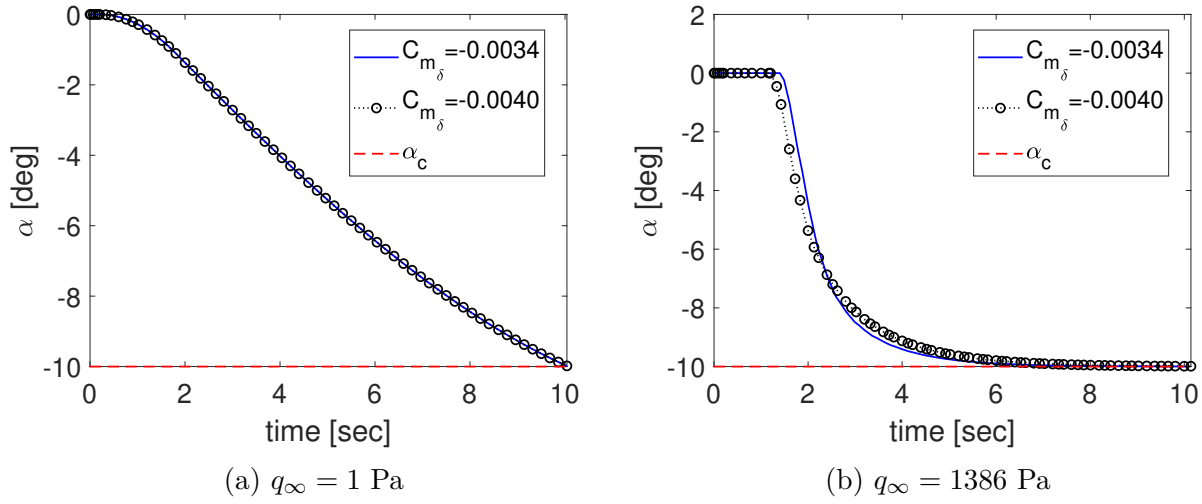
Figure 3.42. The impact of different C_{m_δ} on controller accuracy at different q_∞ conditions.

Managing Attitude Excursions

The inherent static stability of the MES in the continuum flow regime makes the vehicle less susceptible to uncontrollable attitude excursions. This is not the case in the rarefied portions of the aerocapture trajectory because the MES is statically unstable in pitch. It is discussed in Chapter 4 that the guidance system issues a "hold" attitude command during atmospheric exit when the flow becomes increasingly rarefied. Any overshoots of the hold attitude could then potentially lead to irrecoverable attitude excursions due to the vehicle's static instability in rarefied flow. Therefore, the controller must remain active even after the guidance system has stopped issuing attitude commands.

The controller was designed to detect and correct destabilizing behavior. To illustrate this, suppose that the error is positive, $\alpha_c - \alpha > 0$. This condition results in two possible scenarios, which are shown in Figure 3.43. The first scenario is labeled "stabilizing" in the figure, and it occurs when the error rate is such that the error will continue to decrease. In this case, the controller continues to update δ for the same petal. On the other hand, the "destabilizing" scenario shown occurs when the error rate is such that the error will continue to grow. In this case, the controller computes the appropriate δ magnitude, but commands a petal switch to reverse the sign of the error rate and stabilize the vehicle. Before the

controller confirms a petal switch however, the absolute value of the error must also exceed a tolerance value. This was enforced to prevent unnecessary petal switches that may arise due to slight overshoots of α_c. If the error were negative instead (i.e., $\alpha_c - \alpha < 0$), the only changes would be that the stabilizing scenario corresponds with $d\alpha/dt < 0$, while the destabilizing scenario corresponds with $d\alpha/dt > 0$.
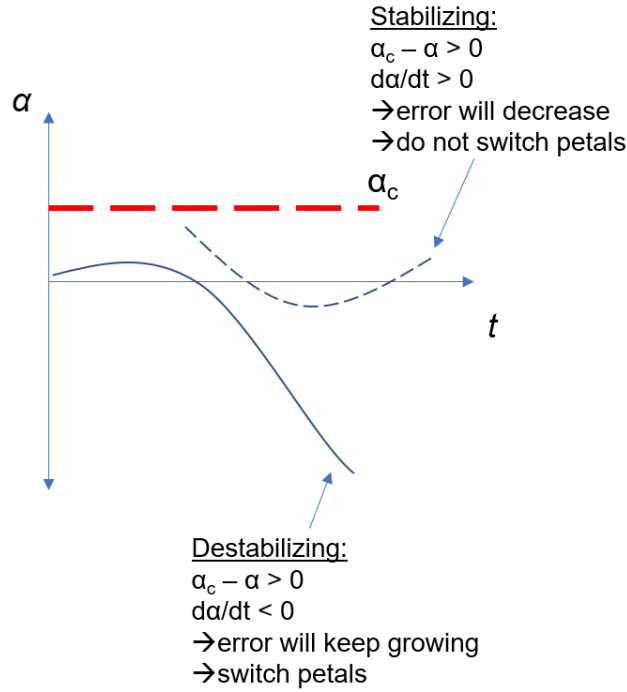
Figure 3.43. The stabilizing and destabilizing scenarios that the controller was designed to detect.

Preventing attitude excursions during atmospheric exit constitutes the only scenario in which P1 and P4 deflections are not exclusively reserved for pitch-down and pitch-up maneuvers, respectively.

3.3.4 Formulation of β Controller Gains

The approach used to derive K_p and K_d for the α controller was repeated to obtain equivalent gain expressions for the sideslip angle controller. As before, the objective was to automate the computation of the gains in response to the changing flight environment. The derivation of the gains are presented below.

To linearize the dynamic equation for yaw, the vehicle is assumed to be trimming at $\alpha = 0$ without roll (i.e., $\dot{\sigma} = 0$). Therefore, the angular kinematics are reduced to:

$$p = 0$$

$$q = 0$$

$$r = -\dot{\beta}$$

Inserting the above result to the yaw dynamic equation, Eq. 3.50, provides:

$$M_z = I_{zz}\dot{r} = -I_{zz}\ddot{\beta} \tag{3.127}$$

The yaw moment M_z can be further expanded as follows:

$$M_z = C_n q_\infty SL = \left(C_{n_\delta}\delta + C_{n_\beta}\beta\right) q_\infty SL$$

Therefore, the linearized yaw moment equation can be rewritten as follows:

$$\left(C_{n_\delta}\delta + C_{n_\beta}\beta\right) q_\infty SL = -I_{zz}\ddot{\beta} \tag{3.128}$$

Once more, the integral term in the PID formulation for δ is temporarily set aside so that the control variable becomes:

$$\delta = K_p\mathrm{e} + K_d\dot{\mathrm{e}} = K_p(\beta_c - \beta) - K_d\dot{\beta}$$

Inserting this result into Eq. 3.128 results in

$$\left(C_{n_\delta}\left[K_p(\beta_c - \beta) - K_d\dot{\beta}\right] + C_{n_\beta}\beta\right) q_\infty SL = -I_{zz}\ddot{\beta}$$

Expanding this expression and isolating the β terms towards one side provides:

$$\ddot{\beta} - \Delta K_d C_{n_\delta}\dot{\beta} + \Delta \left(C_{n_\beta} - C_{n_\delta}K_p\right)\beta = -\Delta C_{n_\delta}K_p\beta_c = const \tag{3.129}$$

where $\Delta = q_\infty SL/I_{zz}$. The above expression is equivalent to the following second-order differential equation:

$$\ddot{\beta} + 2\xi\omega_n\dot{\beta} + \omega_n^2\beta = C$$

Equating the coefficients corresponding with the $\dot{\beta}$ terms, as well as those of the β terms, and then solving for the gains provides the following expressions for K_p and K_d:

$$K_p = \frac{C_{n_\beta} - \omega_n^2/\Delta}{C_{n_\delta}} \tag{3.130}$$

$$K_d = -\frac{2\xi\omega_n}{\Delta C_{n_\delta}} \tag{3.131}$$

3.3.5 β Controller Testing and Implementation

A simulation test bed was again developed for controller testing. As before, the test bed was leveraged to tune the gain parameters ω_n and ξ as well as the integral gain, K_i. The tuning process yielded the values in Table 3.13. Note that unlike the α controller implementation, these parameters were not scheduled according to the dynamic pressure. This was done to simplify the controller implementation especially because the commanded value of β is held constant in the β-to-α control approach investigated in this dissertation. This control approach is discussed in more detail in Section 4.3.

Table **3.13**. The β controller gain parameters.

Range of q_∞ (Pa)	ω_n (rad/s)	ξ	K_i
All	1.95	1.05	0.10

The yaw control authority of the lateral ribs R2 and R5 is characterized by the quantity C_{n_δ} that appears in Eqs. 3.130-3.131. As with C_{m_δ}, this quantity changes based on the flow rarefaction, as demonstrated by the contour in Figure 3.44. To determine how the controller's accuracy is impacted by this dependence, sample values corresponding with two q_∞ conditions were extracted, which are included in Table 3.14. Both values were then used to simulate a positive 1.5 deg step command at the chosen q_∞ conditions. Note that the algebraic sign of C_{n_δ} in Table 3.14 is opposite of what is shown in Figure 3.44 because the

former corresponds with a R2 deflection, whereas the latter corresponds with a R5 deflection.
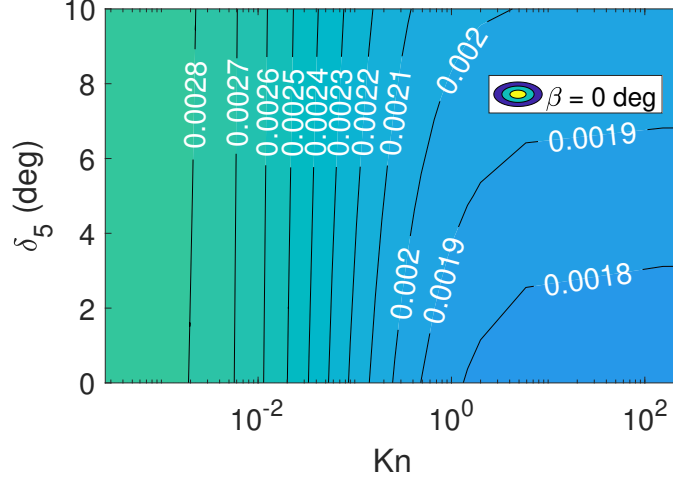
Figure 3.44. C_{n_δ} contour at $\beta = 0$ deg as a function of Kn and δ_5.

Table 3.14. C_{n_δ} value at $\beta = 0$ deg and $\delta_2 = 5$ deg at two flow conditions.

q_∞	Kn	C_{n_δ} [deg^{-1}]	Flow Regime
4	0.10	-0.0022	Rarefied
1174	0.0003	-0.0029	Continuum

Figure 3.45(a) demonstrates that the controlled response is insensitive to the choice of C_{n_δ} in rarefied conditions. Note that this result was included for illustrative purposes only as β control is not expected to occur in the rarefied portions of the trajectory. On the other hand, Figure 3.45(b) does demonstrate a slight difference in the controlled response due to the varied C_{n_δ}. However, this was deemed small enough to warrant keeping C_{n_δ} constant during the β controller implementation. The continuum value of $C_{n_\delta} = \pm 0.0029 \, \text{deg}^{-1}$ was adopted for all simulations of β control.

(a) $q_\infty = 4$ Pa

(b) $q_\infty = 1174$ Pa
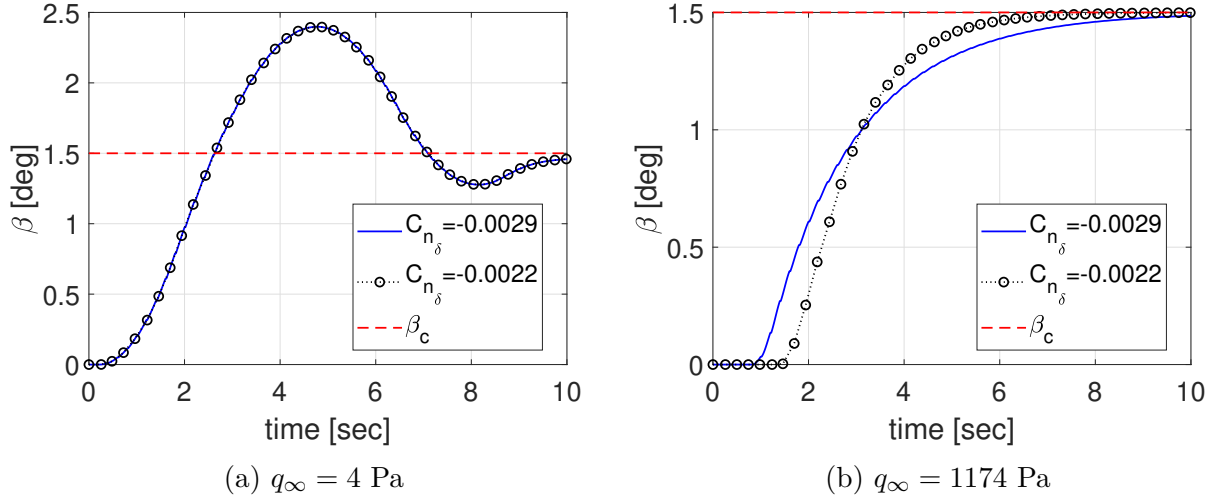
Figure 3.45. The effect on varying C_{n_δ} at different q_∞ conditions.

The yaw stability derivative C_{n_β} of the undeflected MES also appears in Eq. 3.130. Values of this stability derivative in continuum flow conditions were extracted and listed in Table 3.15. Continuum flow values were considered because β control is expected to be active at this flight regime. The values in Table 3.15 correspond with $\alpha = 0$ deg per the assumption of the β controller formulation. In simulations, the range of allowable β was limited to small angles to prevent potentially severe yaw-induced rolling. Therefore, the C_{n_β} values are reported within the range $\beta = [-5, 5]$ deg. As indicated in Table 3.15, the yaw stability derivative does not vary by much in the given β range. Therefore, a constant value of $C_{n_\beta} = 0.0023$ was was adopted for the β controller implementation.

Table 3.15. Continuum flow values of C_{n_β} for a range of β values

β [deg]	C_{n_β} [deg^{-1}]
-5	0.00229
0	0.00233
-5	0.00229

4. AEROCAPTURE RESULTS

This chapter is dedicated to evaluation of direct force controlled aerocapture with the MES. The aerocapture simulation environment is first described in Section 4.1. This is followed by the presentation of α and β control simulation results in Sections 4.2 and 4.3, respectively.

4.1 Aerocapture Simulation Environment

This research leveraged the aerocapture guidance framework developed by Deshmukh [60] to conduct aerocapture simulations of the MES. The framework was designed to be modular to accommodate different vehicle configurations, planetary atmospheres, and simulate any of the three flight control strategies: BAM, DFC, and DM. Deshmukh's framework was originally developed to simulate 3-DOF dynamics. This dissertation extended the framework by adding the rotational EOMs and integrating the PID controller to simulate attitude control. These modifications allowed for 6-DOF simulations of the MES to be carried out. This section discusses the simulation environment in more detail.

4.1.1 Simulation Framework Overview

The simulation framework features a numerical predictor-corrector (NPC) guidance algorithm that determines the ΔV-minimizing α and β profiles. The predictor step of the algorithm numerically propagates the 3-DOF EOMs up to atmospheric exit to predict the in-plane ΔV cost of raising periapsis out of the atmosphere and correcting apoapsis. The corrector step involves an optimization of α to minimize the in-plane ΔV. The optimized α then becomes the guidance command, α_c, issued to the PID controller within the current guidance cycle. To determine the β command, the NPC algorithm minimizes the out-of-plane ΔV cost of correcting the orbit inclination after the aforementioned in-plane optimization. This separate lateral logic assumes that longitudinal and lateral dynamics are decoupled, allowing β to be controlled separately from α. Further details on the algorithm are described by Deshmukh in Ref. [60]. The NPC algorithm is illustrated in Figure 4.1.
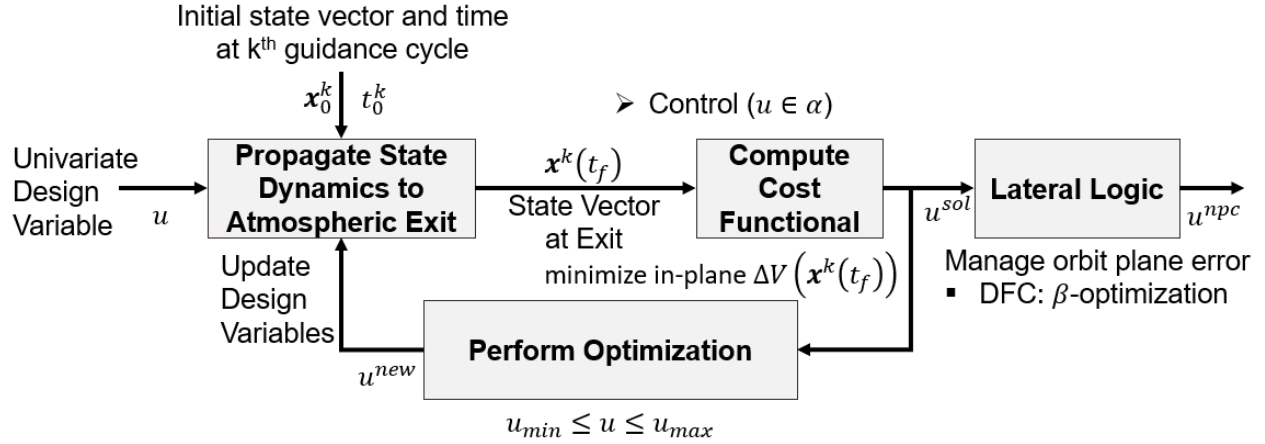
Figure 4.1. A visualization of the NPC guidance algorithm (flow chart adapted from Ref. [60] and modified).

Figure 4.2 describes in pseudo code how the controlled response of the MES to the NPC guidance commands were simulated. As shown, the guidance system (`NPCDFC`) actively issues attitude commands (`UNPC`) while the MES is flying in the appreciable atmosphere as determined by a prescribed g-load trigger (`gtrigger`) of $0.10g$. The guidance call frequency was set to 0.10 Hz, meaning that the attitude command `UNPC` was updated every 10 seconds of flight time. Each guidance cycle was divided into smaller time steps (`dt`) of size 0.20 sec. The controller (`pid`) issued the petal deflections (`UPID`) to track the guidance command. The response of the MES to `UPID` was simulated throughout the duration of `dt` via `SixDofEom`. This process was repeated for a number of times that corresponds with `maxsteps`, which was set equal to the duration of one guidance cycle (10 sec) divided by the time step size (0.20 sec). Therefore, `pid` and `SixDofEom` were called 50 times during each guidance cycle to obtain the controlled response of the MES. Note that the time step size of 0.20 sec was determined using methods discussed in Sec. 3.3.3.

```
while g > gtrigger

        NPCDFC → UNPC = [alpha]

        for step = 1 to maxsteps

                dt = 0.20 sec
                pid → UPID = [deltaP1, deltaP4]
                SixDofEom → state = [r, theta, …, betadot]

        end

end
```

Figure 4.2. An algorithm describing how the controlled response of the MES was simulated.

The closed-loop aerocapture simulation framework employed in this work is illustrated in Figure 4.3. The NPC algorithm ("NPC Model" block) utilizes 3-DOF dynamics and optimal control theory to compute the attitude commands. The "Truth Model" block simulates the full 6-DOF behavior of the MES in the Martian atmosphere. The output of the truth model is the state of the vehicle, which is assumed to be perfect. In turn, this state is fed into the "Feedback Filter" block, which is a fading memory filter that computes the gains used by the NPC algorithm to scale drag, side force, and lift accelerations. The filter allows for a closed feedback loop that improves the state knowledge, and therefore performance, of the guidance algorithm.
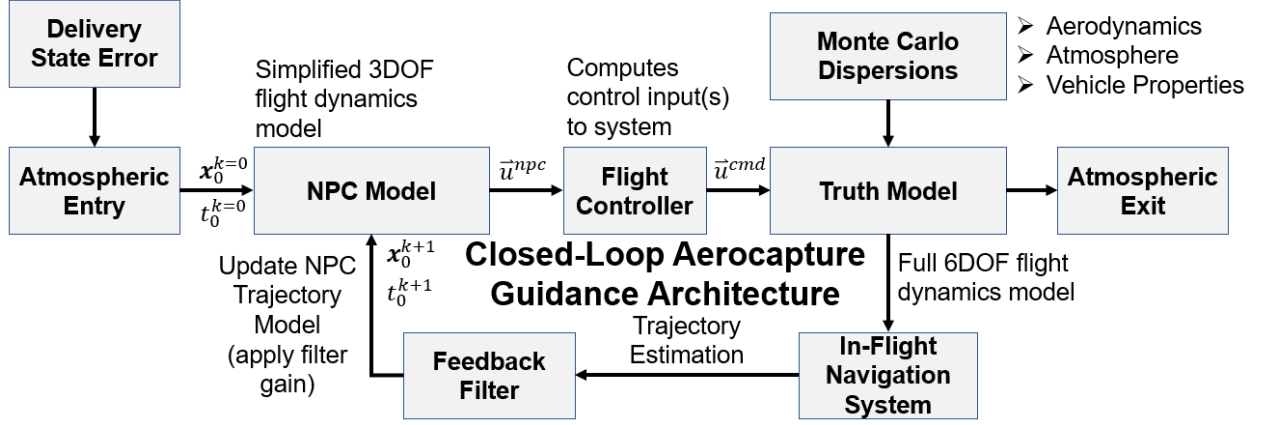
Figure 4.3. The closed-loop aerocapture simulation framework (image adapted from Ref. [60]).

4.1.2 Simulation Setup and Assumptions

Mars was assumed to be an oblate ellipsoid with a non-spherical gravity model to account for the latitudinal variation of gravity in the translational EOMs (see Sec. 3.1). However, it is noted that the reported altitudes in this work were referenced to a sphere with an equatorial radius of 3396 km. The planet's fixed angular velocity was also assumed to be 7.09×10^{-5} rad/sec. For stagnation point convective heating estimates, the Sutton-Graves correlation was used [108]. The Martian atmosphere was modeled using the Mars Global Reference Atmosphere Model (Mars GRAM) [109]. Note that wind was not modeled in the simulations because the velocity of the vehicle is considerably larger than wind speeds on Mars [60]. These environmental parameters are summarized in Table 4.1.

Table 4.1. Mars environment parameters

Parameter	Value
Gravitational parameter, μ	4.28e4 km^3/s^2
Rotation rate, ω	7.09e-5 rad/s
Equatorial radius, R_{e}	3396 km
Polar radius, R_p	3376 km
Sutton-Graves coefficient, C	1.90e-4 kg$^{0.5}$/m
Atmospheric density	MarsGRAM

Figure 4.4 illustrates the representative entry system configuration assumed for all simulations. A cylindrical payload volume (50 cm depth × 20 cm diameter) is attached behind the MES. The nominal location of the center of gravity (c.g.) was assumed to be $0.16D$ (21.6 cm) aft of the nose. This location was chosen to mirror the axial c.g. location used in the Pterodactyl study [110].[1]
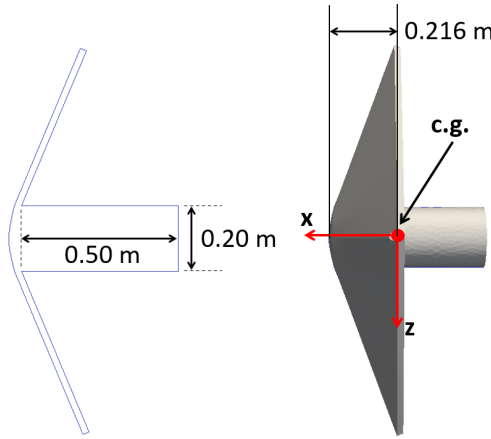
Figure 4.4. Entry configuration of the MES.

The nominal mass estimated for the entire entry system was 75 kg and the corresponding inertia properties are listed in Table 4.2. Note that the inertia properties when P1 is deflected by 15 deg are also included for comparison. It is evident that the change in the values is relatively small even for a significant petal deflection angle. Therefore, the baseline inertia properties were adopted for all simulations and kept constant regardless of the deflection. This simplifying assumption was tested by simulating the controlled response of the MES due to the change in the mass inertia properties. Figure 4.5 illustrates the response of the MES to a 10 deg step change for two different sets of inertia properties. The "Baseline MOI" curve uses the values in the first row of Table 4.2, while the "Deflected MOI" corresponds with the second row. The figure demonstrates that the small change in inertia properties does not greatly impact the controlled response of the MES, thus validating the assumption of constant inertia properties in simulations.

---

[1]↑See Table 5 of Ref. [110].

Table 4.2. Inertia properties of the MES (all units in kg-m^2)

Configuration	I_{xx}	I_{yy}	I_{zz}	I_{xy}	I_{xz}	I_{yz}
Baseline	9.022	5.424	5.555	0.0	-0.017	0.0
P1 deflected, $\delta = 15$ deg	8.465	5.036	5.451	0.0	0.432	0.0
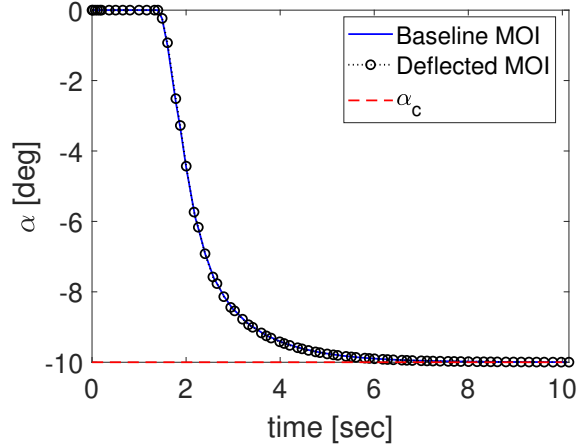
Figure 4.5. The effect of varied inertia properties on the controlled response.

The target orbit around Mars was assumed circular with a 400 km altitude and 30 deg inclination, as summarized in Table 4.3. Atmospheric entry was assumed to occur at a 150 km altitude with an inertial entry velocity of 5.5 km/s. The inertial entry flight path angle (γ_E) was determined using the corridor width assessment of Deshmukh [60] for entry vehicles. The MES' estimated hypersonic L/D capability in continuum flow is approximately 0.25 at $\alpha = -16$ deg, per the aerodatabase. Additionally, the entry ballistic coefficient of the MES was estimated to be 30 kg/m^2. For the assumed entry velocity, L/D, ballistic coefficient, and target orbit altitude, γ_E was calculated to be -10.33 deg. Lastly, the assumed entry orbit inclination was 30 deg.

Table 4.3. The target orbit of the MES

Parameter	Value
Periapsis altitude	400 km
Apoapsis altitude	400 km
Inclination	30 deg

133

Table 4.4. The entry state of the MES

Parameter	Value
Altitude	150 km
Inertial velocity	5.5 km/s
Inertial entry flight path angle	-10.33 deg
Inclination	30 deg

Numerical integration of the 6-DOF EOMs was performed using a variable-step, variable-order solver employing an Adams-Bashforth-Moulton predictor-corrector algorithm.[2] The integration tolerance was set to 1×10^{-3} after a trade of computational cost and accuracy was conducted. As demonstrated in Figure 4.6, the altitude history did not greatly change when the integration accuracy was increased (smaller integration tolerance). On the other hand, the computational cost was markedly affected by tolerance size. As seen in Table 4.5, the smaller the tolerance, the longer it took to complete a full trajectory simulation. Therefore, 1×10^{-3} was adopted as the integration tolerance because it generally led to faster computational times.
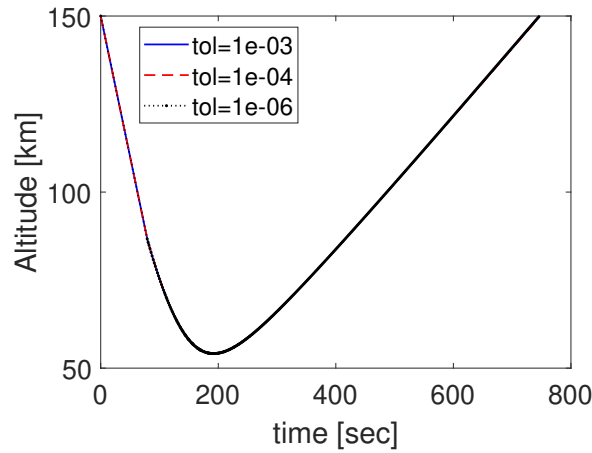
Figure 4.6. The effect of integration tolerances on the aerocapture trajectory.

---

[2]↑See `ode113` solver in MATLAB (https://www.mathworks.com/help/matlab/ref/ode113.html).

Table 4.5. The effect of integration tolerances on the total computational time

Tolerance	Total Compute Time (sec)
1×10^{-3}	10,000
1×10^{-4}	10,200
1×10^{-6}	13,400

The guidance framework was programmed to "shut off" when the sensed acceleration of the vehicle fell below the 0.10 g trigger during the outbound leg of the aerocapture trajectory. At shut-off, the NPC guidance ceases to issue new attitude commands. Instead, the α_c and β_c issued during the final guidance cycle before shut-off are held constant through the remainder of the flight. However, the PID controller remains active to maintain the final attitude commands as well as combat the returning static instability of the vehicle due to rarefied flow conditions experienced during ascent.

All simulations were terminated when the calculated altitude met or exceeded the 150 km mark. A case was deemed a successful capture when it exited the atmosphere on a captured elliptical orbit. To check, the specific energy (E) of the vehicle was computed via:

$$E = \frac{V_I^2}{2} - \frac{\mu}{R_I} \tag{4.1}$$

where V_I is the inertial velocity, R_I is the radial distance of the vehicle from the center of Mars, and μ is the gravitational parameter of Mars. When $E < 0$, then the transfer orbit resulting from the atmospheric flight portion is a bounded ellipse. Otherwise, the vehicle exits the atmosphere on an unbounded parabolic ($E = 0$) or hyperbolic ($E > 0$) trajectory.

The aerocapture ΔV costs are metrics used to assess orbit insertion performance. Lower costs indicate that the vehicle can accurately follow the NPC guidance commands. The three maneuvers involved are the periapsis raise maneuver (PRM), apoapsis correction maneuver (ACM), and inclination correction maneuver (ICM). A PRM is conducted to prevent the vehicle from impacting the surface after one orbit around the post-atmospheric exit transfer trajectory. The ACM and ICM are conducted to enable the vehicle to settle into the correct

orbit shape and orientation. These costs are measured in units of m/s and are computed in the simulation code as follows:

$$\Delta V_{PRM} = \sqrt{2\mu} \left| \sqrt{\frac{1}{r_{a,e}} - \frac{1}{r_{p,t} + r_{a,e}}} - \sqrt{\frac{1}{r_{a,e}} - \frac{1}{2a_e}} \right| \tag{4.2}$$

$$\Delta V_{ACM} = \sqrt{2\mu} \left| \sqrt{\frac{1}{r_{p,t}} - \frac{1}{r_{p,t} + r_{a,t}}} - \sqrt{\frac{1}{r_{p,t}} - \frac{1}{r_{p,t} + r_{a,e}}} \right| \tag{4.3}$$

where $r_{a,e}$ is the apoapsis radius at exit, $r_{p,t}$ is the target periapsis radius, $r_{a,t}$ is the target apoapsis radius, a_e is the semi-major axis of the transfer orbit at exit, and μ is the gravitational parameter of the planet. Because this study assumed circular target orbits, the inclination correction cost was computed as follows:

$$\Delta V_{ICM} = 2\sqrt{\frac{\mu}{r_{a,t}}} \sin\left(\frac{|i_e - i_t|}{2}\right) \tag{4.4}$$

where i_e and i_t are the inclinations of the transfer orbit and target orbit, respectively.

4.2 Angle of Attack Control

This section presents simulations of α-only control with the MES. Modulating α impacts the lift and drag vectors, but not the side force vector. Therefore, α-only control is an in-plane maneuver that reduces PRM and ACM. A nominal trajectory is described in Sec. 4.2.1 to introduce the salient features of an aerocapture entry profile. To assess the robustness of the petal deflection strategy, a Monte Carlo analysis of α-only control was also performed. The experimental setup and results of this robustness study are presented in Sec. 4.2.2.

4.2.1 Nominal Entry Profile

The nominal aerocapture sequence begins with the MES entering the Martian atmosphere at a 150 km altitude with an inertial velocity of 5.5 km/s and γ_E of -10.33 deg.[3] The

---

[3]↑The discussion of the nominal entry results in Sec. 4.2.1 was adapted from Ref. [111] and modified as necessary for narrative flow.

resulting altitude and planet-relative velocity histories are shown in Figure 4.7(a). The MES reaches a minimum altitude of 55 km approximately 196 seconds after entry before spending the remainder of the trajectory coasting out of the atmosphere. The difference between the planet-relative velocities at entry and exit is 2.01 km/s, which represents the aerodynamically-generated ΔV.

The stagnation point convective heat rate and g-loading histories are also shown in Figure 4.7(b). The stagnation point convective heat rate was obtained via the Sutton-Graves correlation using a nose radius of 0.3 m. The maximum convective heat rate is 28.7 W/cm^2 while the integrated heat load is 4475 J/cm^2. A carbon fabric TPS developed for ADEPT [23] may be well-suited to handle this aerothermal environment, although further analysis for more accurate TPS sizing is recommended future work. The peak deceleration is observed to be 1.97 g. For comparison, this g-loading is smaller than the 3.9 g experienced by the ADEPT test article on the Sounding Rocket One (SR-1) flight test on Earth [112]. As expected, the peak deceleration experienced by the MES is smaller than that of the ADEPT test article because Mars has a smaller gravity well than Earth.

(a) Altitude and relative velocity   (b) Heating and acceleration
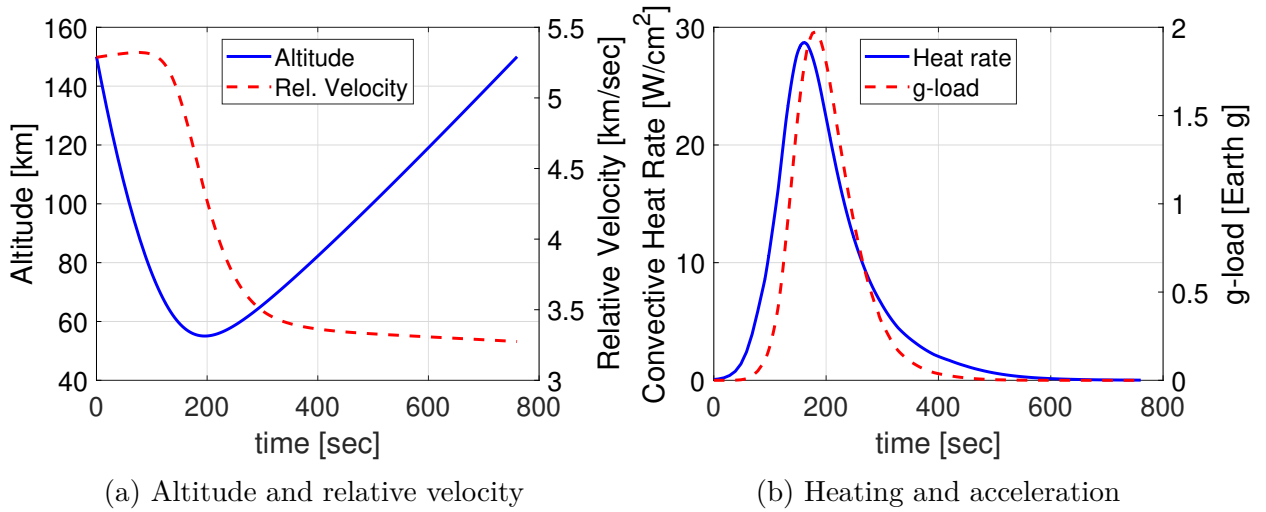
Figure 4.7. Nominal aerocapture trajectory.

The profiles of the controlled α as well as the α-rate are shown in Figure 4.8. The attitude-tracking performance of the PID controller is dependent on the gains. As previously mentioned, the gains were scheduled according to freestream dynamic pressure to

accommodate the changes in the static stability of the MES due to flow rarefaction. According to Figure 4.8(a), the controlled α profile (solid blue line) does not perfectly follow the commanded α profile (dashed red line). The vehicle either undershoots or overshoots the commanded α before guidance hold initiation (i.e., guidance shut-off) at $t = 343$ sec. Additional tuning of the controller gains for the q_∞ range near $t = 343$ sec can improve upon the current attitude-tracking accuracy. Despite the imperfect attitude-tracking, the static stability of the deflected MES in continuum flow is clearly demonstrated by its ability to maintain trimmed attitudes during active guidance. The gains also appear well-tuned for rarefied transitional and free molecular flow conditions, enabling the controller to maintain a stable attitude after guidance hold initiation.

(a) α history   (b) α rate history
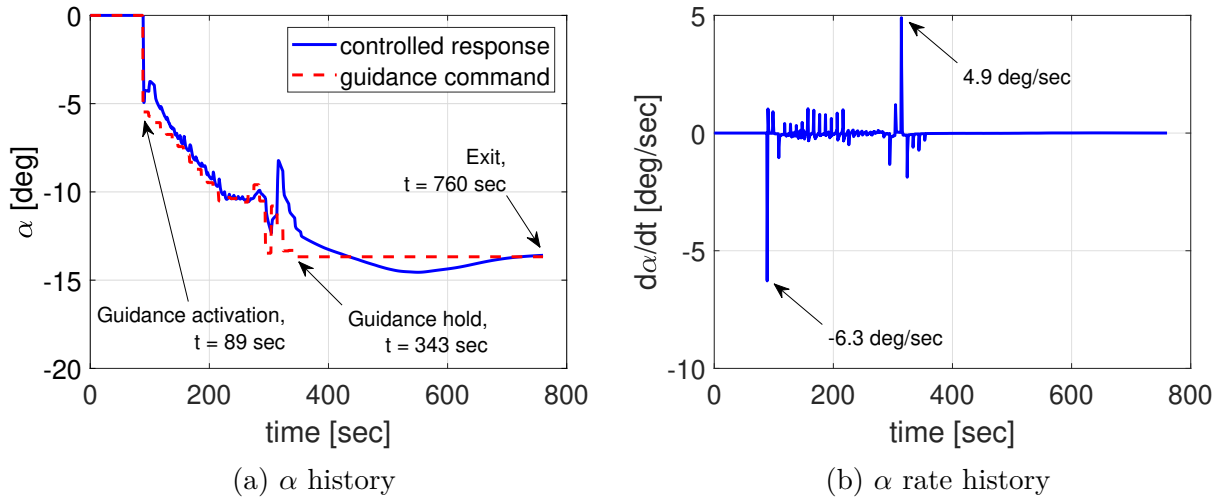
Figure 4.8. Nominal aerocapture controlled attitude profiles.

The peaks in the attitude rate shown in Figure 4.8(b) correspond with the changes in α imparted by petal deflections. The maximum rate magnitude observed is 6.3 deg/s as pointed out in the figure. It corresponds with the initial pitch down maneuver at guidance activation. A secondary peak of 4.9 deg/s occurs later. Besides these dual peaks, the α-rate magnitudes did not exceed 2 deg/s. Note that zero or near-zero rates indicate that the MES was holding a trimmed attitude.

The petal deflection history corresponding with the controlled α profile is shown in Figure 4.9(a). Evidently, the PID controller properly issued P1 deflections to pitch the nose of the

MES down and target the negative α profile commanded by the NPC guidance algorithm. Note that because the guidance only called for negative α values, P4 deflections were never utilized. The purely-negative α profile also suggests that the nominal value of γ_E led to a steeper entry, thereby necessitating the lift vector to be always pointed up (positive lift corresponds to negative α for the MES).

(a) Petal deflections   (b) Petal deflection rates
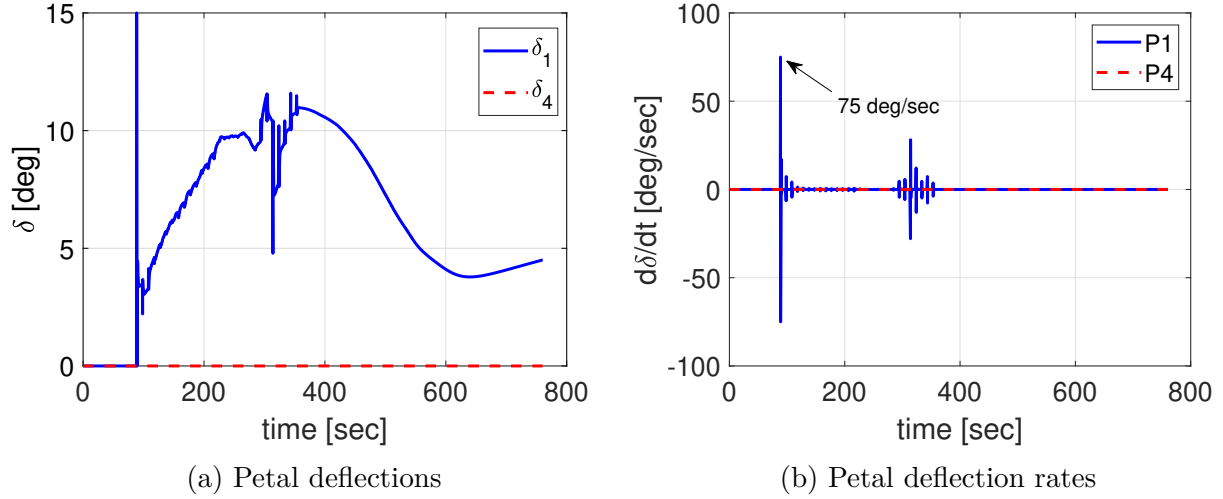
Figure 4.9. Nominal petal deflection profiles.

The deflection rate histories for P1 and P4 are also illustrated in Figure 4.9(b). The rate was computed according to the following:

$$\frac{d\delta}{dt} = \frac{\delta(t_2) - \delta(t_1)}{\Delta t} \tag{4.5}$$

where $\delta(t_2)$ and $\delta(t_1)$ are consecutive deflections and Δt is 0.20 sec. The maximum deflection rate observed is 75 deg/s as pointed out in the figure. This value corresponds with the initial P1 deflection at guidance activation. Because the subsequent deflections were not as large a step as the first command, the associated deflection rates were also considerably smaller than the maximum value. From a mechanical design standpoint, Figure 4.9(b) can be used to inform motor design choices for the petal deflection mechanism.

The periapsis altitude, apoapsis error, and inclination error after atmospheric exit for the nominal case are -19 km, -11 km, and -0.74 deg, respectively. Note that apoapsis error and inclination error were computed using the following expressions:

$$a_{err} = r_a - r_{a,t} \tag{4.6}$$

$$i_{err} = i - i_t \tag{4.7}$$

where r_a is the apoapsis radius of the post-aerocapture transfer orbit, $r_{a,t}$ is the target apoapsis radius, i is the inclination of the post-aerocapture transfer orbit, and i_t is the target inclination. From the above expressions, a negative error indicates undershooting of the target value. The corresponding PRM, ACM, and ICM costs are 99.7 m/s, 2.4 m/s, and 43.3 m/s, respectively. Therefore, the total ΔV cost for the nominal case is 145.4 m/s, which is well within the current capabilities of smallsat propulsion systems [8]. Furthermore, it is markedly smaller than the ΔV achieved through atmospheric drag, which underscores the ΔV savings possible through the aerocapture maneuver. There is a modest inclination correction cost because sideslip angle control was not engaged. However, lateral petal deflections can be used for yaw control to reduce the inclination error.

It is noted that the above ΔV costs are greater than the corresponding optimized costs computed by the NPC guidance algorithm. This is because the guidance algorithm uses 3-DOF translational dynamics to formulate its control laws. By adding attitude dynamics, the simulated 6-DOF trajectories diverge from the optimal trajectories computed by the NPC guidance algorithm.

4.2.2 Monte Carlo Robustness Study

A Monte Carlo dispersion analysis of α-only control was also performed to determine the robustness of the MES to off-nominal flight conditions.[4] In addition to the nominal entry trajectory above, 1000 random trajectories incorporating the combined effects of the uncertainties listed in Table 4.6 were simulated. A sample size of 1001 was chosen to ensure

---

[4]↑The discussion of the Monte Carlo analysis in Sec. 4.2.2 was adapted from Ref. [111] and modified as necessary for narrative flow.

proper distribution of the uncertainties. The experimental setup is explained below and the results are described afterwards.

Experimental Setup

To set the entry state uncertainties for each simulation, the entry state was backwards propagated from the time of atmospheric entry to an assumed data cutoff time before entry [60]. Uncertainties in the position and velocity were then applied at the data cutoff time and the resulting dispersed state was subsequently propagated forward to the entry interface as shown in Figure 4.10. Note that a data cutoff time of 9 minutes before atmospheric entry was assumed based on a previous work [41]. The $\pm 3\bar{\sigma}$ uncertainties in the inertial position and velocity components were assumed to be 1500 m and 1 m/s, respectively [113].[5] These correlate to a $\pm 3\bar{\sigma}$ uncertainty in γ_E of 0.11 deg. The uncertainties in the other inertial state variables at the entry interface are correlated to the propagated dispersed state. A normal distribution of the position and velocity uncertainties were sampled for the simulations.
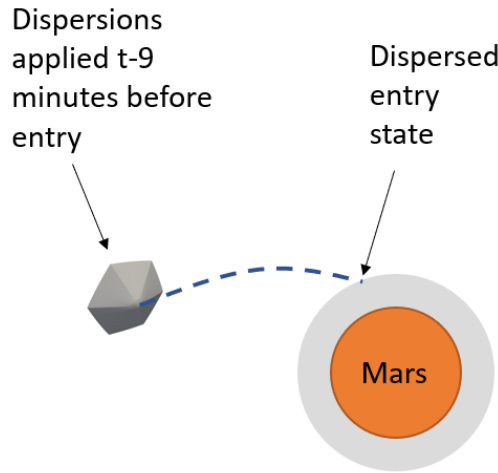
Figure 4.10. Position and velocity uncertainties are applied 9 minutes before entry.

The atmospheric density profile was also varied for the Monte Carlo runs. The scale factor *rpscale* in Mars GRAM controls the scale of the perturbations to the nominal density profile. For computational ease, atmospheric profiles were pre-generated and stored as look-

---

[5]↑Note that $\bar{\sigma}$ is used to denote one standard deviation.

up tables. Nine profiles were generated using *rpscale* values of 0, 0.25, 0.50, 0.75, 1, 1.25, 1.50, 1.75, and 2. The nominal density profile corresponds with *rpscale* equal to 0, whereas factor values of 1 and 2 correspond with the $\pm3\bar{\sigma}$ and $\pm6\bar{\sigma}$ perturbations, respectively. A normal distribution of *rpscale* within the range [0, 2] was sampled and values were rounded to the nearest quarter in order to equal one of the nine available values listed previously. The distribution of *rpscale* values sampled for the Monte Carlo analysis are shown in Appendix C. The so-called "tornado plot" shown in Figure 4.11 illustrates the $\pm3\bar{\sigma}$ and $\pm6\bar{\sigma}$ perturbations to the nominal density profile. Note that wind was not modeled in the simulations.
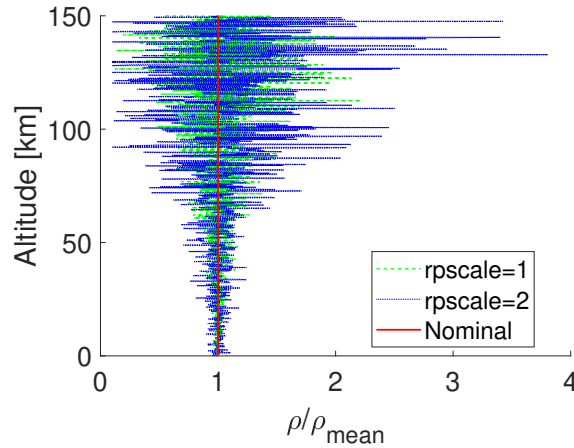
Figure 4.11. A tornado plot showing the $\pm3\bar{\sigma}$ and $\pm6\bar{\sigma}$ perturbations to the nominal Mars density profile.

Aerodynamics uncertainties were defined by comparing high-fidelity computational results to the values contained in the aerodatabase. For example, Figure 3.30 demonstrated that continuum flow values of C_m obtained via DSMC differed by as much as 12% from values queried from the aerodatabase. Therefore, this was assigned as the $\pm3\bar{\sigma}$ variance on C_m for the simulations. The corresponding variances on C_A and C_N were obtained similarly. A normal distribution of the aerodynamics uncertainties was also sampled.

The mission uncertainties included in the Monte Carlo analysis are summarized in Table 4.6.

Table 4.6. Mission uncertainties used in the Monte Carlo simulations

Uncertainty		$\pm 3\bar{\sigma}$ variance or [min, max]	Distribution
	Delivery State		
Inertial position		± 1500 m	Normal
Inertial velocity		± 1 m/s	Normal
γ_E		± 0.11 deg	Correlated
	Atmosphere		
MarsGRAM			
Density (*rpscale*)		[0, 2]	Normal
	Aerodynamics		
Force coefficients			
C_A		$\pm 5\%$	Normal
C_N		$\pm 5\%$	Normal
Moment coefficient			
C_m		$\pm 12\%$	Normal

Monte Carlo Results

All 1001 Monte Carlo cases successfully exited the atmosphere of Mars on bounded elliptical orbits. This indicates that the MES employing the α-only control approach is sufficiently robust against the assumed environmental uncertainties. A summary of the Monte Carlo statistics is provided in Table 4.7. The distributions of different performance metrics are shown in Figures 4.12-4.15.

143

Table 4.7. Monte Carlo simulation statistics (1001 captured cases)

Dispersed quantity	Mean	$\bar{\sigma}$	99$^{\text{th}}$ %-tile	Min	Max
Orbit targeting					
Periapsis altitude, km	-21.5	44.5	5.0	-159.4	15.7
Apoapsis error, km	-22.3	74.0	-0.9	-216.0	16.2
Inclination error, deg	-0.74	0.02	-0.73	-0.80	-0.73
Orbit insertion cost					
PRM ΔV, m/s	100.4	4.0	116.7	90.7	138.5
ACM ΔV, m/s	5.0	5.6	31.0	0.01	50.0
ICM ΔV, m/s	43.4	0.40	45.1	42.5	46.8
Total in-plane ΔV, m/s	105.4	28.2	147.8	91.5	188.1
Total ΔV, m/s	148.8	29.1	192.6	135.0	234.9
Vehicle Environment					
Peak conv. heat rate, W/cm^2	30.7	4.5	34.7	27.4	36.6
Total heat load, J/cm^2	4485.5	145.4	4604.2	4342.8	4656.1
Peak acceleration, g	2.2	0.65	2.8	1.8	3.2
α at peak heating, deg	-7.3	1.1	-4.9	-10.5	-3.9

Figure 4.12(a) illustrates that a majority of the cases exited with negative apoapsis errors. Again, the negative errors correspond with the MES undershooting the target apoapsis, which means that the MES dissipated more energy than needed. From Table 4.7, the mean apoapsis error is -22.3 km (99th %-tile = -0.9 km). The corresponding ACM distribution is provided in Figure 4.12(b) and the mean ACM is 5.0 m/s (99th %-tile = 31.0 m/s).

(a) Apoapsis error distribution (b) Apoapsis correction ΔV distribution
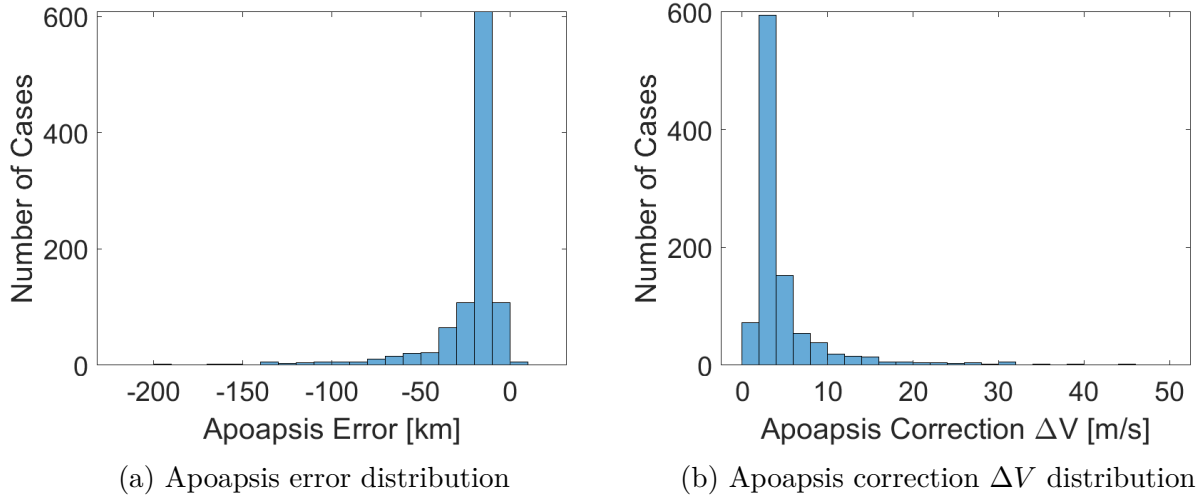
Figure 4.12. Monte Carlo simulation results for apoapsis error and ACM.

The periapsis altitude and PRM distributions are illustrated in Figures 4.13(a) and 4.13(b), respectively. The mean periapsis altitude of the transfer orbit is -21.5 km (99th %-tile = 5.0 km). The negative periapsis indicates the need for a PRM to prevent the vehicle from crashing into the surface of Mars one orbit after the aerocapture periapsis passage. According to Table 4.7, the mean PRM is 100.4 m/s (99th %-tile = 116.7 m/s). Clearly, raising the periapsis was on average more expensive than correcting the apoapsis errors for these cases.

(a) Periapsis altitude distribution (b) Periapsis raise ΔV distribution
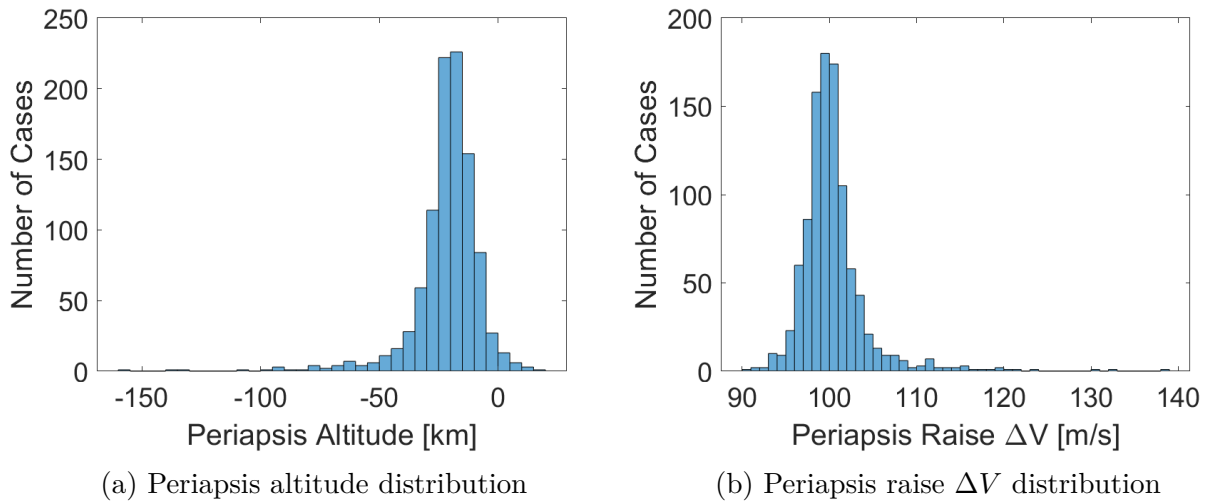
Figure 4.13. Monte Carlo simulation results for periapsis altitude and PRM.

Based on their $\bar{\sigma}$ values, there is a larger spread in the apoapsis errors than there is for the periapsis altitudes. This corresponds to the larger spread in the ACM values. A graphical representation of the spread in the apoapsis and periapsis altitudes is provided in Figure 4.14(a). Note that these altitudes correspond to the transfer orbit immediately following atmospheric exit for the captured cases. It is clear from Figure 4.14(a) that most of the Monte Carlo cases depleted more energy than needed during flight, causing them to undershoot the target apoapsis (black dashed line).

(a) Post-exit orbit state   (b) Total in-plane ΔV distribution
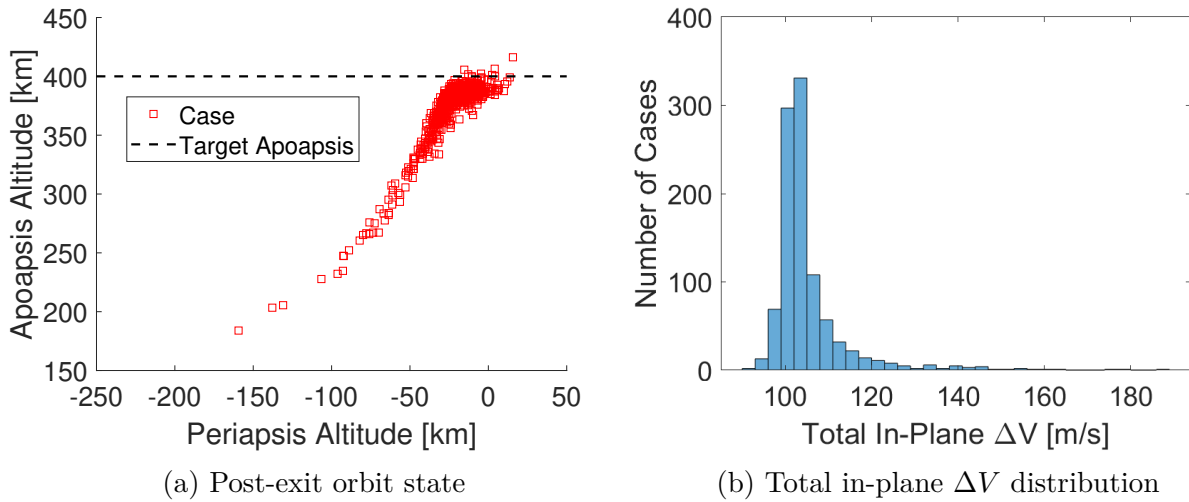
Figure 4.14. Monte Carlo simulation results for orbit targeting performance.

Summing the PRM and ACM values provides the total in-plane ΔV cost. As mentioned previously, the NPC guidance algorithm searches for the α-profile that minimizes this cost. Therefore, a lower number indicates better α-tracking performance by the MES. From Table 4.7, the mean total in-plane ΔV is 105.4 m/s (99th %-tile = 147.8 m/s). The distribution of the total in-plane ΔV is shown in Figure 4.14(b).

Because there was no lateral motion to effect a change in the inclination of the entry orbit, modest ΔV costs were incurred for ICMs. From Table 4.7, the mean ICM is 43.4 m/s (99th %-tile = 45.1 m/s). Adding the ICM to the in-plane ΔV provides the total ΔV cost of the entire aerocapture maneuver. The mean total ΔV is 148.8 m/s with a 99th %-tile value of 192.6 m/s. That is, a ΔV budget of approximately 193 m/s is sufficient to achieve the desired parking orbit for 99% of the captured cases under the present assumptions of

146

this investigation. In a later section, this value is shown to be an order of magnitude smaller than the cost of a fully-propulsive Mars orbit insertion maneuver, further underscoring the ΔV savings achievable via aerocapture.

Knowing the expected aerodynamic and aerothermodynamic loads is also useful to assess whether the aerocapture vehicle can survive a given trajectory profile or not. Figure 4.15(a) shows the distribution of the peak stagnation point convective heat rate based on the Sutton-Graves correlation. The mean peak heat rate is 30.7 W/cm^2 (99th %-tile = 34.7 W/cm^2). The thin Martian atmosphere produces a benign aeroheating environment and TPS materials under development for DEVs appear to be well-suited for this heating environment [23]. Integrating the heat rate with respect to time provides the total heat load, which is used to determine the required thickness of the TPS material. The mean integrated convective heat load at the stagnation point is 4485.5 J/cm^2 (99th %-tile = 4604.2 J/cm^2). A TPS-sizing tool, like that described in Ref. [114], can be used to conduct a detailed study and determine the required thickness to ensure that the MES can survive these heating conditions. However, this is beyond the scope of the present investigation. The peak g-load is also important as it determines the structural stiffness required of the vehicle. The distribution of the peak g-loading is shown in Figure 4.15(b) and the corresponding mean value is 2.2 g (99th %-tile = 2.8 g). The worst-case value is 3.2 g, which is still smaller than the peak loading observed during the ADEPT SR-1 flight test.

(a) Peak convective heat rate distribution   (b) Peak acceleration distribution
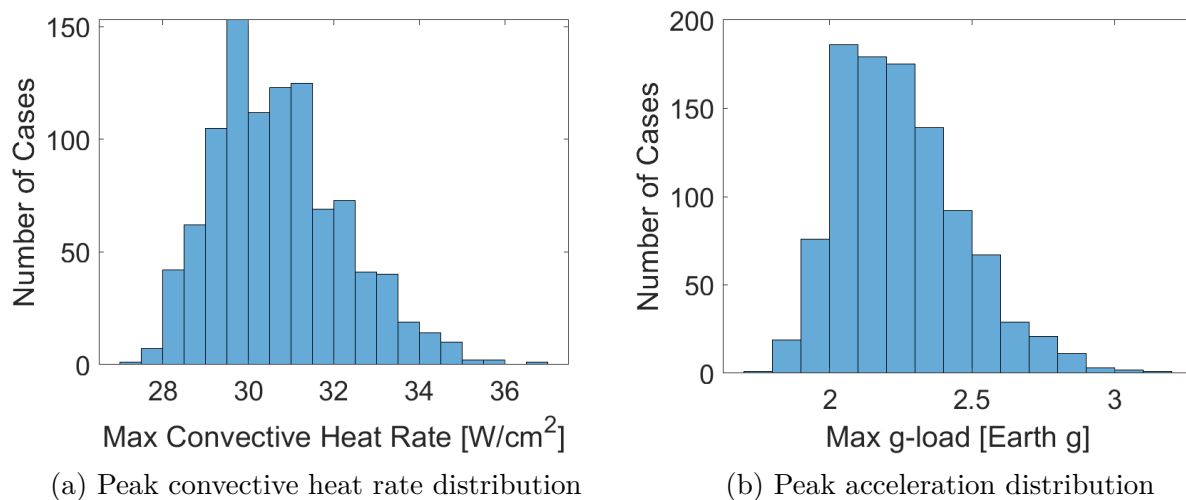
Figure 4.15. Monte Carlo simulation results for aerodynamic heat rate and g-loading.

Flow Impingement Analysis

PID controller failure could result in severe attitude oscillations that lead to the MES assuming large α values. Due to the MES' lack of a backshell, there is a risk of the flow impinging upon the exposed payload under these circumstances, as illustrated in Figure 4.16. Therefore, this study examined the Monte Carlo cases to determine instances of flow impingement.
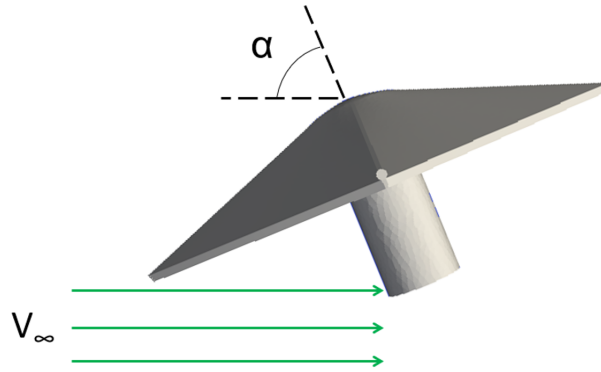
Figure 4.16.

The geometry of flow impingement is shown in Figure 4.17. The flow impingement point, denoted by the red marker, occurs at some distance X aft of the nose of the MES. From the geometry of the flow and of the MES, X can be computed from the following expression:

$$X = x_0 + x_1 + x_2$$
$$= x_0 + L\left(\cos\phi + \frac{\sin\phi}{\tan\alpha}\right) \tag{4.8}$$

where α is the instantaneous angle of attack, L is the fixed length of the deflected pitching petal, and x_0 is the fixed distance of the nose-to-petal transition point behind the tip of the nose cap. The angle ϕ is related to the instantaneous petal deflection δ according to $\phi = 70\deg - \delta$. The flow impinges upon the exposed payload whenever $X < D$, where D is the total depth of the entry configuration measured from the nose tip to the rear edge of the payload. In this investigation, $x_0 = 0.018$ m, $L = 0.61$ m, and $D = (x_0 + 0.50)$ m. The side

of the vehicle containing P4 is at risk of impingement when $\alpha > 0$. Because of symmetry, the side where P1 is located is at risk when $\alpha < 0$.
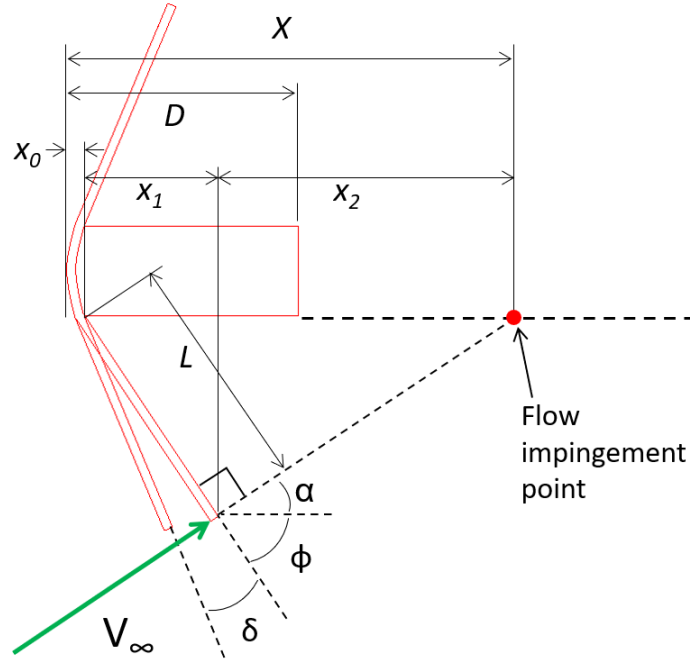
Figure 4.17. Flow impingement geometry.

Using the dimensions of the entry configuration shown previously in Figure 4.4, the variation of the impingement angle of attack with P1 deflections was computed from Eq. 4.8. The result is a quasi-linear relationship, shown as the solid line in Figure 4.18(a). The α and the instantaneous petal deflection at peak convective heating conditions were extracted from each case and plotted in the same figure for comparison. Note that for all 1001 cases, a negative α-command was in effect during peak heating and therefore only P1 was engaged. Furthermore, flow impingement can only occur on the half of the vehicle that includes P1 when α is negative. The α-δ_1 combination at peak heating for all cases are denoted by the open symbols in Figure 4.18(a). Clearly, none of the cases violated the impingement limit, indicating that the exposed payload was safe during the most severe heating condition of each case. Note that due to the symmetry of the MES, the impingement curve is mirrored about the $\alpha = 0$ deg axis for P4 deflections. The distribution of α at peak heating is shown in Figure 4.18(b). The corresponding mean value is -7.3 deg (99th %-tile $= -4.9$ deg).

149
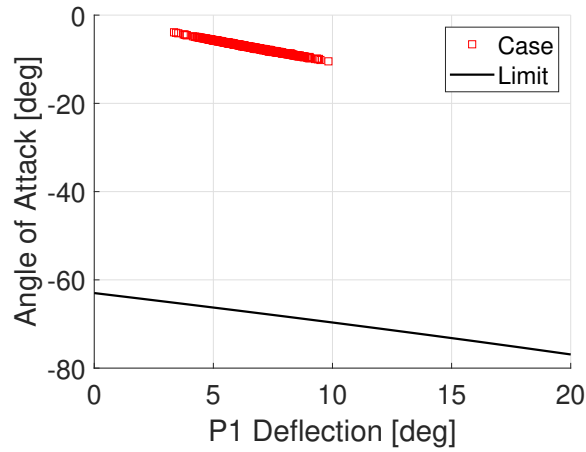
(a) Flow impingement limit
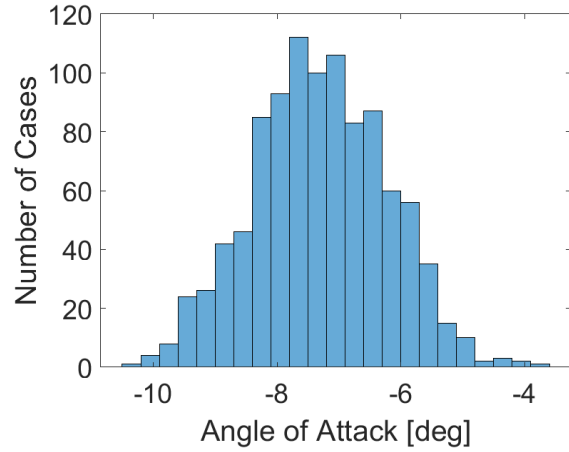
(b) Peak heating angle of attack distribution

Figure 4.18. Monte Carlo results for flow impingement angle of attack at peak convective heating.

All 1001 cases were re-examined to identify occurrences of flow impingement at *any* point in the trajectory. For this analysis, the magnitude of the maximum α was extracted from each trajectory. The corresponding instantaneous petal deflection was then used to compute the magnitude of the flow impingement α. If the maximum α observed for a given trajectory exceeded the instantaneous flow impingement limit, the case was flagged as a failure. Figure 4.19 shows the impingement limit α for each case as a black circle and the maximum α for each case as red squares. This figure indicates that none of the cases violated the limiting α value, and therefore no cases were flagged as failures due to flow impingement.
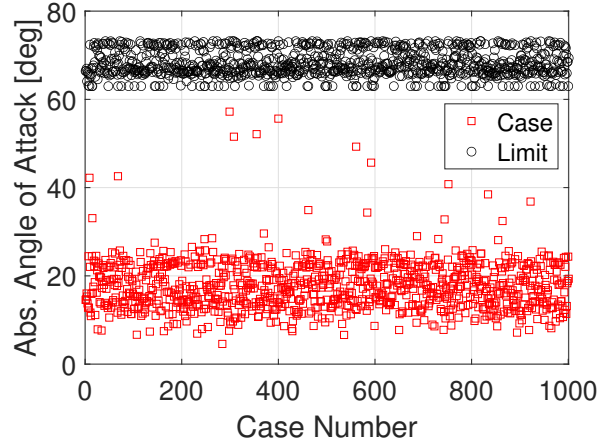
Figure 4.19. Comparison of impingement angle of attack limits and maximum absolute angle of attack for all cases.

Propellant Mass Calculations

As stated in Table 4.7, the 99th-percentile value of the total ΔV cost is approximately 193 m/s. The corresponding propellant mass required for this insertion cost can be estimated from the following expression derived from the ideal rocket equation:

$$\frac{m_p}{m_0} = 1 - \exp\left(\frac{-\Delta V}{I_{sp}g_0}\right) \tag{4.9}$$

where m_p is the propellant mass, m_0 is the wet mass of the entry system, I_{sp} is the specific impulse of the propellant, and g_0 is the standard acceleration due to gravity defined as 9.80665 m/s^2. The I_{sp} of three smallsat chemical propulsion technologies described in Ref. [8] were utilized to perform back-of-the-envelope estimates for the propellant mass required according to Eq. 4.9 and the results are listed in Table 4.8. Because the I_{sp} values do not vary by much from one another, the propellant masses listed are comparable. In terms of the leftover available mass $(m_0 - m_p)$, all three systems allow for at least 68 kg of total dry mass to be dedicated to the payload and the MES flight system.

Table 4.8. Propellant mass estimates for different smallsat chemical propulsion systems (assuming $m_0 = 75$ kg)

Developer	Model	Propellant	I_{sp}	m_p/m_0	m_p [kg]	$m_0 - m_p$ [kg]
Aerojet Rocketdyne	MR-103D	Hydrazine	209	0.089	6.74	68.26
Moog	MONARC-1	Hydrazine	227.5	0.083	6.21	68.79
Aerojet Rocketdyne	MR-106E	Hydrazine	229	0.082	6.17	68.83

The cost of fully-propulsive orbit insertion corresponds with the base ΔV required to place a spacecraft into the target orbit of interest, which can be estimated using orbital mechanics techniques (for example, see Sec. 8.8 of Ref. [115]). The total ΔV required to achieve a 400 km × 400 km circular orbit on Mars was found to be 2.08 km/s, which is approximately 1.89 km/s greater than the 99th-percentile ΔV corresponding with aerocapture. By assuming the Aerojet Rocketdyne MR-106E propulsion system from Table 4.8, the m_p needed to deliver this ΔV was found to be 45.3 kg. The ΔV and propellant mass comparisons between these orbit insertion techniques are summarized in Table 4.9. Note that 60% of the system's wet mass is propellant when employing the fully-propulsive option, which translates to a significant reduction in the available dry mass for the payload and MES flight system.

Table 4.9. Comparison between aerocapture and fully-propulsive orbit insertion (assuming $m_0 = 75$ kg)

Method	Propulsion System	ΔV [m/s]	m_p/m_0	m_p [kg]	$m_0 - m_p$ [kg]
Fully-propulsive (chem)	MR-106E	2080	0.604	45.30	29.7
Aerocapture	MR-106E	193	0.082	6.17	68.83

4.3 Sideslip Angle Control

In this section, simulations of sideslip angle control with the MES are presented. Modulating β introduces side force, which can be used to manage the out-of-plane movement of the MES in the atmosphere. Therefore, β control allows for the reduction of the ICM. Note that mixed petal deflections that could potentially achieve simultaneous non-zero trim α and β were not pursued to simplify the analysis. Instead, a β-to-α control sequence was

employed to demonstrate the lateral control capabilities of the MES. Sec. 4.3.1 provides an overview of this control approach and Sec. 4.3.2 describes the simulation results.

4.3.1 β-to-α Control Overview

In the β-to-α control sequence, pure β-control is engaged once the acceleration trigger of 0.1 g is reached. After a prescribed number of guidance cycles, β is controlled back to zero to null out any residual C_n. Afterwards, pure α-control is engaged to manage the in-plane ΔV. For the β-to-α control sequence to succeed, the entry flight path angle of the MES must be shallow enough that the lack of lift for an extended period does not lead to a surface impact. That is, the MES can still safely guide itself out of the atmosphere once α-control has been engaged despite maintaining zero α for some time.

Because α is essentially zero while β-control is active, the in-plane correction cost determined by the NPC guidance grows. This is demonstrated in Figure 4.20, which shows in-plane correction cost as a function of the guidance cycle for a test case with an entry flight path angle of -10.33 deg. In this test simulation, α-control was set to begin on the 14th guidance cycle. However, the figure indicates that by cycle number 13, the MES has lost too much energy that the NPC guidance predicts surface impact. The guidance outputs 1×10^9 m/s for the in-plane ΔV by default to indicate that surface impact is imminent and the simulation framework subsequently terminates. In this case, the large ΔV is mainly comprised of the periapsis raise maneuver, which is effectively "infinite" for a vehicle that impacts the surface. Figure 4.20 suggests that activating α-control much earlier than the 14th guidance cycle in this case would avoid surface impact.
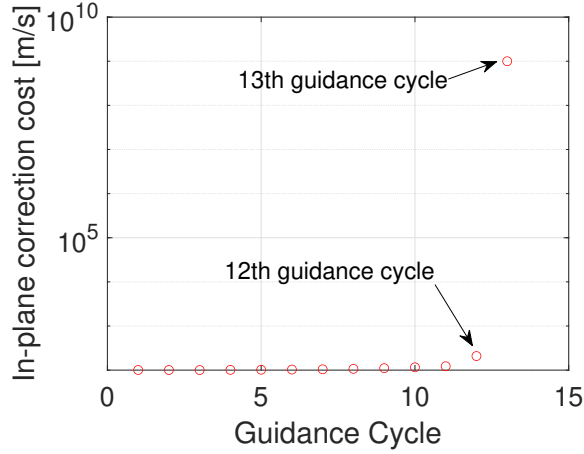
Figure 4.20. The in-plane correction cost (m/s) grows to a very large number when α is left uncontrolled long enough.

Clearly, a major challenge of the β-to-α control approach is predicting when to engage α-control. Intuition dictates that the timing is greatly influenced by the entry flight path angle (i.e., steeper trajectories cannot afford to fly at zero angle of attack for too long, while shallower trajectories can). The relationship between α-control initiation and entry flight path angle is a logical area of investigation that must be pursued to optimize this control approach. However, this was deemed beyond the scope of the current study because demonstrating sideslip angle control with the MES design is the current primary objective.

4.3.2 Simulations of β-to-α Control

A simulation of β-to-α control, referred to here as Case 1, was carried out. The Mars environmental parameters (Table 4.1) as well as the target orbit characteristics (Table 4.3) were kept the same. Because of the reliance on a shallower γ_E, the nominal entry value was set to -10.23 deg instead of -10.33 deg. Aside from this modification, the entry state parameters listed in Table 4.4 were kept. No environmental dispersions were simulated for this control approach.

Figure 4.21 illustrates the controlled sideslip angle profile and the corresponding β rate history. β control was active for 9 total guidance cycles in this demonstration. The first 7 cycles were spent tracking a constant non-zero β command, while the remaining two were

dedicated to controlling β back to zero. As shown in Figure 4.21(a), there is a significant error between β and β_c during the earlier guidance cycles that is attributed to imperfect PID gains. However, the build-up of this error was eventually captured by the integral term of the controller, which helped reduce the β error. Further tuning of the proportional and derivative gains is recommended to improve the accuracy in earlier guidance cycles. The excellent performance of the controller in tracking $\beta_c = 0$ deg is, however, notable.

(a) β history

(b) β rate history
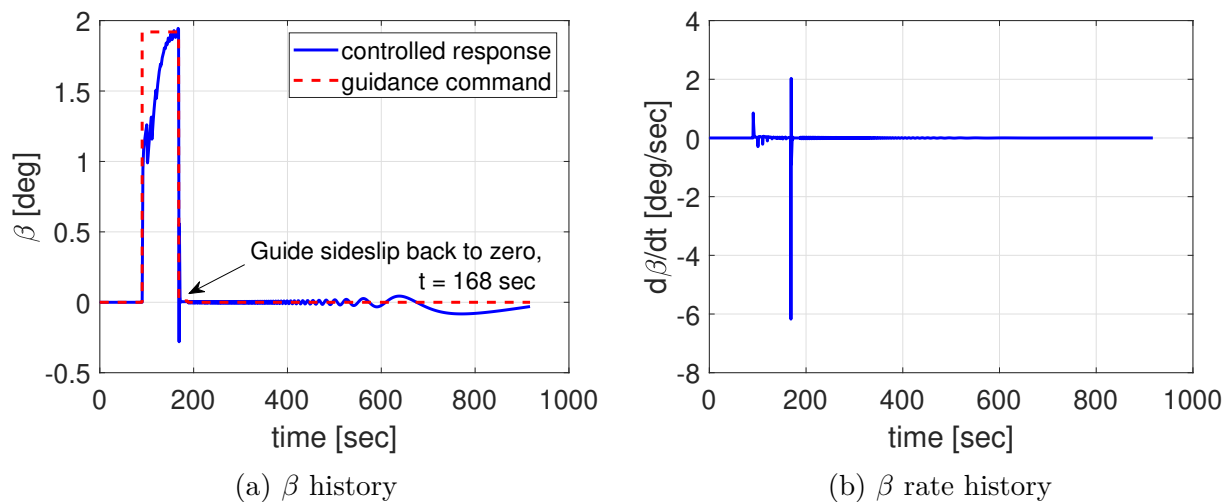
Figure 4.21. Sideslip angle profile.

Figure 4.21(a) shows that β undergoes small oscillations (amplitude of approximately 0.005 deg) after $t = 168$ sec. The associated β rates shown in Figure 4.21(b) also oscillated but did not exceed 0.025 deg/s and eventually damped out to rates as low as 0.0005 deg/s near atmospheric exit. Because the MES is statically unstable in rarefied flows, any residual sideslip can potentially lead to the uncontrollable growth of β when α-control is active. This can actually be observed by the growth in the amplitude of the β oscillations near $t = 800$ sec in Figure 4.21(a). Due to the coupling of roll and yaw demonstrated by Eqs. 3.66-3.68, β excursions also induce growth in $\dot{\sigma}$ and thus σ. This is an undesirable situation because it violates the aerodatabase assumption of zero bank angle, thus resulting in erroneous aerodynamics. This underscores the importance of damping out $\dot{\beta}$ and $\dot{\sigma}$ before engaging α-control by controlling β back to zero.[6]

---

[6]↑Note the use of dot notation to indicate a time derivative (e.g., $\dot{\sigma} = d\sigma/dt$).

Recall that β modulation is accomplished via R2 and R5 deflections. To track the positive β_c issued by the guidance system, only R2 deflections were commanded by the PID controller as illustrated in Figure 4.22(a). It can be observed that the deflection magnitudes are smaller compared to the P1 deflections shown previously. This is expected because β_c is relatively smaller compared to the α_c values seen in Sec. 4.2. The associated deflection rates for R2 and R5 are displayed in Figure 4.22(b). The peak deflection rate magnitude observed is 12.7 deg/s, which is considerably smaller than the peak deflection rate shown for the nominal α-control case in Sec. 4.2.1 (see Figure 4.9(b)).

(a) δ history

(b) δ rate history
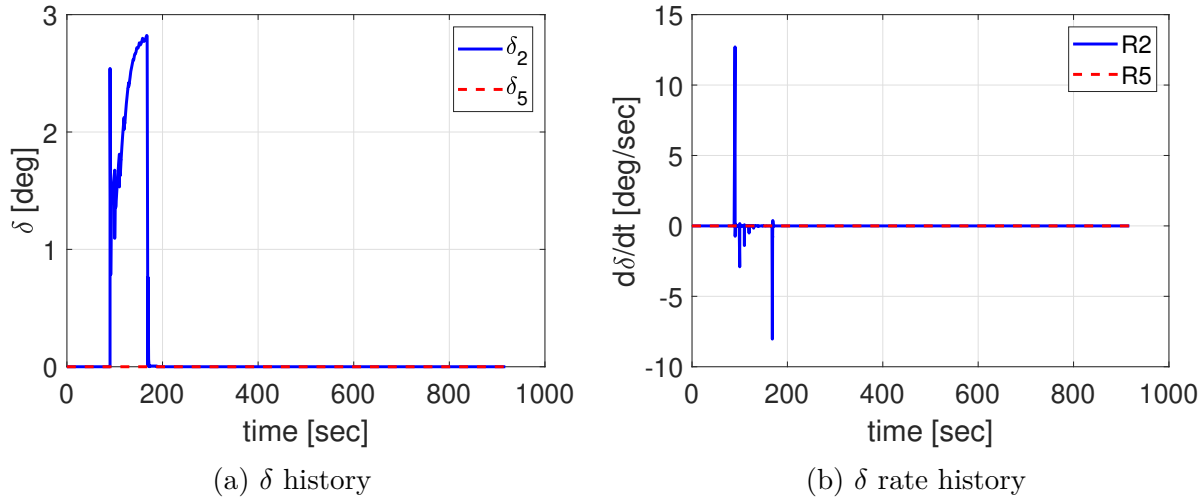
Figure 4.22. Rib deflection profile.

The history of the controlled α response is shown in Figure 4.23. Because α was essentially zero for approximately 200 sec, as seen from Figure 4.23(a), the MES lost enough energy that the NPC guidance issued an all-negative α_c profile to ensure atmospheric exit. The coupling of the Euler angles via the rotational kinematics is further demonstrated by the close-up view of α in Figure 4.23(b). At approximately 88 sec after entry when β-control was initiated, the subsequent non-zero β values "kicked-off" small oscillations of α despite the lack of external pitching moments. As seen in Figure 4.23(b), these oscillations continued up until α-control initiation at approximately 188 sec after entry.
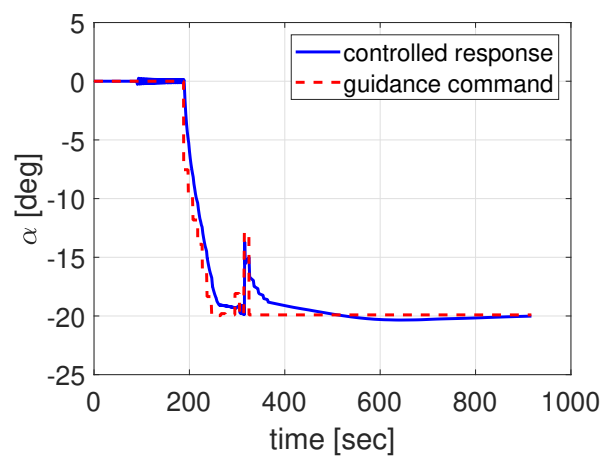
(a) α history
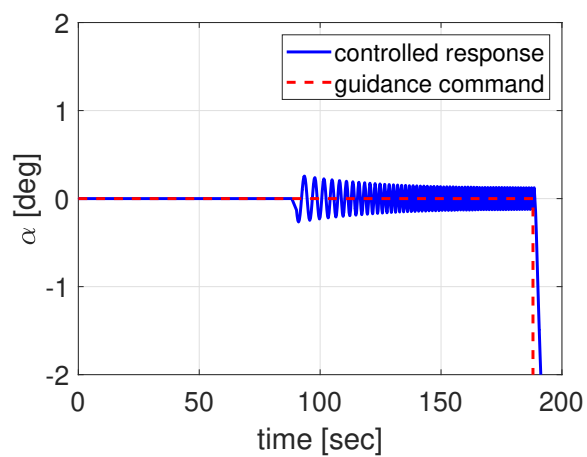
(b) α history zoomed in

Figure 4.23. Angle of attack profile.

The periapsis altitude of the transfer orbit was -118.7 km, which indicates that a significant PRM is required to prevent surface impact. Because the MES flew at zero angle of attack for an extended period, significant energy was lost due to drag, which caused the MES to undershoot the target apoapsis. The resulting apoapsis error was -200.8 km. Lastly, the inclination error was -0.69 deg. The burns needed to correct these errors are listed in Table 4.10.

Table 4.10. ΔV costs for Case 1 of β-to-α control

Maneuver	ΔV (m/s)
PRM	127.3
ACM	45.9
ICM	40.6

Bank Angle Growth

Because of the coupling of the rotational dynamics, non-zero β also introduced finite σ rates. The histories of σ and $\dot{\sigma}$ are shown in Figures 4.24(a) and 4.24(b), respectively. Figure 4.24(a) indicates that σ became finite early in the trajectory, which corresponds with the small, finite rates shown in Figure 4.24(b). Because $\dot{\sigma}$ remained finite, the bank angle steadily decreased until it achieved a value of -2.25 deg at atmospheric exit.

Figure 4.24(c) and 4.24(d) offer closer views of the behavior of σ and $\dot{\sigma}$ near β- and α-control initiations. Small oscillations of σ were introduced after $t = 88$ sec. These oscillations then sloped downward due to the growing negative $\dot{\sigma}$. Even after β was controlled back to zero at $t = 168$ sec, the bank angle rate never returned to zero.

158

(a) σ history

(b) σ rate history

(c) σ history zoomed in

(d) σ rate history zoomed in
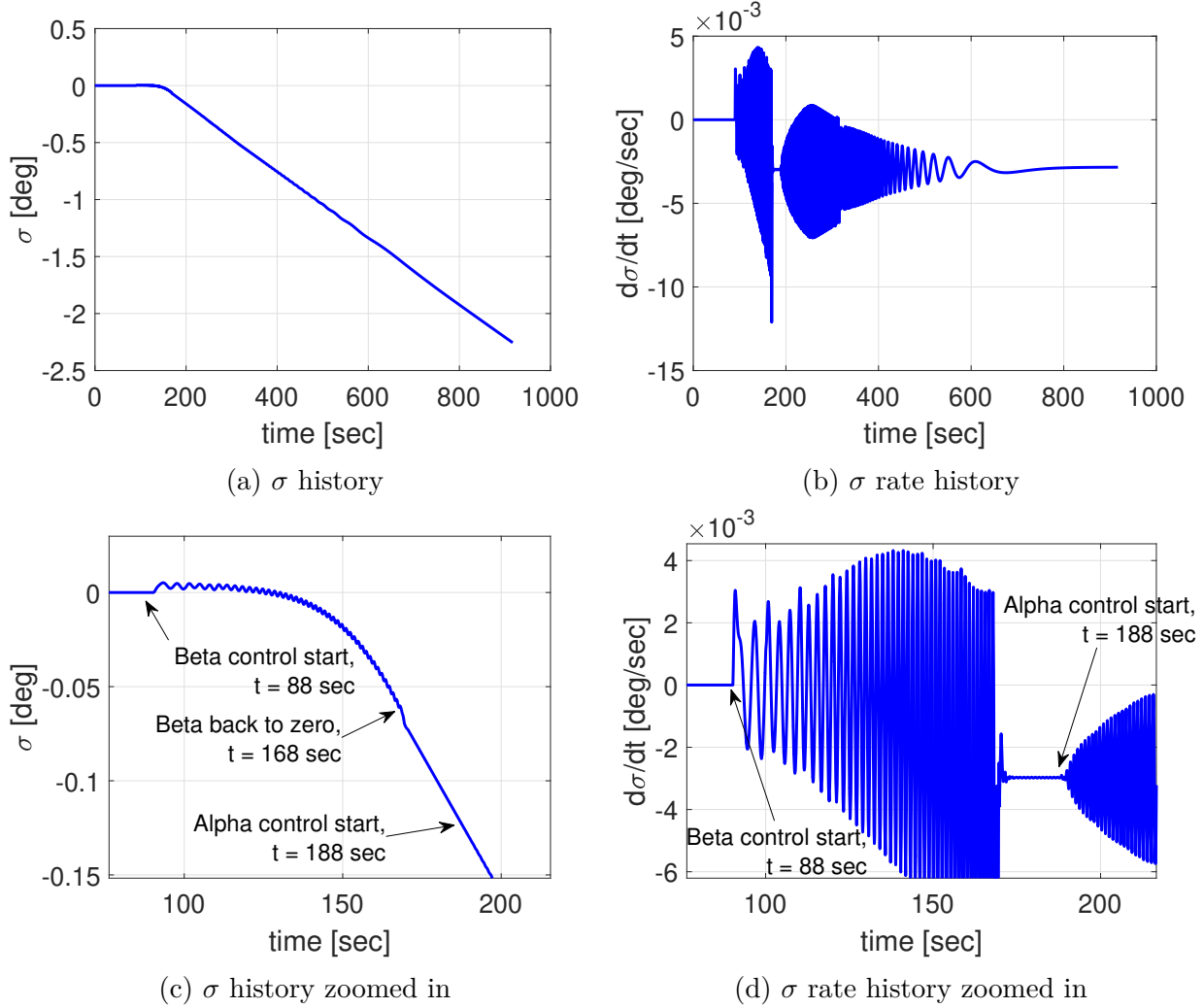
Figure 4.24. Bank angle profile.

As previously mentioned, the aerodynamics database was developed by assuming a zero bank angle. Therefore, the growth of σ during α-control can be expected to introduce errors between the database values and the banked aerodynamics. This error was investigated by computing banked aerodynamics in the continuum and free molecular regimes using the panel codes described in Ch. 3. To simulate a banked MES, the geometry was rotated about the body x-axis by -2.25 deg, -5 deg, and -10 deg. A P1 deflection of 10 deg was assumed for these calculations. Note that because β was very small during α-control, this meant that the velocity vector of the vehicle was contained in the x-z plane as illustrated in Figure 4.25.

Therefore, a rotation about the body x-axis directly translates to σ. The absolute error between the database and banked aerodynamics were computed as follows:

$$\text{Abs}(C) = \text{Abs}(C_0 - C_\sigma) \tag{4.10}$$

where C denotes the aerodynamic coefficient of interest, C_0 corresponds with the aero-database value for C, and C_σ corresponds with the value of C at the banked orientation.
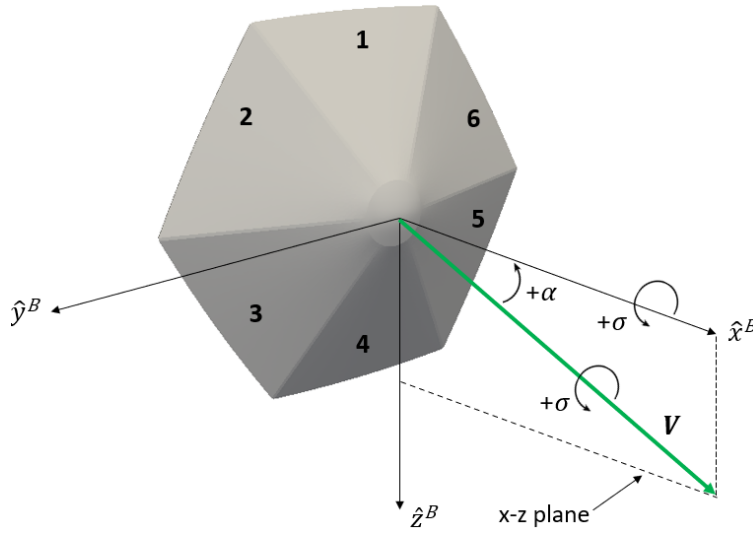
Figure 4.25. The velocity vector is contained within the x-z plane at zero sideslip angle.

The errors in L/D and the three moment coefficients in continuum flow are shown in Figure 4.26. As expected, the error grows with σ, although none of the errors exceed 10^{-2}. The errors corresponding with the free molecular regime are also shown in Figure 4.27. As with the continuum values, none of the errors exceed 10^{-2}. Furthermore, the errors that correspond with $\sigma = -2.25$ deg (i.e., the value at atmospheric exit) are the smallest. These results verify that the aerodynamics being simulated during the period of σ growth shown in Figure 4.24 are reasonable approximations to the banked aerodynamics. However, the results also suggest that σ must be kept relatively small to keep the errors small. In other words, reducing the growth of σ is a critical requirement of sideslip angle control for the

MES given the present assumptions of the aerodatabase. The development of methods to fulfill this requirement is recommended future work.

(a) L/D

(b) C_l

(c) C_m

(d) C_n
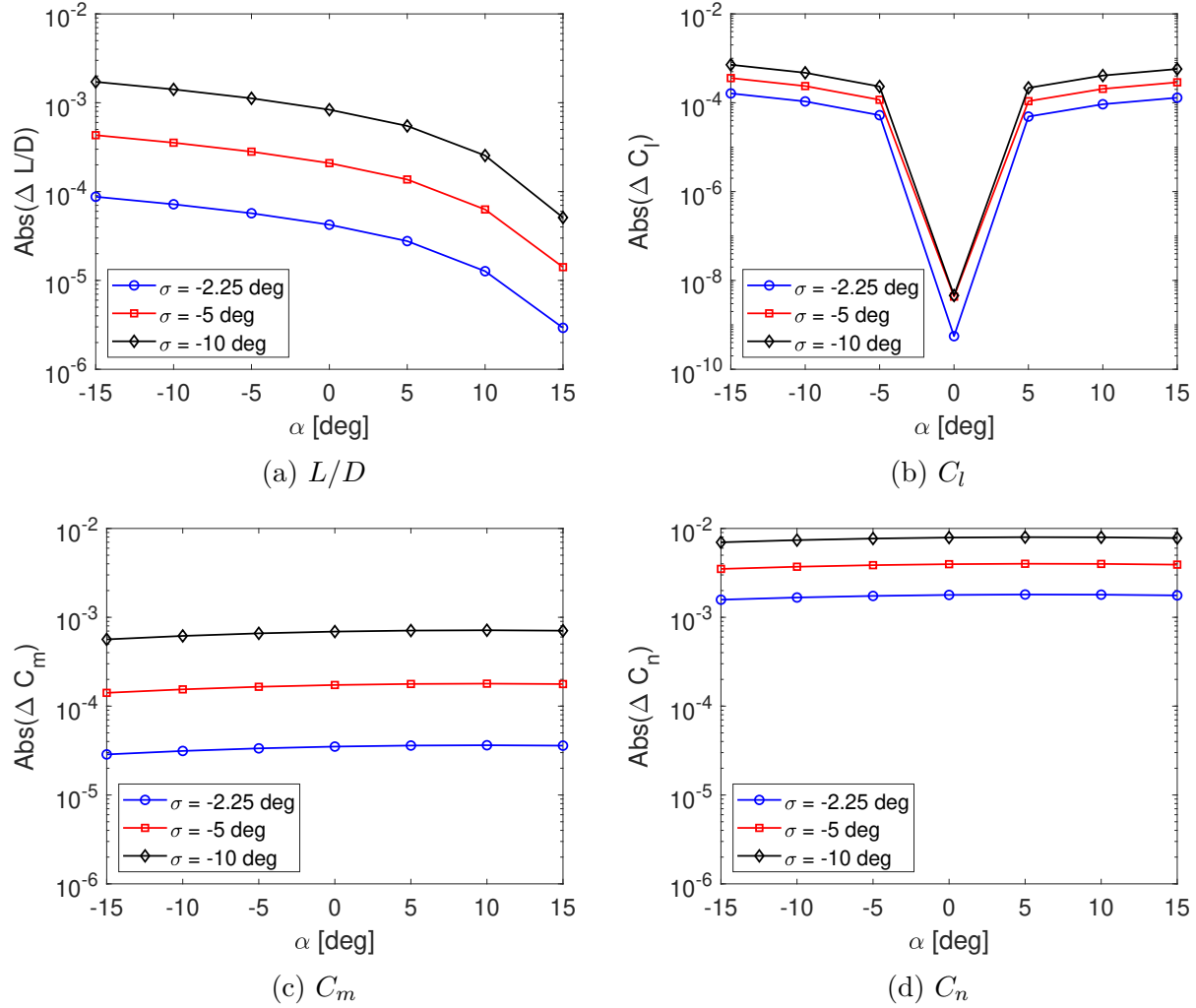
Figure 4.26. Absolute error between aerodatabase and banked aerodynamics in continuum flow conditions ($\delta_1 = 10$deg).
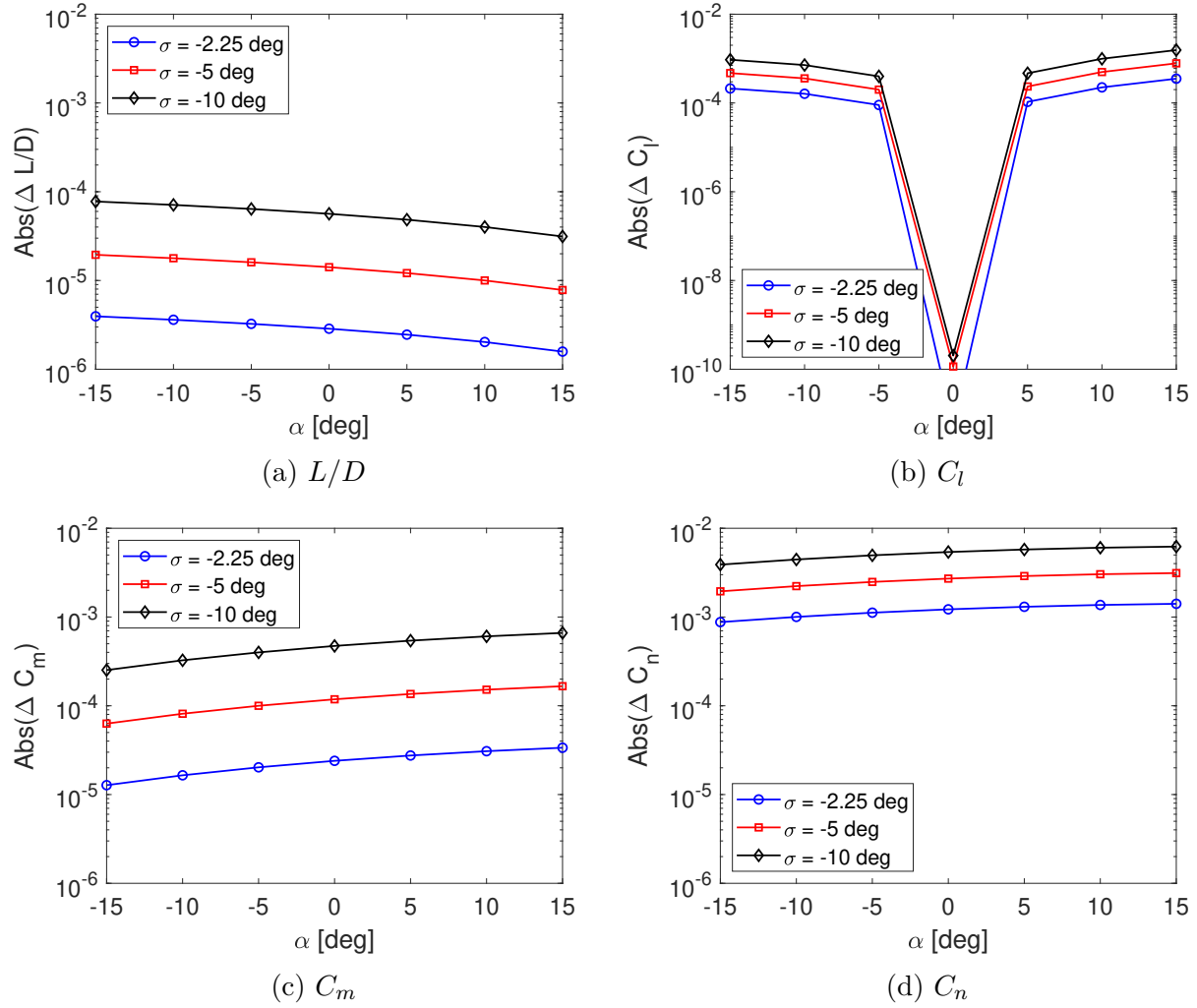
Figure 4.27. Absolute difference between aerodatabase and banked aerodynamics in free molecular flow conditions ($\delta_1 = 10$deg).

Extended β control

By choosing a shallower γ_E, β-control can be run for more guidance cycles to reduce the inclination error and improve the ICM cost listed in Table 4.10. A secondary simulation, referred to here as Case 2, was carried out with γ_E set to -10.11 deg. For Case 2, β-control was active for 22 total guidance cycles (20 cycles spent tracking non-zero β and 2 cycles spent controlling β back to zero).

Figure 4.28 indicates that the MES was able to hold the constant β_c for a majority of the β-control portion of the trajectory. Clearly, the PID gains could benefit from more tuning

to reduce the error faster during the early guidance cycles. It is also evident that after being controlled back to zero ($t = 298$ s), β oscillated about zero at a decreasing frequency but increasing amplitude. The increasing amplitude of the oscillations is consistent with the growing yaw instability of the MES in the upper atmosphere.
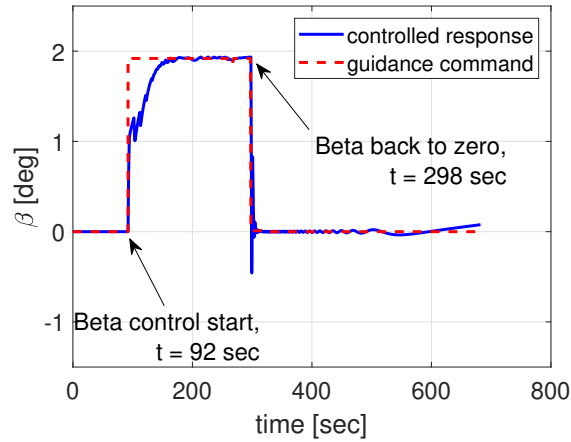
Figure 4.28. β profile for Case 2.

Figure 4.29 shows that $\alpha_c > 0$ after α-control initiation at $t = 318$ s. The positive α profile indicates that the entry was shallow enough that the MES needed to shed more energy via a "lift-down" maneuver to reduce any overshooting of the target apoapsis. Again, the accuracy of the PID controller is demonstrated in Figure 4.29.

Figure 4.29. α profile for Case 2.

163

Figure 4.30 shows that σ initially decreased after β-control was initiated at $t = 92$ s. However, it started to increase after β was controlled back to zero and continued to do so even after α-control activation. Eventually, σ reached the maximum value of 16 deg at atmospheric exit.
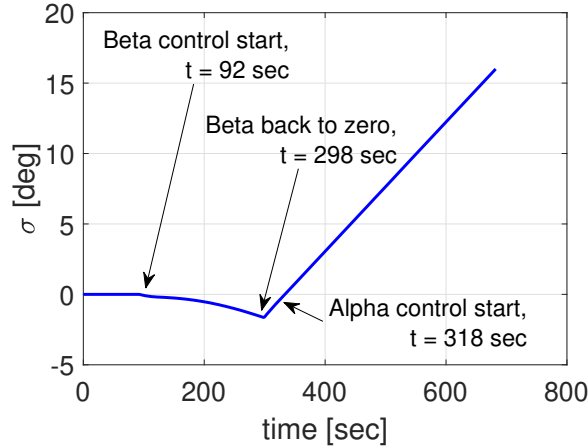
Figure 4.30. σ profile for Case 2.

Based on the aerodynamics comparisons made in Figures 4.26-4.27, a more significant error in the aerodynamics is to be expected at these values of σ. However, such errors are deemed irrelevant this late in the trajectory because aerodynamic forces are small due to flow rarefaction and are therefore not expected to greatly influence the motion of the MES. As mentioned before, erroneous aerodynamics may be avoided by keeping σ small. Alternatively, non-zero σ can be accounted for in the future developments of an aerodatabase for a vehicle like the MES employing α and β control.

The inclination error for Case 2 is -0.33 deg, which is almost half of the error from Case 1 (-0.69 deg). This translates to an ICM of 19.1 m/s as opposed to 40.6 m/s for Case 1. Therefore, Case 2 has demonstrated that running β-control longer helps to reduce the inclination error and thus the ICM. The periapsis altitude of the transfer orbit upon exit is 46.8 km, which translates to a PRM of 78.5 m/s (127.3 m/s for Case 1). The apoapsis error is 753.7 km, which translates to an ACM of 148.4 m/s (45.9 m/s for Case 1). These ΔV costs are summarized in Table 4.11.

Table 4.11. ΔV costs for Case 2 of β-to-α control

Maneuver	ΔV [m/s]
PRM	78.5
ACM	148.4
ICM	19.1

The shallow entry of the MES in Case 2 combined with the limited number of α-control guidance cycles (only 5) did not allow the MES to deplete enough energy to avoid a gross overshooting of the target apoapsis. This suggests that a trade to identify the optimal combination of γ_E and the number of α- and β-control guidance cycles should be conducted. Such an optimal combination of these parameters would balance the ΔV reduction of ACM and ICM. This trade study is recommended future work also.

5. CONCLUSIONS AND FUTURE WORK

This chapter provides a summary of the key findings of this dissertation as well as suggestions for future work.

5.1 Summary

Aerocapture is a technique that can reduce the ΔV cost of inserting a vehicle into a science orbit around a planetary body with a significant atmosphere. The ΔV savings translate to a reduction in the propellant system mass needed for orbit insertion, which is of great benefit to smaller platforms like smallsats. A further reduction in the overall system mass can be achieved by employing an entry aeroshell that also serves as the flight control system. Therefore, this dissertation introduced the morphable entry system (MES), which is a bioinspired deployable entry vehicle envisioned to employ shape morphing for trajectory control during aerocapture of smallsats.

This dissertation set out to demonstrate the feasibility of the MES' aeroshell shape morphing strategy to control its trajectory on Mars. To accomplish this objective, the following four steps were carried out. First, a conceptual design for the MES and the associated shape morphing methodology were established. Next, an aerodynamics database that could be used in trajectory simulations was developed. This database accounted for the change in flow rarefaction to capture the changing static stability characteristics of the vehicle design. Thirdly, a proportional-integral-derivative (PID) controller was developed for the MES. The controller issued the shape deflection commands necessary to achieve a targeted attitude, as commanded by the aerocapture guidance system. Lastly, a six degree-of-freedom aerocapture simulation environment that incorporated the aerodynamics database and the PID controller was developed. With this 6-DOF simulation tool, aerocapture trajectory simulations of the MES were carried out to assess the performance of the vehicle concept.

Out of the three flight control options applicable to aerocapture, direct force control (DFC) has been shown to incur the least ΔV costs at Mars by other authors. Therefore, this dissertation studied the DFC performance of the MES by carrying out simulations of α and β control. These simulations showed that the proposed shape morphing strategy of

the MES is a feasible method for controlling α and β during flight. Furthermore, accurate tracking of α and β was shown to decrease the in-plane and out-of-plane ΔV correction costs, respectively.

A Monte Carlo dispersion analysis of pure α control was carried out to evaluate the robustness of the MES as an aerocapture flight system. This analysis demonstrated that the MES can achieve a 100% aerocapture success rate while subjected to simulated day-of-flight uncertainties. The flow impingement analysis performed in conjunction with the Monte Carlo simulations found that none of the cases violated impingement limits on the angle of attack. This robustness study also revealed that the 99th-percentile value of total ΔV was approximately 193 m/s, which represented savings of almost 1.9 km/s when compared to the fully-propulsive orbit insertion alternative. Furthermore, the aerocapture propellant mass fraction was found to be approximately 9% of the total wet mass for modern smallsat propulsion systems, as opposed to 60% for the fully-propulsive option. This increase in the payload mass delivered to orbit is of great benefit to mass-restricted smallsat systems.

The simulations of β-to-α control also revealed that commanding non-zero β introduced small but finite σ rates that led to the continuous increase or decrease of bank angle. To avoid simulating erroneous aerodynamics, banked configurations of the MES should be incorporated into the aerodynamics database or strategies to minimize $\dot{\sigma}$ should be developed. The β-to-α control approach would also benefit from a trade study to identify the optimal combination of γ_E and the β-to-α control switch time for a given target orbit. The optimized combination would allow for a balanced reduction of the ACM and ICM costs, which would improve the ΔV savings achievable through β-to-α control.

5.2 Suggestions for Future Work

Below are suggestions for future work to further develop the MES as an aerocapture system.

5.2.1 Mechanical and TPS Design

Having established the feasibility of the shape morphing strategy of the MES, a logical future step is to investigate mechanical and TPS implementation. An appropriate control mechanism must be designed to properly actuate the ribs of the MES and achieve the desired shape deflections. The δ rates observed in the simulations can be used to identify the specifications of the mechanism. A TPS material that can accommodate the observed deflections while remaining taut must also be identified. Fluid structure interaction (FSI) analysis methods are likely to be incorporated in the mechanical and TPS design of the MES.

5.2.2 PID Controller Over-Correction

Over-correction is a PID controller failure mode that has been observed in prior test cases. It was addressed in this investigation through gain tuning, limiting the maximum δ magnitude that the controller could issue, and increasing attitude error tolerances. Gain tuning allowed the controller to issue appropriate δ magnitudes that did not over-compensate for a given error state. Limiting the available δ magnitudes helped the controller avoid issuing larger-than-necessary commands that could exacerbate attitude oscillations. Increasing error tolerances allowed the controller to avoid prematurely switching petals, which has been observed to exacerbate over-correction. In general, these three methods were found to be sufficient to avoid controller failure due to over-correction. However, the performance of the controller could be further improved by refining the gains. For example, it is suggested that more dynamic pressure ranges are incorporated in the gain scheduling shown in Table 3.11. This would help eliminate abrupt changes in the magnitude of δ commands during transitions in flow conditions to avoid sudden changes in the attitude error state that could lead to over-corrections.

5.2.3 Improving β-to-α Control

The β-to-α control approach demonstrated that the MES could target non-zero sideslip angles. However, it became evident that further work is needed to optimize this approach to improve its ΔV-savings potential. One limitation of this approach is that the in-plane errors grow significantly if α control is activated too late, leading to large PRM and ACM costs. To address this, a trade study between the entry flight path angle (γ_E) and the β-to-α control switch time is recommended. The objective of this trade is to identify the optimal combination of these two parameters that would lead to a reduction in the in-plane correction costs without sacrificing too much in terms of ICM savings. Another challenge that was discovered is the departure of σ from zero due to β control activation. Because the aerodynamics database was developed with the assumption of zero bank angle, letting σ grow unchecked introduces erroneous aerodynamics into the simulations. Identifying strategies to keep the rate of σ growth small as well as the analysis of non-zero σ during aerodynamics database development are recommended future steps to address this challenge.

5.2.4 Simultaneous Control of α and β

By targeting non-zero α and β profiles simultaneously, unlike the β-to-α approach, the MES could further reduce the in-plane and out-of-plane ΔV costs incurred per flight. One way to achieve concurrent α_c and β_c with the MES is by employing "mixed petal" deflections as shown in Figure 5.1(a). In this example, rib 1 is deflected to pull P1 and P2 away from the flow. These mixed petal deflections induce both pitching and yawing moments that could be used to track α and β, respectively. Aerodynamics calculations must also be carried out to populate the aerodynamics database according to diagonal rib deflections. Preliminary results in the continuum regime were obtained for an R1 deflection of 15 deg, which are shown in Figures 5.1(b)-(d).

(a) Mixed petal deflection

(b) C_l (roll)

(c) C_m (pitch)

(d) C_n (yaw)
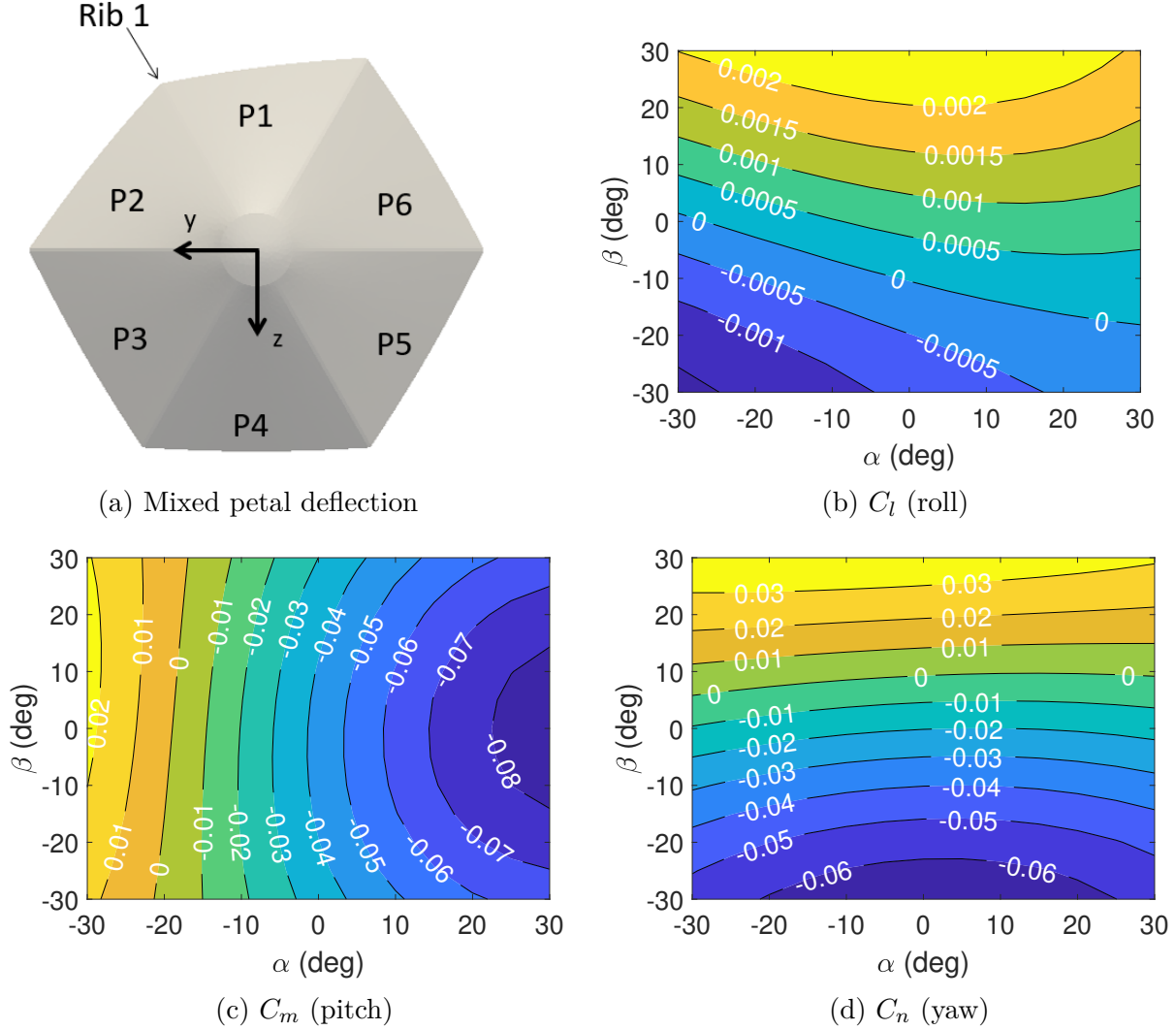
Figure 5.1. Rib 1 deflected away from the flow (δ=15 deg) and the corresponding continuum aerodynamics.

As demonstrated by Figures 5.1(c) and 5.1(d), this R1 deflection allows the MES to trim at $\alpha \approx 20$ deg and $\beta \approx 5$ deg (i.e., C_m and C_n are both zero at this α-β combination). The PID controller should be modified to identify and issue the correct rib deflection according to the guidance command(s). It is evident from Figure 5.1(b) that non-zero roll moments also appear due to the diagonal rib deflection. Effective strategies for mitigating roll must also be explored to avoid impacting α and β tracking performance. These modifications would enable the evaluation of combined α and β control for DFC.

5.2.5 Drag Modulation Flight Control

As previously mentioned in Ch. 1, drag modulated aerocapture with a continuously variable system could even outperform a system employing traditional BAM control at several destinations including Mars. While this dissertation focused on DFC, the deployable-retractable nature of the MES is also well-suited for drag modulated aerocapture. Therefore, a future assessment of the MES as a drag modulation system is highly encouraged. For this application, all ribs of the MES are deflected by the same amount to change the drag area. Instead of using petal/rib deflections, the aerodynamics database would use the cone angle of the aeroshell as a query variable. This necessitates carrying out additional calculations with the tools discussed in Ch. 3. Furthermore, the PID controller would also need to be modified to issue cone angle instead of P1/P4 and R2/R5 deflections. The methods of gain tuning discussed before are also suggested to optimize drag modulation performance.

REFERENCES

[1] A. Klesh, B. Clement, C. Colley, *et al.*, "MarCO : Early Operations of the First CubeSats to Mars," *32nd Annual AIAA/USU Conference on Small Satellites*, pp. 1–6, 2018.

[2] NASA, "State-of-the-Art: Small Spacecraft Technology," Small Spacecraft Systems Virtual Institute, Ames Research Center, Tech. Rep. NASA/TP-2020-5008734, Oct. 2020.

[3] C. R. Mercer, "Small Satellite Missions for Planetary Science," *33nd Annual AIAA/USU Conference on Small Satellites*, 2019.

[4] D. Sweeney, C. Ao, P. Vergados, N. Rennó, D. Kass, and G. Martínez, "Enabling mars radio occultation by smallsats," in *2021 IEEE Aerospace Conference (50100)*, IEEE, 2021, pp. 1–12.

[5] R. J. Lillis, D. Mitchell, L. Montabone, *et al.*, "Mars orbiters for surface-atmosphere-ionosphere connections (mosaic)," in *AGU Fall Meeting 2020*, AGU, 2020.

[6] J. E. Graf, R. W. Zurek, H. J. Eisen, B. Jai, M. D. Johnston, and R. Depaula, "The Mars Reconnaissance Orbiter mission," *Acta Astronautica*, vol. 57, no. 2-8, pp. 566–578, 2005, ISSN: 00945765. DOI: 10.1016/j.actaastro.2005.03.043.

[7] G. A. Soffen and C. W. Snyder, "The First Viking Mission," *Science*, vol. 193, no. 4255, pp. 759–766, 1975. DOI: 10.1126/science.193.4255.759.

[8] S. Miller, M. L. Walker, J. Agolli, and J. Dankanich, "Survey and performance evaluation of small-satellite propulsion technologies," *Journal of Spacecraft and Rockets*, vol. 58, no. 1, pp. 222–231, 2021. DOI: 10.2514/1.A34774.

[9] A. Freeman, "Exploring our solar system with CubeSats and SmallSats: the dawn of a new era," *CEAS Space Journal*, vol. 12, no. 4, pp. 491–502, 2020. DOI: 10.1007/s12567-020-00298-5.

[10] S. S. Board, E. National Academies of Sciences, Medicine, *et al.*, *Achieving science with CubeSats: Thinking inside the box*. National Academies Press, 2016.

[11] D. A. Spencer and R. Tolson, "Aerobraking cost and risk decisions," *Journal of Spacecraft and Rockets*, vol. 44, no. 6, pp. 1285–1293, 2007.

[12] D. T. Lyons, J. G. Beerer, P. Esposito, M. D. Johnston, and W. H. Willcockson, "Mars Global Surveyor: Aerobraking mission overview," *Journal of Spacecraft and Rockets*, vol. 36, no. 3, pp. 307–313, 1999. DOI: 10.2514/2.3472.

[13] J. C. Smith and J. L. Bell, "2001 Mars Odyssey aerobraking," *Journal of Spacecraft and Rockets*, vol. 42, no. 3, pp. 406–415, 2005. DOI: 10.2514/1.15213.

[14] H. S. London, "Change of satellite orbit plane by aerodynamic maneuvering," *Journal of the Aerospace Sciences*, vol. 29, no. 3, pp. 323–332, 1962. DOI: 10.2514/8.9416.

[15] M. Cruz, "The aerocapture vehicle mission design concept," in *Conference on Advanced Technology for Future Space Systems*. American Institute of Aeronautics and Astronautics, 1979. DOI: 10.2514/6.1979-893.

[16] J. L. Hall, M. A. Noca, and R. W. Bailey, "Cost-benefit analysis of the aerocapture mission set," *Journal of Spacecraft and Rockets*, vol. 42, no. 2, pp. 309–320, 2005. DOI: 10.2514/1.4118.

[17] T. R. Spilker, M. Adler, N. Arora, *et al.*, "Qualitative assessment of aerocapture and applications to future missions," *Journal of Spacecraft and Rockets*, vol. 56, no. 2, pp. 536–545, 2019. DOI: 10.2514/1.A34056.

[18] E. M. Repic, M. G. Boobar, and F. G. Chapel, "Aerobraking as a potential planetary capture mode," *Journal of Spacecraft and Rockets*, vol. 5, no. 8, pp. 921–926, 1968. DOI: 10.2514/3.29389.

[19] H. S. Wright, D. Y. Oh, C. H. Westhelle, *et al.*, "Mars Aerocapture Systems Study," Tech. Rep. NASA/TM-2006-214522, Nov. 2006.

[20] H. J. Allen and A. J. Eggers Jr, "A study of the motion and aerodynamic heating of ballistic missiles entering the earth's atmosphere at high supersonic speeds," Tech. Rep. NACA Report 1381, 1958.

[21] T. K. West and A. M. Brandis, "Stagnation-point aeroheating correlations for mars entry," *Journal of Spacecraft and Rockets*, vol. 57, no. 2, pp. 319–327, 2020. DOI: 10.2514/1.A34602.

[22] "ESPA User's Guide," *Moog Space & Defense Group*, Nov. 2018. [Online]. Available: https://www.moog.com/content/dam/moog/literature/Space_Defense/spaceliterature/structures/moog-espa-users-guide-datasheet.pdf.

[23] A. M. Cassell, B. P. Smith, P. F. Wercinski, *et al.*, "ADEPT, A Mechanically Deployable Re-Entry Vehicle System, Enabling Interplanetary CubeSat and Small Satellite Missions," *Small Satellite Conference*, 2018. [Online]. Available: https://digitalcommons.usu.edu/cgi/viewcontent.cgi?article=4077&context=smallsat.

[24] R. A. Dillman, A. Slagle, A. M. Korzun, R. A. Lugo, and A. M. Dwyer-Cianciolo, "Low lift-to-drag morphing shape design," in *AIAA Scitech 2020 Forum*, Jan. 2020.

[25] *Low-Earth Orbit Flight Test of an Inflatable Decelerator (LOFTID)*, https://www.nasa.gov/mission_pages/tdm/loftid/index.html, Accessed: Dec 21, 2021.

[26] A. M. Dwyer-Cianciolo, R. A. Dillman, A. J. Brune, *et al.*, "Human mars entry, descent and landing architecture study: Deployable decelerators," *2018 AIAA SPACE and Astronautics Forum and Exposition*, 2018. DOI: 10.2514/6.2018-5191.

[27] A. M. Cassell, P. F. Wercinski, B. P. Smith, *et al.*, "Adept sounding rocket one flight test overview," *AIAA Aviation 2019 Forum*, 2019. DOI: 10.2514/6.2019-2896.

[28] C. A. Graves and J. C. Harpold, "Apollo Experience Report: Mission Planning for Apollo Entry," Tech. Rep. TN D-6725, Mar. 1972.

[29] J. C. Harpold and C. A. Graves, "Shuttle Entry Guidance," Tech. Rep. TM-79949, Feb. 1979.

[30] G. F. Mendeck and L. Craig McGrew, "Entry guidance design and postflight performance for 2011 mars science laboratory mission," *Journal of Spacecraft and Rockets*, vol. 51, no. 4, pp. 1094–1105, 2014. DOI: https://doi.org/10.2514/1.A32737.

[31] A. Nelessen, C. Sackier, I. Clark, *et al.*, "Mars 2020 entry, descent, and landing system overview," in *2019 IEEE Aerospace Conference*, 2019. DOI: 10.1109/AERO.2019.8742167.

[32] A. Alunni, S. N. D'Souza, B. Yount, *et al.*, "Pterodactyl: Trade study for an integrated control system design of a mechanically deployed entry vehicle," in *AIAA SciTech 2020 Forum*, Jan. 2020. DOI: 10.2514/6.2020-1014.

[33] Z. R. Putnam and R. D. Braun, "Drag-modulation flight-control system options for planetary aerocapture," *Journal of Spacecraft and Rockets*, vol. 51, no. 1, pp. 139–150, 2014. DOI: 10.2514/1.A32589.

[34] R. R. Rohrschneider and R. D. Braun, "Survey of ballute technology for aerocapture," *Journal of Spacecraft and Rockets*, vol. 44, no. 1, pp. 10–23, 2007. DOI: 10.2514/1.19288.

[35] S. Hughes, R. Dillman, B. Starr, *et al.*, "Inflatable re-entry vehicle experiment (irve) design overview," in *18th AIAA aerodynamic decelerator systems technology conference and seminar*, 2005.

[36] A. Austin, A. Nelessen, B. Strauss, *et al.*, "Smallsat aerocapture to enable a new paradigm of planetary missions," in *2019 IEEE Aerospace Conference*, 2019. DOI: 10.1109/AERO.2019.8742220.

[37] M. S. Werner and R. D. Braun, "Mission design and performance analysis of a smallsat aerocapture flight test," *Journal of Spacecraft and Rockets*, vol. 56, no. 6, pp. 1704–1713, 2019. DOI: 10.2514/1.A33997.

[38] G. Falcone, J. Williams, and Z. Putnam, "Assessment of aerocapture for orbit insertion of small satellites at mars," *Journal of Spacecraft and Rockets*, vol. 56, no. 6, pp. 1689–1703, 2019. DOI: https://doi.org/10.2514/1.A34444.

[39] E. Roelke and R. Braun, "Discrete-event drag-modulated guidance performance for venus aerocapture," *Journal of Spacecraft and Rockets*, vol. 58, no. 1, pp. 190–199, 2021. DOI: 10.2514/1.a34761.

[40] E. Roelke, J. W. McMahon, and P. D. Hattis, "Multi-event drag modulation aerocapture guidance under uncertainty," in *AAS/AIAA Astrodynamics Specialist Conference*, 2020.

[41] R. Deshmukh, J. V. Cabrera, and D. Spencer, "Smallsat aerocapture using a generalized numerical predictor corrector guidance architecture," in *AIAA Scitech 2021 Forum*, 2021.

[42] A. Dwyer Cianciolo and R. W. Powell, "Entry, descent, and landing guidance and control approaches to satisfy mars human mission landing criteria," in *AAS/AIAA Space Flight Mechanics Meeting*, 2017.

[43] R. G. Deshmukh, D. A. Spencer, and S. Dutta, "Investigation of direct force control for aerocapture at Neptune," *Acta Astronautica*, vol. 175, pp. 375–386, Feb. 2020. DOI: 10.1016/j.actaastro.2020.05.047.

[44] M. K. Lockwood, B. R. Starr, D. A. Kontinos, *et al.*, "Aerocapture Systems Analysis for a Neptune Mission," Tech. Rep. TM-2006-214300, Apr. 2006.

[45] D. A. Matz and C. Cerimele, "Development of a numeric predictor-corrector aerocapture guidance for direct force control," in *AIAA Scitech 2020 Forum*, 2020. DOI: 10.2514/6.2020-0847.

[46] D. A. Matz, C. Cerimele, and R. R. Sostaric, "Comparison of aerocapture performance using bank control and direct force control with two human-scale vehicles at mars," in *AIAA Scitech 2020 Forum*, 2020. DOI: 10.2514/6.2020-1738.

[47] A. D. Olds, R. E. Beck, D. M. Bose, *et al.*, "IRVE-3 post-flight reconstruction," in *AIAA Aerodynamic Decelerator Systems Conference*, 2013. DOI: 10.2514/6.2013-1390.

[48] W. Okolo, B. Margolis, S. D'Souza, and J. Barton, "Pterodactyl: Development and comparison of control architectures for a mechanically deployed entry vehicle," in *AIAA SciTech 2020 Forum*, 2020. DOI: 10.2514/6.2020-1012.

[49] B. Yount, A. Cassell, and S. D'Souza, "Pterodactyl: Mechanical designs for integrated control design of a mechanically deployable entry vehicle," in *AIAA SciTech 2020 Forum*, 2020. DOI: 10.2514/6.2020-1009.

[50] R. I. Sammonds and R. R. Dickey, "Effectiveness of several control arrangements on a mercury-type capsule," Tech. Rep. NASA TM X-579, 1961.

[51] L. Neal Jr, "An exploratory investigation at a mach number of 6.9 into the use of aerodynamic controls for modulating the lift-drag ratio of an apollo type configuration," Tech. Rep. NASA TM X-816, May 1963.

[52] M. C. Ivanov, E. M. Blood, B. T. Cook, *et al.*, "Entry, Descent and Landing Systems analysis study: Phase 2 Report on Mars Science Laboratory Improvement," Tech. Rep. NASA TM-2011-216988, Jan. 2011.

[53] Z. B. Hays, B. Yount, B. Nikaido, *et al.*, "Pterodactyl: Thermal protection system for integrated control design of a mechanically deployed entry vehicle," in *AIAA SciTech 2020 Forum*, 2020. DOI: 10.2514/6.2020-1013.

[54] B. W. Margolis, W. A. Okolo, B. E. Nikaido, J. D. Barton, and S. N. D'Souza, "Control and simulation of a deployable entry vehicle with aerodynamic control surfaces," in *AAS/AIAA Astrodynamics Specialist Conference*, 2019.

[55] S. Reza, R. Hund, F. Kustas, *et al.*, "Aerocapture inflatable decelerator (aid) for planetary entry," in *19th AIAA Aerodynamic Decelerator Systems Technology Conference and Seminar*, 2007. DOI: 10.2514/6.2007-2516.

[56] J. S. Green, "Morphing hypersonic inflatable aerodynamic decelerator," M.S. thesis, University of Virginia, Charlottesville, VA, 2012.

[57] J. S. Green, R. E. Lindberg, and B. J. Dunn, "Morphing hypersonic inflatable aerodynamic decelerator," in *AIAA Aerodynamic Decelerator Systems Conference*, 2013. DOI: 10.2514/6.2013-1256.

[58] A. C. M. Slagle, "Morphing hypersonic inflatable aerodynamic decelerator (hiad) mechanisms and controls," Ph.D. dissertation, Virginia Polytechnic Institute and State University, Blacksburg, VA, 2018.

[59] B. Smith, B. Yount, C. Kruger, *et al.*, "Nano-ADEPT aeroloads wind tunnel test," in *IEEE Aerospace Conference Proceedings*, 2016. DOI: 10.1109/AERO.2016.7500719.

[60] R. Deshmukh, "System analysis of a numerical predictor-corrector aerocapture guidance architecture," Ph.D. dissertation, Purdue University, West Lafayette, Indiana, May 2021.

[61] W. M. Wood, "Thermonasty in tulip and crocus flowers," *Journal of Experimental Botany*, vol. 4, no. 1, pp. 65–77, 1953. DOI: 10.1093/jxb/4.1.65.

[62] B. Smith, A. Cassell, C. Kruger, E. Venkatapathy, C. Kazemba, and K. Simonis, "Nano-ADEPT: An entry system for secondary payloads," in *IEEE Aerospace Conference Proceedings*, 2015. DOI: 10.1109/AERO.2015.7119095.

[63] D. A. Spencer, R. C. Blanchard, R. D. Braun, P. H. Kallemeyn, and S. W. Thurman, "Mars Pathfinder entry, descent, and landing reconstruction," *Journal of Spacecraft and Rockets*, vol. 36, no. 3, pp. 357–366, 1999. DOI: 10.2514/2.3478.

[64] C. D. Karlgaard, P. Kutty, M. Schoenenberger, *et al.*, "Mars science laboratory entry atmospheric data system trajectory and atmosphere reconstruction," *Journal of Spacecraft and Rockets*, vol. 51, no. 4, pp. 1029–1047, 2014. DOI: 10.2514/1.A32770.

[65] J. O. Arnold, K. H. Peterson, B. C. Yount, N. Schneider, and J. Chavez-Garcia, "Thermal and structural performance of woven carbon cloth for adaptive deployable entry and placement technology," in *AIAA Aerodynamic Decelerator Systems Technology Conference*, 2013. DOI: 10.2514/6.2013-1370.

[66] J. A. Del Corso, W. E. Bruce III, S. J. Hughes, *et al.*, "Flexible thermal protection system development for hypersonic inflatable aerodynamic decelerators," in *9th International Planetary Probe Workshop*, 2012.

[67] K. D. Hicks, *Introduction to Astrodynamic Reentry*, Second. CreateSpace, 2014.

[68] N. X. Vinh, A. Busemann, and R. D. Culp, *Hypersonic and Planetary Entry Flight Mechanics.* The University of Michigan Press, 1980.

[69] D. T. Greenwood, *Principles of Dynamics.* Prentice-Hall, 1988.

[70] P. A. Gnoffo, R. D. Braun, K. J. Weilmuenster, R. A. Mitcheltree, W. C. Engelund, and R. W. Powell, "Prediction and validation of Mars Pathfinder hypersonic aerodynamic database," *Journal of Spacecraft and Rockets*, vol. 36, no. 3, pp. 367–373, 1999. DOI: 10.2514/2.3455.

[71] A. Dyakonov, M. Schoenenberger, and J. Van Norman, "Hypersonic and supersonic static aerodynamics of mars science laboratory entry vehicle," in *43rd AIAA Thermophysics Conference*, 2012. DOI: https://doi.org/10.2514/6.2012-2999.

[72] R. A. Mitcheltree, J. N. Moss, F. M. Cheatwood, F. A. Greene, and R. D. Braun, "Aerodynamics of the Mars Microprobe entry vehicles," *Journal of Spacecraft and Rockets*, vol. 36, no. 3, pp. 392–398, 1999. DOI: 10.2514/2.3458.

[73] G. J. Bobskill, P. C. Parikh, R. K. Prabhu, and E. D. Tyler, "Aerodynamic database development for Mars Smart Lander vehicle configurations," *Journal of Spacecraft and Rockets*, vol. 43, no. 2, pp. 303–310, 2006. DOI: 10.2514/1.19223.

[74] W. L. Wells, "Measured and predicted aerodynamic coefficients and shock shapes for aeroassist flight experiment (afe) configuration," Tech. Rep. NASA TP-2956, Jan. 1990.

[75] R. W. Powell and R. D. Braun, "Six-degree-of-freedom guidance and control analysis of mars aerocapture," *Journal of Guidance, Control, and Dynamics*, vol. 16, no. 6, pp. 1038–1044, 1993. DOI: 10.2514/3.21125.

[76] A. M. Korzun, S. Dutta, R. D. McDaniel, C. D. Karlgaard, and J. A. Tynis, "Aerodynamics for the adept sr-1 flight experiment," in *AIAA Aviation 2019 Forum*, 2019. DOI: 10.2514/6.2019-2897.

[77] B. Nikaido, Z. B. Hays, and B. J. Reddish, "Pterodactyl: Aerodynamic and aeroheating database development for integrated control design of a mechanically deployed entry vehicle," in *AIAA SciTech 2020 Forum*, 2020. DOI: https://doi.org/10.2514/6.2020-1010.

[78] B. Reddish, V. M. Hawke, Z. B. Hays, H. Kang, and S. N. D'Souza, "Pterodactyl: Aerodynamic and aeroheating model for a symmetric deployable entry vehicle with flaps," in *AIAA SciTech 2021 Forum*, 2021. DOI: https://doi.org/10.2514/6.2021-0763.

[79] J. D. Anderson, *Introduction to Flight*, Sixth. New York: McGraw-Hill, 2008.

[80] G. A. Bird, *Molecular gas dynamics and the direct simulation of gas flows*, ser. Oxford Engineering Science Series. New York: Oxford University Press, 1994.

[81] G. A. Bird, "Approach to translational equilibrium in a rigid sphere gas," *The Physics of Fluids*, vol. 6, no. 10, pp. 1518–1519, 1963. DOI: 10.1063/1.1710976.

[82] K. Koura and H. Matsumoto, "Variable soft sphere molecular model for inverse-power-law or lennard-jones potential," *Physics of Fluids*, vol. 3, pp. 2459–2465, 1991.

[83] K. Koura and H. Matsumoto, "Variable soft sphere molecular model for air species," *Physics of Fluids*, vol. 4, pp. 1083–1085, 1992.

[84] R. G. Wilmoth, R. C. Blanchard, and J. N. Moss, "Rarefied transitional bridging of blunt body aerodynamics," *21st International Symposium on Rarefied Gas Dynamics*, 1998.

[85] J. V. Cabrera, R. Deshmukh, and D. Spencer, "Aerodynamic database development using a bridging function for a conceptual morphable entry system," *AIAA Scitech 2021 Forum*, 2021. DOI: 10.2514/6.2021-0935.

[86] J. V. Cabrera, R. G. Deshmukh, and D. A. Spencer, "Aerodynamics database for aerocapture of a conceptual morphable entry system at mars," *Journal of Spacecraft and Rockets*, vol. 59, no. 2, pp. 674–684, 2022. DOI: 10.2514/1.A35110.

[87] M. Ivanov, G. Markelov, S. Gimelshein, L. Mishina, A. Krylov, and N. Grechko, "High-altitude capsule aerodynamics with real gas effects," *Journal of Spacecraft and Rockets*, vol. 35, no. 1, pp. 16–22, 1998.

[88] K. A. Hart, S. Dutta, K. Simonis, B. A. Steinfeldt, and R. D. Braun, "Analytically-derived aerodynamic force and moment coefficients of resident space objects in free-molecular flow," in *AIAA Atmospheric Flight Mechanics Conference*. 2014. DOI: 10.2514/6.2014-0728.

[89] K. A. Hart, K. R. Simonis, B. A. Steinfeldt, and R. D. Braun, "Analytic free-molecular aerodynamics for rapid propagation of resident space objects," *Journal of Spacecraft and Rockets*, vol. 55, no. 1, pp. 27–36, 2018. DOI: 10.2514/1.A33606.

[90] J. Moss, C. Glass, and F. Greene, "Dsmc simulations of apollo capsule aerodynamics for hypersonic rarefied conditions," in *9th AIAA/ASME Joint Thermophysics and Heat Transfer Conference*. 2006. DOI: 10.2514/6.2006-3577.

[91] J. N. Moss, R. C. Blanchard, R. G. Wilmoth, and R. D. Braun, "Mars Pathfinder rarefied aerodynamics: Computations and measurements," *Journal of Spacecraft and Rockets*, vol. 36, no. 3, pp. 330–339, 1999. DOI: 10.2514/2.3475.

[92] S. J. Plimpton, S. G. Moore, A. Borner, *et al.*, "Direct simulation Monte Carlo on petaflop supercomputers and beyond," *Physics of Fluids*, vol. 31, no. 8, 2019. DOI: 10.1063/1.5108534.

[93] J. N. Moss, R. G. Wilmoth, and J. M. Price, "Dsmc simulations of blunt body flows for mars entries - mars pathfinder and mars microprobe capsules," in *32nd AIAA Thermophysics Conference*, 1997.

[94] J. N. Moss, R. C. Blanchard, R. G. Wilmoth, and R. D. Braun, "Mars Pathfinder Rarefied Aerodynamics: Computations and Measurements," in *36th AIAA Aerospace Science Meeting and Exhibit*, 1998.

[95] D. B. Hash and H. A. Hassan, "Monte Carlo simulation of entry in the martian atmosphere," *Journal of Thermophysics and Heat Transfer*, vol. 7, no. 2, pp. 228–232, 1993. DOI: 10.2514/3.411.

[96] J. N. Moss, R. G. Wilmoth, and J. M. Price, "Direct simulation Monte Carlo calculations of aerothermodynamics for Mars Microprobe capsules," *Journal of Spacecraft and Rockets*, vol. 36, no. 3, pp. 399–404, 1999. DOI: 10.2514/2.3459.

[97] C. G. Justus and R. D. Braun, "Atmospheric environments for entry, descent and landing (edl)," in *5th International Planetary Probes Workshop and Short Course*, 2007.

[98] K. B. Thompson, R. R. Hollis, A. Mazaheri, V. R. Lessard, C. O. Johnston, and B. Kleb, "Laura Users Manual : 5.6," Tech. Rep. NASA/TM-2020-220566, Feb. 2020.

[99] J. D. Anderson, *Hypersonic and High-Temperature Gas Dynamics*, Third. Reston, Virginia: American Institute of Aeronautics and Astronautics, 2019.

[100] K. T. Edquist, P. N. Desai, and M. Schoenenberger, "Aerodynamics for Mars Phoenix entry capsule," *Journal of Spacecraft and Rockets*, vol. 48, no. 5, pp. 713–726, 2011. DOI: 10.2514/1.46219.

[101] L. Lees, "Hypersonic Flow," *Journal of Spacecraft and Rockets*, vol. 40, no. 5, pp. 700–735, 2003. DOI: 10.2514/2.6897.

[102] M. Grant and R. Braun, "Analytic hypersonic aerodynamics for conceptual design of entry vehicles," in *48th AIAA Aerospace Sciences Meeting Including the New Horizons Forum and Aerospace Exposition*, 2010. DOI: 10.2514/6.2010-1212.

[103] B. J. Griffith and D. E. Boylan, "Postflight apollo command module aerodynamic simulation tests," *Journal of Spacecraft and Rockets*, vol. 5, no. 7, pp. 843–848, 1968. DOI: 10.2514/3.29368.

[104] P. A. Gnoffo, K. J. Weilmuenster, R. D. Braun, and C. I. Cruz, "Influence of sonic-line location on Mars Pathfinder Probe aerothermodynamics," *Journal of Spacecraft and Rockets*, vol. 33, no. 2, pp. 169–177, 1996. DOI: 10.2514/3.26737.

[105] B. Margolis, W. Okolo, S. N. D'Souza, and B. J. Johnson, "Pterodactyl: Guidance and Control of a Symmetric Deployable Entry Vehicle using an Aerodynamic Control System," in *AIAA Scitech 2021 Forum*, 2021. DOI: 10.2514/6.2021-0764.

[106] P. Brugarolas, A. S. Martin, and E. Wong, "Attitude controller for the atmospheric entry of the mars science laboratory," in *AIAA Guidance, Navigation and Control Conference and Exhibit*, 2008. DOI: 10.2514/6.2008-6812.

[107] B. J. Johnson, C. J. Cerimele, S. Stachowiak, R. R. Sostaric, D. A. Matz, and P. Lu, "Mid-lift-to-drag ratio rigid vehicle control system design and simulation for human mars entry," in *2018 AIAA Guidance, Navigation, and Control Conference*, 2018. DOI: 10.2514/6.2018-0615.

[108] K. Sutton and R. A. Graves Jr, "A general stagnation-point convective heating equation for arbitrary gas mixtures," Tech. Rep. NASA TR R-376, Nov. 1971.

[109] C. Justus, A. Duvall, and V. Keller, "Atmospheric models for aerocapture systems studies," in *AIAA Atmospheric Flight Mechanics Conference and Exhibit*, 2004. DOI: 10.2514/6.2004-4952.

[110] S. N. D'Souza, A. Alunni, B. Yount, *et al.*, "Pterodactyl: System analysis of an asymmetric and symmetric deployable entry vehicle for precision targeting using flaps," in *AIAA SciTech 2021 Forum*, 2021. DOI: 10.2514/6.2021-0762.

[111] J. V. Cabrera and D. A. Spencer, "Dispersion analysis of small satellite aerocapture at mars using a morphable entry system," in *AIAA SciTech 2022 Forum*, 2022. DOI: 10.2514/6.2022-1654.

[112] S. Dutta, C. D. Karlgaard, A. M. Korzun, *et al.*, "Adaptable deployable entry and placement technology sounding rocket one modeling and reconstruction," *Journal of Spacecraft and Rockets*, vol. 59, no. 1, pp. 236–259, 2022. DOI: 10.2514/1.a35090.

[113] T. J. Martin-Mur, G. L. Kruizinga, P. D. Burkhart, F. Abilleira, M. C. Wong, and J. A. Kangas, "Mars science laboratory interplanetary navigation," *Journal of Spacecraft and Rockets*, vol. 51, no. 4, pp. 1014–1028, 2014. DOI: 10.2514/1.A32631.

[114] Y. K. Chen and F. S. Milos, "Multidimensional finite volume fully implicit ablation and thermal response code," *Journal of Spacecraft and Rockets*, vol. 55, no. 4, pp. 914–927, 2018. DOI: 10.2514/1.A34184.

[115] H. D. Curtis, *Orbital Mechanics for Engineering Students*, Third. Elsevier Ltd., 2014.

A. DSMC MODELING PARAMETERS

Modeling assumptions and constants associated with the DSMC simulations are presented in this section.

A.1 COSPAR temperature vs. altitude data

COSPAR temperature data included in Ref. was fitted to generate the following fourth-order polynomial expression used to estimate the ambient freestream temperature (T_∞) given the altitude (h):

$$T_\infty(h) = 1.7572\text{E-06}\,h^4 - 3.5296\text{E-04}\,h^3 + 3.0818\text{E-02}\,h^2 - 2.1288\,h + 218.30 \qquad \text{(A.1)}$$

where the altitude must be in kilometers and the temperature is returned in Kelvin. T_∞ is required to compute mean free path and the thermal speed of the gas, which are both needed to compute the DSMC simulation time step.

A.2 Constants

The constants listed in this section were used to compute input variables to the SPARTA solver, including mean free path and simulation timestep.

Table A.1. Constants related to DSMC calculations

Constant	Symbol	Value
Avogadro's constant	N_A	6.022E23 parts/mole
Boltzmann constant	k_B	1.3806E-23 m^2 kg s^{-2} K^{-1}
Emissivity (PICA TPS)	ε	0.80
Stefan-Boltzmann constant	σ	5.67E-08 W m^{-2} K^{-4}

Table A.2. Constants related to the CO_2 species

Quantity	Value
Molar mass	0.04401 kg/mol
Mass (1 molecule)	7.306E-26 kg
Molecular diameter (1 atm, 273 K)	5.54E-10 m
Viscosity index (1 atm, 273 K)	0.93
Ideal gas constant	188.92 J/kg/K
Ratio of specific heats	1.33

A.3 Chemical Species Properties

This section lists more properties associated with the carbon dioxide (CO_2) and nitrogen (N_2) species that make up the flow mixtures assumed for DSMC calculations. Note that the rotational and vibrational data are used by the SPARTA solver to perform molecular collisions between species.

Table A.3. CO_2 properties

Property	Value
Rotational DOF	2
Rotational relaxation number	5
Vibrational DOF	6
Vibrational relaxation number	50
Vibrational temperature (K)	959

Table A.4. N_2 properties

Property	Value
Molar mass	0.02802 kg/mol
Mass (1 molecule)	4.65E-26 kg
Rotational DOF	2
Rotational relaxation number	5
Vibrational DOF	2
Vibrational relaxation number	50
Vibrational temperature (K)	3371.0

B. AERODYNAMIC HEATING

Aerodynamic heating impacts the design of aerospace vehicles. For preliminary design purposes, estimates of stagnation point convective and radiative heating can be computed using engineering correlations. This dissertation utilized the Sutton-Graves correlation for generating first-order estimates of the stagnation point convective heat rate ($\dot{q}_c$) on the MES. The Sutton-Graves correlation is formulated as follows:

$$\dot{q}_c = K \left(\frac{\rho_\infty}{R_n}\right)^{1/2} V_\infty^3 \tag{B.1}$$

where K is the Sutton-Graves constant, ρ_∞ is the freestream density, R_n is the nose radius of the vehicle, and V_∞ is the freestream velocity. The constant K is dependent on the chemical composition of the flow mixture and is therefore dependent on the planetary atmosphere. At Mars, $K = 1.9\text{E-}04$ kg$^{1/2}$/m. Note that $R_n = 0.30$ m for the MES.

An updated stagnation point radiative heating correlation for Mars entry flows was developed by West and Brandis [21] has the following functional form:

$$\dot{q}_r = \mathrm{e}^{f(V, \ln(\rho), R_n)} \tag{B.2}$$

where $\dot{q}_r$ is the radiative heat rate, V is the freestream velocity, ρ is the freestream density, and R_n is the nose radius of the vehicle. The function f is a fourth-order polynomial whose coefficients are provided in Table 3 of Ref. [21]. Using the West-Brandis correlation, the stagnation point radiative heat rate history for Case 1 (no dispersions) was estimated and compared to the convective heat rate. As illustrated by Figure B.1, the radiative heat rate is smaller than the convective heat rate by two orders of magnitude. This justifies neglecting radiative heating in this research.
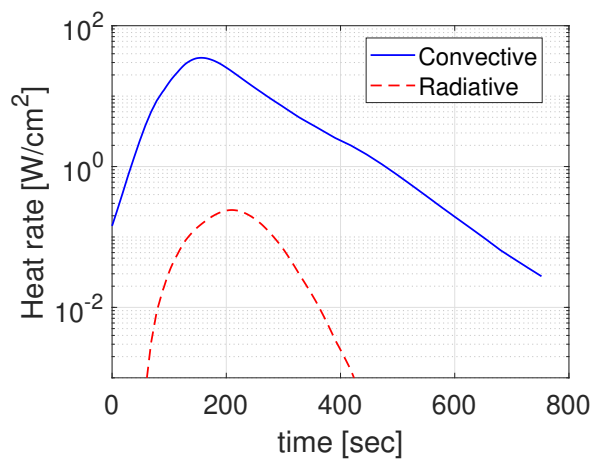
Figure B.1. Comparison of stagnation point convective and radiative heat rates for Case 1.

C. MONTE CARLO DISCUSSION

Supplemental discussion regarding the Monte Carlo results are included in this section.

C.1 Simulated Perturbations

The distribution of the dispersed entry flight path angle (γ_E) is shown in Figure C.1(a). The distribution of the sampled *rpscale* values is shown in Figure C.1(b).

(a) γ_E (mean, $\gamma_E = -10.33$ deg)

(b) *rpscale* (nominal, *rpscale*=0)
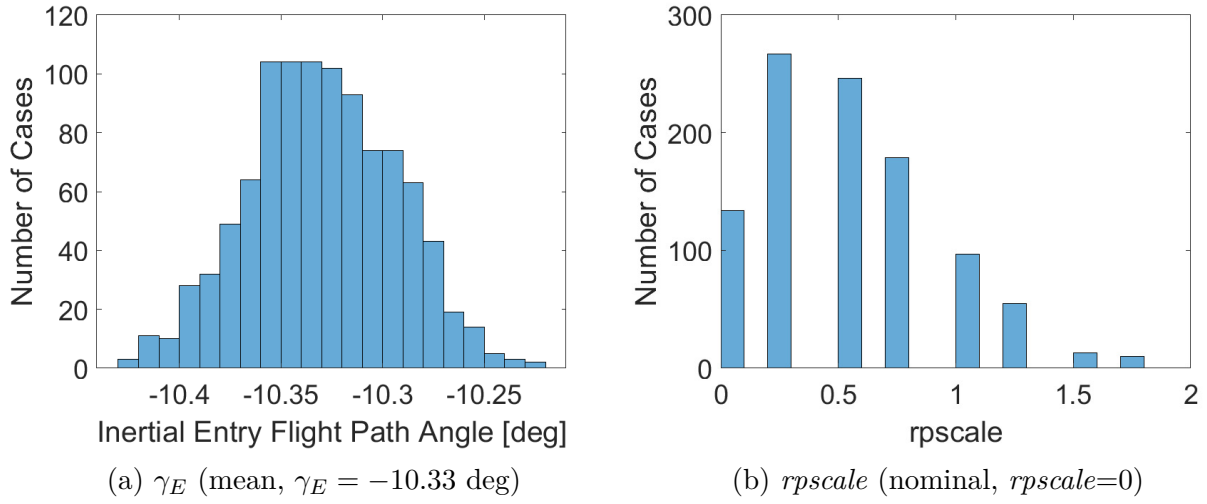
Figure C.1. The dispersed values of the entry flight path angle and *rpscale*.

C.2 Impact of Perturbations

The dispersed entry flight path angle (γ_E) can impact the periapsis altitude (h_p) and apoapsis targeting performance of an aerocapture vehicle. Figure C.2 below demonstrates that steeper (more negative) entries correspond with more negative periapsis altitudes and apoapsis errors. This is expected because the MES penetrates deeper into the Martian atmosphere and loses more energy due to the increased atmospheric drag. The resulting transfer orbit has a smaller apoapsis altitude that does not quite reach the target value of 400 km, hence the large negative apoapsis error (a_{err}) values corresponding with the steeper entries.

(a) Periapsis altitude

(b) Apoapsis error
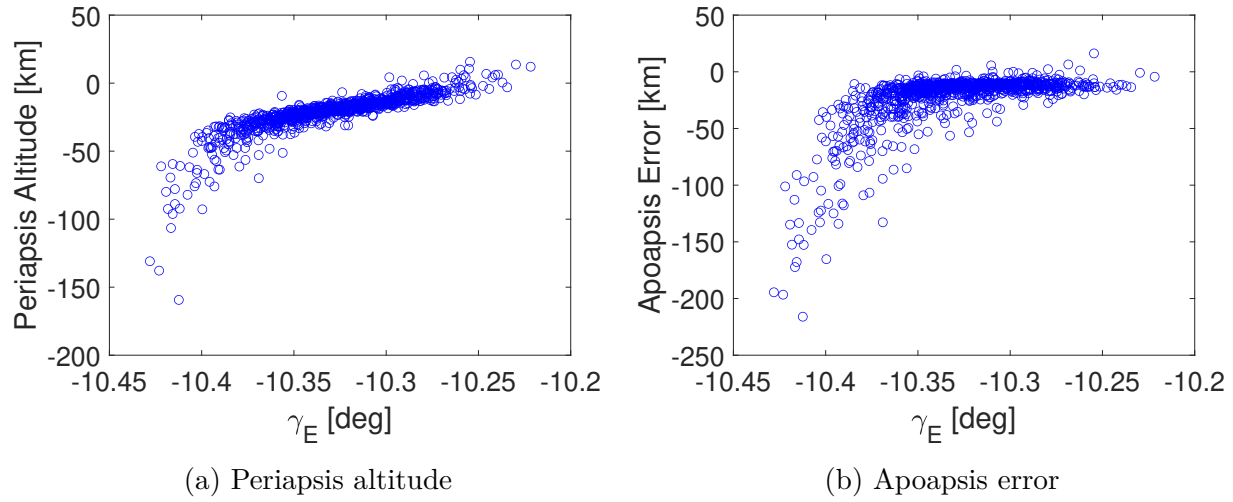
Figure C.2. Impact of dispersed entry flight path angle (Nominal value, γ_E =-10.33 deg).

Figure C.3 shows the impact of the dispersed atmospheric density profile on h_p and a_{err}. It can be observed that increased density perturbations did not greatly affect h_p and a_{err} values. For example, there were cases that flew in a nominal atmosphere (*rpscale*=0) that undershot the target apoapsis by as much as other cases that flew in a perturbed atmosphere (non-zero *rpscale*).
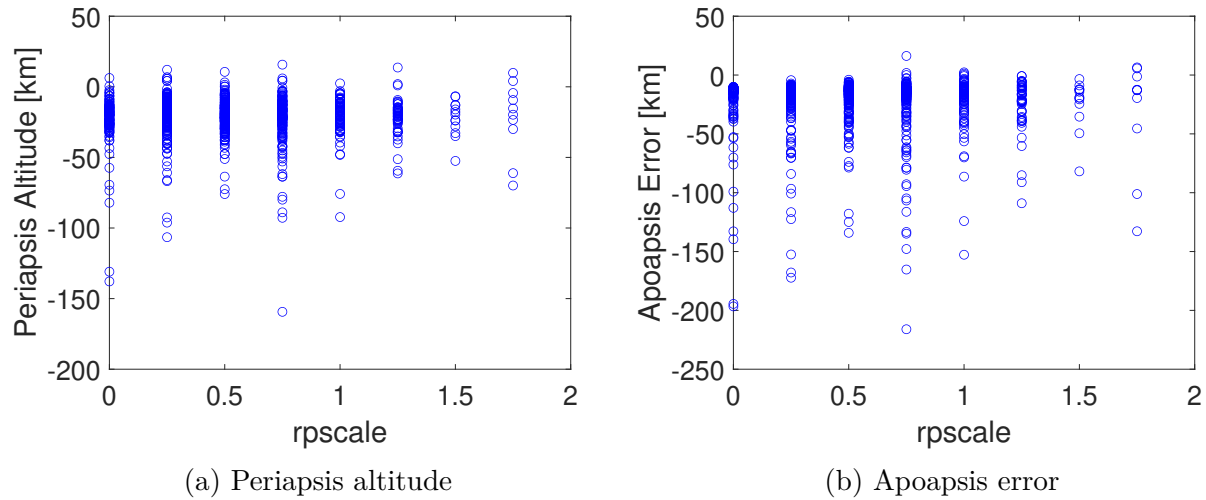

(a) Periapsis altitude

(b) Apoapsis error

Figure C.3. Impact of dispersed density profile (Nominal value, rpscale=0).

Figure C.4 shows the impact of perturbed C_m values on h_p and a_{err}. Once again, neither is heavily impacted by dispersions in C_m as cases with reduced pitching capability (multiplier

less than 1) undershot the target apoapsis by as much as cases with increased pitching capability (multiplier greater than 1).

(a) Periapsis altitude (b) Apoapsis error
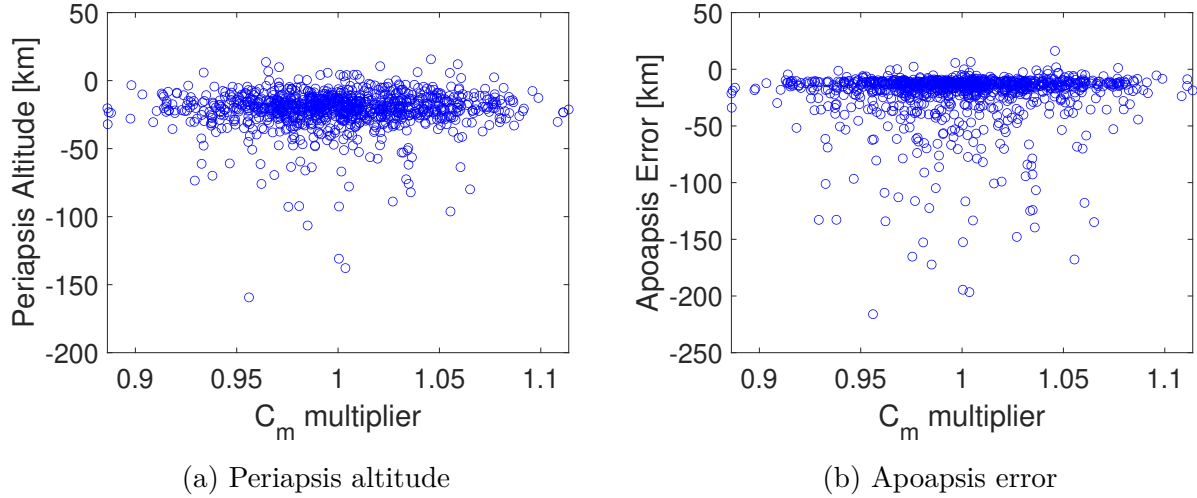
Figure C.4. Impact of dispersed pitch moment coefficient multiplier (Nominal value, 1.0).

C.3 Law of Large Numbers

Sample sizes for Monte Carlo simulations tend to be large to ensure that the results are statistically meaningful. In this dissertation, 1001 cases were run to ensure proper distribution of the environmental uncertainties. To verify that this sample size is large enough, the average of the apoapsis error and periapsis altitude values from all cases were plotted against the sample number as shown in Figure C.5. It can be observed from Figure C.5(a) that the mean apoapsis error approaches the overall sample mean indicated in Table 4.7 as the sample number grew. This is a representation of the law of large numbers, which states that the mean value of a result of interest approaches its expected mean value as more trials are performed. The same "flat-lining" behavior can be observed for the periapsis altitude in Figure C.5(b). These results provide qualitative verification that the sample size used in this investigation is large enough for the reported sample means to be close to their expected values.
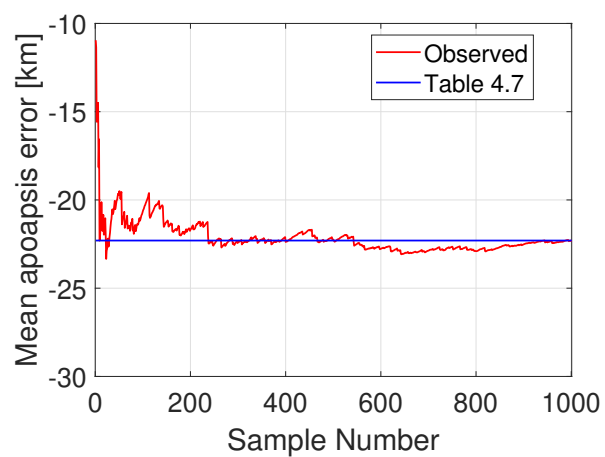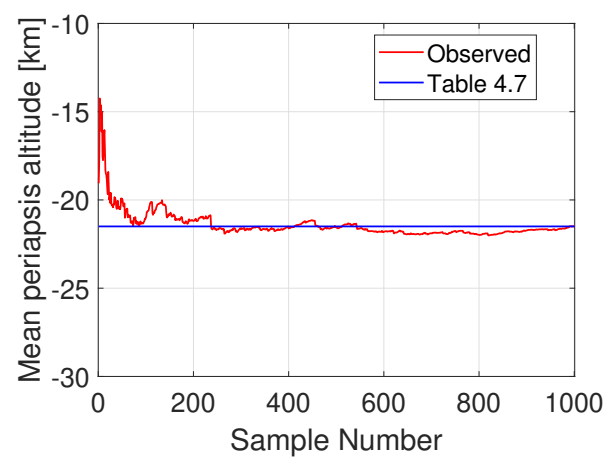
(a) Apoapsis error   (b) Periapsis altitude

Figure C.5. Mean values of apoapsis error and periapsis altitude.

D. PANEL CODE LISTING

This section lists the Python source codes for the modified Newtonian and free molecular aerodynamics panel methods.

D.1   Modified Newtonian Source Code

Below is the Python source code for the modified Newtonian panel method, `newtonPanel.py`, described in Chapter 3.

```python
#!/usr/bin/env python2
# -*- coding: utf-8 -*-
"""
Created on Sun Nov  3 13:41:05 2019

@author: jannuel v. cabrera, jannuel.cabrera@gmail.com
"""

''' This is a panel method that computes the aerodynamic force coefficients
[CA, CS, CN] using Newtonian flow theory for hypersonic flow.'''

import numpy as np
from stl import mesh
import math
'''numpy-stl must be installed on the machine; pip install numpy-stl==2.10.1
    '''

def returnNormal(stlfilename):
    # return the outward unit normal vectors of each facet
    myMesh = mesh.Mesh.from_file(stlfilename)
    return -myMesh.units #return inward unit normal for Newtonian flow
    purposes

def returnAreas(stlfilename):
    # return area of each facet
    myMesh = mesh.Mesh.from_file(stlfilename)
```

```python
25      return myMesh.areas
26  '''to compute moments, need to compute stl surf element centers and the moment
         arm'''
27  def returnv0(stlfilename):
28      # returns the position vectors of the first vertex of each surface element
29      myMesh = mesh.Mesh.from_file(stlfilename)
30      return myMesh.v0
31
32  def returnv1(stlfilename):
33      # returns the position vectors of the second vertex of each surface
        element
34      myMesh = mesh.Mesh.from_file(stlfilename)
35      return myMesh.v1
36
37  def returnv2(stlfilename):
38      # returns the position vectors of the third vertex of each surface element
39      myMesh = mesh.Mesh.from_file(stlfilename)
40      return myMesh.v2
41
42  def computeCentroid(v0,v1,v2,ith_element):
43      # computes the coordinates of the centroid of the ith surface element
44      # see https://www.mathopenref.com/coordcentroid.html for reference on
        computing the centroid of a triangle
45      #v0 = myMesh.v0 # vertex 1
46      #v1 = myMesh.v1 # vertex 2
47      #v2 = myMesh.v2 # vertex 3
48      i=ith_element
49
50      Cx = (v0[i][0] + v1[i][0] + v2[i][0])/3
51      Cy = (v0[i][1] + v1[i][1] + v2[i][1])/3
52      Cz = (v0[i][2] + v1[i][2] + v2[i][2])/3
53
54      return [Cx,Cy,Cz] #centroid coordinates of the ith element in the stl file
55
56  def computeMomentArm(centroid_i,r_MRP):
57      # centroid_i == position vector of the ith surface element's centroid
```

191

```python
58      # r_MRP == position vector of the moment reference point (MRP)
59      momentArm = centroid_i-r_MRP
60      return momentArm
61
62  '''functions for application of Newtonian sine-squared law'''
63  def computeCpmax(Mach,gamma):
64      A=math.pow((((gamma+1)**2*Mach**2/(4*gamma*Mach**2-2*(gamma-1)))),(gamma/(
        gamma-1)))
65      B=(1-gamma+2*gamma*Mach**2)/(gamma+1)
66      cpmax=(2/gamma/Mach**2)*(A*B-1)
67      return cpmax
68
69  def computeCp(Vinf,facetNormal,Mach,gamma):
70      cpmax = computeCpmax(Mach,gamma) # reasonably accurate for large Mach
        numbers
71      shadow_check=np.dot(Vinf,facetNormal)
72      if shadow_check <= 0.0:
73          Cp = 0.0 #flow shadowing (a.k.a hypersonic shielding)
74      else:
75          Cp = cpmax*(shadow_check)**2 # Newtonian cosine-squared law
76
77      return Cp
78
79  '''force computation functions'''
80  def dCA(Cp,nx,dA): # differential axial force coefficient contribution of a
        surface element
81      return Cp*nx*dA
82
83  def dCS(Cp,ny,dA): # differential side force coefficient contribution of a
        surface element
84      return Cp*ny*dA
85
86  def dCN(Cp,nz,dA): # differential normal force coefficient contribution of a
        surface element
87      return Cp*nz*dA
88
```

```python
89  '''moment computation functions'''
90  def dCl(Cp,r_i_cg,nhat_vec,dA):
91      #Inputs:
92      # r_i_cg == moment arm
93      xhat = [1,0,0]
94      return Cp*dA*np.dot(np.cross(r_i_cg,nhat_vec),xhat)
95
96  def dCm(Cp,r_i_cg,nhat_vec,dA):
97      yhat = [0,1,0]
98      return Cp*dA*np.dot(np.cross(r_i_cg,nhat_vec),yhat)
99
100 def dCn(Cp,r_i_cg,nhat_vec,dA):
101     zhat = [0,0,1]
102     return Cp*dA*np.dot(np.cross(r_i_cg,nhat_vec),zhat)
103
104 '''main computation function'''
105 def panelMethod(stlfilename,refArea,refLength,r_MRP,alpha,beta,Mach,gamma):
106     # Inputs:
107     # r_MRP == position vector of the moment reference point with respect to
108     the body fixed origin of the stl file
108     nhat_vec=returnNormal(stlfilename) #inward normal vectors
109     dA_vec=returnAreas(stlfilename)    #area of each element
110
111     v0 = returnv0(stlfilename) # [x,y,z] coordinates of the first vertex of
        each surface trangle element
112     v1 = returnv1(stlfilename) # [x,y,z] coordinates of the second vertex of
        each surface trangle element
113     v2 = returnv2(stlfilename) # [x,y,z] coordinates of the third vertex of
        each surface trangle element
114
115     Vinf = np.array([-np.cos(alpha)*np.cos(beta), -np.sin(beta), -np.cos(beta)
        *np.sin(alpha)]) #unite direction of freestream velocity
116
117     Cp = np.array([])
118     for i in nhat_vec:
119         result=computeCp(Vinf,i,Mach,gamma)
```

```python
120          Cp=np.append(Cp,result)
121
122      CA = np.array([])
123      for i in range(len(Cp)):
124          result=dCA(Cp[i],nhat_vec[i,0],dA_vec[i])
125          CA=np.append(CA,result)
126
127      CY = np.array([])
128      for i in range(len(Cp)):
129          result=dCS(Cp[i],nhat_vec[i,1],dA_vec[i])
130          CY=np.append(CY,result)
131
132      CN = np.array([])
133      for i in range(len(Cp)):
134          result=dCN(Cp[i],nhat_vec[i,2],dA_vec[i])
135          CN=np.append(CN,result)
136
137      CA=np.sum(CA)/refArea
138      CY=np.sum(CY)/refArea
139      CN=np.sum(CN)/refArea
140
141      '''compute moments'''
142      Cl = np.array([])
143      Cm = np.array([])
144      Cn = np.array([])
145      for i in range(len(Cp)):
146          centroid_i = computeCentroid(v0,v1,v2,i)
147          momentArm_i = computeMomentArm(centroid_i,r_MRP)
148          Cl = np.append(Cl,dCl(Cp[i],momentArm_i,nhat_vec[i],dA_vec[i]))
149          Cm = np.append(Cm,dCm(Cp[i],momentArm_i,nhat_vec[i],dA_vec[i]))
150          Cn = np.append(Cn,dCn(Cp[i],momentArm_i,nhat_vec[i],dA_vec[i]))
151
152      Cl = np.sum(Cl)/refArea/refLength
153      Cm = np.sum(Cm)/refArea/refLength
154      Cn = np.sum(Cn)/refArea/refLength
155
```

```
156    results=[-CA,CY,-CN,Cl,Cm,Cn]

157

158    return results

159

160 def liftdrag(CACYCN,alpha,beta):
161    '''this method computes the lift and drag coefficients from the newtonian
162    results for CA, CN, and CS; assumes that the roll-angle (sigma) is zero'''

163

164    ca = np.cos(alpha)
165    cb = np.cos(beta)
166    sa = np.sin(alpha)
167    sb = np.sin(beta)
168    CD = CACYCN[0]*ca*cb - CACYCN[1]*sb + CACYCN[2]*cb*sa   #drag coefficient
169    CS = CACYCN[0]*ca*sb + CACYCN[1]*cb + CACYCN[2]*sb*sa  #side-force
      coefficient
170    CL = -CACYCN[0]*sa - CACYCN[1]*0.0 + CACYCN[2]*ca  #lift coefficient
171    L2D = CL/CD

172

173    results = [CD,CS,CL,L2D]

174

175    return results
```

Below is a Python script illustrating the usage of the `newtonPanel.py` method to compute the hypersonic aerodynamics given an STL file called `bv.stl`.

```
1 #!/usr/bin/env python2
2 # -*- coding: utf-8 -*-
3 """
4 Created on Thu Apr  2 11:41:03 2020

5

6 @author: jannuel v. cabrera, jannuel.cabrera@gmail.com

7

8 This script is for running newtonPanel.py to get aerodynamic force and moment
      coefficient estimates in the hypersonic continuum regime
9 """

10

11 import newtonPanel as pan
```

```python
12 import numpy as np
13 import csv
14 import time
15 import math
16
17 dtr=np.pi/180.0 # deg to rad conversion factor
18
19 alpha = [-15,-10,-5,0,5,10,15] # deg
20 beta=[0] # deg
21
22 Aref=1.32 # meters^2
23 gamma=1.33 # spec. heat ratio for CO2 (Mars atmosphere)
24 refLength=1.35 # meters^2
25 r_MRP=np.array([-0.405,0.0,0.0]) # c.g. location
26 config=['bv'] #name of stl file
27 machNumber=23.9825
28
29 with open('bv_aero.csv', 'a') as csvFile:
30     writer = csv.writer(csvFile)
31     writer.writerow(['Config','Mach','Alpha (deg)','Beta (deg)','CA','CY','CN'
    ,'Cl','Cm','Cn','CD','CS','CL','L2D'])
32     for item in config:
33         stlfilename = item+'.stl'
34         for B in beta:
35             for A in alpha:
36                 Alpha=dtr*A
37                 Beta=dtr*B
38                 res=pan.panelMethod(stlfilename,Aref,refLength,r_MRP,Alpha,
    Beta,machNumber,gamma)
39                 res2=pan.liftdrag(res,Alpha,Beta)
40                 writer.writerow([item,machNumber,A,B,res[0],res[1],res[2],res
    [3],res[4],res[5],res2[0],res2[1],res2[2],res2[3]])
41 csvFile.close()
```

D.2 Free Molecular Source Code

Below is the Python source code for the free molecular panel method, `freemolPanel.py`, described in Chapter 3.

```python
#!/usr/bin/env python2
# -*- coding: utf-8 -*-
"""
Created on Sat Apr 18 15:45:14 2020

@author: jannuel v. cabrera, jannuel.cabrera@gmail.com
"""

"""
This code is a free-molecular aerodynamics estimator
"""
import numpy as np
import math
from stl import mesh
import time
import csv

'''Some auxiliary functions'''

def returnNormal(stlfilename):
    # return the outward unit normal vectors of each facet
    myMesh = mesh.Mesh.from_file(stlfilename)
    return myMesh.units #return outward unit normal

def returnAreas(stlfilename):
    # return area of each facet (facet==surface element)
    myMesh = mesh.Mesh.from_file(stlfilename)
    return myMesh.areas

def returnSurfAlpha(V_inf,unit_normal):
```

```python
31      # based on definition used by Hart et. al., Eq. (8) in "Analytic free-
        molecular aerodynamics for rapid propagation of resident space objects",
        2018.
32      sina = np.dot(-V_inf,unit_normal)
33      surfAlpha = math.asin(sina) #inclination angle of the surface element
34      return surfAlpha
35
36  def returnv0(stlfilename):
37      # returns the position vectors of the first vertex of each surface element
38      myMesh = mesh.Mesh.from_file(stlfilename)
39      return myMesh.v0
40
41  def returnv1(stlfilename):
42      # returns the position vectors of the second vertex of each surface
        element
43      myMesh = mesh.Mesh.from_file(stlfilename)
44      return myMesh.v1
45
46  def returnv2(stlfilename):
47      # returns the position vectors of the third vertex of each surface element
48      myMesh = mesh.Mesh.from_file(stlfilename)
49      return myMesh.v2
50
51  def computeCentroid(v0,v1,v2,ith_element):
52      # computes the coordinates of the centroid of the ith surface element
53      # see https://www.mathopenref.com/coordcentroid.html for reference on
        computing the centroid of a triangle
54      #v0 = myMesh.v0 # vertex 1
55      #v1 = myMesh.v1 # vertex 2
56      #v2 = myMesh.v2 # vertex 3
57      i=ith_element
58
59      Cx = (v0[i][0] + v1[i][0] + v2[i][0])/3
60      Cy = (v0[i][1] + v1[i][1] + v2[i][1])/3
61      Cz = (v0[i][2] + v1[i][2] + v2[i][2])/3
62
```

```python
63      return [Cx,Cy,Cz] #centroid coordinates of the ith element in the stl file

64

65 def computeMomentArm(centroid_i,r_MRP):
66      # centroid_i == position vector of the ith surface element's centroid
67      # r_momrefpt == position vector of the moment reference point (MRP)
68      momentArm = centroid_i-r_MRP
69      return momentArm

70

71 def computePressure(surfAlpha,speedRatio,specularFraction,reflectedTemp,
    freestreamTemp):
72      # Based on Eq. 7.58 in G.A. Bird's "Molecular Gas Dynamics and the Direct
    Simulation of Gas Flows", 1994
73      # this function computes the Cp_i of a surface element "i"

74

75      #reassign variables
76      Tr = reflectedTemp #Kelvin
77      Tinf = freestreamTemp #Kelvin
78      E = specularFraction #nondimensional
79      a = surfAlpha #radians == angle of incidence of the surface element "i"
    with respect to the flow velocity vector
80      s = speedRatio #meters/sec
81      sina = np.sin(a)

82

83      if np.abs(a) > np.pi/2: # leeward side surface element == assume no
    pressure forces
84          Cp = 0.0
85      else:
86          A = (1+E)*s*sina/np.sqrt(np.pi) + 0.5*(1-E)*np.sqrt(Tr/Tinf)
87          B = (1+E)*(0.5+math.pow(s*sina,2)) + 0.5*(1-E)*np.sqrt(Tr/Tinf)*np.
    sqrt(np.pi)*s*sina
88          #note: error in Eq. 7.58 in Bird, in which he raises the second (Tr/Tf
    )
89          #        term (i.e. in the "B" quantity above) to the (-1/2) power.
90          #        The correct power is (1/2). This is validated by the
    expressions used in
91          #        Hart et. al.
```

```python
92
93        pressure_ratio = A * math.exp(-math.pow(s*sina,2)) + B * (1+math.erf(s
      *sina))
94        Cp = pressure_ratio/math.pow(s,2)
95
96     return Cp
97
98 def computeShear(surfAlpha,speedRatio,specularFraction):
99     # Based on Eq. 7.61 in G.A. Bird's "Molecular Gas Dynamics and the Direct
      Simulation of Gas Flows", 1994
100    # this function computes the Cf_i of a surface element "i"
101
102    #reassign variables
103    E = specularFraction #nondimensional
104    a = surfAlpha #radians
105    s = speedRatio #meters/sec
106    sina = np.sin(a)
107    cosa = np.cos(a)
108
109    if np.abs(a) > np.pi/2: # leeward side surface element == assume no shear
      forces
110        Cf = 0.0
111    else:
112        A = (1-E)*s*cosa/np.sqrt(np.pi)
113
114        shear_ratio = A * (math.exp(-math.pow(s*sina,2))+np.sqrt(np.pi)*s*sina
      *(1+math.erf(s*sina)))
115        Cf = shear_ratio/math.pow(s,2)
116
117    return Cf
118
119 def dCF(Cp_i,Cf_i,nhat_i,dA_i,Vhat):
120    # Inputs:
121    # Cp_i == pressure coefficient of the surface element "i"
122    # Cf_i == shear friction coefficient of the surface element "i"
```

```python
123        # n_hat_i == unit normal vector of the surface element "i" (outward normal
           )
124        # Vhat == unit direction of the velocity vector
125        # dA_i == area of the surface element "i"
126        #this computes the individual contribution of a surface element to the x-
           force, y-force, and z-force
127        A = np.dot(Cp_i,nhat_i)
128        t_hat_i = np.cross(nhat_i,np.cross(-Vhat,nhat_i))/np.sqrt(1.0-math.pow(np.
           dot(Vhat,nhat_i),2)) #C = np.cross(n,np.cross(-V,n))/np.sqrt(1.0-math.pow(
           np.dot(V,n),2))
129        B = np.dot(Cf_i,t_hat_i)
130        dCF_vector = (A + B) * dA_i
131        return dCF_vector # returns a numpy array
132
133 def dCM(dCF_i,momentArm_i):
134        # Inputs:
135        # dCF_i == vector containing the x, y, and z force contribution of the ith
            panel
136        # momentArm_i == position vector of the ith panel with respect to the
           moment ref. point (MRP)
137        #this function computes the moment contribution vector of the ith panel;
           returns a vector [dCl_i, dCm_i, dCn_i]
138        dCM_vector = np.cross(momentArm_i,dCF_i)
139        return dCM_vector # returns numpy array of three elements
140
141 '''main code to compute the force and moment coefficients'''
142 def computeCoefficients(stlfilename,refArea,refLength,reflectedTemp,
           freestreamTemp,specularFraction,speedRatio,angleOfAttack,sideslip,
           moment_ref_pt):
143        # This is the big function that computes the force and moment coefficients
            in the body frame.
144        alpha = angleOfAttack
145        beta = sideslip
146        Vhat = np.array([-np.cos(alpha)*np.cos(beta), -np.sin(beta), -np.cos(beta)
           *np.sin(alpha)]) #unit-direction of freestream velocity
147
```

```python
148    nhat_vectors = returnNormal(stlfilename) # returns a numpy.ndarray
149    surf_areas = returnAreas(stlfilename) # returns a numpy.ndarray
150    v0 = returnv0(stlfilename)
151    v1 = returnv1(stlfilename)
152    v2 = returnv2(stlfilename)
153
154    CFx = np.array([])
155    CFy = np.array([])
156    CFz = np.array([])
157    Cl = np.array([]) # roll moment
158    Cm = np.array([]) # pitch moment
159    Cn = np.array([]) # yaw moment
160
161    for i in range(len(nhat_vectors)):
162        surfAlpha = returnSurfAlpha(Vhat,nhat_vectors[i])
163        dA_i = surf_areas[i]
164        nhat_i = nhat_vectors[i]
165        Cp_i = computePressure(surfAlpha,speedRatio,specularFraction,
    reflectedTemp,freestreamTemp)
166        Cf_i = computeShear(surfAlpha,speedRatio,specularFraction)
167        dCF_i = dCF(Cp_i,Cf_i,nhat_i,dA_i,Vhat) # returns a vector the force
    contribution of the current surface element: [dCFx, dCFy, dCFz]
168
169        CFx = np.append(CFx,dCF_i[0]) # array of the CFx_i of each surface
    element
170        CFy = np.append(CFy,dCF_i[1]) # array of the CFy_i of each surface
    element
171        CFz = np.append(CFz,dCF_i[2]) # array of the CFz_i of each surface
    element
172
173        '''for the moment computations'''
174        centroid_i = computeCentroid(v0,v1,v2,i)
175        momArm_i = computeMomentArm(centroid_i,moment_ref_pt)
176        dCM_i = -dCM(dCF_i,momArm_i) # added the minus sign to account for the
    reverse moment created by a dF vector pointing outward (due to outward
    normal vector of each surface)
```

```
177
178          Cl = np.append(Cl,dCM_i[0]) # array of roll moment coefficients
179          Cm = np.append(Cm,dCM_i[1]) # array of roll moment coefficients
180          Cn = np.append(Cn,dCM_i[2]) # array of roll moment coefficients
181
182      # To compute overall force coefficients in the x, y, and z directions, sum
183      # all elements in CFx, CFy, and CFz and normalize by the total reference
184      # area of the body/vehicle.
185      CA = np.sum(CFx)/refArea
186      CY = np.sum(CFy)/refArea
187      CN = np.sum(CFz)/refArea
188      # To compute overall moment coefficients, sum moment contributions of all
189      # panels over the entire geometry and normalize by the total reference
         area
190      # and referent length of the body/vehicle
191      Cl = np.sum(Cl)/refArea/refLength
192      Cm = np.sum(Cm)/refArea/refLength
193      Cn = np.sum(Cn)/refArea/refLength
194
195      return [CA, CY, CN, Cl, Cm, Cn]
196
197 def liftdrag(CACYCN,alpha,beta):
198      '''this method computes the lift and drag coefficients from the free-
         molecular
199      results for CA, CY, and CN; assumes that the roll-angle (sigma) is zero'''
200
201      ca = np.cos(alpha)
202      cb = np.cos(beta)
203      sa = np.sin(alpha)
204      sb = np.sin(beta)
205      CD = CACYCN[0]*ca*cb - CACYCN[1]*sb + CACYCN[2]*cb*sa   #drag coefficient
206      CS = CACYCN[0]*ca*sb + CACYCN[1]*cb + CACYCN[2]*sb*sa  #side-force
         coefficient
207      CL = -CACYCN[0]*sa - CACYCN[1]*0.0 + CACYCN[2]*ca  #lift coefficient
208      L2D = CL/CD
209
```

```
210    results = [CD, CS, CL, L2D]
211
212    return results
```

Below is a Python script illustrating the usage of the `freemolPanel.py` method to compute the free molecular aerodynamics given an STL file called `bv.stl`.

```python
1  #!/usr/bin/env python2
2  # -*- coding: utf-8 -*-
3  """
4  Created on Thu Apr 23 10:13:35 2020
5
6  @author: jannuel v. cabrera, jannuel.cabrera@gmail.com
7
8  This script is for running freemolPanel.py to get aerodynamic force
       coefficient estimates in the free-molecular regime
9  """
10 import numpy as np
11 import freemolPanel as fm
12 import time
13 import csv
14
15 config = ['bv'] # name of stl file
16 dtr = np.pi/180.0 # deg to rad conversion factor
17 refArea = 1.32 # meters^2 reference area of the MES, based on the baseline
       frontal area
18 reflectedTemp = 349.9538 # Kelvin
19 freestreamTemp = 290.7275 # Kelvin
20 specularFraction = 0.0 # specularFraction = E --> fully-specular if E=1, which
        means sigma=0; fully-diffusive if E=0, which means sigma=1
21 Vinfinity = 5286.90# meters/sec
22 R = 188.92 #specific gas constant of carbon dioxide (CO2) in J/kg/K
23 gamma = 1.33
24 speedRatio = Vinfinity/np.sqrt(2*R*freestreamTemp)
25 angleOfAttack = [-30,-25,-20,-15,-10,-5,0,5,10,15,20,25,30] #deg
26 sideslip = [0] # deg
27 Knudsen=232.24
```

```python
28  moment_ref_pt=np.array([-0.405,0.0,0.0]) # c.g. location
29  refLength=1.35 # meters
30
31
32  with open('bv_aero.csv', 'a') as csvFile:
33      writer = csv.writer(csvFile)
34      writer.writerow(['Config','Alpha','Beta','CA','CY','CN','Cl','Cm','Cn','CD
        ','CS','CL','L2D'])
35      for item in config:
36          mystlfile = item+'.stl'
37          for B in sideslip:
38              for A in angleOfAttack:
39                  aoa = A*dtr
40                  beta = B*dtr
41                  res = fm.computeCoefficients(mystlfile,refArea,refLength,
        reflectedTemp,freestreamTemp,specularFraction,speedRatio,aoa,beta,
        moment_ref_pt)
42                  res2 = fm.liftdrag(res,aoa,beta)
43                  writer.writerow([item,A,B,res[0],res[1],res[2],res[3],res[4],
        res[5],res2[0],res2[1],res2[2],res2[3]])
44  csvFile.close()
```

VITA

Jannuel Cabrera received his B.S. in Aerospace Engineering from Syracuse University in 2016. He joined the Spaceflight Projects Laboratory research group in early 2017 and subsequently received his M.S. in Aeronautics and Astronautics from Purdue University in 2018. Cabrera started a Pathways position with the Vehicle Analysis Branch at NASA Langley Research Center in 2020. Outside of research, Cabrera plays second base for the Aero Assault graduate softball team and goes on extended jogs around the West Lafayette area. In addition to staying active, Cabrera also enjoys playing music and watching anime. Having been born and raised in the Philippines, Cabrera is fluent in two other languages besides English: *Tagalog* and *Ilocano*.